

Probing the High Pressure Effect on Morphinone Reductase Using Computational Methods

A thesis submitted to The University of Manchester for the degree of
Doctor of Philosophy
in the Faculty of Engineering and Physical Sciences

2011

Thomas Anthony McGrory

School of Chemical Engineering and Analytical Science

Table of Contents

| | |
|---|----|
| Table of Contents..... | 2 |
| List of Figures..... | 5 |
| List of Tables..... | 11 |
| List of Abbreviations..... | 13 |
| Abstract..... | 14 |
| Declaration..... | 15 |
| Copyright Statement..... | 15 |
| Acknowledgements..... | 16 |
| Publications From This Thesis..... | 17 |
| Introduction..... | 18 |
| PREFACE..... | 19 |
| 1.1 ENZYME CATALYSIS..... | 20 |
| 1.1 ENZYME CATALYSIS..... | 20 |
| 1.1.1 Introduction..... | 20 |
| 1.1.2 Transition State Theory..... | 21 |
| 1.1.3 Quantum Considerations for Catalysis..... | 24 |
| 1.1.3.1 Semi-Classical TST..... | 24 |
| 1.1.3.2 Kinetic Isotope Effect (KIE)..... | 25 |
| 1.1.3.3 Hydrogen Tunneling..... | 26 |
| 1.1.3.4 Hydrogen Tunneling in Enzyme Catalysed Reactions..... | 28 |
| 1.1.4 Enzyme Dynamics..... | 29 |
| 1.2 MORPHINONE REDUCTASE..... | 33 |
| 1.2.1 Flavoproteins..... | 33 |
| 1.2.2 Structure and Function..... | 35 |
| 1.2.3 Mechanism..... | 37 |
| 1.2.4 Hydrogen Tunneling Implications..... | 38 |
| 1.3 PRESSURE EFFECT ON ENZYMES..... | 42 |
| 1.3.1 Experimental Studies of Proteins at High Pressure..... | 43 |
| 1.3.2 Computational Studies of Proteins at High Pressure..... | 45 |
| 1.3.3 High Pressure Effect on MR..... | 47 |
| 1.4 COMPUTATIONAL CHEMISTRY..... | 48 |
| 1.4.1 Molecular Dynamics..... | 48 |
| 1.4.2 Quantum Mechanical Techniques..... | 49 |
| 1.4.3 Combined QM/MM..... | 50 |
| 1.5 SUMMARY & AIMS OF PROJECT..... | 51 |
| Methodology..... | 54 |
| PREFACE..... | 55 |
| 2.1 INTRODUCTION TO COMPUTATIONAL CHEMISTRY..... | 56 |
| 2.1.1 Molecular Mechanics..... | 56 |
| 2.1.2 Force Fields..... | 57 |
| 2.1.3 Energy Minimisation..... | 60 |
| 2.1.4 Molecular Dynamics..... | 61 |
| 2.1.5 Quantum Mechanics..... | 64 |
| 2.1.5.1 Introduction..... | 64 |
| 2.1.5.2 Basis Sets..... | 66 |

| | |
|--|-----|
| 2.1.5.3 Hartree-Fock Method..... | 67 |
| 2.1.5.4 Density Functional Theory..... | 67 |
| 2.1.5.5 Hybrid QM/MM Simulations..... | 69 |
| 2.1.5.6 ONIOM..... | 70 |
| 2.2 METHODOLOGY USED IN THIS THESIS..... | 70 |
| 2.2.1 Molecular Dynamics Simulations of Waterbox..... | 70 |
| 2.2.2 MD Simulations of the AK-peptide..... | 72 |
| 2.2.3 MD Simulations of MR..... | 73 |
| 2.2.3.1 System Setup..... | 73 |
| 2.2.3.2 Minimisation and MD Simulations..... | 75 |
| 2.2.4 Analysis of MD Trajectories..... | 76 |
| 2.2.4.1 Ptraj..... | 76 |
| 2.2.4.2 Visual Molecular Dynamics (VMD)..... | 77 |
| 2.2.4.3 Normal Mode Analysis..... | 78 |
| 2.2.4.4 Principal Components Analysis..... | 79 |
| 2.2.4.5 Essential Dynamics..... | 79 |
| 2.2.5 QM/MM Methods..... | 80 |
| 2.2.5.1 Benchmarking the Method..... | 80 |
| 2.2.5.2 QM/MM Setup in ONIOM..... | 81 |
| 2.2.5.3 QM/MM Potential Energy Scans..... | 82 |
| High Pressure Molecular Dynamics Simulations..... | 83 |
| PREFACE..... | 84 |
| 3.1 WATER BOX..... | 85 |
| 3.1.1 Results at Atmospheric Pressure..... | 85 |
| 3.1.2 Effect of Increasing Pressure..... | 87 |
| 3.1.3 Comparison with Experiment..... | 89 |
| 3.1.4 Summary of the Benchmark Simulation of a Waterbox..... | 92 |
| 3.2 SIMULATIONS OF HELICAL PEPTIDE AT CONSTANT PRESSURE..... | 92 |
| 3.2.1 Stability of Peptide..... | 93 |
| 3.2.2 Radius of Gyration..... | 95 |
| 3.2.3 End to End Distance..... | 97 |
| 3.2.4 Water coordination..... | 99 |
| 3.2.5 AK Peptide Summary..... | 100 |
| 3.3 SIMULATIONS OF MR AT CONSTANT PRESSURE..... | 101 |
| 3.3.1 Protein Stability..... | 101 |
| 3.3.2 Secondary Structure..... | 105 |
| 3.3.3 Volume of Protein..... | 107 |
| 3.3.4 Pressure Effect on Water MR Simulations of MR..... | 111 |
| 3.4 CONCLUSIONS..... | 112 |
| Atomistic Analysis of the Pressure Effect on Morphinone Reductase..... | 115 |
| PREFACE..... | 116 |
| 4.1 SUBSTRATE & COFACTOR..... | 117 |
| 4.1.1 Donor-Acceptor Distance..... | 118 |
| 4.1.2 Distribution of Donor-Acceptor Distances..... | 121 |
| 4.1.3 1.5 kbar Donor-Acceptor Distance..... | 123 |
| 4.1.4 Motion of Nicotinamide..... | 125 |
| 4.1.5 Substrate & Cofactor Summary..... | 130 |
| 4.2 ANALYSIS OF ACTIVE SITE RESIDUES..... | 131 |

| | |
|--|-----|
| 4.2.1 RMSDs / RMSFs of Active Site Residues..... | 132 |
| 4.2.2 Essential Dynamics | 134 |
| 4.2.3 Tryptophan 106 | 136 |
| 4.2.4 Tyrosine 72 / Phenylalanine 246..... | 138 |
| 4.2.5 Active Site Summary..... | 140 |
| 4.3 RESIDUES OUTSIDE ACTIVE SITE..... | 140 |
| 4.3.1 Dynamic Domain | 141 |
| 4.3.2 Valine 108..... | 143 |
| 4.3.3 Significance of Valine 108..... | 144 |
| 4.3.4 Outside the Active Site Summary | 145 |
| 4.4 MOLECULAR DYNAMICS ON MUTANT MR | 146 |
| 4.4.1 Simulations of Mutated Morphinone Reductase..... | 147 |
| 4.4.2 Donor-Acceptor Distances in MR_N189A..... | 148 |
| 4.4.3 Overlap of Nicotinamide and Isoalloxazine | 151 |
| 4.4.5 Mutant MR Summary | 153 |
| 4.5 CONCLUSIONS..... | 154 |
| QM/MM Studies of the Hydride Transfer Step Catalysed by Morphinone Reductase | 157 |
| PREFACE..... | 158 |
| 5.1 BENCHMARKING | 159 |
| 5.1.1 Gas Phase Calculations..... | 159 |
| 5.1.2 QM/MM Benchmarking | 162 |
| 5.2 QM/MM CALCUALTIONS AT HIGH AND LOW PRESSURES | 165 |
| 5.2.1 Representative Structures | 166 |
| 5.2.2 Geometry Optimisation | 169 |
| 5.2.3 Potential Energy Scans | 171 |
| 5.3 FURTHER ANALYSIS OF QM/MM | 177 |
| 5.3.1 Reaction Coordinate | 177 |
| 5.3.2 KIE Calculation..... | 181 |
| 5.3.3 Frequency Analysis | 183 |
| 5.4 CONCLUSIONS..... | 184 |
| Conclusions and Future Perspectives..... | 188 |
| 6.1 GENERAL CONCLUSIONS..... | 189 |
| 6.2 IMPACT ON OTHER RESEARCH..... | 192 |
| 6.3 FUTURE PERSPECTIVES..... | 193 |
| Appendix A | 195 |
| Appendix B..... | 198 |
| Appendix C..... | 199 |
| Appendix D | 200 |
| Appendix E..... | 201 |
| Appendix F..... | 202 |
| References | 204 |

Word count: 40,188

List of Figures

Chapter 1

| | |
|---|----|
| Figure 1.1. Simple representation of Transition State Theory | 22 |
| Figure 1.2. Reaction profile for hydrogen transfer with semi-classical TST Hydrogen isotope transfer reaction profile for semi-classical TST | 24 |
| Figure 1.3. Propagation of a wavefunction through a symmetrical energy barrier..... | 26 |
| Figure 1.4. Reaction profile for hydrogen transfer with semi-classical TST with Bell Correction..... | 27 |
| Figure 1.5. The rate of a hydrogen transfer reaction as a function of temperature. | 29 |
| Figure 1.6. Illustration of vibrationally coupled H-tunneling | 32 |
| Figure 1.7. Structure of FAD/FMN | 34 |
| Figure 1.8. Structure of NAD(P)H | 35 |
| Figure 1.9. Active site of MR in complex with NADH ₄ | 36 |
| Figure 1.10. Representation of one monomer of MR | 36 |
| Figure 1.11. Catalytic mechanism of MR | 38 |
| Figure 1.12. Principal component analysis from 10 ns molecular dynamics simulations of wild-type and N189A MR. (b) Relative positions of FMN (isoalloxazine), NADH (nicotinamide), Asn/Ala-189, and His-186 | 40 |
| Figure 1.13. Free energy of activation | 41 |
| Figure 1.14. Effect of pressure on the deuterium isotope effect on hydride transfer | 44 |
| Figure 1.15. Possible pressure induced motion to shorten donor-acceptor distance between cofactors in MR | 47 |
| Figure 1.16. An example of a QMMM approach..... | 51 |

Chapter 2

| | |
|--|----|
| Figure 2.1. Figure to show minimum energy paths for steepest descent and conjugate gradients minimisation methods..... | 60 |
|--|----|

| | |
|--|-----|
| Figure 2.2. Periodic Boundary Conditions represented in two dimensions..... | 62 |
| Figure 2.3. Morphinone Reductase in 15 Å ³ waterbox | 74 |
| Figure 2.4. Figure to illustrate the effect of mutating Asn189 to alanine..... | 75 |
| Figure 2.5. Diagram showing the QM region used in the QM/MM method..... | 81 |
| Chapter 3 | |
| Figure 3.1. Properties of waterbox at atmospheric pressure | 85 |
| Figure 3.2. Properties of waterbox across pressure range | 87 |
| Figure 3.3. Graph showing the agreement of experimental density of water across the pressure range to density calculated in waterbox simulations | 89 |
| Figure 3.4. The oxygen-oxygen radial distribution function for the water box compared to the experimental values..... | 90 |
| Figure 3.5. The oxygen-oxygen radial distribution function, as calculated in VMD for the waterbox simulations at 1 bar, 1 kbar and 2 kbar | 91 |
| Figure 3.6. The structure of the AK Peptide | 93 |
| Figure 3.7. The RMSD of the peptide backbone for the 5 ns simulation. | 94 |
| Figure 3.8. Bending of the helix characterized by peaks on the RMSD plot | 94 |
| Figure 3.9. The RMSF of the peptide backbone for the 5 ns simulation..... | 95 |
| Figure 3.10. Radius of Gyration of the α-carbons of the peptide at different pressures across the 5 ns production simulation..... | 96 |
| Figure 3.11. Distance in Å between the α-carbon of Ala2 and the α-carbon of Tyr23 across the 5 ns production trajectory | 98 |
| Figure 3.12. Average number of water molecules coordinated to each carbonyl of the peptide backbone at different pressures | 99 |
| Figure 3.13. RMSD of protein backbone of MR across pressure range..... | 102 |
| Figure 3.14. RMSF of protein α-carbons of MR across pressure range..... | 103 |
| Figure 3.15. Comparison of crystallographic B-factors with atomic fluctuations taken from simulation at atmospheric pressure..... | 104 |

| | |
|--|-----|
| Figure 3.16. Secondary structure of MR at 1 bar, over a 10 ns trajectory..... | 105 |
| Figure 3.17. Pie charts showing the average percentage of each secondary structure sampled by MR at 1 bar | 106 |
| Figure 3.18. Average secondary structure of MR across pressure range | 107 |
| Figure 3.19. Radius of Gyration of protein α -carbons of MR during 10 ns simulation at different pressures..... | 108 |
| Figure 3.20. Solvent Accessible Surface Area of MR during 10 ns simulation at different pressures..... | 109 |
| Figure 3.21. Plot showing average Radius of Gyration and Solvent Accessible Surface Area..... | 110 |
| Figure 3.22. Number of water molecules within 3 Å of core of MR across pressure range..... | 111 |
| Figure 3.23. Average number of water molecules within 3 Å of core of MR across pressure range..... | 112 |
| Chapter 4 | |
| Figure 4.1. (a) The active site of MR in the protein environment. (b) Magnification of substrate and cofactor..... | 117 |
| Figure 4.2. Figure showing how the C4-N5 distance varies at each pressure | 118 |
| Figure 4.3. The distribution of C4-N5 distances sampled at each pressure..... | 120 |
| Figure 4.4. Distribution of C4-N5 distances from 1 bar, 1 kbar and 2 kbar..... | 122 |
| Figure 4.5. Figure showing the C4-N5 distance across 1.5 kbar trajectory with the average distance from the first half of the trajectory shown for comparison | 124 |
| Figure 4.6. Figure showing the position of Phe246 for (a) the first 5.7 ns of the 1.5 kbar simulation and (b) the remainder of the simulation..... | 124 |
| Figure 4.7. 2D-RMSD analysis of the nicotinamide ring at 1 bar and 2 kbar | 126 |
| Figure 4.8. Figure showing Principal Components Analysis of the 2D-RMSD performed on the nicotinamide..... | 128 |

| | |
|---|-----|
| Figure 4.9. The nicotinamide average structure obtained from the cluster of 1 bar frames circled green in Figure 4.8(b), overlaid on the the average structure of 2 kbar frames..... | 129 |
| Figure 4.10. Figure showing an atomistic representation of the active site of MR | 132 |
| Figure 4.11. Figure showing RMSDs of the C- α 's of active site residues: Thr32, Tyr72, Trp106, Phe137, His186, Asn189, Phe246 and Tyr356 | 133 |
| Figure 4.12. Figure showing RMSFs of the C- α 's of active site residues: Thr32, Tyr72, Trp106, Phe137, His186, Asn189, Phe246 and Tyr356 | 133 |
| Figure 4.13. Eigenvectors from the PCA on a covariance matrix of the heavy atoms of the nicotinamide ring, isoalloxazine ring and 8 selected active site residues..... | 134 |
| Figure 4.14. Tyr72 and Trp106 in the active site | 136 |
| Figure 4.15. (a) The distance between the nicotinamide ring the tryptophan ring at low and high pressures. (b) The distance between the isoalloxazine ring and the tryptophan ring at low and high pressures | 137 |
| Figure 4.16. Correlation of the distance between the isoalloxazine ring and the tryptophan ring with the donor-acceptor distance..... | 138 |
| Figure 4.17. Correlation of the distance between the isoalloxazine ring and (a) the tyrosine ring at low pressure; (b) the tyrosine ring at high pressure; (c) the phenylalanine ring at low pressure; and (d) the phenylalanine ring at high pressure with the donor-acceptor distance | 139 |
| Figure 4.18. Figure to show movement of residues 108-156 with respect to the rest of the protein | 141 |
| Figure 4.19. RMSFs of domain 108 – 156 at 1 bar and at 2 kbar | 142 |
| Figure 4.20. Dihedral angle to represent configuration of Valine 108 C α -C β bond..... | 143 |
| Figure 4.21. Diagram showing the different transformations that occur in the Valine 108 dihedral at low pressure and high pressure, from the crystal structure..... | 144 |
| Figure 4.22. Figure showing (a) Asn189 in the active site of wild-type MR (a) Ala189 residue in the active site of MR_N189A..... | 146 |

| | |
|---|-----|
| Figure 4.23. RMSDs of protein backbone of MR_N189A..... | 147 |
| Figure 4.24. Figure showing the C4-N5 distance varies for 1 bar and 2 kbar WT and N189A MR..... | 148 |
| Figure 4.25. The distribution of C4-N5 distances sampled for 1 bar and 2 kbar WT and N189A MR..... | 149 |
| Figure 4.26. Figure showing the distribution of donor acceptor distances from MR_N189A at 1 bar and at 2 kbar..... | 150 |
| Figure 4.27. Figure showing the dihedral angle that represents the overlap between the nicotinamide and isoalloxazine rings..... | 151 |
| Figure 4.28. Figure showing how the overlap between the nicotinamide and isoalloxazine rings varies across the 10 ns trajectory for 1 bar and 2 kbar WT and N189A MR..... | 152 |
| Chapter 5 | |
| Figure 5.1. A simplified structure of the active site of MR..... | 159 |
| Figure 5.2. The optimised geometries of the simplified active site gas phase calculations using BH&H and B3LYP..... | 160 |
| Figure 5.3. Potential Energy Scan for the gas phase QM calculations using the BH&H DFT functional with three different basis sets..... | 161 |
| Figure 5.4. Potential energy scans from the benchmark QM/MM calculations using BH&H and B3LYP and 3 different basis sets..... | 164 |
| Figure 5.5. Representation of the active site of MR in the representative structures from 1 bar and 2 kbar..... | 167 |
| Figure 5.6. The RMSDs of the active site residues Tyr72, Trp106 and Phe246..... | 168 |
| Figure 5.7. Figure to show the minimised geometry of the 20 structures used in the QM/MM calculations..... | 171 |
| Figure 5.8. Potential energy scans from the 20 QM/MM calculations using BH&H with the 6-31+G* basis set..... | 175 |

| | |
|---|-----|
| Figure 5.9. The potential energy scan for 1 bar frames 299, 331, 336, 363 and 401 with the reaction coordinate represented as the bond-breaking minus the bond-forming..... | 179 |
| Figure 5.10. The potential energy scan for 2 kbar frames 011, 033, 062, 083 and 233 with the reaction coordinate represented as the bond-breaking minus the bond-forming..... | 180 |
| Figure 5.11. Motion represented in the 100 -180 cm-1 region of frequencies from the optimized reactant geometry | 184 |
| Figure 5.12. Figure showing correlation between donor-acceptor distance and activation energy | 186 |
| Appendix | |
| Figure A.1. The sequence and DSSP secondary structure assignment of MR | 195 |
| Figure A.2. Number of water atoms within particular distances of the core of the MR .. | 196 |
| Figure C.1. Figure showing the heavy atoms of the nicotinamide ring of the NADH substrate, with atom number detail..... | 199 |
| Figure C.2. Figure showing the heavy atoms of the isoalloxazine ring of the FMN cofactor, with atom number detail | 199 |
| Figure D.1. 2D-RMSD analysis of the nicotinamide ring at 1 bar and 2 kbar | 200 |
| Figure E.1. Radius of Gyration (RadGyr) of MR_N189A..... | 201 |
| Figure E.2. Solvent Accessible Surface Area (SASA) of MR_N189A | 201 |
| Figure F.1. The potential energy scan for 1 bar frames 025, 232, 289, 325 and 430 with the reaction coordinate represented as the bond-breaking minus the bond-forming..... | 202 |
| Figure F.2. The potential energy scan for 2 kbar frames 004, 112, 120, 215 and 358 with the reaction coordinate represented as the bond-breaking minus the bond-forming..... | 203 |

List of Tables

Chapter 3

| | | |
|------------|--|-----|
| Table 3.1. | Average values at of various waterbox properties at atmospheric pressure ... | 86 |
| Table 3.2. | Average values at of various waterbox properties across the pressure range . | 88 |
| Table 3.3. | Comparison between experimental density for water and average densities from waterbox simulations | 89 |
| Table 3.4. | Average values for the Radius of Gyration of the α -carbons..... | 96 |
| Table 3.5. | Average distance in Å between of the α -carbon of Ala2 and the α -carbon of Tyr23 | 98 |
| Table 3.6. | Averages values of the RMSD of the protein backbone of MR for the 10 ns trajectories at different pressures | 102 |
| Table 3.7. | Averages values of the RMSF of the α -carbons of MR for the 10 ns trajectories at different pressures | 103 |
| Table 3.8. | Average and standard deviations of Radius of Gyration for α -carbons of MR over 10 ns simulation at different pressures | 108 |
| Table 3.9. | Average and standard deviations of Solvent Accessible Surface Area of MR over 10 ns simulation at different pressures | 110 |

Chapter 4

| | | |
|------------|---|-----|
| Table 4.1. | Average values for the C4-N5 distance | 119 |
| Table 4.2. | Distribution tests for C4-N5 distance | 121 |
| Table 4.3. | Distances from projection of eigenvector 1 in IED | 135 |
| Table 4.4. | Output from DynDom | 142 |
| Table 4.5. | Average values for the C4-N5 distance before and after the change of configuration (flip) of Val108 | 145 |
| Table 4.6. | Average values for the C4-N5 distance of MR_N189A and WT MR at 1 bar and 2 kbar | 148 |

| | | |
|------------|--|-----|
| Table 4.7. | Distribution tests for C4-N5 distance in MR_N189A | 150 |
| Table 4.8. | Average values for the overlap between the nicotinamide and isoalloxazine rings..... | 152 |
| Table 4.9. | Number of configurations within a given range of angles to represent differing degrees of nicotinamide-isoalloxazine overlap | 153 |

Chapter 5

| | | |
|------------|---|-----|
| Table 5.1. | The lowest vibrational frequencies calculated from optimized geometries using 2 different DFT methods (BH&H and B3LYP) and 3 different basis sets for each method: 6-31G*, 6-31+G* and 6-311++G** | 163 |
| Table 5.2. | The potential energy taken from the potential energy scans in Figure 5.4... .. | 165 |
| Table 5.3. | The frames chosen for QM/MM from the RMSD shown in Figure 5.6..... | 170 |
| Table 5.4. | Table summarizing the potential energy scans for frames taken from the 1 bar trajectory..... | 173 |
| Table 5.5. | Table summarizing the potential energy scans for frames taken from the 2 kbar trajectory..... | 174 |
| Table 5.6. | The imaginary vibrational frequencies from the structures taken at the TS . | 176 |
| Table 5.7. | The KIEs calculated by the WKB model for the QM/MM..... | 182 |

Appendix

| | | |
|------------|---|-----|
| Table A.1. | Secondary structure percentages of MR at 1 bar..... | 195 |
| Table A.2. | Amino acids that form the beta-barrel in the centre of MR | 196 |
| Table A.3. | Average number of water atoms at different distances from core of MR at 1 bar | 197 |
| Table B.1. | Table showing the binned values for different ranges of donor-acceptor distances | 198 |
| Table E.1. | Average values for Radius of Gyration and Solvent accessible surface area of MR_N189A at 1 bar and 2 kbar | 201 |

List of Abbreviations

| | |
|------------------------------|--|
| 2D-RMSD | Two-dimensional Root Mean Square Deviation |
| AMBER | Assisted Model Building with Energy Refinement |
| DFT | Density Function Theory |
| DSSP | Dictionary of Secondary Structure Prediction |
| FAD | Flavin Adenine Dinucleotide |
| FMN | Flavin Mononucleotide |
| GHO | Generalised Hybrid Orbital |
| g(R) | Radial Distribution |
| HF | Hartree Fock |
| IED | Interactive Essential Dynamics |
| KIE | Kinetic Isotope Effect |
| KS | Kolmogorov Smirnov |
| LCAO | Linear Combination of Atomic Orbitals |
| MEP | Minimum Energy Path |
| MD | Molecular Dynamics |
| MM | Molecular Mechanical |
| MO | Molecular Orbital |
| MR | Morphinone Reductase |
| MRC | Multiple Reactive Configurations |
| NADH | Nicotinamide Adenine Dinucleotide |
| NADPH | Nicotinamide Adenine Dinucleotide Phosphate |
| NMA | Normal Mode Analysis |
| OHR | Oxidative Half Reaction |
| PBC | Periodic Boundary Condition |
| PCA | Principal Component Analysis |
| PES | Potential Energy Surface |
| PME | Particle-Mesh-Ewald |
| QM | Quantum Mechanical |
| QM/MM | Quantum Mechanical/Molecular Mechanical |
| RadGyr | Radius of Gyration |
| RC | Reaction Coordinate |
| RHR | Reductive Half Reaction |
| RMSD | Root Mean Square Deviation |
| RMSF | Root Mean Square Fluctuation |
| RS | Rank Sum |
| SASA | Solvent Accessible Surface Area |
| SCF | Self-Consistent Field |
| TS | Transition State |
| TST | Transition State Theory |
| VMD | Visual Molecular Dynamics |
| WT | Wild-type |
| ZPE | Zero Point Energy |
| ΔG | Free Energy |

Abstract

Thomas McGrory

Probing the High Pressure Effect on Morphinone Reductase Using Computational Methods

This thesis was submitted to the University of Manchester for the degree of Doctor of Philosophy (PhD) in 2010.

Enzymes are highly efficient catalysts, achieving rate enhancements of up to 10^{21} , however it is not fully understood how they work. Transition State Theory (TST) is the dominant model used to describe the catalytic power of enzymes. Although TST has proven to be successful for many biological reactions, a recent paradigm shift has attempted to incorporate the quantum behaviour of hydrogen into TST. The de Broglie wavelength of hydrogen is short enough that it needs to be considered in reactions that include hydrogen transfer - comprising over half of all known enzyme catalysed reactions. These transfers can occur by a partial or full quantum mechanical tunneling mechanism. Morphinone reductase (MR) is an enzyme which employs a deep tunneling mechanism in its reductive half-reaction – the hydride transfer from the NADH-C4 atom to the FMN-N5 atom. This mechanism is thought to be assisted by a promoting vibration which decreases the distance between the donor and acceptor atoms. Experimental work using the pressure dependence of kinetic isotope effects (KIEs) as a probe for hydrogen tunneling has suggested an increase in pressure, from 1 bar to 2 kbar, decreases the donor-acceptor distance. Using pressure is a novel approach for probing hydrogen tunneling in enzymes, complementing the established use of temperature dependence. Pressure can be used as a tool to shift the equilibrium of systems – in this instance it shifts the equilibrium of cofactor and substrate configurations towards the tunneling ready configuration. In this research, computational chemistry techniques are used to provide atomistic insight into the pressure effect on MR. Molecular Dynamics (MD) simulations were carried out to probe the rate of structural changes in MR as a function of pressure. The protein is shown to be stable across the range of pressures used. Trajectory analysis showed a decrease of 0.19 Å in the average distance between the donor and acceptor atoms, as the pressure is increased from 1 bar to 2 kbar. This is due to the pressure restricting the conformational space in which the nicotinamide can move. These observations suggest that there is a compression of the reaction barrier as the pressure is increased. The research is extended to analyse the pressure effect on the active site residues in an attempt to identify which of these may be involved in the barrier compression. It is suggested that the pressure affects the configuration of several residues, and this combined effect is responsible for limiting the conformational space around the nicotinamide. The effect of the high pressure configuration on the reaction barrier is also studied, via a combined Quantum Mechanical/Molecular Mechanical (QM/MM) method. There is a decrease in the average barrier height for structures taken from the high pressure MD simulations, compared to the simulations at atmospheric pressure. This is accompanied by an increase in the KIE – two observations that are consistent with experimental work. This work gives the first atomistic insight into the effect of pressure on the tunneling reaction, through the shortening of the donor-acceptor distance. It also provides an example of how pressure can be used as a probe to study a tunneling reaction, using a QM/MM method.

Declaration

No portion of the work referred to in the thesis has been submitted in support of an application for another degree or qualification of this or any other university or other institute of learning.

Copyright Statement

- i. The author of this thesis (including any appendices and/or schedules to this thesis) owns certain copyright or related rights in it (the “Copyright”) and s/he has given The University of Manchester certain rights to use such Copyright, including for administrative purposes.
- ii. Copies of this thesis, either in full or in extracts and whether in hard or electronic copy, may be made only in accordance with the Copyright, Designs and Patents Act 1988 (as amended) and regulations issued under it or, where appropriate, in accordance with licensing agreements which the University has from time to time. This page must form part of any such copies made.
- iii. The ownership of certain Copyright, patents, designs, trade marks and other intellectual property (the “Intellectual Property”) and any reproductions of copyright works in the thesis, for example graphs and tables (“Reproductions”), which may be described in this thesis, may not be owned by the author and may be owned by third parties. Such Intellectual Property and Reproductions cannot and must not be made available for use without the prior written permission of the owner(s) of the relevant Intellectual Property and/or Reproductions.
- iv. Further information on the conditions under which disclosure, publication and commercialisation of this thesis, the Copyright and any Intellectual Property and/or Reproductions described in it may take place is available in the University IP Policy (see <http://documents.manchester.ac.uk/DocuInfo.aspx?DocID=487>), in any relevant Thesis restriction declarations deposited in the University Library, The University Library’s regulations (see <http://www.manchester.ac.uk/library/aboutus/regulations>) and in The University’s policy on Presentation of Theses.

Acknowledgements

I should start by saying that I cannot include everybody I'd like to on this short sheet of paper. To thank all the people who have helped me through the past few years, I would need to write another thesis! First of all, I must acknowledge my supervisor, Professor Mike Sutcliffe. When I stumbled into his office for an interview, on crutches and with a broken leg, dressed in ripped jeans and a hoody, he could have been forgiven for being uncertain about my potential as a PhD student. However, he took a chance on me and I'd like to think I have repaid him over course of the PhD. His continued support and insight have been much appreciated. A special note of thanks must also go to Dr Jiayun Pang, who has acted as a second supervisor to me during my PhD. I am certain that I wouldn't have made it through without her help. It would be criminal of me not to mention my other colleagues in the MIB. Thanks to everybody else in the Sutcliffe and Scrutton groups. I have learnt a lot and made some great friends.

I'd also like to take this opportunity to thank all of my friends and family that have made my life so incredibly enjoyable, before, during and hopefully after the PhD stage of my life. My housemates from Cawdor and from Moseley made university life as fun as possible, whilst still allowing some degree of productivity. The FC Chud team continually provided me with the inspiration and motivation needed to work hard and never give up, despite being beaten down week after week! And all my friends from St Ambrose College (along with the associated gang), who have kept in touch with each other for over 15 years now – I'm not sure what I'm thanking you guys for, but I suppose you deserve a mention!

Without sounding too cheesy, I owe a huge debt of gratitude to my mum, dad, brothers and sisters for their continued love and support, for trying to show an interest when they have no clue about science, and for always being there for a chat! And for food – gotta love mum's roast chicken. I'd also like to express my gratitude to the rest of my family, whom are far too numerous to list, although I would like to mention my uncle Mike, in particular.

My final acknowledgement comes from the heart and is directed towards my beautiful, wonderful and loving girlfriend, Rachelle. I love you honey and this thesis is for you.

Publications From This Thesis

Hay, S., Pudney, C.R., **McGrory, T.A.**, P., Pang, J. Y., Sutcliffe, M. J. and Scrutton, N. S. (2009). "Barrier Compression Enhances an Enzymatic Hydrogen-Transfer Reaction." *Angewandte Chemie-International Edition* 48: 1452-1454.

Pudney, C.R., **McGrory, T.A.**, Lafite, P., Pang, J. Y., Hay, S., Leys, D., Sutcliffe, M. J. and Scrutton, N. S. (2009). "Parallel Pathways and Free-Energy Landscapes for Enzymatic Hydride Transfer Probed by Hydrostatic Pressure." *Chembiochem* 10: 1379-1384.

Chapter 1

Introduction

PREFACE

This thesis studies the atomistic effect of high pressure on a well characterized flavoprotein, Morphinone Reductase (MR). Enzyme catalysis is a very complex issue, and theories used to try to understand the complexity are continually undergoing refinement. The most recent models of enzyme catalysis try to incorporate the quantum mechanical properties of light particles into the popular, although simplistic, Transition State Theory (TST).

The size of an enzyme relative to the substrate that it catalyses is another topic that provokes debate. It is not hard to imagine that the large, intricate nature of protein structure must somehow have evolved in tandem with the extraordinary catalytic ability. This concept of ‘structure gives function’ is another idea that comes under scrutiny by the scientific community. A more recent proposal would be that of ‘structure gives dynamics; dynamics gives function’. Therefore protein motions are of huge interest to enzymology research.

The atomistic nature of enzyme function has led to the necessary involvement of computational chemistry to study enzyme mechanisms. Combining experimental observations, with spectroscopic techniques and physical laws of motion, it is possible to use computer programs to simulate and analyse protein motions and enzyme catalysis. The collaboration between computational chemists and experimental enzymologists has proven to be fundamental in successfully understanding catalytic mechanisms.

1.1 ENZYME CATALYSIS

1.1.1 Introduction

Enzyme catalysis has been a major topic in biological chemistry for over a century. (McGuire and George Falk, 1923, Sherman, 1918, Osborne and Harris, 1903). Enzymes are capable of increasing the rate of reactions by up to 10^{21} (Lad et al., 2003). To put this rate increase into perspective, the same reaction without the enzyme would take over 1 trillion years (100 times longer than the age of the universe). This remarkable catalytic power is the result of millions of years of evolution, producing enzymes that are highly specific and optimised for particular biological processes and reactions (Powell et al., 2001). However, it is not precisely understood how enzymes have evolved for particular processes. One topic of immense importance is the structure-function relationship of enzymes. The structure of an enzyme can be very complex, with several types of secondary and tertiary elements throughout the structure (Kabsch and Sander, 1983). In addition to this, they can range in size from around 62 residues (Chen et al., 1992) to 2,500 residues (Smith, 1994) – this is somewhat bewildering, since the substrates they act on are typically much smaller and only 3-4 of these residues are normally directly involved in catalysis. It is noted that local features of the active site of an enzyme contribute to specificity and catalysis, but this is not to say that the rest of the enzyme is not important.

Enzymes increase the rate of reaction by lowering the activation energy. The primary aim of enzymology research is to understand the mechanism by which an enzyme does this. Over the last century, several ideas have been proposed and subsequently adapted to account for newer experimental evidence. Enzymatic activity was first observed in the

1830's (Haldane, 1930). The high specificity of enzymes led to the proposition of the 'Lock and Key' model by Fischer in 1894 (Fischer, 1894). However, a limitation of this model is that the substrate does not fit the active site as perfectly as had been suggested, leading to the proposal of the 'Induced Fit' model (Koshland Jr, 1973), where the active site changes shape upon substrate binding. In 1935 it had been revealed that the reactants are in equilibrium with a transition state (TS) (Gladstone, 1941, Eyring, 1935). This leads to the widely accepted model to explain enzyme catalysis, still used today.

1.1.2 Transition State Theory

Transition State Theory (TST) was first proposed in 1946 (Pauling, 1946). It is the widely accepted paradigm for describing how enzymes catalyse reactions. TST is derived from two fundamental principles of physical chemistry: absolute reaction-rate theory and the thermodynamic cycle. TST describes an enzyme as a flexible molecular template, designed to complement the reactants in their transition state geometry. In this way, the TS is bound strongly by the enzyme, increasing its concentration and the rate of the reaction. Figure 1.1 shows the reactant and product separated by a potential energy barrier. The reactant needs enough potential energy to surmount this barrier.

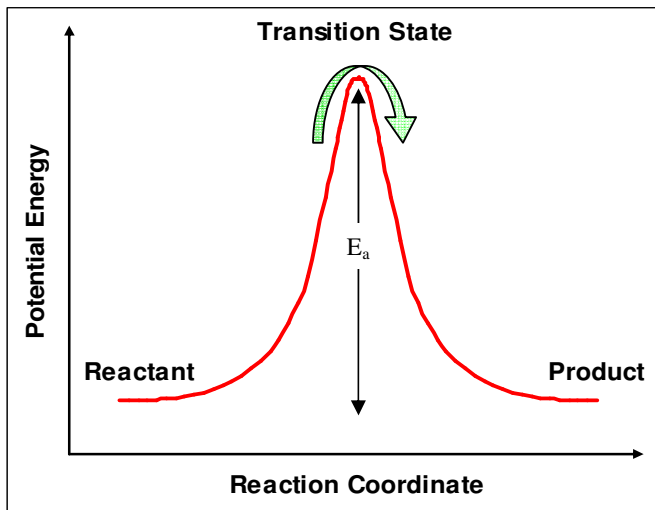


Figure 1.1: Simple representation of Transition State Theory. The potential energy curve is shown in red. For the reaction to proceed, the reactant must have enough energy to surmount the barrier. This is termed the activation energy (E_a)

Figure 1.1 gives a simple two-dimensional representation of TST, where the rate of reaction follows a minimum energy path (MEP) from reactant, through the TS, to the product. The Arrhenius equation can be used to calculate the rate.

$$k = A \cdot \exp(-E_a / RT) \quad (1.1)$$

where A is the Arrhenius pre-exponential factor, E_a is the activation energy, R is the gas constant, and T is the temperature of the system. It is possible to use equation 1.1 to obtain activation energy by plotting $\ln(k)$ versus $1/T$, known as the Arrhenius plot, where the gradient is equal to $-E_a/R$. The Arrhenius pre-factor can be calculated from the y-intercept, $\ln(A)$. At constant temperature, the rate determining factor in equation 1.1 is the activation energy.

Kurz derived an equation to show strength of binding of the TS versus ground state (Kurz, 1963). It was shown that transition state analogues bind stronger than substrates and proposed that this can provide clues to the mechanism of catalysis in enzymes (Lienhard, 1973, Koshland Jr, 1973, Wolfenden, 1972, Wolfenden, 1969). TST is based on certain assumptions and approximations and is not exact. However it has undergone extensive

refinement and is widely accepted as conceptually accurate. The following equation shows the basis for TST:

$$k_e/k_n \approx K_S/K_T \quad (1.2)$$

where k_e and k_n refer to the enzymatic and non-enzymatic catalysed reaction rates, and K_S and K_T refer to the dissociation constants for the substrate and the transition state (Kraut, 1988).

According to TST, catalysis causes a rate enhancement by reducing the potential energy of the TS (such as by stabilising it with electrostatic interactions in the active site - binding it more tightly). Although this is an effective model for catalysis, it does not factor in the entropies of reactant, TS and product. It is better to use the Gibb's free energy, than the potential energy, as a barrier to reaction.

$$k = A \cdot \exp(-\Delta G^\ddagger / RT) \quad (1.3)$$

Taking this into consideration, TS stabilisation can now be achieved by increasing the entropy. An example of this is chalcone isomerise, which increases entropy at the TS by releasing water molecules (Hur and Bruice, 2003).

TST is widely applicable to most enzyme systems. However, as will be described in more detail below, it cannot describe completely the mechanism of enzyme catalysis. Hydrogen tunneling is a quantum phenomenon that is particularly important topic in enzyme catalysis, since ~50% of reactions catalysed by enzymes involve the transfer of hydrogen. It is noted that the over simplification of TST is at the expense of data regarding quantum effects and dynamics.

1.1.3 Quantum Considerations for Catalysis

1.1.3.1 Semi-Classical TST

An important factor to consider in TST is the zero point energy (ZPE) of a particle. Classical TST assumes that the reactant is at the bottom of a potential energy well and needs a certain amount of energy to pass over the reaction barrier. However, the Heisenberg uncertainty principle states that a particle cannot occupy the potential energy minimum. Therefore any physical system, even at a temperature of absolute zero, has an energy greater than zero. At its lowest energy state, the particle has a ZPE. The lighter the particle, the greater the ZPE (Knapp and Klinman, 2002b). The ZPE of a hydrogen atom (H) can be calculated as $\frac{1}{2}h\nu_H$, where h is Planck's constant and ν_H is the vibrational frequency of the atom. It follows that a deuterium atom would have a lower ZPE due to its higher mass, as demonstrated in Figure 1.2.

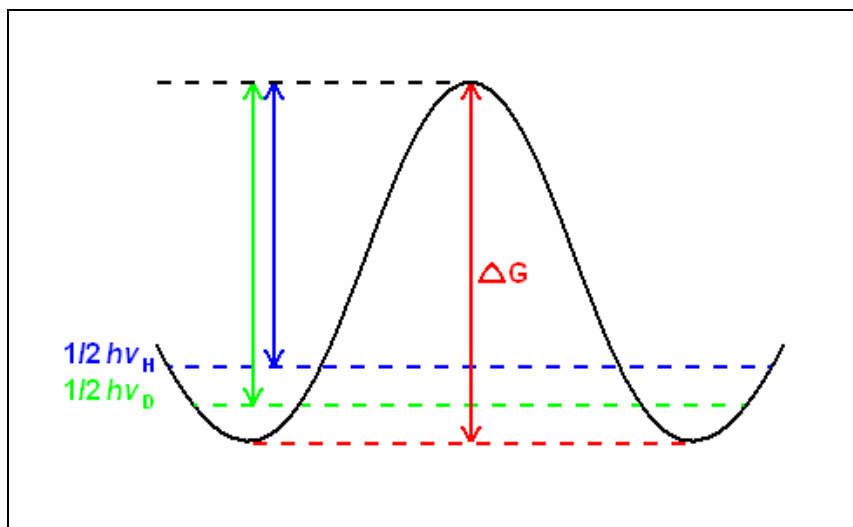


Figure 1.2: Reaction profile for hydrogen transfer with semi-classical TST. The energy needed to surmount the barrier (ΔG) is reduced by the ZPE. For the deuterium isotope, the ZPE is lower, resulting in different rates for different isotopes. [Adapted from (Knapp and Klinman, 2002b)]

Incorporating the ZPE into equation 1.3, gives:

$$k_{\text{H}} = A_{\text{H}} \exp\left(-\frac{(\Delta G^{\ddagger} - \frac{1}{2}h\nu_{\text{H}})}{RT}\right) \quad (1.4)$$

The difference in ZPEs for hydrogen and deuterium result in different activation energies and different rates.

1.1.3.2 Kinetic Isotope Effect (KIE)

KIEs are a very useful tool to enzymologists, as they are used frequently to isolate the rate determining step in an enzyme catalysed reaction. As stated in the previous section, substituting an atom for one of its isotopes gives a difference in rate. The ratio of these rates is the KIE:

$$KIE = \frac{k_{\text{H}}}{k_{\text{D}}} \quad (1.5)$$

Equation 1.5 shows how KIEs are calculated. k_{H} and k_{D} are the reaction rate constants of hydrogen and deuterium respectively. KIEs of hydrogen are the most pronounced (due to the large mass ratio between hydrogen and its isotopes); at 300 K, the KIE of a hydrogen transfer reaction, with semi-classical TST invoked, can be as high as 7. Reactions with KIEs of a greater magnitude suggest a more complex quantum mechanism that cannot be explained using semi-classical TST alone. The temperature dependence of the KIEs is also of interest to enzymologists. This, combined with the magnitude can be used to elucidate the reaction mechanism (Schramm, 1998).

It should be noted here that the KIE discussed above is the primary (1°) KIE. It is the ratio observed when the transferring particle is substituted for its isotope. The secondary (2°)

KIE can also be of use. It corresponds to the difference in the rates when the atom adjacent to the transferring particle is substituted for its isotope.

1.1.3.3 Hydrogen Tunneling

Tunneling of a particle is a quantum phenomenon, arising from the wave-particle duality of matter. Recalling Heisenberg's uncertainty principle, the location of the particle should be described by its wavefunction, since it has a probability of existing in numerous locations. In terms of a reaction barrier, if barrier is narrow enough, the particle has a probability of being on either side of the barrier. It is therefore entirely possible that it can tunnel through the barrier from reactant to product, without going through the TS. Figure 1.3 illustrates this.

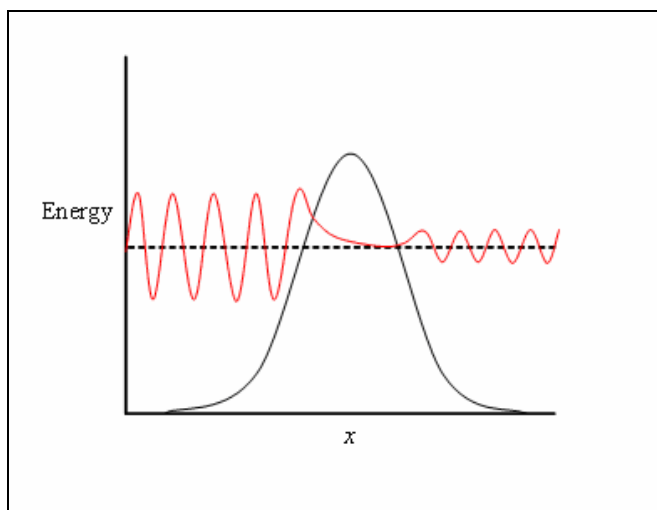


Figure 1.3: Schematic of the propagation of a wavefunction (red line) through a symmetrical energy barrier (solid black line) along a reaction coordinate x . Adapted from (Sutcliffe and Scrutton, 2000)

The de Broglie wavelength of a particle is an important property in this scenario. This is calculated as:

$$\lambda = h/mv \quad (1.6)$$

where h is Planck's constant m is the mass and v is the velocity of the particle. The propagation of the wavefunction through the barrier, illustrated in Figure 1.3, occurs when there is sufficient wavefunction overlap of the reactant and product. This is known as tunneling - the reaction can proceed without having enough energy to surmount the barrier. This becomes more likely higher up the barrier, since the width of the barrier is shorter. Lighter particles will have a longer de Broglie wavelength, thus they can tunnel further down the barrier.

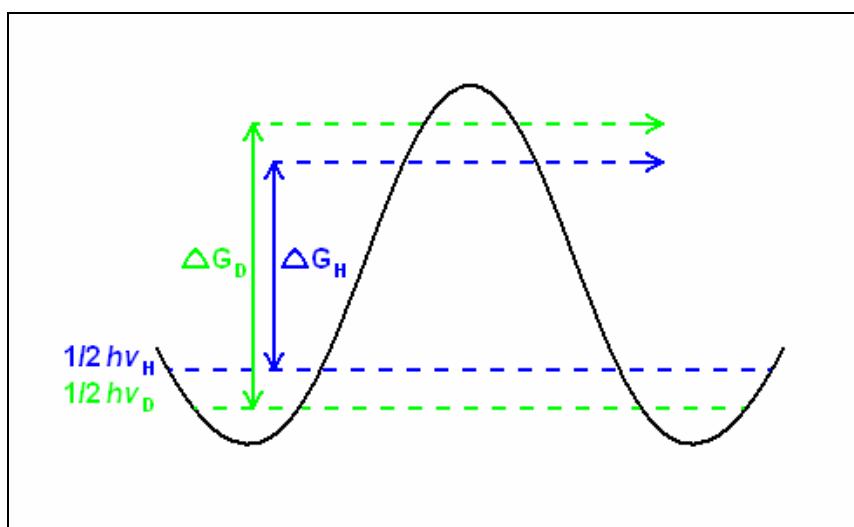


Figure 1.4: Reaction profile for hydrogen transfer with semi-classical TST with Bell Correction. Tunneling occurs just below the TS (further below for hydrogen, than for deuterium [Adapted from (Knapp and Klinman, 2002a)]

Quantum tunneling in biological electron transfer reactions is a well documented mechanism (Marcus and Sutin, 1985). It can occur over distances as large as 25 Å (Miyashita et al., 2005, Balabin and Onuchic, 2000, Wilson et al., 1995). A proton is much heavier than an electron and subsequently cannot travel such distances via quantum tunneling. For the same probability of an electron tunneling 25 Å, a proton can tunnel 0.58 Å (Scrutton et al., 1999). Since a hydrogen transfer normally occurs over distances shorter than 1 Å, quantum tunneling can be a very significant factor.

1.1.3.4 Hydrogen Tunneling in Enzyme Catalysed Reactions

The importance of hydrogen tunneling has become an important topic in the study of enzyme-catalysed reactions. For small molecular systems, both modelling of reaction dynamics and experimental observations suggest that hydrogen tunneling only becomes significant at temperatures too low to be of biological importance (Kohen and Klinman, 1998). However, in enzymes, it has been suggested that the environment of the active site enhances the tunneling probability. Experiments on more than 10 enzymes and mutants demonstrated behaviour that cannot be explained without invoking hydrogen tunneling (Kohen and Klinman, 1998). This study from over 10 years ago concluded that there is enough evidence to suggest that, under physiological conditions, hydrogen tunneling may play an important part in enzyme-catalysed reactions that involve the transfer of hydrogen.

To understand enzymes function, it is important to try to incorporate the effect of quantum mechanical tunneling into TST. The Bell Correction (Bell, 1980) attempts to explain non-classical behaviour of a hydrogen transfer reaction, allowing tunneling to occur just below the TS, as shown in Figure 1.4. Although the Bell Correction accounts for small deviations from semi-classical behaviour, over the past two decades, experimental evidence has gathered for several enzymes that cannot be explained using this model.

Klinman discusses the oxidation of linoleic acid catalysed by soybean lipoxygenase (SBL) - an example where the Bell Correction fails to account for the degree of tunneling (Jonsson et al., 1996). Figure 1.5 describes how the temperature dependence of the rate will be affected by the degree of tunneling.

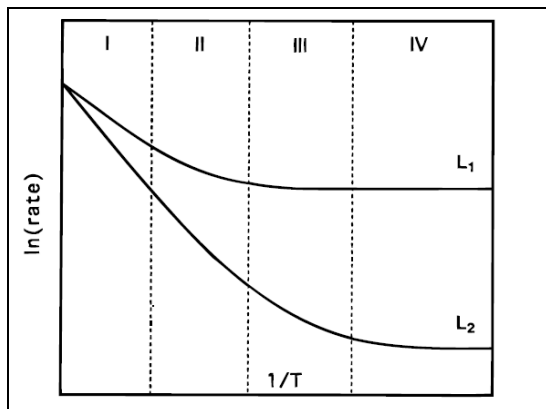


Figure 1.5: A general diagram describing the rate of a hydrogen transfer reaction as a function of temperature. Two curves (L_1 and L_2) are presented for illustrative purposes; however, these pertain to all three isotopes of H. The regions designated I-IV are described in text. [Taken from (Jonsson et al., 1996)]

Region I shows semi-classical behaviour and Region II shows semi-classical behaviour with the Bell Correction. The reaction rates in these regimes are temperature dependant because of the energy required to move up the barrier. The reaction catalysed by SBL has a highly elevated KIE (>80), but its rate is not temperature dependant – conforming to Region IV on Figure 1.5. This is a case of extreme tunneling, where the hydrogen transfer occurs by ground state tunneling alone, rather than a combination of tunneling and ‘over the barrier’ transfer.

There have been several studies since that have provided further evidence for extreme tunneling. An important issue to consider in this type of tunneling is the role of protein dynamics to optimise the barrier width. This is discussed in the next section.

1.1.4 Enzyme Dynamics

‘Dynamics’ is a term that can be used in several contexts in enzymes. Protein motions can be short timescale atomic vibrations (occurring on the femto- to picosecond timescale); medium timescale configurational changes, such as side-chain rotation (nanosecond timescale or longer); and long timescale motions which include large conformational

changes, such as domain movements (occurring on the micro- to millisecond timescale) (Swift and McCammon, 2008). Citrate synthase provides an example of an important long timescale protein motion. The enzyme binds coenzyme A, causing a rotation of the small domain to close the cleft, in preparation for the reaction to occur (Wiegand and Remington, 1986, Huber and Bennett, 1983, Remington et al., 1982). Another example of long timescale protein dynamics is that of membrane channel opening, which involves large conformational changes (Valadie et al., 2003).

The correlation of longer timescale dynamics with the rate of reaction has been studied by nuclear magnetic resonance (NMR) methods (Eisenmesser et al., 2002). However, medium to short timescale motions, occurring on an atomistic scale, such as the conformational change of an amino acid, or, faster still, atomic vibrations, localised in the active site, are more likely to have an impact on the reaction. The suggested role of these types of dynamics in hydrogen tunneling reactions has been studied intensely in recent years.

When considering how protein motions affect enzyme function, the width of the potential energy barrier to reaction becomes a focus for theoretical study (Truhlar et al., 2002, Knapp et al., 2002, Kuznetsov and Ulstrup, 1999, Antoniou and Schwartz, 1997, Borgis and Hynes, 1996, Bruno and Bialek, 1992). This idea was first proposed for electron tunneling, with protein motions responsible for optimizing the donor-acceptor distance for tunneling to occur.

There are two types of protein dynamics that are considered in the context of H-tunneling. These are termed 'active' and 'passive' dynamics (Sutcliffe et al., 2006). Active dynamics

describe non-equilibrated, thermally induced motions. These motions occur on the sub-picosecond timescale and are coupled to the reaction coordinate. They are sometimes referred to as ‘promoting motions’. This term is used since these motions are thought to act to promote catalysis by quantum tunneling, e.g. by decreasing the donor-acceptor distance, which increases the wave-function overlap (effectively reducing the width of the barrier). A key indicator for the involvement of active dynamics in a H-tunneling mechanism is a temperature dependant KIE (Knapp and Klinman, 2002b).

Passive dynamics are slower (nanosecond – millisecond) protein fluctuations that are thermally equilibrated. The KIE of a mechanism with passive dynamics is temperature independent. These motions are not coupled to the reaction coordinate, but they cause a pre-organised configuration of the enzyme that enhances catalysis. This configuration can be described as a “tunneling-ready” configuration (Pudney et al., 2006).

Several models for vibrationally-assisted tunneling have been developed since extreme KIEs and other kinetic data that could not be accounted for by semi-classical TST were first observed (Bruno and Bialek, 1992). The model of environmentally coupled hydrogen tunneling (Knapp and Klinman, 2002b, Northrop, 1999) allows for the contribution of passive and active dynamics. Figure 1.6 illustrates this model:

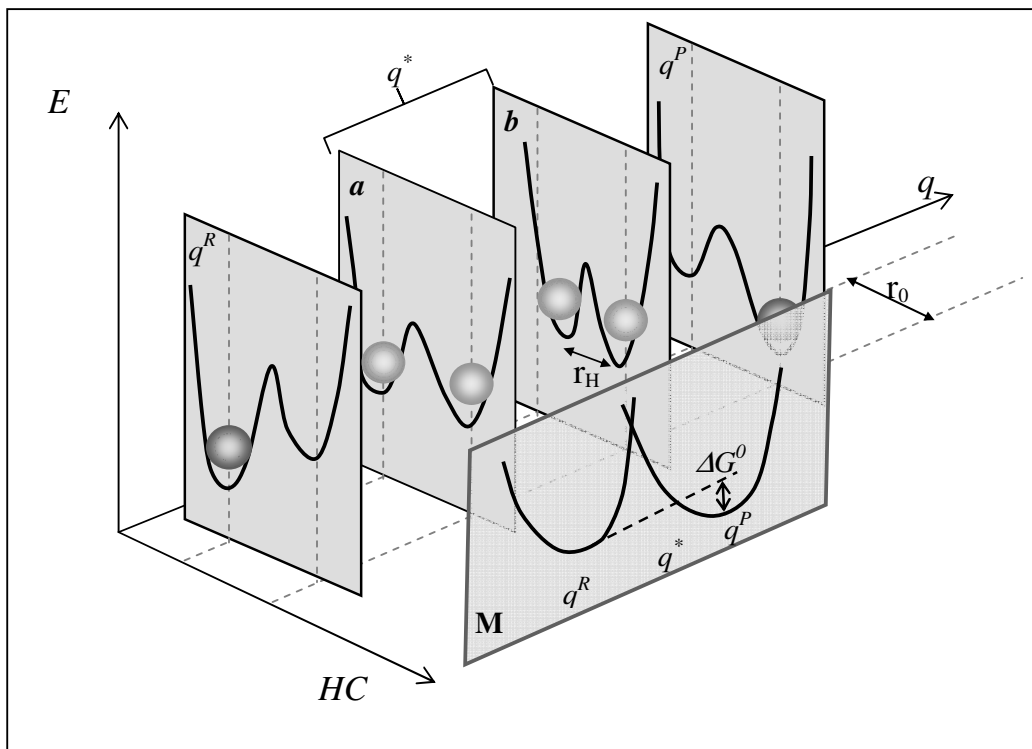


Figure 1.6: Illustration of vibrationally coupled H-tunneling. The axes are E , energy; q , environmental coordinate and HC , the hydrogen coordinate. The vertical panels show the potential energy curves at 4 points on the environmental coordinate: q^R represents the reactant, q^* the transition state with degenerate reactant and product wells, and q^P the product. The grey spheres represent the ground state vibrational wavefunction of the hydrogen nucleus. Panel M shows a Marcus like view of the free energy curves as a function of the environmental coordinate. The motions of the environment modulate the double well allowing the wavefunctions to reach degenerate quantum states. Panels **a** and **b** show two different scenarios. In **a** there is no motion along the HC coordinate, the two potential wells being at the equilibrium distance, r_0 , while in **b** there is a gating motion which reduces the distance along the HC axis (r_H), between the two degenerate potential wells. This gating increases the probability of tunneling at q^* . [Taken from (Masgrau et al., 2004)]

Masgrau *et al.* (2004) studied the tunneling mechanisms in two quinoproteins: methylamine dehydrogenase (MADH) and aromatic amine dehydrogenase (AADH). These proteins are very similar structurally and functionally. These proteins have been studied intensely, both experimentally and computationally (Johannissen et al., 2007, Sutcliffe et al., 2006, Masgrau et al., 2006), and the catalysis is shown to be dominated by an environmentally coupled tunneling mechanism.

This research is collected along with other recent insights from both experimental and theoretical studies, in a themed issue of *Philosophical Transactions of The Royal Society B* (Dutton et al., 2006), which deals specifically with quantum catalysis in enzymes. Many of the papers attempt to link protein dynamics to catalysis and hydrogen tunneling. Allemann and Wang describe how structural mutations, both near and far from the active site of the enzyme, can have an effect on the hydrogen transfer. This suggests that these residues may be in some way associated with the enzyme dynamics that is involved in increasing the tunneling probability (Wang et al., 2006, Allemann et al., 2006). Klinman reviews her work on soybean lipoxygenase and demonstrates the need for protein dynamics to bring donor and acceptor atoms close enough together for tunneling (Klinman, 2006). Northrop describes how hydrostatic pressure can be exploited as a probe for H-tunneling (Northrop, 2006). This is of particular significance to this thesis and will be discussed in Section 1.3.

1.2 MORPHINONE REDUCTASE

1.2.1 Flavoproteins

Flavoproteins are enzymes that use flavins as cofactors and they are involved in a variety of reactions. There are two types of flavoprotein, classified by the cofactor that they utilise: flavin adenine dinucleotide (FAD) or flavin mononucleotide (FMN). The structures of FAD and FMN are shown in Figure 1.7 (Fraaije and Mattevi, 2000). A common feature of these cofactors is the isoalloxazine ring. The N5 atom on this ring can act as an acceptor and then as a donor in redox reaction.

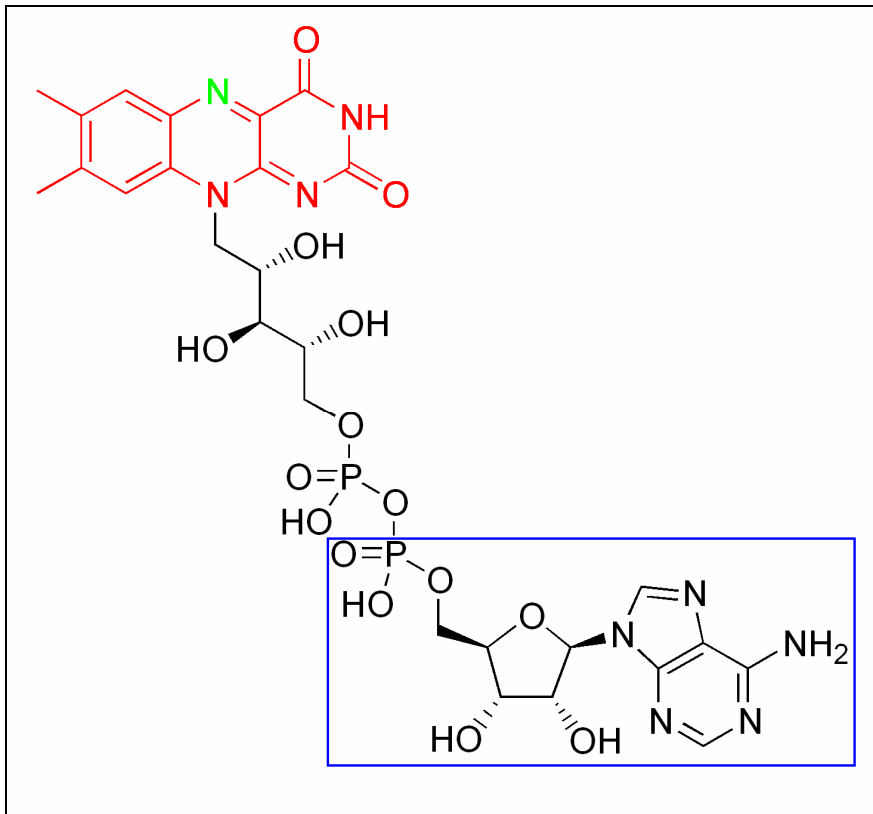


Figure 1.7: Structure of flavin adenine dinucleotide (FAD) and flavin mononucleotide (FMN). The isoalloxazine ring is coloured red, with the N5 atom coloured green. For FMN, the group highlighted in the blue box is replaced by a hydrogen atom. Adapted from (Fraaije and Mattevi, 2000)

Morphinone Reductase (MR) is part of the Old Yellow Enzyme (OYE) family of flavoproteins. The OYE family is a large group of FMN-dependant, NAD(P)H-dependent oxidases (Hay et al., 2009b). FMN is initially reduced by the nicotinamide adenine dinucleotide (NADH). NAD⁺ (the oxidised form of NADH) can then act on the substrate. Nicotinamide adenine dinucleotide phosphate is another substrate used by the OYE family and differs in structure to NADH by the additions of a phosphate group. The structure of NADPH is shown in Figure 1.8.

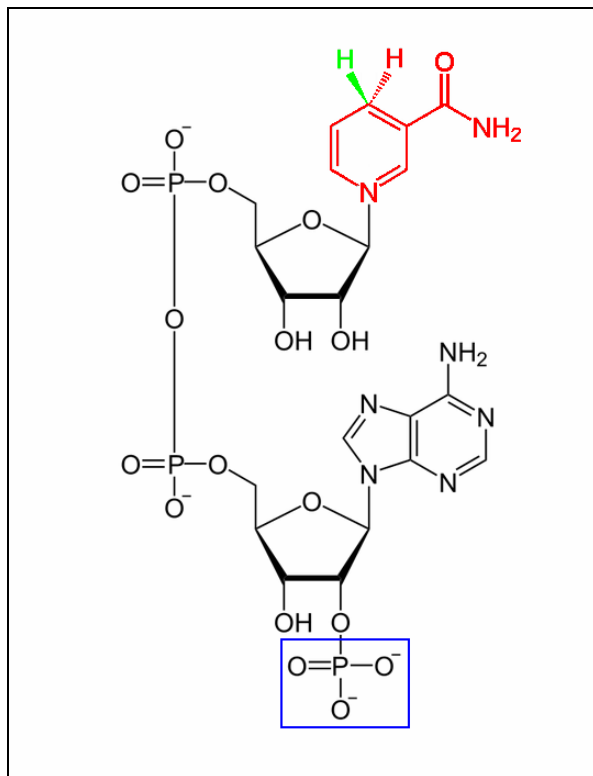


Figure 1.8: Structure of nicotinamide adenine dinucleotide phosphate (NADPH) and nicotinamide adenine dinucleotide (NADH). The nicotinamide ring is coloured red, with the pro R hydrogen, connected to the C4 donor atom coloured green. For (NADH), the phosphate group highlighted in the blue box is replaced by a hydrogen atom. Adapted from (Fraaije and Mattevi, 2000)

Pentaerythritol tetranitrate reductase (PETNR) is a closely related member of the OYE family. Although PETNR can react with both NADH and NADPH, MR reacts only with NADH. Incidentally, PETNR has a preference for NADPH.

1.2.2 Structure and Function

The crystal structure of MR, isolated from *Pseudomonas putida* M10, has been solved (to a resolution of 1.30 Å), using a non-reactive substrate analogue (NADH₄) to trap the binary charge transfer (CT) complex (Pudney et al., 2007). It can be found on the Protein Data Bank (Bernstein et al., 1977) as entry 2R14. Figure 1.9 shows a representation of the active site of MR, taken from the crystal structure.

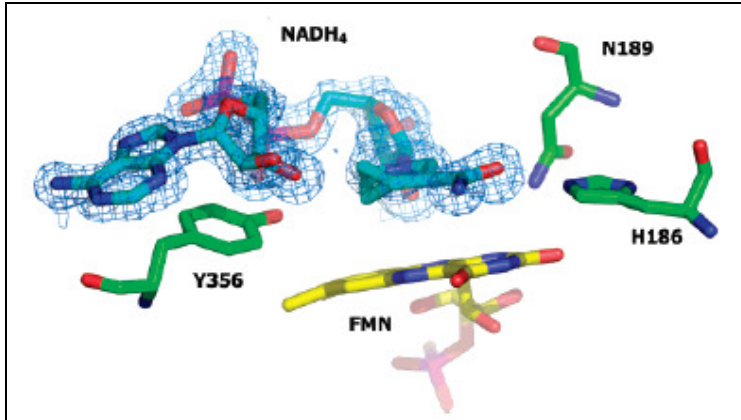


Figure 1.9: Active site of MR in complex with NADH₄. Key residues and both FMN and NADH₄ are shown in atom coloured sticks, with carbons coloured green for amino acids, yellow for the FMN and cyan for the NADH₄. The sigmaA weighted 2FoFc map surrounding the NADH₄ is contoured at 1.5 sigma and shown as a blue mesh. [Taken from (Pudney et al., 2007)]

MR exists as a homo-dimer. The crystal structure represents only one subunit, 377 amino acid residues long. The structure is assigned as 33% helical (15 helices; 126 residues) and 16% beta sheet (16 strands; 63 residues) by the Dictionary of Protein Secondary Structure (DSSP) (Kabsch and Sander, 1983). A representation of the macromolecular structure of MR is shown in Figure 1.10.

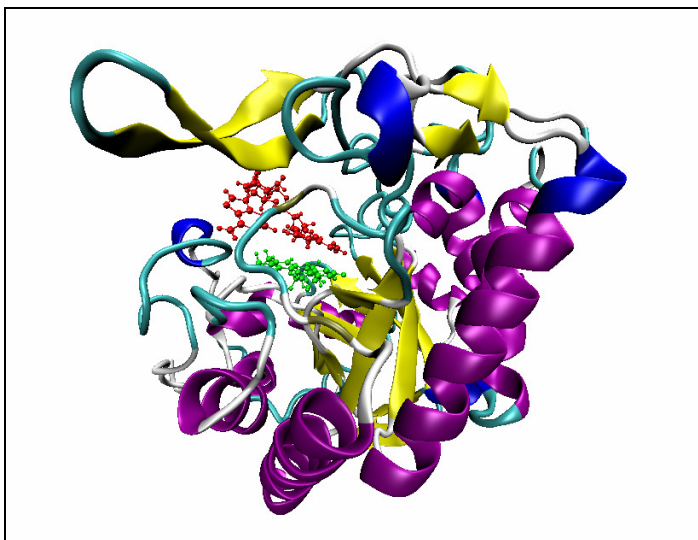


Figure 1.10: Representation of one monomer of MR, shown with the secondary structure represented. The FMN cofactor (green) and NADH substrate (red) are shown in the active site.

MR catalyses the NADH-dependant saturation of the carbon-carbon double bond of morphinone and codeinone (Craig et al., 1998, French and Bruce, 1994). MR has the potential of being used in a biosensor for morphine and heroin, or as a biocatalyst in the production of semi-synthetic opiate drugs (French and Bruce, 1994). Morphinone is converted by MR to hydromorphone, which is seven times stronger than morphine (Craig et al., 1998).

1.2.3 Mechanism

The reaction by which MR catalyses the reduction of its substrate is split into two half reactions: reductive (RHR) and oxidative (OHR). The RHR involves the reduction of the FMN cofactor via a hydride transfer: the pro-*R* hydrogen on the NADH C4 atom is transferred to the N5 atom on FMN. The OHR then involves the oxidation of the FMN: the previously transferred hydrogen is now abstracted by an oxidative substrate. To fully saturate the double bond of this substrate it is likely that an active site amino acid also donates a proton (Basran et al., 2003). Figure 1.11 shows a mechanistic scheme for the conversion of morphinone into hydromorphone by MR.

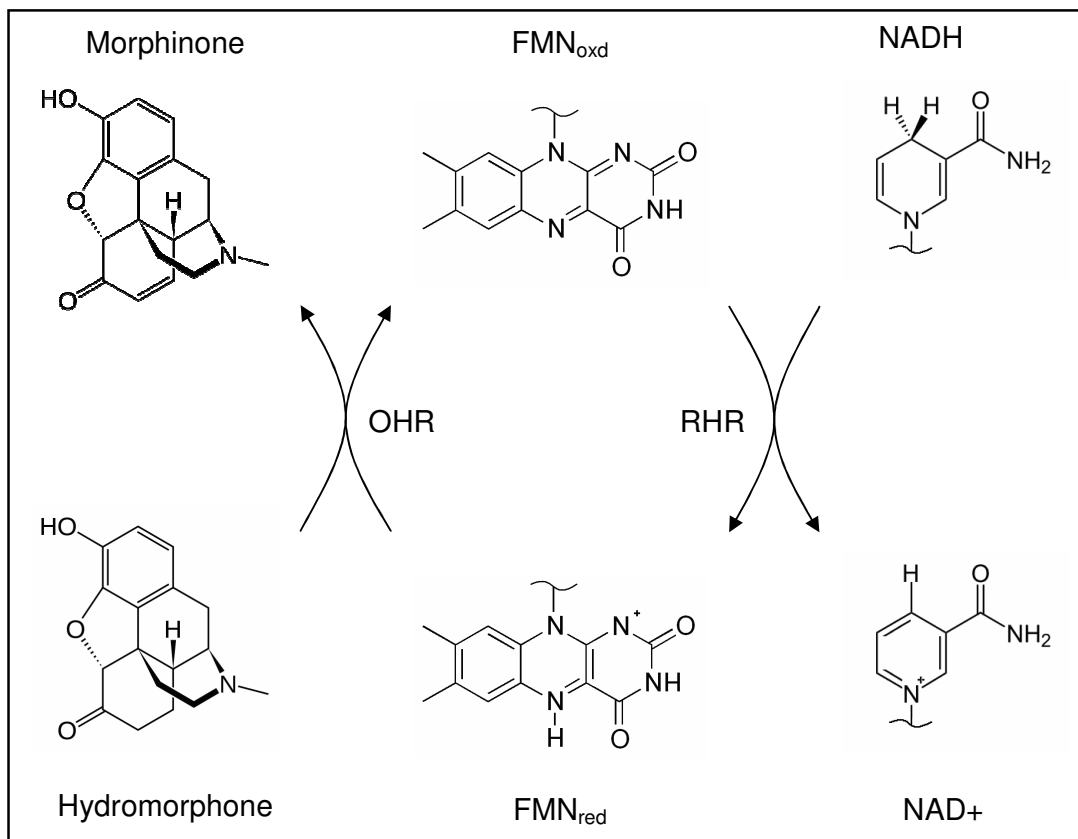


Figure 1.11: Catalytic mechanism of morphinone reductase. A hydride is transferred from the C4 of the NADH to the N5 of the FMN in the reductive half reaction (RHR). The reduced FMN in turn oxidizes the substrate, hydromorphone to morphinone in the oxidative half reaction (OHR)

It is important to illustrate the OHR, although it is beyond the scope of this study. In this thesis, the RHR is focused upon. As mentioned before, it is the pro-*R* hydrogen that is transferred to the FMN. This stereo-specificity is achieved since MR can only bind the NADH in the orientation shown in Figure 1.9, which holds the pro-*R* hydrogen over the N5 acceptor atom on the FMN.

1.2.4 Hydrogen Tunneling Implications

Hydrogen tunneling in flavoproteins and quinoproteins has been studied in depth recently (Masgrau et al., 2006). There is an emphasis on the role of protein motion to promote

tunneling. Their KIEs and their temperature dependencies have been used to identify enzymes that catalyze reactions by pure quantum tunneling. Protein dynamics is thought to modulate these reactions. In order to understand how the tunneling reaction proceeds, computational methods are required to provide an atomistic scale interpretation of the kinetic data. Alongside MR and PETNR, two quinoproteins are included in this review: MADH and AADH, as discussed in section 1.1.4.

The kinetic studies of the RHR of MR reveal temperature dependent primary KIEs, alongside a temperature dependant rate, indicating a quantum mechanical tunneling mechanism, with active dynamics, plays a part in the hydride transfer. This is in contrast to PETNR, which has no temperature dependency to the primary KIE, despite a strongly temperature dependant rate. The RHR for PETNR has no active dynamics and, instead, passive dynamics plays a major role. It is suggested that the active site of PETNR is better configured for hydride transfer, but in MR barrier compression is required to facilitate the reaction. The OHR is also studied and it is concluded that there is no gating motion required to assist the reaction, making MR the first enzyme to show both passive and active dynamics as a feature of hydrogen tunneling in the same enzyme (Pudney et al., 2006).

More recently, a mutated form of MR has been studied (Pudney et al., 2007). An asparagine residue (Asn189) in the active site was mutated to an alanine residue, effectively knocking out a hydrogen bond between the nicotinamide and Asn189. Molecular dynamics (MD) simulations were performed to identify differences in the

geometry of the substrate in the N189A mutant, compared to the wild-type (WT) enzyme.

Figure 1.12 is taken from this paper.

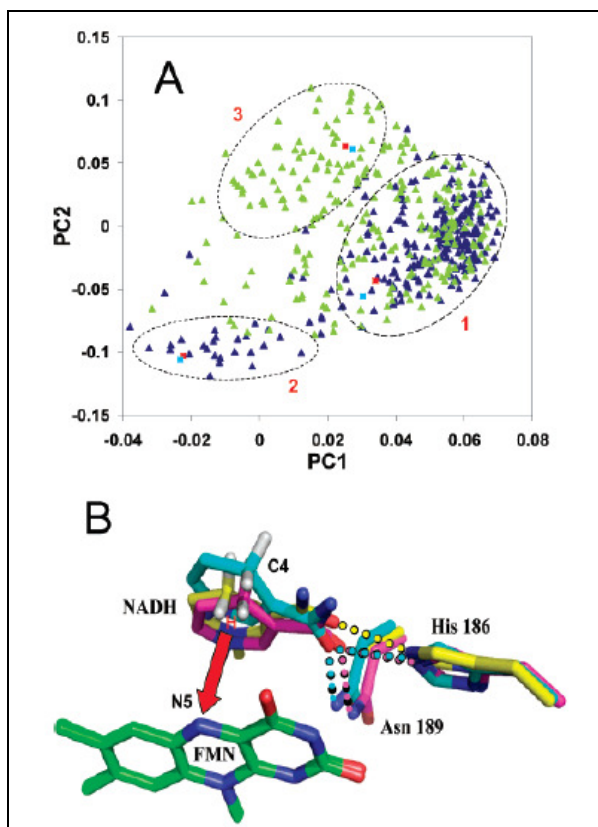


Figure 1.12: (A) Principal component analysis from 10 ns molecular dynamics simulations of wild-type (dark blue triangles) and N189A (green triangles) MR. Two major FMN-NADH configurations (labeled 1 and 2) are observed in wild-type, with an additional configuration (3) only observed in the N189A MR simulations. (B) Relative positions of FMN (isoalloxazine), NADH (nicotinamide), Asn/Ala-189, and His-186 in configurations 1 (carbon atoms in pink), 2 (carbon atoms in cyan), and 3 (carbon atoms in yellow). The transferred hydrogen is shown in red; distances from this hydrogen to N5 are 3.5 ± 0.4 , 4.4 ± 0.4 , and 3.2 ± 0.4 Å in configurations 1, 2 and 3, respectively. Hydrogen bonds between protein and nicotinamide are depicted as dotted lines. (The isoalloxazine rings of FMN in the three configurations have been overlaid.)

[Taken from (Pudney et al., 2007)]

Figure 1.12A shows a principal components analysis which was performed to analyse the conformational space occupied by the nicotinamide ring of NADH in wild-type MR and N189A MR. Two clusters were observed for wild-type. The same clusters were observed for the N189A mutant, with an additional cluster also. This additional cluster is only possibly due to the removal of the hydrogen bond between Asn189 and the nicotinamide. The configurations of the nicotinamide represented by the cluster are also shown in Figure 1.12B. The significance of the extra configuration observed in N189A is that the nicotinamide ring shows greater overlap with the isoalloxazine ring. This would suggest a faster rate of H-transfer in the N189A mutant and this is verified by the experiments.

Further computational study on MR has been carried out by Pang et al. (Pang et al., 2008), using a QM/MM method to model the transfer of the hydrogen from the nicotinamide ring to the isoalloxazine ring. It is concluded that ‘deep tunneling’ dominates the reaction, with 99% of the reaction proceeding via tunneling. This is despite the fact that the KIE lies below the semi-classical limit. This study also supports a theory of reorganization, prior to the tunneling reaction. Figure 1.13 illustrates the reorganisation

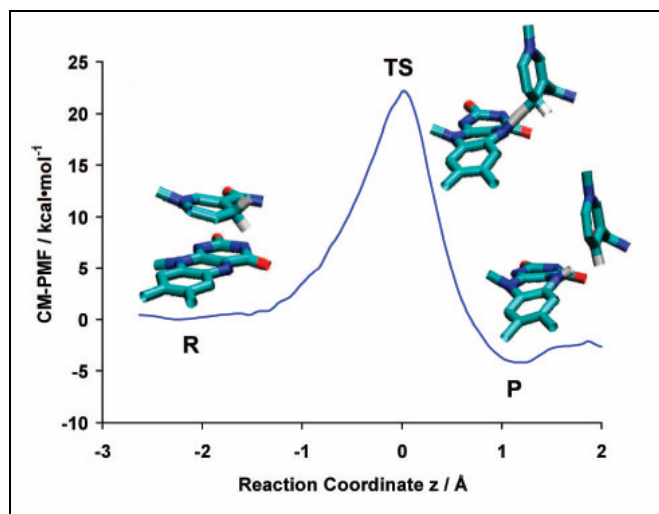


Figure 1.13: Free energy of activation: Computed CM-PMF with representative relative configurations of FMN and NAD(H) displayed in the reactant (R), transition-state (TS), and product (P) regions. For clarity, only the isoalloxazine moiety of FMN and the nicotinamide moiety of NAD(H) are shown. [Taken from (Pang et al., 2008)]

The paper suggests that, during the hydride transfer, the nicotinamide ring almost becomes perpendicular to the isoalloxazine ring.

The pressure effect on the KIEs in MR has also been studied experimentally by Hay et al. (Hay et al., 2007). This is particularly relevant to this thesis and is discussed in Section 1.3.3.

1.3 PRESSURE EFFECT ON ENZYMES

The effect of pressure on proteins is of great interest to the biological community. Pressure can be used to alter the equilibration, since, in accordance with Le Chatelier's principle, a system at equilibrium subjected to stress will adjust to relieve the stress and restore equilibrium (Northrop, 2006). Pressure studies on proteins in the past have mainly been focussed on the pressure induced unfolding mechanism, since it is assumed that by understanding how a protein unfolds, it may give insight into how it folds, which would be a milestone in protein engineering. However more recently, and thanks mainly to the work of Northrop, *et al.*, it has been recognized that pressure can potentially be used as a probe for understanding catalytic mechanisms.

Temperature and mutation are used frequently in kinetic studies of enzyme catalysed reactions. The realisation that pressure can alter the equilibrium of conformational states however, without denaturing the enzyme (which is caused by severe temperatures) or causing any binding problems (which can be a problem in mutation studies), makes high pressure experiments an attractive prospect. It is thought that pressures up to several kbar (1 bar = 100 kPa ~ atmospheric pressure) do not cause significant denaturation of a protein (Kundrot and Richards, 1987), giving a broad pressure range that can be exploited for experimental observation. Since the absolute rate of a reaction is based upon an equilibrium between the reactant and product, and changing the pressure perturbs the equilibrium, pressure can have an effect on enzyme catalysis.

1.3.1 Experimental Studies of Proteins at High Pressure

As mentioned already, the majority of experimental pressure studies have focussed on exploring the unfolding of proteins. Early research into the effect of high pressure on proteins reports a denaturation of proteins at pressures of 400 MPa and higher (Bridgman, 1914). This denaturation, although not identical to that of temperature, was not studied in great detail, since temperature denaturation could be studied much more easily. Technological advances towards the end of the 20th century, however, have made it possible for the majority of methods used at atmospheric pressure to be used at high pressure also (Mozhaev et al., 1996).

A growing understanding of pressure induced unfolding has identified some stark contrasts to that of temperature unfolding. Where high temperatures cause the protein to unfold, exposing hydrophobic regions to the solvent; high pressures force water to infiltrate the protein core, destabilizing the hydrophobic residues. The high pressure unfolded state of a protein is compact, contrasting with the open chain high temperature unfolded state (Hummer et al., 1998).

It has already been mentioned that the pressure can influence the rate of reaction. Northrop discusses the kinetic effect of hydrostatic pressure to enzyme catalysed reactions (Northrop, 2006). According to semi-classical theory, the impact of pressure on the isotope effect of a reaction should be negligible at pressures up to a few kbar. This is because the vibrational frequencies responsible for the differences in ZPE are not affected by pressures in this range.

As detailed in Section 1.3.3, however, semi-classical TST is not the complete picture. The effect on pressure on hydrogen tunneling was first studied by Isaacs (Isaacs et al., 1978). It was found that for eight cases examined, the KIE decreased as the pressure was increased. Northrop et al. takes this study further and shows that the increase in pressure seems to affect the component of the KIE associated with H-tunneling, leaving a pressure-insensitive component, associated with semi-classical transition state theory (Northrop, 1999). Figure 1.14 illustrates this.

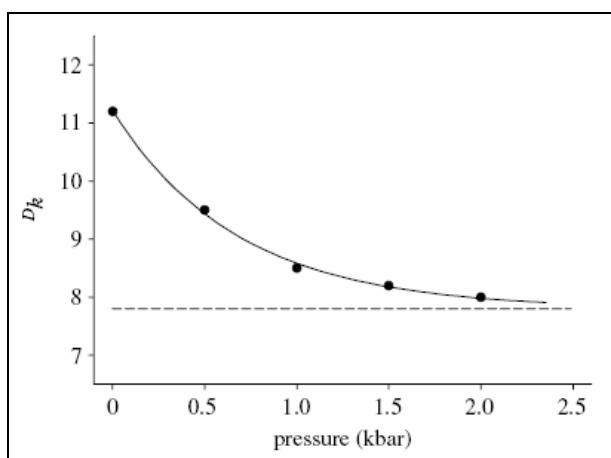


Figure 1.14: *Effect of pressure on the deuterium isotope effect on hydride transfer from chloranil to leuco-crystal violet. [Taken from(Northrop, 2006)]*

Northrop extends his study to enzymatic hydrogen tunneling with the study of yeast alcohol dehydrogenase (YADH) (Northrop and Cho, 2000), again finding that the isotope effects are sensitive to high pressure. It is expected that the KIE for a pure transition state reaction should not be pressure dependent. Thus, Northrop's findings provide a new probe for exploring the potential contribution of hydrogen tunneling to a reaction mechanism: the pressure dependence of KIEs.

1.3.2 Computational Studies of Proteins at High Pressure

High temperature molecular dynamics has been readily explored (Hünenberger et al., 1995a, Daggett and Levitt, 1993). There are fewer examples of molecular dynamics at elevated pressure. A major debate is whether current force fields (developed at atmospheric pressure) are appropriate for high pressure simulations. Paci *et al.* discusses several studies of the pressure effect on biomolecules (Paci, 2002). In the majority of cases, the high pressures slows down the dynamics. This is attributed to an increase in the density of the system. It is concluded that, although high pressure studies would be useful, the timescales that are computationally possible are too short to study the dynamics of macromolecules. However, since this study, there have been several other studies that have made effective use of high pressure in computational methods. A selection of these are discussed below.

Pressure and temperature was used to study the unfolding of a 20 amino acid, alpha-helical peptide (Paschek et al., 2005). A VTREMD (volume-temperature replica exchange molecular dynamics) approach is employed to enhance sampling of conformations, thus allowing pressures up to 1000 MPa (10 kbar) and temperatures up to 547 K to be studied. This study produces good agreement with experimental predictions for the pressure effect on a peptide. It also gives an atomistic description of volume and structure changes in a solvated peptide as pressure is increased. A slight decrease in the radius of gyration is observed, but on the whole, the structure of the peptide remains intact. An increase in the number of water molecules coordinated to the protein backbone is also recorded.

High pressure MD simulations have been performed on a mutated form of T4 Lysozyme using AMBER6, with ff94 (Collins et al., 2005). The simulations were performed at constant temperature and pressure (using pressures of 0.1 MPa and 200 MPa), to support a high pressure x-ray crystallography study into the pressure-induced water filling of a non-polar cavity. The study adds insight into the mechanism by which a protein is unfolded. Cavity filling is more favourable at higher pressures and as new cavities form, the protein is unfolded. Although the x-ray crystallography is used to show how the number of water molecules inside the cavity increases at high pressure, the MD is also useful in this case because it gives an atomistic analysis into how these water molecules behave. It is suggested that increasing the number of water molecules inside the cavity is favourable, since the water molecules form hydrogen bonds with each other. This counters the free-energy penalty of the interaction between the water and the hydrophobic core.

MD simulations are also used to study the Arc Repressor across a varying temperature and pressure range (Trzesniak et al., 2006). The study uses pressures up to 10 kbar, but even at the highest pressures, there is very little evidence of protein denaturation. Increase in temperature to 400 K does cause denaturation, but increasing the temperature alongside the pressure does not. It is concluded that pressure slows down the dynamics and that a longer simulation time is required to observe high pressure denaturation of protein. It is also suggested that temperature can be used as a tool to enhance the dynamics in a high pressure study. This study gives an atomistic level interpretation of the Arc Repressor at high pressure and is an example of how MD simulations can be performed on a solvated protein at high pressure.

It can be concluded from these recent studies that high pressure MD simulations can be used to successfully probe the structure and dynamics of peptides and enzymes in a solvated environment. Stable simulations have been performed at pressures as high as 10 kbar, with no unfolding of the protein below 2 kbar. A reduction in the radius of gyration, together with a slight increase in water infiltration is expected as the pressure is increased, but in general the secondary structure remains stable.

1.3.3 High Pressure Effect on MR

Hay et al. recently performed a high-pressure stopped-flow study of the hydride transfer during the reductive half reaction (RHR) of MR with NADH (Hay et al., 2007). Increasing the pressure from 1 bar to 2 kbar increases the hydride transfer rate from 50 to 161 s⁻¹ for protium and from 31 to 31 s⁻¹ for deuterium. However, this is accompanied by a slight increase in the primary KIE from 4.0 to 5.2. This cannot be accounted for using the model Northrop developed (mentioned in Section 1.3.1), or with a non-adiabatic H-tunneling model where pressure causes a compression of the reaction barrier (Hay et al., 2009b). It is possible to account for these observations, by invoking a promoting motion that changes frequency with pressure. It is suggested that this motion would shorten the distance between the NADH C4 and the FMN N5 atoms (the donor and acceptor in the hydrogen tunneling reaction). Figure 1.15 is taken from this paper.

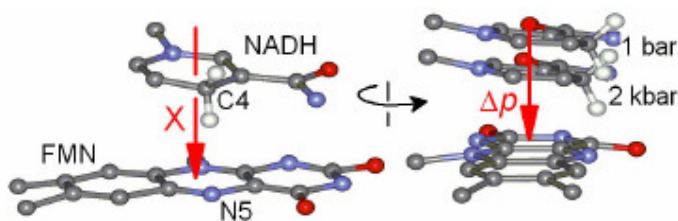


Figure 1.15: Possible pressure induced motion to shorten donor-acceptor distance between cofactors in morphinone reductase. [Taken from (Hay et al., 2007)]

An extension to this study is reported by Pudney et al., where the relative population of multiple reactive configurations (MRCs) is measured across the same pressure range (Pudney et al., 2009). A previous study had shown that a mutation to the active site residue (N189A) in MR induced MRCs (Pudney et al., 2007). It is suggested that as the pressure is increased, the relative population of these MRCs changes.

1.4 COMPUTATIONAL CHEMISTRY

This section gives a brief background to the computational chemistry techniques that are relevant to this thesis. The methods are described in further detail in Chapter 2.

1.4.1 Molecular Dynamics

Molecular dynamics (MD) is a computer simulation, based on molecular mechanics (MM), which allows atoms and molecules to interact for a period of time under Newtonian laws of physics. Atoms and bonds are modelled as balls and springs respectively. Electrons are treated implicitly, through a partial charge.

The first macromolecular MD simulation was published in 1977 (Mccammon et al., 1977). This was performed using the CHARMM program (Brooks et al., 1983) and the simulation was on 500 atoms for 9.2 ps. The protein in this simulation was bovine pancreatic trypsin inhibitor (which to this date is probably the best studied protein in terms of folding and kinetics). Since this publication, many other simulations have been published, with one of the major limitations on the quality/accuracy of the simulation being computer power. With this increasing all the time, simulations are becoming longer and can be performed on

larger systems. For example, in 2006, the complete satellite tobacco mosaic virus (STMV) was simulated. The system consisted of 1 million atoms and was simulated for 50 ns (Freddolino et al., 2006).

There are several programs to perform MD simulations. CHARMM is mentioned above; the other major programs are AMBER (Case et al., 2005b), GROMACS (Van Der Spoel et al., 2005) and NAMD (Phillips et al., 2005).

In its infancy, MD was probably considered to be limited by computational power. However, in the short time since the first simulation, this is no longer the case, as demonstrated by the study on STMV. MD is now considered to be an inexpensive method, relative to other methods (as detailed in the next section). MD can be used to simulate large proteins for long periods of time, allowing the observation of protein dynamics that include large conformational changes (domain movements) and smaller, atomistic scale, configurational changes (side chain rotation) (Mulholland, 2008).

1.4.2 Quantum Mechanical Techniques

The limitation of MM comes in its implicit treatment of the electrons. MM methods treat atoms classically, but the electrons have considerable quantum behaviour and so they cannot be described using classical mechanics. Quantum theory must therefore be invoked for computational studies of reactions catalysed by enzymes.

First principle (*ab-initio*) methods use full quantum mechanical formulae to calculate the properties of the systems. Several programs have been developed to perform *ab-initio* calculations. The most popular of these is GAUSSIAN (M. J. Frisch, 2003). Gaussian 70 was released in 1970 and has been updated continuously since, the most recent being the 19th major release, Gaussian 09.

QM methods are much more accurate than MM methods, but this accuracy comes with a considerable increase in computational expense. The limitation of QM methods therefore comes in the size of the system that can be studied. Proteins generally contain thousands to tens of thousands of atoms, thus, treating the entire enzyme quantum mechanically is beyond the current available computing power and in many cases is not necessary.

1.4.3 Combined QM/MM

A popular approach for computational studies into enzyme catalysed reactions is to use a quantum mechanics/molecular mechanics (QM/MM) method. The majority of the system is treated using an empirical MM force field; the part of the active site where the reaction occurs is treated by a QM method (Mulholland, 2008).

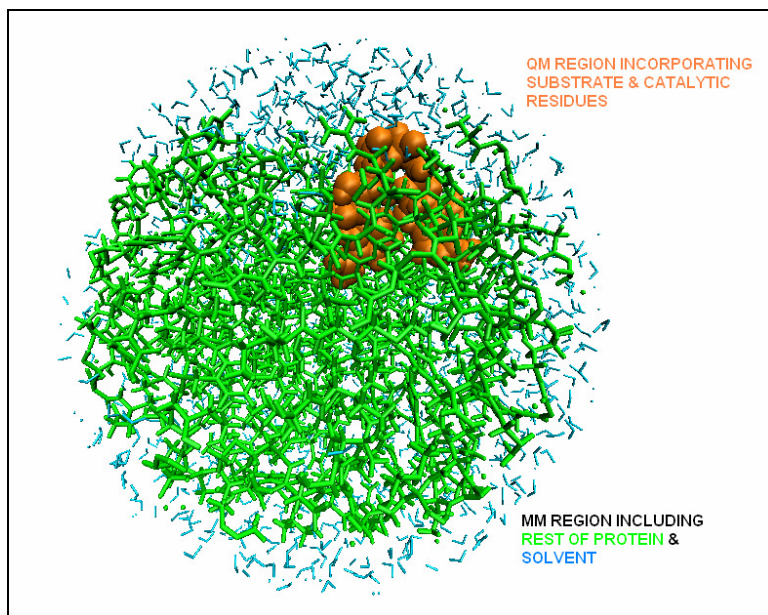


Figure 1.16: An example of a QMMM approach. The substrate, along with catalytic active site residues is represented by the VDW volume in orange. The rest of the protein (green) and solvent (cyan) are represented as sticks. [Adapted from (Mulholland, 2008)]

The QM/MM approach enables the modelling of reactions, quantum mechanically, with the effect of the protein environment incorporated by MM. They are used frequently to study enzyme mechanisms, since the reaction is modelled and atomistic detail of the rest of the enzyme and solvent is provided. The success of any computational approach is best measured by the agreement of the results with experimental studies. In this regard, QM/MM calculations can usually reproduce reaction barrier heights, compared to experimental measurements (Mulholland, 2007, Claeysens et al., 2006).

1.5 SUMMARY & AIMS OF PROJECT

It has become apparent over the past few decades that TST does not provide a full understanding of enzyme catalysis. There has been a paradigm shift to incorporate quantum tunneling into TST to provide more accurate models, although this has made the topic broadly more contentious and confusing. It is a topic that demands attention though, since half of all known enzyme catalyzed reactions involve at least one hydrogen transfer.

In many cases it has been shown that these reactions can proceed by full or partial tunneling (Hay et al., 2009a).

Referring back to Section 1.3, experimental pressure studies of the KIE in MR have suggested that a promoting motion exists in MR, that will bring the donor and acceptor atoms closer together to assist the tunneling reaction. The frequency of this motion is predicted to increase with pressure (Hay et al., 2007). Using high pressure as a probe in enzyme catalysis is uncommon, but not unprecedented. Northrop pioneered this and suggests that the scientific community should be more aware of the potential of pressure as a mechanistic probe (Northrop, 2006).

Computational techniques have the ability to provide atomistic insight into kinetic observations. The collaboration between experimental and theoretical study is paramount to success in the study of enzyme catalysed reactions. Experiments drive computational study; simulations can give details of, for example, which residues of an enzyme are important; this feedback drives further experiments. The results obtained by Hay are not in full agreement with the expectations proposed by Northrop for the pressure effect on catalysis. To understand these results, atomistic insight is required.

The aim of this research is to use pressure as a probe to study the hydride transfer process in the RHR of MR. In order to achieve this, the first technique used will be MD simulations, using a pressure range from 1 bar up to 2 kbar. This study will use the same program and force field that has been successful in previous studies on MR (Pudney et al., 2007), although an immediate issue to address is the suitability of this force field for high

pressure simulations, since it was developed at atmospheric conditions. The force field will be tested on a simulation of a waterbox, with the results compared to experimentally determined properties water at high pressure. It is also necessary to test the force field on a peptide. The ‘AK peptide’, previously studied successfully at high pressure, has been chosen for this (Paschek et al., 2005). This benchmarking of the method for high pressure MD simulations is in Chapter 3.

The hypothesis that the donor-acceptor distance decreases at high pressure can be investigated and verified with the MD simulations. Atomistic analyses of the substrate and cofactor will be carried out to try differentiate between the low and the high pressure configurations. Following this, the effect of pressure on the active site residues will also be studied. One such residue is Asn189, which has previously been studied via mutagenesis experiments (Pudney et al., 2007). The impact of pressure on this mutant will be considered. The ultimate aim of the MD will be to verify that the donor-acceptor distance decreases at high pressure and to determine how the protein environment is involved. An atomistic analysis of the MD simulations is presented in Chapter 4.

Finally, to study catalysis, MM methods are not sufficient and so the research will be expanded with a QM/MM investigation into how the high pressure configuration of MR impacts on the hydrogen transfer between the NADH and FMN. The rate of reaction and KIEs will be calculated and compared to the experimental observations. The QM/MM studies are reviewed in Chapter 5.

Chapter 2

Methodology

PREFACE

Computational chemistry can be considered to be applied theoretical chemistry. By applying physical laws to problems in chemistry and biology, and combining these with experimentally observed data, it has become a powerful tool for predicting the structures and properties of molecules. It is also widely used in the drug design process. The complexity of computational chemistry becomes apparent when one considers that such physical laws need to be implemented on an atomistic scale. At this scale, the level of physical understanding required needs to include quantum mechanical principles.

In recent years, knowledge and insight into quantum mechanics has increased. Alongside this, computational technology has gathered pace and the power of computers has improved considerably. However, even with larger memory capacities and better processing capabilities, it is still not possible for a computer to be able to simulate accurately the quantum mechanical behaviour of all of the atoms in a large system, such as a protein. Therefore, there are several methods that can be used, involving varying degrees of approximation, depending on the size of the system and the context of the study (Mulholland, 2008).

This chapter will introduce the computational methods relevant to this study and explain the techniques used to analyse the vast amount of data that is produced by the simulation programs. The programs and methods used in this research will be described in detail.

2.1 INTRODUCTION TO COMPUTATIONAL CHEMISTRY

2.1.1 Molecular Mechanics

The potential energy of a system can be calculated using Molecular Mechanics (MM) force fields. In such a system, atoms and bonds are treated as hard spheres and as springs respectively. Atoms have a specific mass, radius and a constant net charge, all of which are defined in the force field. The bonds, angles and dihedral angles are springs which are allowed to stretch, bend and rotate, but cannot break. The equilibrium bond length and the strength of the bond are also defined in the force field. The parameters in an MM force field are normally derived from experimentally observed values or values calculated by high level quantum mechanical (QM) methods.

A MM model ignores the electrons of each atom, instead assigning a charge to the atom. The reason for this approximation is that the difference in mass between the electrons and the nuclei is large (1.008 for a hydrogen atom compared to 5.486×10^{-4} for an electron (Mohr et al., 2008)), and, combined with the fast motions of the electrons, means that they can be considered to react immediately to the motions of the nuclei. Using this approximation, it is possible to calculate the potential energy of the system, based on the coordinates of the atoms, without taking the electrons into account. MM methods and QM methods are used to study different problems. It has been shown that for a large system, molecular mechanics calculations can reproduce the accuracy of high level QM calculations (Leach, 2001). This is a welcome observation, since MM methods are generally chosen for large systems, such as enzymes, as QM methods are limited to smaller systems due to computational expense. The limitation of MM methods is that the springs

(representing the bonds) cannot break – therefore they cannot be used to study processes that involve breaking and forming of bonds.

2.1.2 Force Fields

The force field is a set of parameters which contains the information necessary to compute the potential energy of the system. The total potential energy of a system, E_{total} , is the sum of the energies that arise from bonded, E_{bonded} , and non-bonded, $E_{non-bonded}$, interactions. The E_{bonded} term accounts for the energy needed to stretch, bend or rotate a bond, angle or dihedral angle. The $E_{non-bonded}$ term includes the energies that arise from interactions between atoms that are separated by three or more covalent bonds. Equation 2.1 gives the potential energy function of the system:

$$E_{total} = E_{bonded} + E_{non-bonded} \quad (2.1)$$

This potential function is the basis for any force field used in molecular mechanics. However the exact form of this can differ between different force fields used to perform MM calculations. There are several programs for MM, which these force fields can be implemented in, such as ‘Chemistry at HARvard Macromolecular Mechanics’ (CHARMM) (MacKerell Jr et al., 1998), ‘Assisted Model Building with Energy Refinement’ (AMBER) (Cornell et al., 1995), and ‘GRONingen Machine for Chemical Simulations’ (GROMACS) (Berendsen et al., 1995); most of these packages have their own version of the MM force field. AMBER refers to both the software package and to the force field, which can be implemented in other MM programs. The software package contains a group of programs

focussed on molecular dynamics and free energy calculations of proteins, nucleic acids and carbohydrates, which can use a variety of force fields, depending on the type of molecule being studied (Case et al., 2005a). The functional form of the AMBER force field is described in equation 2.2 (Weiner et al., 1984, Cornell et al., 1995).

$$E_{total} = \sum_{bonds} K_r (r - r_{eq})^2 + \sum_{angles} K_\theta (\theta - \theta_{eq})^2 + \sum_{dihedrals} \frac{V_n}{2} [1 + \cos(n\phi - \gamma)] + \sum_{i < j} \left[\frac{A_{ij}}{R_{ij}^{12}} - \frac{B_{ij}}{R_{ij}^6} + \frac{q_i q_j}{\epsilon R_{ij}} \right] \quad (2.2)$$

The force fields used for MM calculations in this thesis are the AMBER *ff96* and *ff03* force fields, and is implemented in the AMBER8 molecular dynamics package (Duan et al., 2003).

Each of the terms from Equation 2.2 will now be discussed in more detail. For the first two terms, a harmonic potential is used: the energetic penalty for deviation away from the equilibrium value is calculated using Hooke's Law – the strain is directly proportional to the stress applied. This is not strictly accurate, since natural bond stretching and angle bending are not harmonic; however since the values deviate very little from the equilibrium value, this is a reasonable approximation.

$$E_{bonds} = K_r (r - r_{eq})^2 \quad (2.3)$$

$$E_{angles} = K_\theta (\theta - \theta_{eq})^2 \quad (2.4)$$

Equation 2.3 describes the stretching of a particular bond. The force constant for the relevant bond is given by K_r , the length of the bond is given by r and is compared to the equilibrium length r_{eq} . In equation 2.4 the same form is used, with the bond length r being replaced by the angle θ to describe angle-bending, the equilibrium angle being θ_{eq} and the force constant associated with bending given by K_θ .

$$E_{dihedrals} = \frac{V_n}{2} [1 + \cos(n\phi - \gamma)] \quad (2.5)$$

The third term of the *ff03* force field equation is the dihedral term. This gives the energy required to rotate a dihedral angle. The dihedral angle is given as ϕ , V_n is the potential energy barrier for the rotation. n is the minimum number of points that the dihedral can occupy as it is rotated 360° and γ is a phase factor determining the minima of the angle.

The van der Waals (VDW) and electrostatic interactions are combined in the fourth and final term of the equation – the non-bonded term.

$$E_{non-bonded} = \left[\frac{A_{ij}}{R_{ij}^{12}} - \frac{B_{ij}}{R_{ij}^6} + \frac{q_i q_j}{\epsilon R_{ij}} \right] \quad (2.6)$$

For two atoms (i and j), attractive (A) and repulsive (B) forces are calculated relative to the distance (R) between them and combined using the Lennard-Jones 6-12 potential. This gives the VDW interactions. The electrostatic interactions are calculated using Coulomb's Law. They are dependant on the distance (R) between two atoms (i and j), the partial charge of the atom (q) and the dielectric constant (ϵ).

The most computationally expensive part of the force field is the non-bonded term. For a system containing N atoms, there will be $N(N-1)/2$ non-bonded interactions. Since MM calculations are normally performed on large systems, this represents an enormous amount of interactions. To improve computational efficiency, long range non-bonded interactions are not calculated because they are not supposed to have a significant effect on the system. A non-bonded cut-off distance is specified, normally between 8 Å and 15 Å. Interactions between atoms which are further apart than this distance are ignored.

2.1.3 Energy Minimisation

The parameters of the MM force field are used as criteria for finding the lowest energy conformation of a molecule. There are several different algorithms that can be used to search for a local minimum. In a first order minimisation, the forces acting upon the atoms (as calculated by the force field), indicate the direction in which the minimum energy conformation lies. Each atom is moved down this energy gradient to achieve an optimised structure. Two first order minimisation methods are the steepest descent method and the conjugate gradient method.

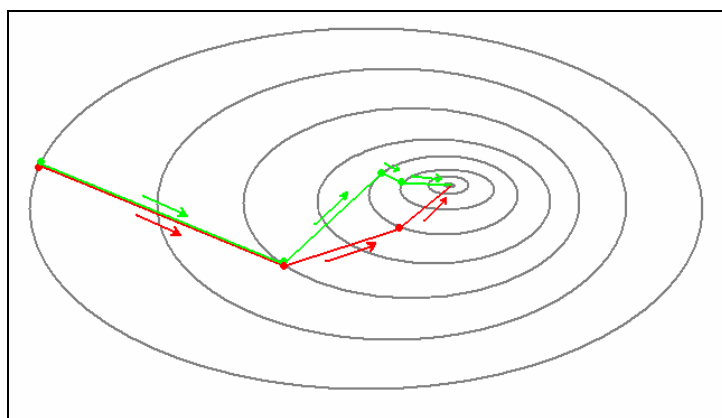


Figure 2.1: Figure to show minimum energy paths for steepest descent (green line) and conjugate gradients (red line) minimisation methods.

The steepest descent method is generally used at the beginning of a minimisation procedure, since it is simpler and faster than other methods. The potential energy is rapidly reduced with a removal of steric clashes and extreme angle strains. The conjugate gradient method is more refined and is applied as the potential energy approaches the minimum. It is similar to steepest descent, but at each step, the gradient from the previous step is also considered, making it more efficient, as illustrated in Figure 2.1 (Leach, 2001).

2.1.4 Molecular Dynamics

Molecular dynamics (MD) simulations use MM force fields to sample the conformational space available to a molecular system. The atoms in the system are allowed to interact for a period of time, giving a simulation of the motion (or *dynamics*) of the atoms. An MD simulation makes use of Newton's second law of motion, $F=ma$ (describing the acceleration, a , of a particle of mass, m , when a force, F , is exerted upon it). Integrating this gives:

$$\frac{d^2x_i}{dt^2} = \frac{F_{x_i}}{m_i} \quad (2.7)$$

When a force F_{x_i} acts on a particle of mass m_i , along a coordinate x_i , the motion of the particle in that direction is described by equation 2.7. The particles in an MD simulation are the atoms, each with its own specific mass. The force on the atom is calculated at time t , using the force field and is therefore dependant on the position of the atom with respect to all other atoms in the system. Using the force, the accelerations of the atoms are calculated. These are combined with the positions and velocities of the atoms at time t to calculate the

positions and velocities of the atoms at $t + \Delta t$, where Δt is the timestep. The timestep should be large enough to explore as much phase space possible, but small enough, so that two atoms do not become too close. A typical timestep for classical MD simulations is 1 fs – an order of magnitude lower than the highest frequency motions in the system. However, if the SHAKE method (Ryckaert et al., 1977) is used, the timestep can be increased to 2 fs, since it constrains the carbon-hydrogen bond-stretching freedom, which is the fastest motion.

As mentioned in section 2.1.2, the most computationally expensive part of the force field calculation is the non-bonded interactions. A cut off distance can be applied to improve computational efficiency, but this does cause errors with the calculation of the Coloumbic forces that act on the atoms (Loncharich and Brooks, 1989). To minimise the errors, the Particle-Mesh-Ewald (PME) method can be used (Darden et al., 1993), alongside the Periodic Boundary Condition (PBC). PBC concerns the solvation environment and is illustrated in Figure 2.2.

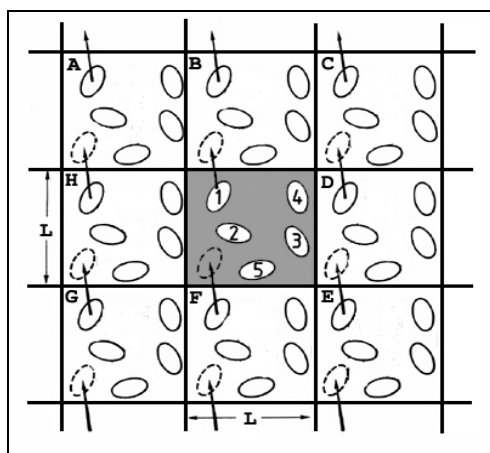


Figure 2.2: *Periodic Boundary Conditions represented in two dimensions. If molecule 1 moves from the central box into box B, it is replaced by its image which moves from box F into the central box. This movement is replicated across all the boxes. (Adopted from the tutorial of AMBER programme: (http://amber.scripps.edu/tutorial/polyA-polyT_New/minandmd3.html))*

PBC duplicates the simulated solvent box in three dimensions. If a solvent molecule moves out of the box, it will be replaced by the equivalent molecule from the box on the opposite

side. This allows for an explicit solvent environment with a large number of solvent molecules. An implication of PBC is that the cut-off distance must be less than half of the box size, so that each atom can only interact with one copy of every other atom. Using PME alongside PBC allows a particle to interact with all other particles within the simulated box and all of the surrounding boxes. A fast Fourier transform is used to speed up the treatment of interactions in the image boxes, thus improving the accuracy of the force field calculation at minimal computational expense.

There are three ensembles that can be used in MD simulations. In the microcanonical ensemble (NVE), the number of particles, the volume and the energy of the system are kept constant. This can cause a problem with the temperature of the system. For example, in an enzyme, when an exothermic conformational change occurs, it naturally raises the temperature of the system. To keep the temperature constant, the canonical ensemble (NVT) can be used, where the energy of endothermic and exothermic processes is exchanged with a thermostat, keeping the number of particles, the volume and the temperature constant. This is probably the most common ensemble used in MD simulations.

The ensemble used for the majority of the simulations in this work, however, is the Isothermal-Isobaric (NPT) ensemble – in which the number of particles, temperature and pressure remain constant. In addition to the thermostat, a barostat is used, to allow constant pressure dynamics to be performed. This ensemble replicates the laboratory conditions better than the other ensembles. Pressure can be calculated in an MD simulation using Clausius virial theorem The barostat employed in AMBER, which is used for the MD

simulations in this work, program is the Berendsen barostat (Berendsen et al., 1984). This is a weak coupling algorithm, which regulates the pressure by adjusting the volume of the unit cell by small amounts in each step so that the computed pressure approaches the target pressure. The algorithm is shown below:

$$dP/dt = (P_0 - P)/\tau_P \quad (2.8)$$

where P is the instantaneous pressure, P_0 is the target pressure and τ_P is the barostat relaxation time. If the instantaneous pressure is lower than the target pressure, the program will decrease the volume of the unit cell; if it is higher, it will increase the volume. The optional parameters for constant pressure MD in AMBER are isotropic or anisotropic position scaling, the compressibility factor and the pressure relaxation time (the coupling constant). For the purposes of this study, isotropic position scaling is used, since anisotropic is inappropriate for solutes dissolved in water; the default setting for the compressibility factor is used ($44.6 \times 10^{-6} \text{ bar}^{-1}$), which is the compressibility of water. The recommended value for the coupling constant is between 1 and 5 ps, with the default value set at 1 ps, but with the option of increasing it if the trajectories are unstable.

2.1.5 Quantum Mechanics

2.1.5.1 Introduction

MM methods are useful for studying the dynamics of macromolecules, such as proteins, and can provide useful insight into conformational changes in a protein (Swift and McCammon, 2008). They have also been used in the study of proteins at high pressure

(Trzesniak et al., 2006) and in studies of hydrogen tunnelling (Johannissen et al., 2007) – both of which are relevant to this thesis. However, as mentioned in the previous section, these methods do not explicitly include electrons and therefore cannot be used to study the breakage or formation of chemical bonds. Quantum Mechanical (QM) methods can be employed to study these processes. Electrons exhibit behaviour of both particles and waves and therefore cannot be described using the same physical laws of motion used for MM methods. The first step of a QM calculation is to attempt to solve the Schrödinger equation:

$$H\psi = E\psi \quad (2.9)$$

In this equation, H is the Hamiltonian which operates on the molecular wavefunction ψ and E is the total molecular energy. It is only possible to accurately solve the Schrödinger equation for very small systems. QM methods simplify this by using the Born-Oppenheimer approximation. The motion of the electrons is considered to be separate to the motion of the nuclei, due to the distance in mass discussed in Section 2.1.1. The wavefunction then depends only upon the position of the nuclei and the total energy can be calculated at fixed nuclei positions. The total energy of the system includes the nuclear energy (from the nuclei-nuclei interactions) and the electronic energy. The electronic energy is the total of the kinetic energy and potential energy of the electrons and the interactions between electrons.

The most widely used QM theory for treating molecular systems is the molecular orbital (MO) theory, although there are other approaches, such as Density Functional Theory (DFT). MO theory uses the Linear Combination of Atomic Orbitals (LCAO)

approximation, where the atomic orbitals are combined to form molecular orbitals that cover the whole molecule. The Hartree Fock (HF) method is one method employed to solve the Schrödinger equation in MO theory, as discussed in section 2.1.5.3. Firstly though, it is important to discuss the basis set that is required to calculate the wavefunction in QM methods.

2.1.5.2 Basis Sets

The basis set is a series of numbers that is used to construct the molecular/atomic orbital. This is required to calculate the wavefunction, thus describing the positions of the electrons relative to the nuclei and to each other. Minimal basis sets, such as STO-3G and STO-6G treat all electrons equally. Split-valence basis sets, such as 3-21G and 6-31G use a more rigorous and accurate calculation on valence electrons, since these are involved in the reaction. Arguably the most popular basis set used in computational chemistry is 6-31G, which is classed as a double-zeta basis set, since the wavefunction of the valence electrons is calculated twice. The 6-311G triple-zeta basis set is even more accurate.

There are two other functions that can be added to basis sets if necessary. Polarization functions allow electrons to move into an orbital that they would not typically be, i.e. for an electron in a carbon atom to move into a d-orbital, which would happen if the orbital was distorted by a neighbouring atom. A polarized basis set is normally indicated by the orbital name, or by a “*”, such as 6-31(d) or 6-31*. Another function is a diffuse basis set, indicated with a “+”. This increases the distance that electrons are allowed to be found away from the nucleus. This is important when considering excited states.

2.1.5.3 Hartree-Fock Method

The Hartree-Fock (HF) method is an *ab initio* quantum chemistry method. This means that there is no empirical data used and the calculation is purely from first principles. HF theory is the simplest *ab initio* method - its simplicity arising from the assumption that each electron experiences the average field of all of the other electrons, rather than calculating all of the electron-electron interactions. The Fock operator is the term used to describe the Hamiltonian that includes the electron interactions. This is dependant on the spin orbitals of the other electrons, which is not known. To overcome this, the Fock operator is first constructed using a fabricated set of spin orbitals. This is used to solve the HF equations and gives a new set of spin orbitals. The process is repeated until a self-consistent field is obtained. This method is known as the self-consistent field method (SCF) (Leach, 2001).

The HF method acts as the initial step for all molecular orbital methods – more accurate and more approximate methods are based on HF. The major draw back of HF is that it does not include electron correlation, which decreases the accuracy. HF *ab initio* methods can be very computationally expensive for larger molecules. To reduce the computational expense, semi-empirical methods have been developed (such as AM1), which only consider the valence electrons and apply empirical parameters, since these are the electrons involved in the reaction.

2.1.5.4 Density Functional Theory

Density Functional Theory (DFT) has become more popular in computational chemistry in recent years (Johnson et al., 1993, Zhao and Truhlar, 2007). DFT methods are considered to be more accurate than HF methods, since they take into account electron correlation.

Also they are not as computationally expensive as HF methods, since they do not attempt to calculate the wavefunctions of all of the electrons in the molecule. Instead, the energy of the molecule is calculated as the functional of the electron density. The Kohn Sham theory (Kohn and Sham, 1965) describes how the energy is calculated from the electron density.

$$E_{DFT}[\rho] = T[\rho] + E_{ne}[\rho] + J[\rho] + E_{xc}[\rho] \quad (2.10)$$

Each of the terms in equation 2.10 is a function of the electron density, ρ . E is the total energy, T is the kinetic energy of the electrons, E_{ne} is the nuclear-electron attraction energy and J is the electron-electron repulsive energy. These first three terms can be calculated with *ab initio* methods. The fourth term, E_{xc} , represents the electron-electron exchange-correlation energy. There are several different approximations that can be used to try to calculate this energy. In order of increasing accuracy, DFT methods can be classed as Local Density Approximation (LDA), Local Spin Density Approximation (LSDA), Generalized Gradient Approximations (GGA) and meta-GGA.

The increased use of DFT as a method for computational chemistry in recent years is due to the proven ability of the approximations. This is owed much to the development of hybrid functionals which increase the accuracy of the exchange and correlation by combining an exact portion of exchange calculated using HF with exchange and correlation calculated using from other methods (such as LDA or empirical methods). B3LYP (Stephens et al., 1994) is one such functional and is arguably the most popular DFT method used in computational chemistry (Mulholland, 2007). The acronym describes

the two functionals combined: the Becke 3-term correlation functional and the Lee, Yang and Parr exchange functional.

Although the B3LYP functional is popular amongst computational chemists, there are new functionals being developed all the time. Some of these can be more accurate than others in different situations. One such functional that has been applied to this research is the Becke's half-and-half functional (BH&H) (Becke, 1993). It has been suggested that this hybrid DFT functional, combined with a modest basis set can calculate accurate energies for configurations where π -stacking interactions are important (Waller et al., 2006).

2.1.5.5 Hybrid QM/MM Simulations

It would be a huge computational expense to attempt to treat a system of more than a few hundred atoms quantum mechanically. For an enzyme, it is unnecessary to treat the whole system using a QM method, since in the case of an enzyme-catalysed reaction, the active site is very small in comparison to the size of the enzyme. With this in mind, hybrid QM/MM methods have been developed that treat the majority of the system molecular mechanically, whilst treating the key catalytic residues, the substrate and any cofactors quantum mechanically.

An issue in QM/MM simulations is the boundary between the QM and MM regions, particularly when a covalent bond crosses the boundary. One way of dealing with this issue is the link atom method. This method adds a hydrogen to the QM atom, that is not experienced by the MM atoms. This allows the electron density to be terminated in the QM region, without disrupting the valence, and maintains the bonded interaction between the

QM and MM atom (Singh and Kollman, 1986). An alternative to the link atom approach is the generalised hybrid orbital (GHO) method (Gao et al., 1998). A sp^3 carbon is chosen as the boundary atom and considered as both a QM and a MM atom. The GHO atom has a set of hybrid orbitals placed between the QM and MM region. The orbital that points towards the QM atoms is called the active orbital and is included in the SCF calculation in the QM region. The other three hybrid orbitals are called auxiliary orbitals and generate an MM potential for the boundary atom.

2.1.5.6 ONIOM

The ONIOM (Our own N-layered Integrated molecular Orbital and Molecular mechanics) approach is a QM/MM method implemented in the Gaussian suite of programs. It allows a maximum of three different levels of theory to be applied to a molecular system. The energies of the three individual layers can then be combined. In a two layer ONIOM, the total energy of the MM region is added to the total energy of the QM region and then the MM energy derived for the atoms in the QM region is subtracted. Covalent bonds that cross the boundaries between the layers are dealt with using the link atom approach.

2.2 METHODOLOGY USED IN THIS THESIS

2.2.1 Molecular Dynamics Simulations of Waterbox

A 15 \AA^3 waterbox was created using the LEaP program of the AMBER8 package. Firstly a water molecule was loaded into xleap and then solvated with a 15 \AA^3 waterbox. This was

saved in the protein data bank file format (.pdb), along with its associated parameter and topology files.

Sander (the program that performs MD simulations in AMBER) was used to perform the MD simulation. The system was minimized in 2000 steps: the first 50 steps of minimization using the steepest descent method, and the remaining steps using the conjugate gradient method. A 9 Å cut-off was used for non-bonded interactions. Once minimised, the system was heated to 298.13 K in an MD simulation at constant volume, for a period of 100 ps. The NVT ensemble was used, with the temperature being set to 298.13 K.

After the heating step, the NPT ensemble was used to perform for constant pressure dynamics. At this point the simulation was branched into 5 simulations: 1 bar, 500 bar, 1 kbar, 1.5 kbar and 2 kbar. The temperature was constant at 298.13 K for the simulations. The system was equilibrated at each pressure for 100 ps and the MD simulation continued for a further 500 ps production run.

The trajectories were saved every 0.5 ps. The properties of the waterbox were saved to the output file every 0.5 ps. A perl script obtained from the AMBER website (http://amber.scripps.edu/tutorials/basic/tutorial1/files/process_mdout.perl) was used to print out the properties of the waterbox. These properties included the water density. The calculated water density across the pressure range was compared with the experimental water density, obtained from the NIST Chemistry WebBook at

<http://webbook.nist.gov/chemistry/fluid/> (E.W. Lemmon). (See Figure 3.3 in Chapter 3 for details)

2.2.2 MD Simulations of the AK-peptide

The AK-peptide was created by building an α -helical peptide with the sequence: Ac-AKAA(AAKAA)₃AA_Y-Nme using Molecular Operating Environment (MOE) (CCG, 2008). The peptide was saved as a .pdb file and imported into LEaP. It was then solvated in an octahedral water box, using the TIP3P model, with at least 10 Å between the peptide and the edge of the waterbox. 4 Cl⁻ ions were added to neutralize the charge of the system. The total number atoms in the system was 12787, with 24 amino acid residues, the Na⁺ ions and 4164 water molecules.

The energy of the system was minimised using a 2000 step minimisation procedure (50 steps using the steepest descent method, then the remaining steps using the conjugate gradient method) – as for the waterbox. A 9 Å cut-off was used for non-bonded interactions and periodic boundary conditions were employed. The protein atoms were restrained in the minimization with a force constant of 10.0 kcal mol⁻¹. Following the minimization, the system was equilibrated to achieve the desired temperature and pressure. It was first heated to 298.13 K, using constant volume MD for 100 ps. During this, the force restraints imposed upon the protein were decreased to 5.0 kcal mol⁻¹. The NVT ensemble was used with the temperature set to 298.13 K. Further equilibration steps were carried out at constant pressure, using the NPT ensemble, keeping the temperature constant at 298.13 K.

For the pressure equilibration, the simulation was branched into five different simulations at the five pressures: 1 bar, 500 bar, 1 kbar, 1.5 kbar and 2 kbar. The first two equilibration steps were both for 100 ps, but with the force restraints being decreased. The first equilibration had a restraint of 5.0 kcal mol⁻¹, the final equilibration had a force restraint of 0.5 kcal mol⁻¹. Following this, the system was allowed to equilibrate without restraints for 1 ns at constant pressure. Finally, the production trajectories were collected for the 5 ns at each of the five pressures. A time step of 2 fs was used and the coordinates were saved every 1000 steps (2 ps). The SHAKE algorithm was used to perform constraints for bonds involving hydrogen.

2.2.3 MD Simulations of MR

2.2.3.1 System Setup

The MD simulations were performed using the AMBER8 package with the AMBER ff03 force field. The crystal structure of Morphinone Reductase (MR) was taken from the protein data bank with the cofactor FMN and NADH₄ bound in the active site (2R14.pdb). Hydrogens were added using the LEaP program in AMBER. The protein was solvated in an octahedral water box, using the TIP3P model, with at least 10 Å between the protein and the edge of the waterbox. 18 Na⁺ ions were added to neutralize the charge of the system. The protonation states of the residues were determined using H++ (Gordon et al., 2005). The total number atoms in the system was 31673, with 357 protein residues, the 121 atoms of the cofactor and substrate, the Na⁺ ions and 8707 water molecules.

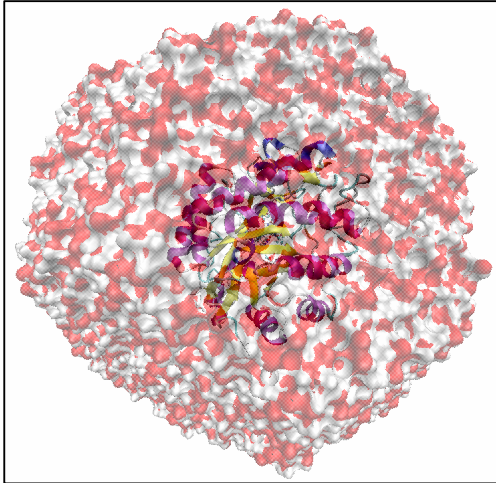


Figure 2.3: MR in 15 Å³ waterbox. The protein is represented by its secondary structure, with the waterbox shown using a 'surf' representation. Created using VMD (Humphrey et al., 1996)

The extra parameters required for the substrate and cofactor (not included in the AMBER ff03 force field) were obtained from the AMBER parameter database on the Bryce Group website (<http://www.pharmacy.manchester.ac.uk/bryce/amber>) (Walker et al., 2002, Schneider and Suhnel, 1999)

MD simulations were also performed on a mutated MR (MR_N189A). The residue that was mutated was Asn189 and was replaced with an alanine. To set up this simulation, the wild-type MR was used (2R14.pdb), with the side-chain of Asn189 from the C_β outwards deleted and a hydrogen atom was added, as shown in Figure 2.4. The set-up then followed the same procedure as for the wild-type MR.

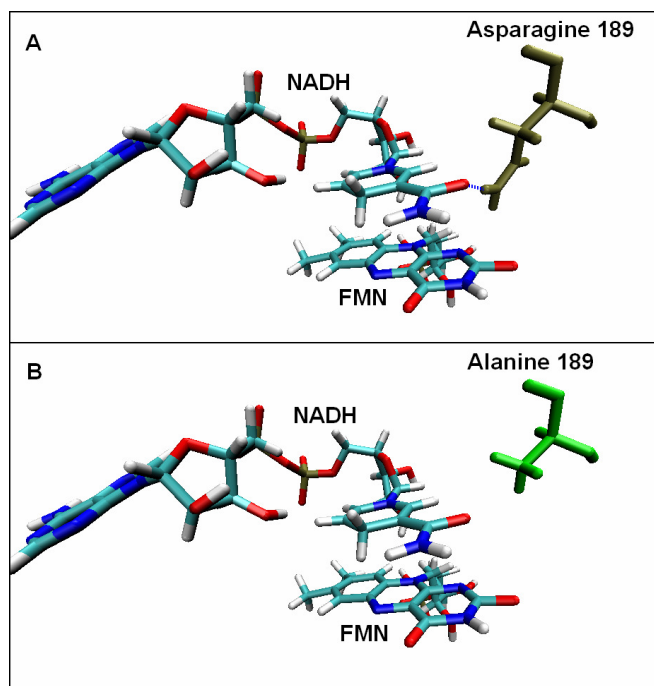


Figure 2.4: Figure to illustrate the effect of mutating Asn189 to alanine

2.2.3.2 Minimisation and MD Simulations

The energy of the system was minimised using a 2000 step minimisation procedure (50 steps using the steepest descent method, then the remaining steps using the conjugate gradient method) – as for the waterbox. A 9 Å cut-off was used for non-bonded interactions and PBC were employed. The protein, cofactor and substrate atoms were restrained in the minimization with a force constant of 10.0 kcal mol⁻¹. Following the minimization, the system was equilibrated to achieve the desired temperature and pressure. It was first heated to 298.13 K, using constant volume molecular dynamics for 100 ps. During this, the force restraints imposed upon the protein substrate and cofactor were decreased to 5.0 kcal mol⁻¹. The NVT ensemble was used with the temperature set to 298.13 K. Further equilibration steps were carried out at constant pressure, using the NPT ensemble, keeping the temperature constant at 298.13 K.

For the pressure equilibration, the simulation was branched into five different simulations at the five pressures: 1 bar, 500 bar, 1 kbar, 1.5 kbar and 2 kbar. The first two equilibration steps were both for 100 ps, but with the force restraints being decreased. The first equilibration had a restraint of $5.0 \text{ kcal mol}^{-1}$, the final equilibration had a force restraint of $0.5 \text{ kcal mol}^{-1}$. Following this, the system was allowed to equilibrate without restraints for 2 ns at constant pressure. Finally, the production trajectories were collected for the 10 ns at each of the five pressures. A time step of 2 fs was used and the coordinates were saved every 1000 steps (2 ps). The SHAKE algorithm was used to perform constraints for bonds involving hydrogen.

The simulations performed on the mutated MR followed the same procedure as the wild-type. In order to compare the how the constant pressure and constant volume MD might differ, the simulation for wild-type MR at 1 bar was repeated, using the NVT ensemble, rather than NPT. The minimisation and heating steps were identical to the other simulations. Where the other simulations were branched for equilibration at the respective pressures, the NVT simulation was equilibrated for the same period of time at constant volume and temperature, before the 10 ns production trajectory was collected.

2.2.4 Analysis of MD Trajectories

2.2.4.1 Ptraj

Ptraj is a program implemented in the AMBER molecular dynamics package. It is used to process and analyze sets of 3-D coordinates. Basic functions of ptraj include calculating distances between atoms, angles and dihedral angles of interest. Ptraj is also used to

calculate the root-mean-square-deviation (RMSD) and root-mean-square-fluctuation (RMSF) of proteins. The equation for calculating the RMSD is shown below:

$$RMSD = \sqrt{\frac{\sum_{i=1}^N d_i^2}{N}} \quad (2.11)$$

In equation 2.11, N is the number of atoms for which the RMSD is calculated and d_i is the distance between the coordinate of atom i of the two structures that are being compared. The RMSF is the average RMSD over a period of time. The RMSD of the protein backbone plotted against time in a trajectory can give an indication of the stability of the protein during the simulation. The RMSF, plotted against protein residues, highlights the more flexible/dynamic parts of the protein. It is also possible to compare the RMSF to B-factors from crystallographic studies (Hunenberger et al., 1995b) and it is possible to convert the RMSF into suitable units in ptraj. Ptraj can also be used to generate covariance matrices for essential dynamics analysis, which is described further in section 2.3.3.

2.2.4.2 Visual Molecular Dynamics (VMD)

VMD is a molecular visualization program for displaying, animating, and analyzing large biomolecular systems using 3-D graphics and built-in scripting (Humphrey et al., 1996). There are certain plugins in VMD which have proved useful for analyzing the structure and dynamics of the protein. These are: Timeline, which allows analysis of secondary structure against time; RMSD Trajectory Tool, which allows the trajectory to be aligned on an atom selection for further analysis with respect to that set of atoms; VolMap, which creates volumetric maps as isosurfaces, based on a selection of atoms and can be used to plot the space sampled by a particular set of atoms across the trajectory.

2.2.4.3 Normal Mode Analysis

In normal mode analysis (NMA) the potential energy function is approximated, using a harmonic model, for a conformation at a potential energy minimum. The mass-weighted second derivatives of the potential energy function with respect to the Cartesian coordinates form the Hessian matrix. The number of second derivatives is dependant on the number of atoms – a system containing N atoms will have $3N \times 3N$ second derivatives. Diagonalizing the Hessian matrix gives the eigenvectors and eigenvalues. The eigenvectors are often referred to as the normal modes and their associated eigenvalues can be converted into the frequencies. An NMA can be used for various purposes, such as to characterize a stationary point on a potential energy surface, or to identify conformational changes. In proteins and macromolecules lower frequency normal modes can normally be attributed to the large atomic displacements; the higher frequencies normal modes are more localised with fewer atoms involved.

elNemo (Tirion, 1996) is a web-based program that can be used to compute the low frequency normal modes of a protein. The equilibrated structure was used as the input for elNemo; the lowest frequency normal mode of the protein was analysed and two conformations were obtained. DynDom (Hayward and Lee, 2002) is another web-based program that can be used to determine domains, hinge axes and hinge binding residues in proteins where two conformations are possible. The conformations obtained from elNemo were used as the input for DynDom to determine whether or not there is a dynamic domain present in the protein. The elNemo and DynDom analysis is contained in Section 4.3.1.

2.2.4.4 Principal Components Analysis

Principal Components Analysis (PCA) is a powerful tool that is used to reduce a multidimensional set of data into the dimensions that represent the majority of the data. The dataset is transformed into a set of principal components (PC's) where the PC1 contains the most variation in the dataset, PC2 contains the second most, etc. By analysing the first principal components and discarding the others, PCA aids in finding the most significant deviations in a data set.

A PCA was performed on the 2D-RMSD matrix generated in Chapter 4 (Section 4.1.4). The matrix generated by the 2D-RMSD contains an enormous amount of information. By utilising PCA, the most significant deviations can be extrapolated from this matrix. Plotting the first two principal components gives a representation of the different areas of conformational space sampled by the selection that the original RMSD was calculated for.

2.2.4.5 Essential Dynamics

Essential Dynamics is a method used to analyse MD trajectories. It involves the construction of a covariance matrix from trajectory data fitted to a reference structure. A PCA is performed on the covariance matrix, allowing correlated, significant motions to be separated from random, insignificant ones. The first principal component represents the vector motion with the most deviation and the deviation decreases for successive principal components.

Interactive Essential Dynamics (IED) (Mongan, 2004) is a program that is used in combination with molecular dynamics packages, such as AMBER, and with VMD. The

essential dynamics calculation is performed in ptraj and the output can then be visualised using VMD with the IED plugin.

2.2.5 QM/MM Methods

2.2.5.1 Benchmarking the Method

The first step of performing the QM/MM calculations was to benchmark the method, in order to decide which DFT functional and which basis set were best for the QM/MM. To achieve this, gas phase calculations were performed on a simplified structure of the cofactor and substrate, comprising 51 atoms in total: 31 atoms representing the isoalloxazine ring of the cofactor FMN and 20 atoms representing the nicotinamide ring of the substrate NADH.

Gaussian 03 was used to perform the DFT calculations. Two different functionals were tested to compare how well they modelled the π - π stacking interaction which is crucial in the cofactor-substrate geometry. The two functionals used were BH&H and B3LYP. These were tested using three different basis sets: 6-31G*, 6-31+G* and 6-311++G**. The geometry was optimised and analysed. For geometries that appeared reasonable, the frequencies were calculated and potential energy scans were performed by applying a distance constraint between the transferring hydride on the substrate and acceptor nitrogen on the cofactor. This distance was decreased to force the reaction. The benchmarking results are detailed in Section 5.1.

2.2.5.2 QM/MM Setup in ONIOM

Following the benchmarking of the QM level to be used, QM/MM calculations were performed using the ONIOM method, implemented in Gaussian 03. The starting structures were obtained from MD simulations performed previously. However, since ONIOM applies the ff96 force field to represent the MM part of the system, it was necessary to re-equilibrate the system with ff96 and take snapshots from MD simulations using this force field. The MD simulations used the NPT ensemble and were performed at low (1 bar) and high (2 kbar) pressures. Structures were chosen from each of these re-equilibrated simulations, which had active site configurations that were representative of the pressure.

Each structure taken from MM was setup as follows: all water molecules further than 8 Å from the transferring hydride were deleted. The QM region was defined as a 44 atom region, including the nicotinamide ring of NADH and the isoalloxazine ring of FMN, as shown in Figure 2.4. The link-atom method was employed to treat covalent bonds between the QM and MM region. The MM region within 20 Å of the transferring hydride was free to move, but the atoms in the MM region further away were frozen.

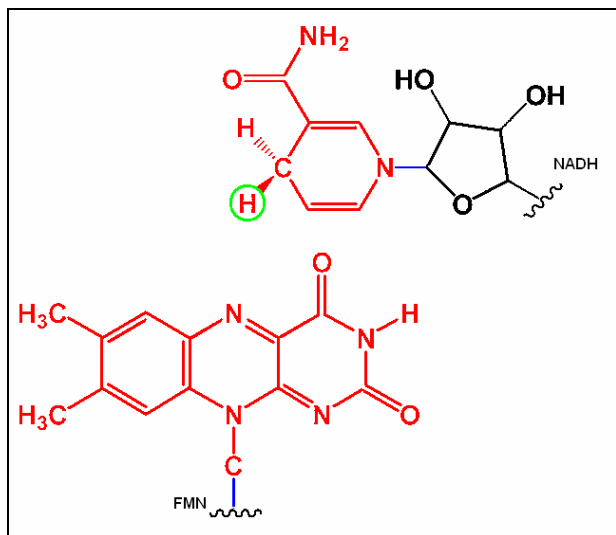


Figure 2.5: Diagram showing the QM region (red) used in the QM/MM method. Link atoms were required to replace the bonds shown in blue. The hydrogen circled is the transferring hydride. Atom numbers are detailed in Appendix C

2.2.5.3 QM/MM Potential Energy Scans

The geometry of each structure was optimised using the BH&H functional and the basis set 6-31+G* for the QM region and the AMBER ff96 force field, as implemented in Gaussian 03, for the MM region. The stationary points on the potential energy surface (PES), represented by the optimised geometry was characterised by performing frequency calculations. For those frames that represented a true minimum at the reactant (i.e. with no negative frequencies), potential energy scans were performed as for the gas phase calculations – moving the hydride from the donor carbon of NADH to the acceptor nitrogen of FMN at an interval of between 0.02 Å and 0.1 Å for each scan. The transition state for each of these scans was confirmed by running frequency calculations, with one negative frequency corresponding to the breaking and forming bond.

The analysis of the energies obtained from the QM/MM simulations, including the calculations of tunneling contributions, is discussed in Chapter 5.

Chapter 3

High Pressure Molecular Dynamics

Simulations

PREFACE

The effect of hydrostatic pressure on proteins has been studied both experimentally and computationally for several years (Bridgman, 1914, Northrop, 2006, Collins et al., 2005). However, there is currently no particular molecular dynamics simulation algorithm, or force field, that has been developed specifically to replicate the pressure effect. The aim of this research is to use pressure as a probe to study the dynamics, and possibly catalysis of Morphinone Reductase, by computational approaches. To be able to carry out such research, it is important that we are confident that the algorithm and force field chosen are able to replicate the experimental effect of pressure efficiently.

The force field used to represent the solvation environment is also very important. In the present study, the TIP3P model for water will be used, since this has been shown to be successful in several molecular dynamics studies in the past. Therefore the first step must be to ensure that the water in the simulation responds appropriately to the pressure increase, by comparing a theoretical waterbox with experimental results. To step up from the waterbox at high pressure to a protein at high pressure, an intermediate stage of the investigation involves testing the chosen force field representing the protein for a solvated peptide at high pressure. Upon satisfaction that the force field is able to cope with the high pressure, simulations on Morphinone Reductase are performed. The stability of the simulations and the macromolecular changes associated with the increase of pressure are analysed.

3.1 WATER BOX

MD simulations were performed at constant pressure on a 15 \AA^3 water box, using the TIP3P force field. The pressures used were 1 bar (0.1 MPa) – approximately equal to one atmosphere, 500 bar, 1 kbar, 1.5 kbar 2 kbar, 2.5 kbar, 5 kbar, 7.5 kbar and 10 kbar.

3.1.1 Results at Atmospheric Pressure

Figure 3.1 shows how the total potential energy, temperature, pressure and volume of the system varied with time at atmospheric pressure.

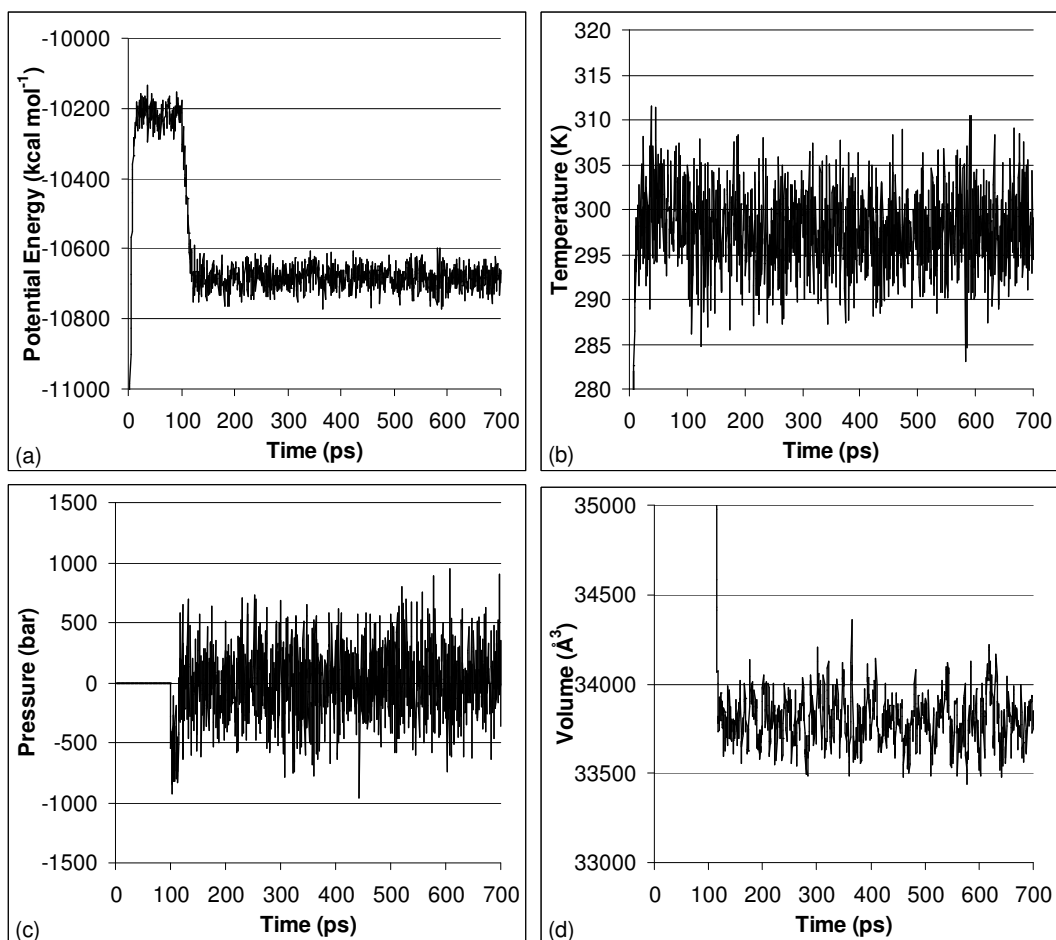


Figure 3.1: The potential energy (a), temperature (b), pressure (c) and volume (d) of the waterbox system during the 700 ns simulation time, including heating (0-100 ps), equilibration at constant pressure (100-200 ps) and production (200-700 ps)

The first 100 ps are the heating step, which was performed at constant volume. The potential energy of the system increases from the minimised structure by approximately 4600 kcal mol⁻¹, and fluctuates around 10200 kcal mol⁻¹ during the heating step. The temperature quickly reaches its target temperature of 298.13 K and remains stable for the duration of the constant volume and constant pressure MD simulations. When the simulation algorithm is switched from constant volume to constant pressure, the potential energy decreases slightly by ~450 kcal mol⁻¹. It is noted that the pressure (Figure 3.1 (c)) appears to fluctuate significantly from its target value of 1 bar. The procedure followed by AMBER to maintain a constant pressure is to change the volume by small amounts each step (as can be seen in Figure 3.1 (d)). The volume decreases initially to obtain the desired pressure and reaches an equilibrium value of around 33800 Å³ after 20 ps, where the volume then fluctuates slightly for the remainder of the simulation. The average values for the production run (as seen in Table 3.1) show that the average pressure is close to the target pressure of 1 bar.

| Phase of Trajectory: | Heating | Equilibrium | Production |
|--|----------------|--------------------|-------------------|
| Kinetic Energy (kcal mol ⁻¹) | 1939.70 | 1976.65 | 1974.12 |
| Potential Energy (kcal mol ⁻¹) | -10308.10 | -10645.45 | -10682.12 |
| Total Energy (kcal mol ⁻¹) | -8368.41 | -8668.80 | -8708 |
| Temperature (K) | 292.2 | 297.77 | 297.39 |
| Volume (Å ³) | - | 34876.78 | 33800.91 |
| Pressure (bar) | - | -101.52 | 0.489 |
| Density (g ml ⁻¹) | - | 0.961 | 0.986 |

Table 3.1: *The average values at 1bar for the 100 ps heating step at constant volume, 100 ps equilibration step at constant pressure and 500 ps production step at constant pressure*

3.1.2 Effect of Increasing Pressure

The other simulations follow the same trend as the simulation at atmospheric pressure. The simulations branch after the heating step (at 100 ps) and the different values from this point onwards are due to the different pressures, as illustrated in Figure 3.2.

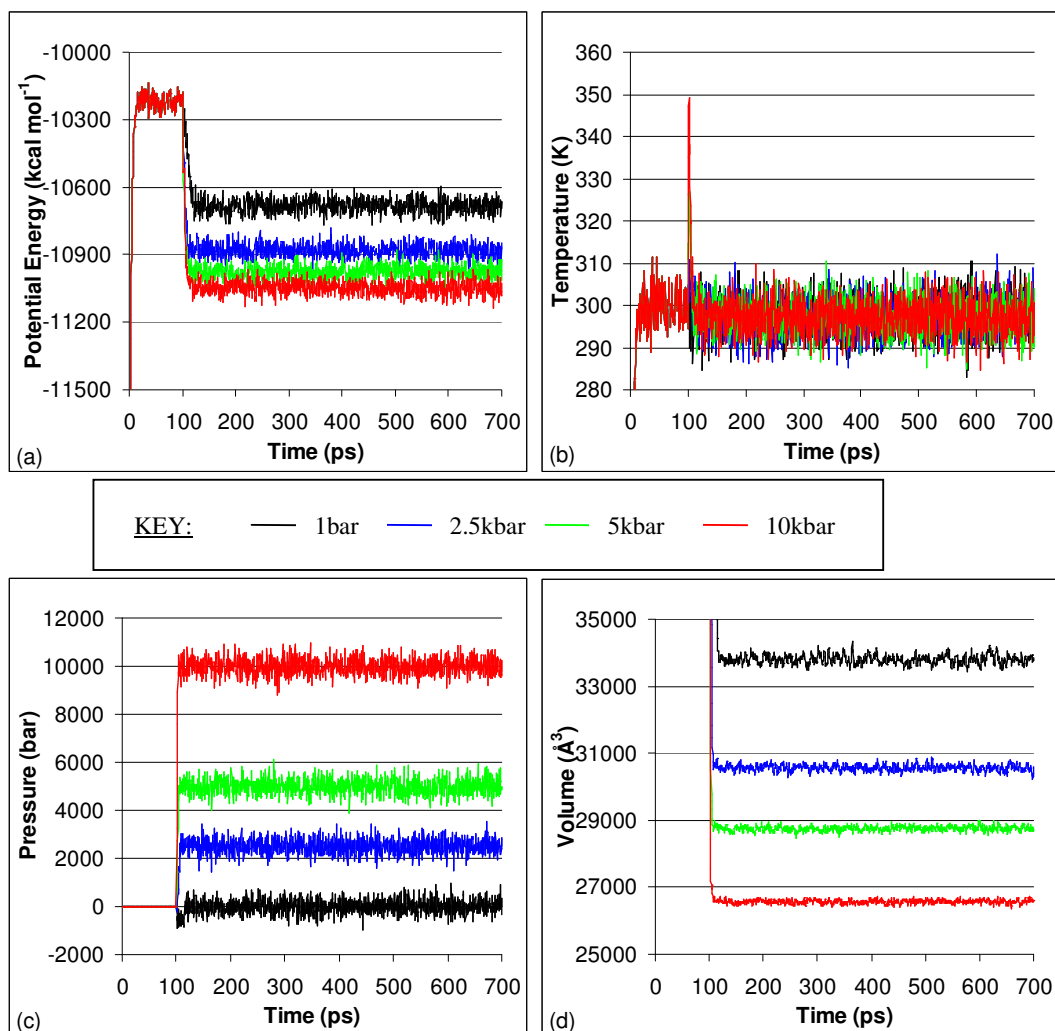


Figure 3.2: The potential energy (a), temperature (b), pressure (c) and volume (d) of the waterbox system during the 700 ns simulation time. The simulation at 1 bar is shown in black, 2.5 kbar in blue, 5 kbar in green and 10 kbar in red

The pressures are shown in Figure 3.2(c) and fluctuate around the constant pressure set in each simulation. Although there is an initial jump in the temperature for the higher pressure simulations, the temperature quickly reaches the desired value and fluctuates around this for the remainder of the simulations. The volume and potential energy decrease with an increase in pressure. The average figures for each of the properties were calculated from the final 500 ps of each trajectory. These are shown for each pressure in Table 3.2.

| Simulation | E_K (kcal mol ⁻¹) | E_P (kcal mol ⁻¹) | E_T (kcal mol ⁻¹) | T (K) | V (Å ³) | P (bar) | D (g ml ⁻¹) |
|------------|------------------------------------|------------------------------------|------------------------------------|----------|------------------------|------------|----------------------------|
| 1 bar | 1974.12 | -10682.1 | -8708.00 | 297.39 | 33800.9 | 0.489 | 0.986 |
| 500 bar | 1973.83 | -10740.5 | -8766.65 | 297.34 | 32918.5 | 483.59 | 1.012 |
| 1 kbar | 1974.36 | -10783.6 | -8809.25 | 297.42 | 32201.0 | 1007.6 | 1.035 |
| 1.5 kbar | 1973.43 | -10824.6 | -8851.21 | 297.28 | 31561.8 | 1496.7 | 1.056 |
| 2 kbar | 1974.19 | -10856.6 | -8882.43 | 297.40 | 31045.4 | 1993.0 | 1.074 |
| 2.5 kbar | 1973.05 | -10881.4 | -8908.30 | 297.22 | 30562.7 | 2499.7 | 1.090 |
| 5 kbar | 1974.73 | -10974.9 | -9000.21 | 297.48 | 28751.3 | 4996.6 | 1.159 |
| 7.5 kbar | 1972.87 | -11023.8 | -9050.98 | 297.20 | 27504.9 | 7497.4 | 1.212 |
| 10 kbar | 1973.22 | -11047.7 | -9074.47 | 297.25 | 26568.6 | 9993.3 | 1.254 |

Table 3.2: The average values for various properties across the pressure range. E_K is kinetic energy, E_P is potential energy, E_T is total energy, T is Temperature, V is Volume, P is Pressure and D is Density. Units of each property are shown in brackets

The instantaneous pressure fluctuations make the trajectories appear unstable. However, comparison to other constant pressure simulations that use the NPT ensemble and Berendsen barostat in AMBER 8 suggests that this fluctuation should be expected (Berendsen et al., 1984). The averages in Table 3.2 indicate an increasing trend for the observed pressure as the target pressure in the simulation is increased. An accompanying volume decrease that would be expected with increased pressure is also apparent. The trajectories are typically stable, thus it is felt that using the default settings for the coupling constant and compressibility factor are appropriate for these simulations.

3.1.3 Comparison with Experiment

The experimental density of water was obtained for the pressures used in the simulations, using the NIST Chemistry WebBook: <http://webbook.nist.gov/chemistry/fluid/> (E.W. Lemmon). These were compared to the average density taken from the simulations and are shown in Table 3.3 and Figure 3.3.

| | | | | | |
|----------------------|------------------|------------------|------------------|------------------|------------------|
| Pressure (bar) | 1 | 500 | 1000 | 1500 | 2000 |
| Dens _{Exp} | 0.997 | 1.018 | 1.038 | 1.056 | 1.072 |
| Dens _{Calc} | 0.986 (0.004) | 1.012 (0.003) | 1.035 (0.004) | 1.056 (0.004) | 1.074 (0.003) |
| Pressure (bar) | 2500 | 5000 | 7500 | 9500 | 10000 |
| Dens _{Exp} | 1.087 | 1.149 | 1.198 | 1.231 | - |
| Dens _{Calc} | 1.090 (0.004) | 1.159 (0.003) | 1.212 (0.003) | - | 1.254 (0.003) |

Table 3.3: Comparison between experimental density ($Dens_{Exp}$) for water and average densities from waterbox simulations ($Dens_{Calc}$), with the standard deviations in brackets. Pressure is given in bar, density values are in $g\ ml^{-1}$. Note: the highest pressure that experiment values were available for was 9500 bar.

The data clearly shows a good agreement with experiment for the density calculated using the TIP3P force field, implemented in AMBER. The average percentage agreement between the densities is 99.4%, with the minimum percentage agreement 98.2%. Figure 3.3 illustrates this.

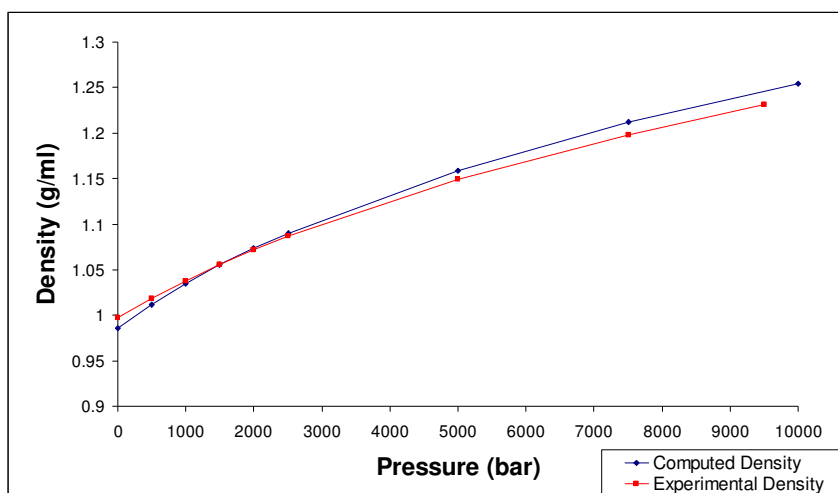


Figure 3.3: Graph showing the agreement of experimental density (red) of water across the pressure range to density calculated in waterbox simulations (blue).

The Radial Distribution ($g(R)$) can be used to illustrate the structural properties of the water. The oxygen to oxygen (O-O) $g(R)$ was calculated in VMD (Humphrey et al., 1996) for the 1 bar simulation. Figure 3.4 shows the comparison between this and the experimental $g(R)$ calculated by Soper and Phillips (Soper and Phillips, 1986) at atmospheric pressure and 298 K.

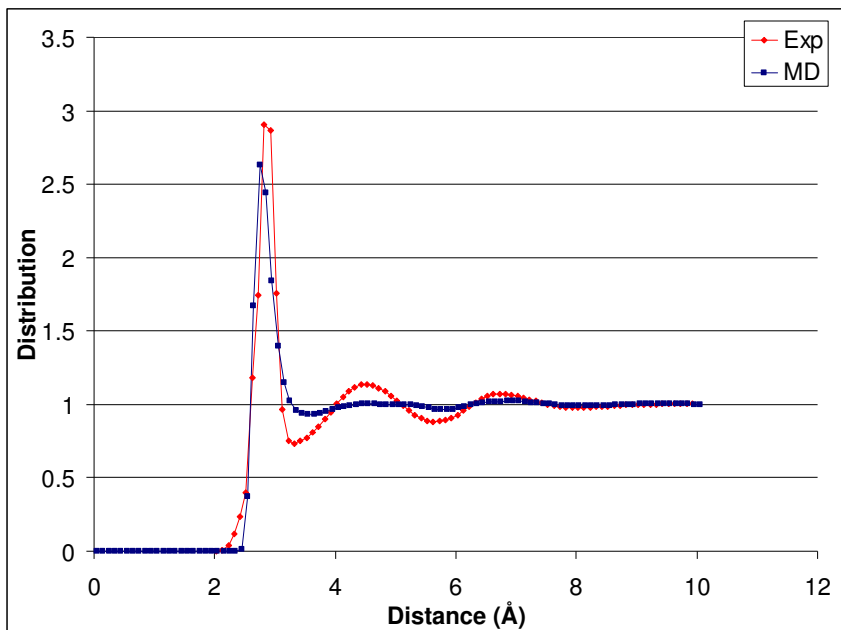


Figure 3.4: The oxygen-oxygen radial distribution function calculated in VMD for the water box (blue) and compared to the experimental values (red), as calculated by Soper and Phillips (Soper and Phillips, 1986).

The $g(R)$ calculated in VMD has shown a lower intensity than the experimental $g(R)$. This is consistent with previous computational calculations on $g(R)$, using the TIP3P water model (Mason and Brady, 2007), and should not be misconstrued as an inaccuracy of these simulations. The objective of this analysis is not to scrutinise the TIP3P water model at atmospheric pressure, but to assess its response to pressure. The pressure effect on the O-O $g(R)$ has been studied experimentally by Gorbaty & Demianets (Gorbaty and Demianets, 1985) at 20°C, across the pressure range from 1 bar to 2 kbar. Increasing the pressure to 2

kbar has no noticeable effect on the first peak, but with a reduction in the other peaks., as the structure of water becomes disordered at greater distances. VMD was again used to calculate the O-O $g(R)$ for the waterbox simulations at 1 kbar and 2 kbar. This is combined with the values from 1 bar to give Figure 3.5, allowing comparison between the experimental and simulated pressure effects.

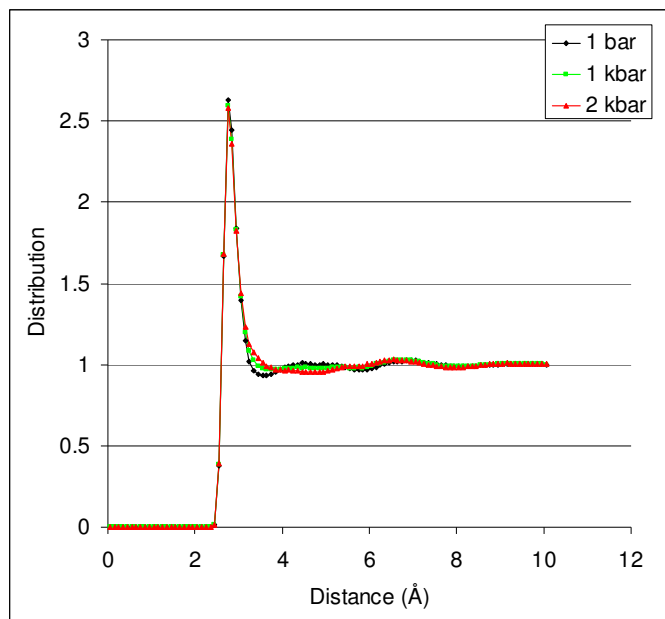


Figure 3.5: The oxygen-oxygen radial distribution function, as calculated in VMD for the waterbox simulations at 1 bar (black), 1 kbar (green) and 2 kbar (red)

The same effect observed in the experiments can be seen with the results of the O-O $g(R)$ calculated by VMD. The first peak is unaffected by the pressure increase, but the other peaks are reduced. This would suggest that the structure of the water is responding to the increase in pressure, as would be expected from experimental studies.

3.1.4 Summary of the Benchmark Simulation of a Waterbox

The results from the study of the waterbox at high pressure are used to validate the choice of force field to proceed onto protein simulations with. The system remains stable with the temperature being constant throughout the simulations. The instantaneous pressure fluctuates somewhat more than one might expect for a 'constant pressure' simulation, but the average pressure is at the desired value and the volume of the waterbox remains constant.

The density of the waterbox across the range of pressures agrees very closely with experimentally calculated values. The radial distribution is not replicated perfectly in the intensity of the peaks, but the positions of the peaks are reproduced. Experimental studies of the $g(R)$ at different pressures show that the pressure increase causes a decrease in tetrahedral ordering. This is also observed in the calculations from the simulations.

The simulation of the waterbox at atmospheric pressure and, more importantly, the pressure effect on the waterbox agrees closely enough with the experimental values. It is assumed that the program (AMBER8) and force field (ff03), along with the TIP3P water model, are robust enough to use for a high pressure molecular dynamics simulation.

3.2 SIMULATIONS OF HELICAL PEPTIDE AT CONSTANT PRESSURE

MD simulations were performed on a solvated peptide. The peptide chosen (the AK peptide) has been used in a previous computational study by Paschek *et al.* (Paschek et al.,

2005), to investigate its properties at varying pressures and temperatures. This study is discussed in Section 1.3.2 of this thesis. Comparing the findings of the previous study with the simulations performed here validates the method used to study a peptide at high pressure.

The peptide is an α -helical peptide of 22 amino acids, with the sequence: Ac-AKAA(AAKAA)₃AAY-Nme. Figure 3.6 shows the minimised structure of the peptide.

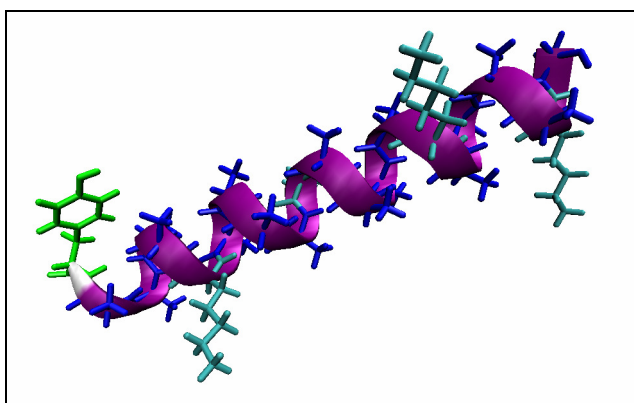


Figure 3.6: *The structure of the AK Peptide. The helix is illustrated in purple, with the residues coloured blue (alanine), cyan (lysine) and green (tyrosine)*

3.2.1 Stability of Peptide

The root mean square deviations (RMSDs) of the peptide backbone were calculated for the 5 ns production stage of the simulations at each pressure (Figure 3.7). This demonstrates how stable the peptide is across the pressure range.

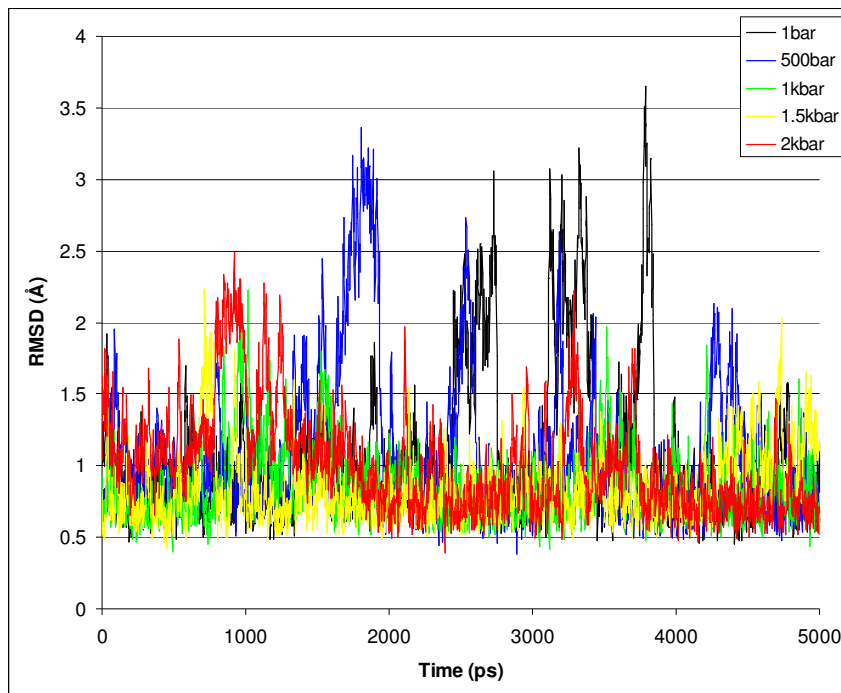


Figure 3.7: The RMSDs of the peptide backbone for the 5 ns simulation, post-equilibration. RMSDs for all five pressures are shown: 1 bar (black), 500 bar (blue) 1 kbar (green), 1.5 kbar (yellow) and 2 kbar (red)

Although the peptide structure appears to be unstable, particularly at 1 bar and 500 bar, it is generally stable majority of the simulations, at around 1 Å. The sudden increase in the RMSDs in each case arised from a bending of the helix, as illustrated by Figure 3.8.

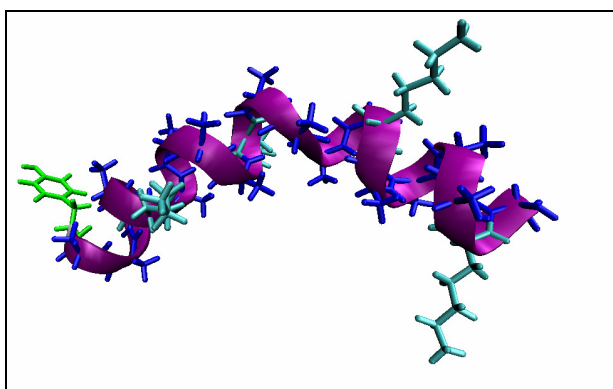


Figure 3.8: Bending of the helix characterized by peaks on the RMSD plot in Figure 3.7. The helix is illustrated in purple, with the residues coloured blue (alanine), cyan (lysine) and green (tyrosine)

Each time the helix bends, it soon returns to a more characteristic straight helix. It is noted from Figure 3.7 that increasing the pressure seems to have a stabilising effect on the

protein dynamics, as the sudden increases in RMSD have been reduced at higher pressure. To assess the peptide dynamics on a residue-per-residue basis across the pressure range, the root-mean-squared-fluctuations (RMSFs) were calculated for the backbone of the peptide and is shown in Figure 3.9:

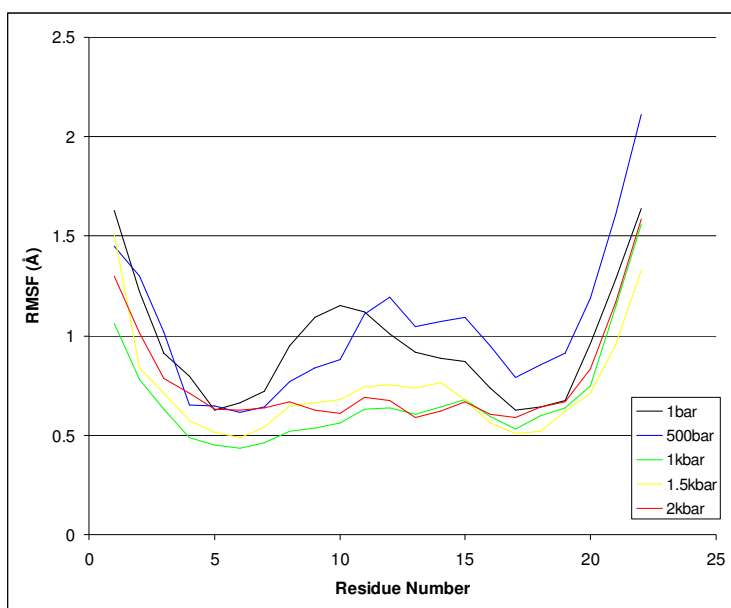


Figure 3.9: The RMSF of the peptide backbone for the 5 ns simulation, post-equilibration. RMSFs for all five pressures are shown: 1 bar (black), 500 bar (blue) 1 kbar (green), 1.5 kbar (yellow) and 2 kbar (red)

The RMSF reiterates that the fluctuations decrease with an increase in pressure - the residues in the middle of the peptide in particular fluctuate more at the lower pressures. This is attributed to the bending of the helix. It is noted here that there is no apparent unwinding of the helix at any of the 5 pressures.

3.2.2 Radius of Gyration

The Radius of Gyration (RadGyr) of the peptide can be used to demonstrate the compressibility of the peptide as the pressure is increased. Figure 3.10 shows the RadGyr of the α -carbons of the AK peptide, during the 5 ns simulation after the equilibration period.

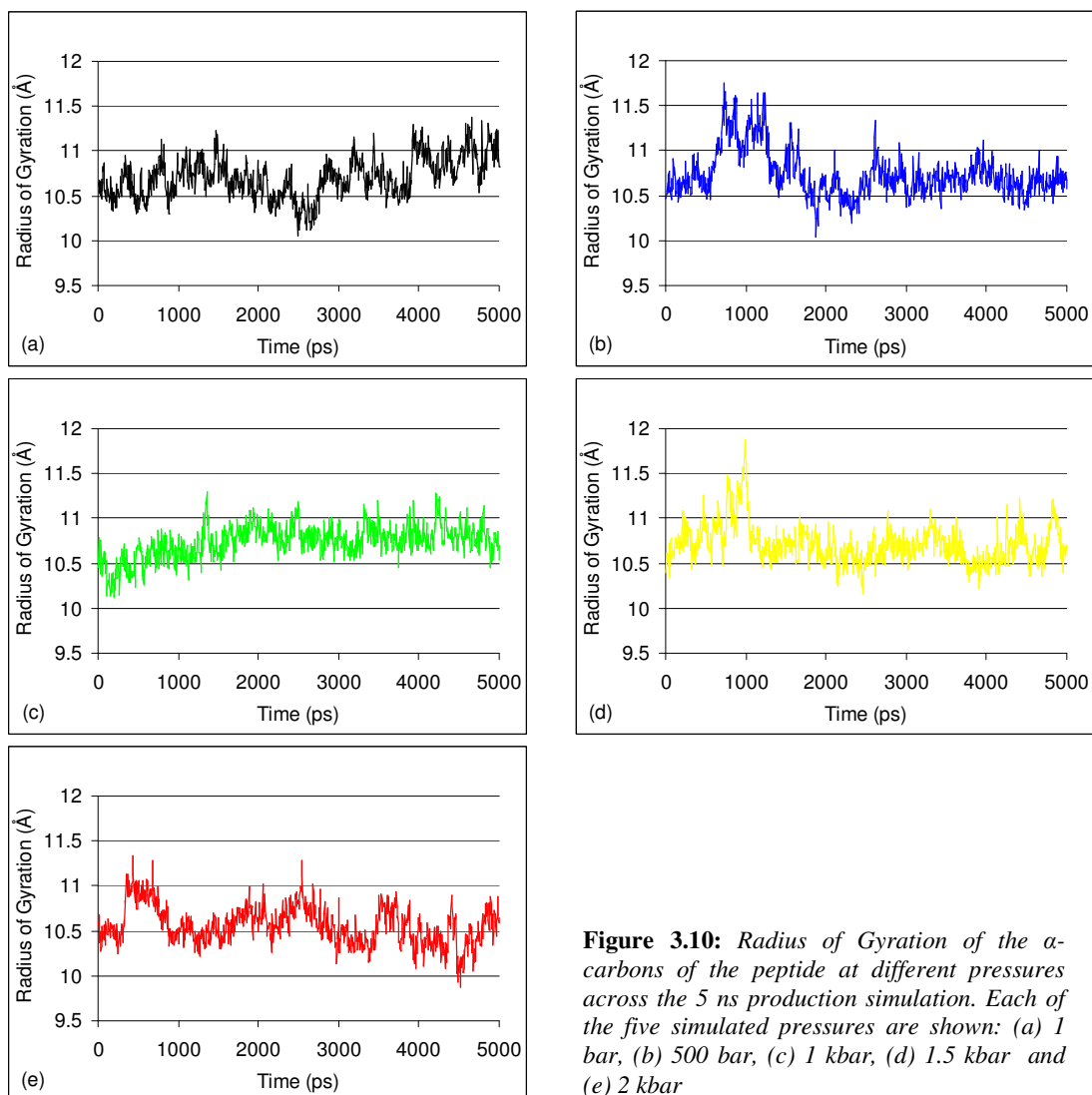


Figure 3.10: Radius of Gyration of the α -carbons of the peptide at different pressures across the 5 ns production simulation. Each of the five simulated pressures are shown: (a) 1 bar, (b) 500 bar, (c) 1 kbar, (d) 1.5 kbar and (e) 2 kbar

It can be observed that the RadGyr fluctuates over the 5 ns in each simulation, but not considerably. The average values are shown in Table 3.4:

| Pressure (bar) | 1 | 500 | 1000 | 1500 | 2000 |
|----------------|-----------------|-----------------|-----------------|-----------------|-----------------|
| RadGyr (Å) | 10.71 (0.23) | 10.73 (0.26) | 10.74 (0.19) | 10.71 (0.22) | 10.56 (0.21) |

Table 3.4: Average values for the Radius of Gyration of the α -carbons. Averages were taken from 5 ns production trajectory. Standard deviations are shown in brackets

There does not appear to be a decreasing trend associated with the pressure increase, as one might expect. However, this is consistent with the observations by Paschek *et al.* – that it

takes pressures significantly higher than 200 MPa (2 kbar) to see a decrease in the RadGyr of this peptide. It is not necessary to run simulations above 2 kbar, since this is the upper limit of pressure that will be used in the studies on the enzyme. The RadGyr data provides more evidence that the simulations are stable across the pressure range.

3.2.3 End to End Distance

It is difficult to use the RadGyr as a measure of compressibility, since it does not alter by large amounts in the pressure range studied. An alternative measure of compressibility used by Paschek *et al.* is the helix end to end distance. This has been calculated as the distance between the α -carbons of the terminal amino acids: Ala2 and Tyr23. The distance plotted against time is shown in Figure 3.11, with the average values shown in Table 3.5.

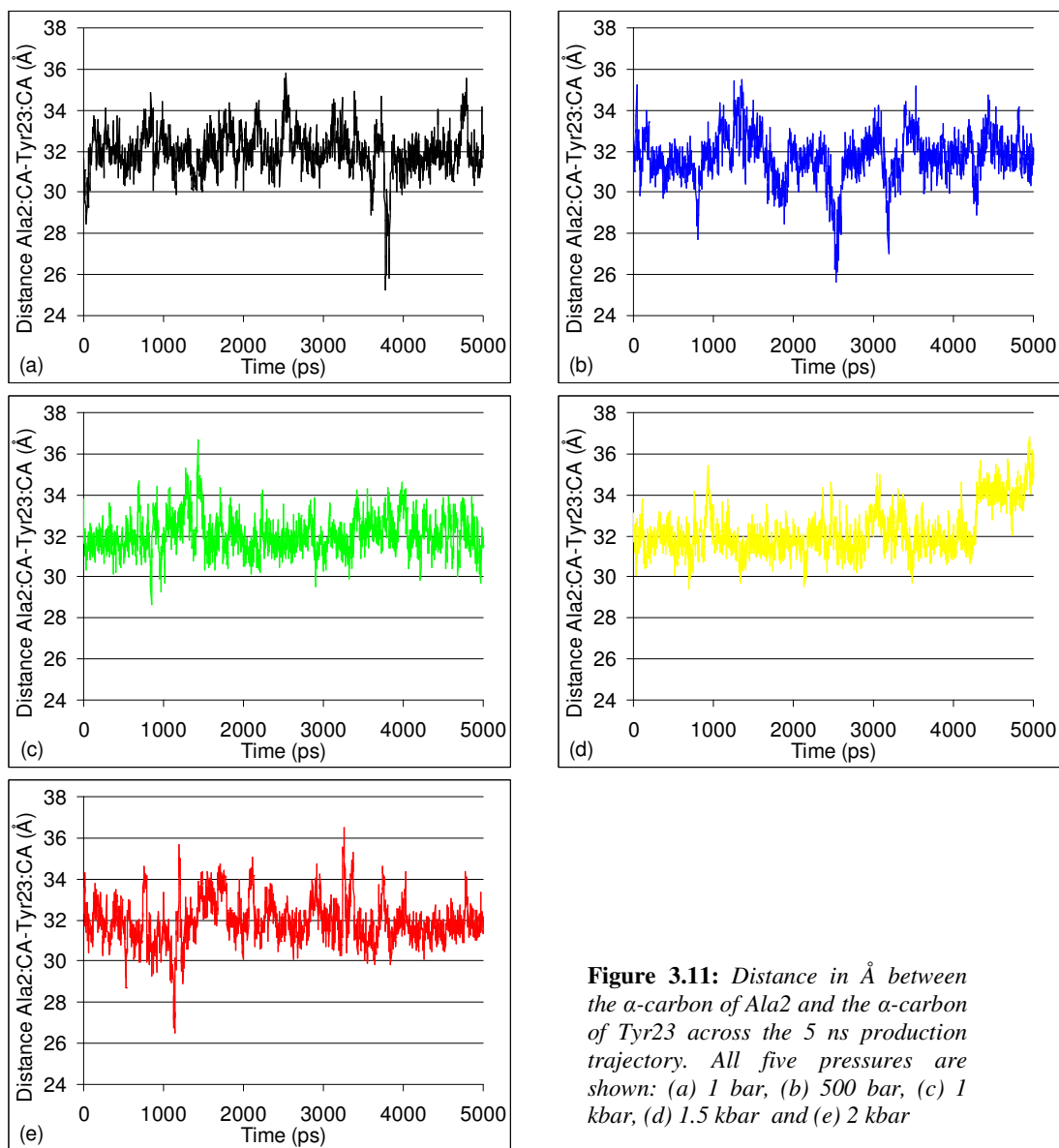


Figure 3.11: Distance in Å between the α -carbon of Ala2 and the α -carbon of Tyr23 across the 5 ns production trajectory. All five pressures are shown: (a) 1 bar, (b) 500 bar, (c) 1 kbar, (d) 1.5 kbar and (e) 2 kbar

| Pressure (bar) | 1 | 500 | 1000 | 1500 | 2000 |
|----------------------|--------|--------|--------|--------|--------|
| Average distance (Å) | 31.98 | 31.69 | 32.04 | 32.21 | 31.91 |
| | (1.06) | (1.19) | (0.89) | (1.14) | (1.07) |

Table 3.5: Average distance in Å between the alpha-carbon of Ala2 and the alpha-carbon of Tyr23 across the 5 ns production trajectory. Standard deviations are shown in brackets

Paschek *et al.* calculate the compressibility as the fractional linear extension with pressure, giving a value of 6×10^{-4} per MPa at 300 K. By using the averages from these simulations and converting the units to MPa, a value of 2×10^{-5} per MPa is calculated as the

compressibility factor. Therefore, this MD does not replicate the compressibility factor to the same extent as previously observed. A possible explanation for this discrepancy could be the bending of the helix at the lower pressures, which would shorten the end-end distance without the peptide being compressed. It is also noted that the previous study calculates the compressibility factor over a larger range of pressures. It is possible that the pressures much higher than 2 kbar result in a high compressibility factor.

3.2.4 Water coordination

Water coordination to the peptide backbone is a property that is commonly associated with pressure studies on the denaturation of proteins (Hummer et al., 1998). Figure 3.12 shows the number of water molecules, on average, that are coordinated to the backbone carbonyls of the AK peptide at different pressures.

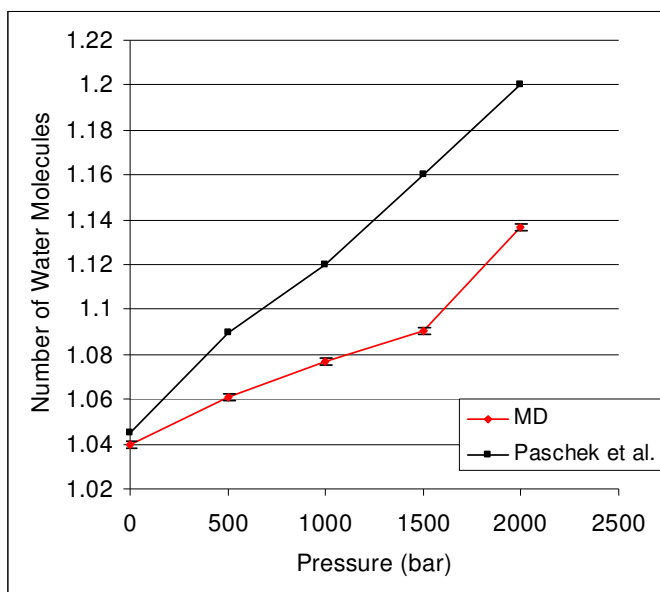


Figure 3.12: Average number of water molecules coordinated to each carbonyl of the peptide backbone at different pressures (red). Averages calculated for 5 ns production trajectory, with the standard deviation shown as error bars. The data from Paschek et al. (black) is shown for comparison

A maximum number would be two water molecules. At atmospheric pressure, there is an average of one water molecule per backbone carbonyl in the peptide, but as the pressure is

increased, this number increases. Although there is not a quantitative agreement with the findings by Paschek *et al.*, it shows the same trend.

3.2.5 AK Peptide Summary

The results of the high pressure MD simulations on an α -helical peptide are encouraging. The simulations are stable across the pressure range. The main difference in protein dynamics is that the residues in the middle of the peptide do not fluctuate as much at higher pressures. It appears that increasing the pressure stabilises the protein dynamics. At certain points during the simulations, particularly at lower pressures, the helix bends. This bend is only momentary however and there is no permanent unwinding of the peptide

The radius of gyration does not decrease considerably with an increase in pressure. Although prior intuitive thinking would lead one to expect a decrease, the lack of a trend is in agreement with previous studies in the same pressure range (Paschek *et al.*, 2005). It is expected to decrease at much higher pressures, but pressures greater than 2 kbar are not relevant to this work.

A decrease in the end to end distance is shown as the pressure is increased. This agrees qualitatively with the findings by Paschek *et al.*, although the compressibility factor is calculated to be more than an order of magnitude lower. This is likely because the pressure range sampled is much smaller than that studied by Paschek *et al.*, but could also be attributed to the bend in the helix. The water coordination to the peptide backbone, agrees very closely with the work done by Paschek *et al.* in the pressure range studied. A general

conclusion on AK peptide at high pressure can be drawn as follows: this work replicates and agrees with a prior study on the AK peptide, which showed agreement with experiment. It can therefore be assumed that the procedure, previously validated for the waterbox (see section 3.1), has now been successfully benchmarked for an MD study of a solvated peptide.

3.3 SIMULATIONS OF MR AT CONSTANT PRESSURE

MD simulations were performed on Morphinone Reductase (MR) using the procedure validated for the waterbox and for a solvated peptide. The simulations were analysed to assess the stability of the simulation, the protein dynamics, and the global properties of the protein and solvent at increased pressure. The data from the minimisation and equilibration can be found in the appendix.

3.3.1 Protein Stability

The RMSDs of the protein backbone were calculated for the 10 ns simulations at each pressure to analyse the stability of the protein as the simulation progressed. These are shown in Figure 3.13, with the average values in Table 3.6.

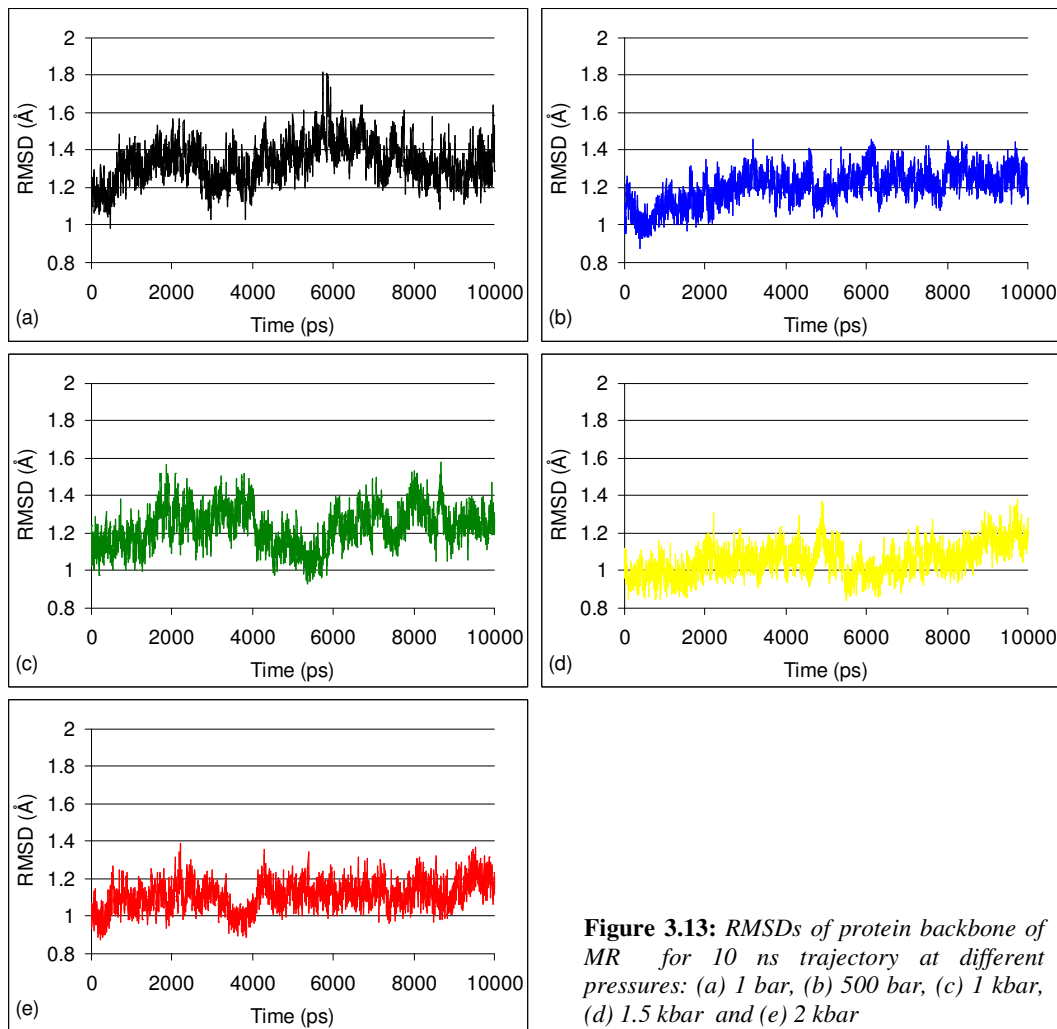


Figure 3.13: *RMSDs of protein backbone of MR for 10 ns trajectory at different pressures: (a) 1 bar, (b) 500 bar, (c) 1 kbar, (d) 1.5 kbar and (e) 2 kbar*

| Pressure (bar) | 1 | 500 | 1000 | 1500 | 2000 |
|------------------|------------------|------------------|------------------|------------------|------------------|
| Average RMSD (Å) | 1.334 (0.105) | 1.204 (0.093) | 1.232 (0.104) | 1.056 (0.087) | 1.112 (0.077) |

Table 3.6: *Averages values of the RMSDs of the protein backbone of MR for the 10 ns trajectories at different pressures. Standard deviations are shown in brackets*

The RMSDs are very stable during the 10 ns trajectory at each pressure. This is an indication of a well equilibrated system. The simulations are much more stable than those that were carried out on the AK peptide in Section 3.2 – likely because the tertiary structure of the protein is more complex and has more stabilising interactions. One

comparable feature of these RMSDs to the AK peptide is the increasing stability with pressure.

The RMSFs were also calculated for the 10 ns trajectories at each pressure and are shown in Figure 3.14.

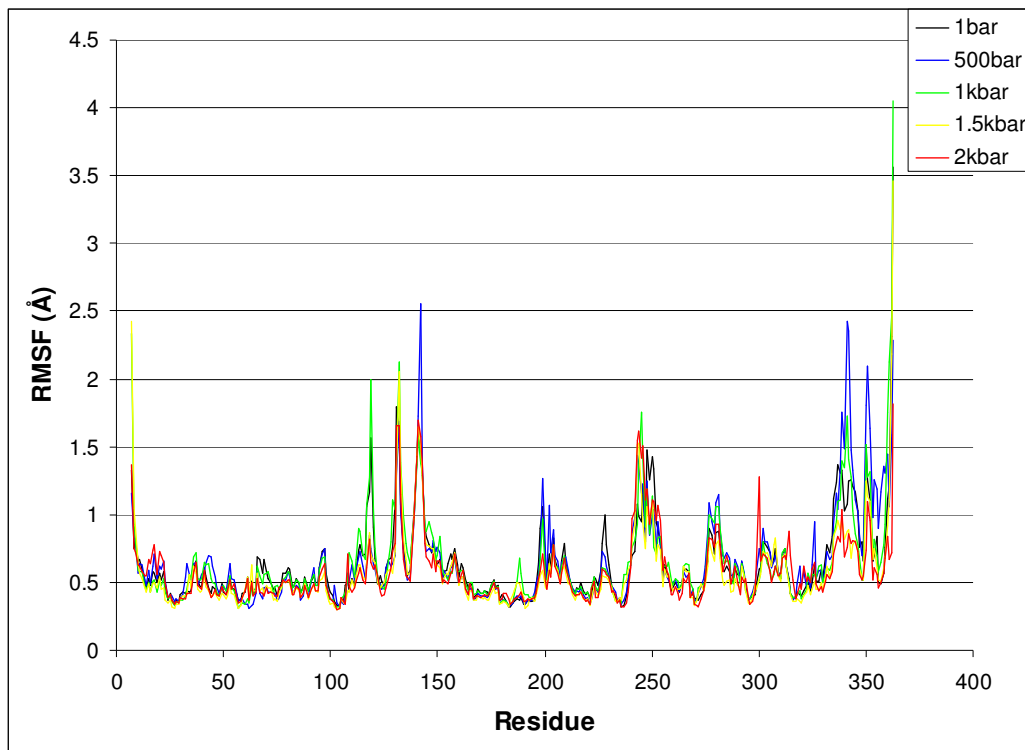


Figure 3.14: RMSFs of protein α -carbons of MR for 10 ns trajectory at different pressures: 1 bar (black), 500 bar (blue), 1 kbar (green), 1.5 kbar (yellow) and 2 kbar (red)

The RMSF results show a similar pattern of fluctuations for each pressure. The average and standard deviations of these results are shown in Table 3.7.

| Pressure (bar) | 1 | 500 | 1000 | 1500 | 2000 |
|------------------|------------------|------------------|------------------|------------------|------------------|
| Average RMSD (Å) | 0.634 (0.321) | 0.650 (0.347) | 0.647 (0.370) | 0.573 (0.308) | 0.576 (0.251) |

Table 3.7: Averages values of the RMSFs of the α -carbons of MR for the 10 ns trajectories at different pressures. Standard deviations are shown in brackets

There are two regions on the plot of RMSFs that show a visible difference between high and low pressures. These are residues 113-122 and 335-353. Both of these regions are at on the surface of the protein although residues 113-122 are located very close to the active site of MR. This will be discussed in the next chapter that focuses on the active site residues. The RMSDs and RMSFs combined show a similar trend with an increase in pressure – the deviations are lower, suggesting that the flexibility of protein is reduced at higher pressures.

An additional validation of an MD simulation is to compare the RMSFs with the crystallographic B-factors. Although there are no B-factors available for MR at high pressure (since there are no high pressure crystal structures), Figure 3.15 shows how the RMSFs calculated at atmospheric pressure align with the B-factors taken from the 2R14.pdb crystal structure.

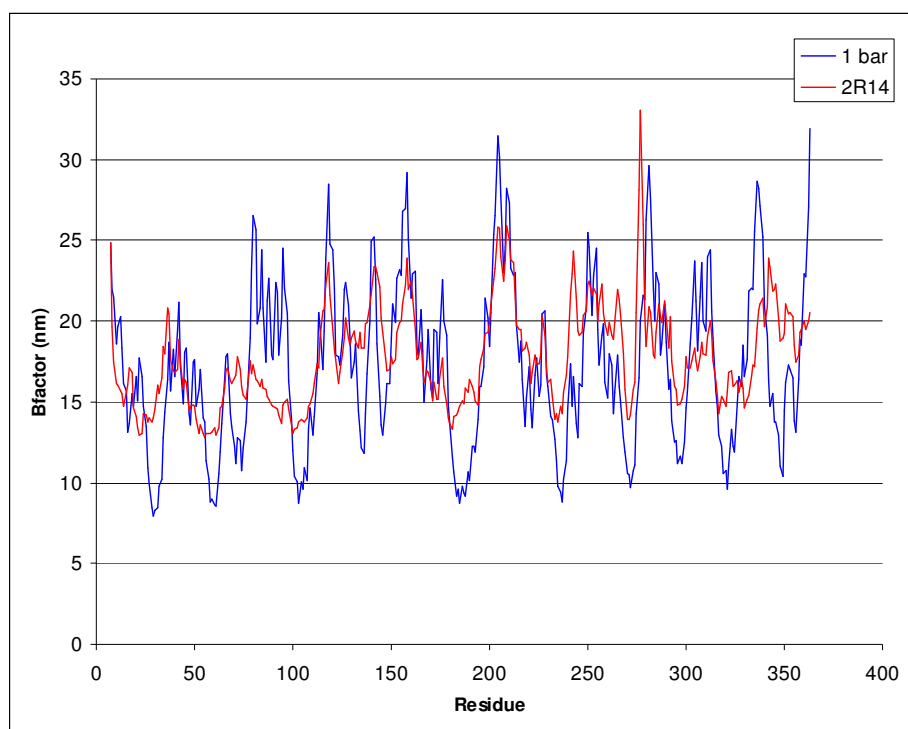


Figure 3.15: Comparison of crystallographic B-factors (red) with atomic fluctuations taken from simulation at atmospheric pressure (blue)

When the RMSFs are converted into the same units as the crystallographic B-factors, they show a good agreement. There is one region that seems to fluctuate considerably more in the simulations than the B-factors suggest that it should – residues 78 to 98. This region of the protein represents an alpha-helix and is on the surface. It is not unusual for the RMSF values at the solvent exposed edge of the protein to be slightly higher than the temperature factors from the crystallographic data.

3.3.2 Secondary Structure

VMD was used to calculate the secondary structure of the protein. A frame was read into the program for every 4 ps of the 10 ns trajectory (totalling 2500 frames), for each pressure. The output from VMD for the 1 bar simulation is shown below.

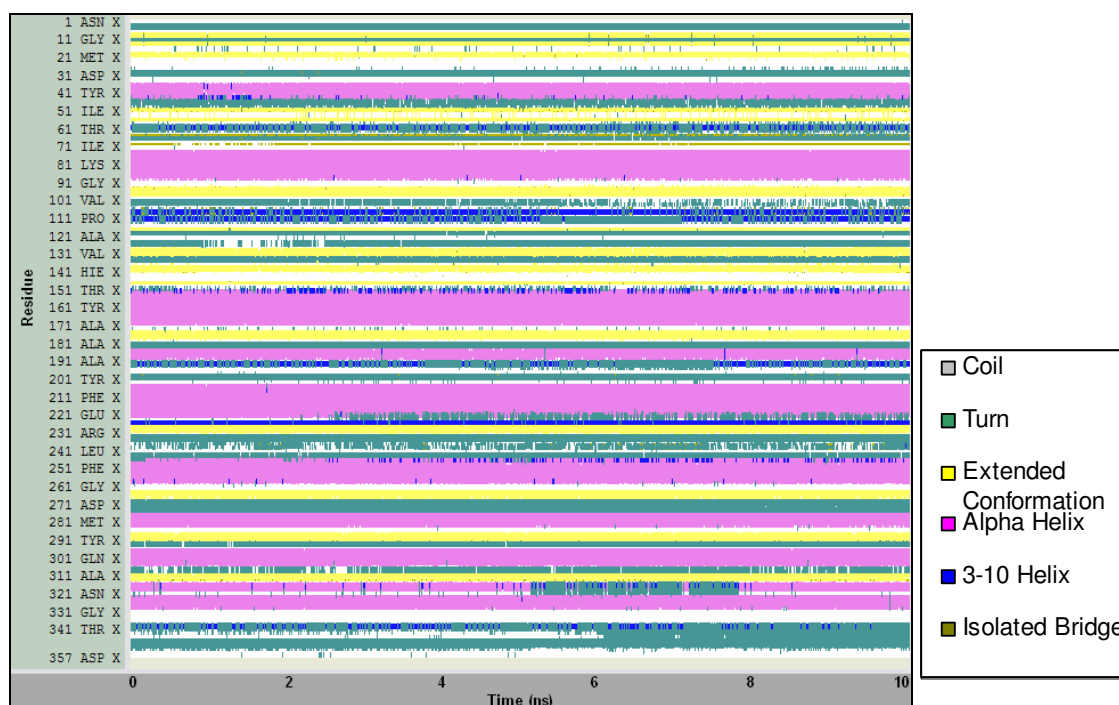


Figure 3.16: Secondary structure of MR at 1 bar, over a 10 ns trajectory. Calculated using VMD

The figure above shows how the structure of the protein changes with time. There are no drastic changes in structure over the trajectory. The secondary structure map was converted into a pie chart to show the average structural composition of the protein over the course of the simulation. This is shown in Figure 3.17. The secondary structure was also calculated for the crystal structure. Incidentally, the structural composition for the single frame of the crystal structure is identical to the percentages shown for the 1 bar trajectory in Figure 3.17.

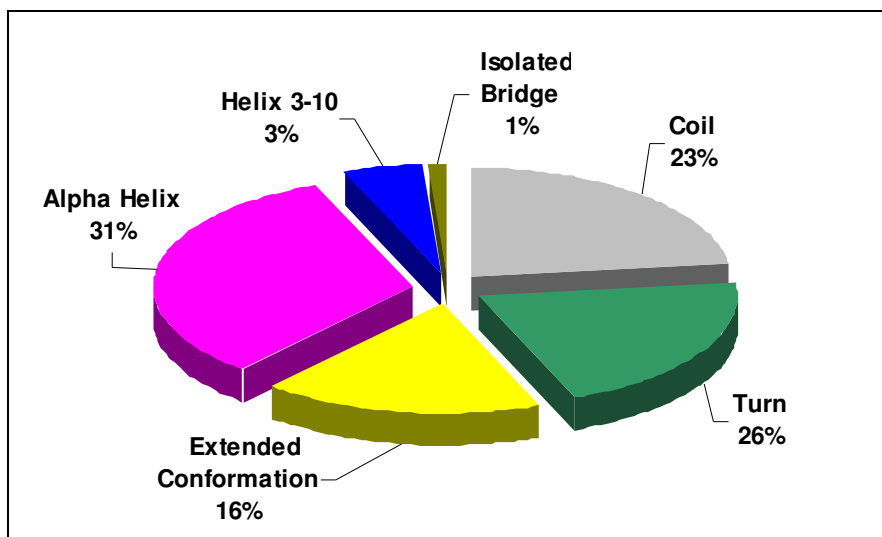


Figure 3.17: Pie chart showing the percentage of each structural motif sampled by MR over the 10 ns trajectory at atmospheric pressure. Calculated using VMD

These secondary structure plots were calculated for all five pressures. The pie chart for 1 bar shown in Figure 3.17 was generated by writing the data from Figure 3.16 to a file, allowing a more quantitative analysis of the secondary structure. This was repeated for the other pressures and Figure 3.18 shows the comparison across the pressure range.

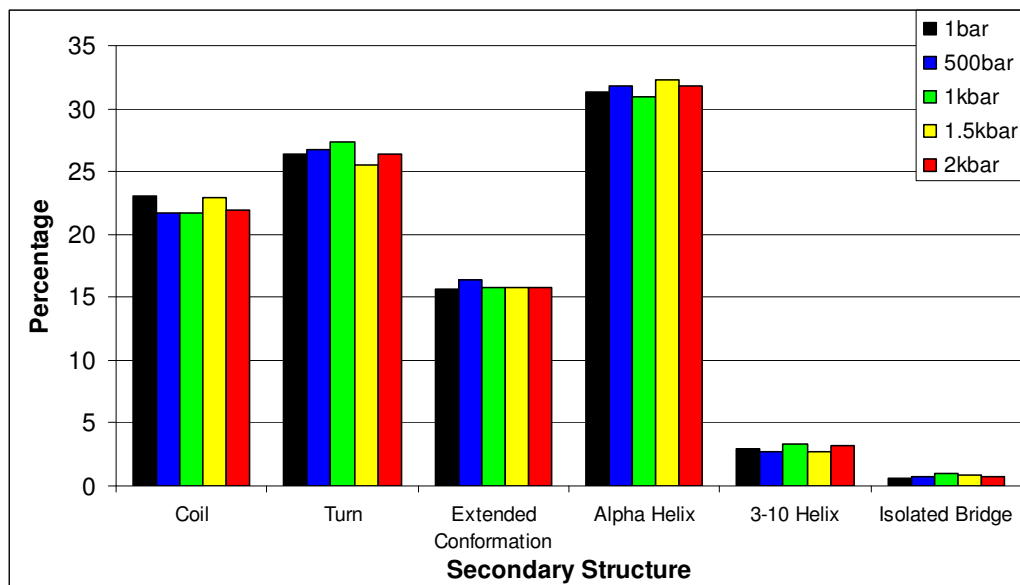


Figure 3.18: Secondary structure of MR calculated as average over 10 ns trajectory at different pressures: 1 bar (black), 500 bar (blue), 1 kbar (green), 1.5 kbar (yellow) and 2 kbar (red)

The average values represented in Figure 3.18 are collected in Appendix A. The secondary structure analysis does not show any particular difference across the pressure range. This is unsurprising, since it is not expected for the protein to be denatured in this pressure range. This analysis does reconfirm that the simulations are stable. It is suggested at this point that the effect of pressure may be more of a dynamic effect, although this is a macroscopic analysis and does not consider the effect on the atomistic structure of the protein.

3.3.3 Volume of Protein

To analyse how the pressure affects the global volume of the protein, the Radius of Gyration (RadGyr) was calculated in VMD over the pressure range. The 10 ns trajectories were read in, with a stride of 20 ps.

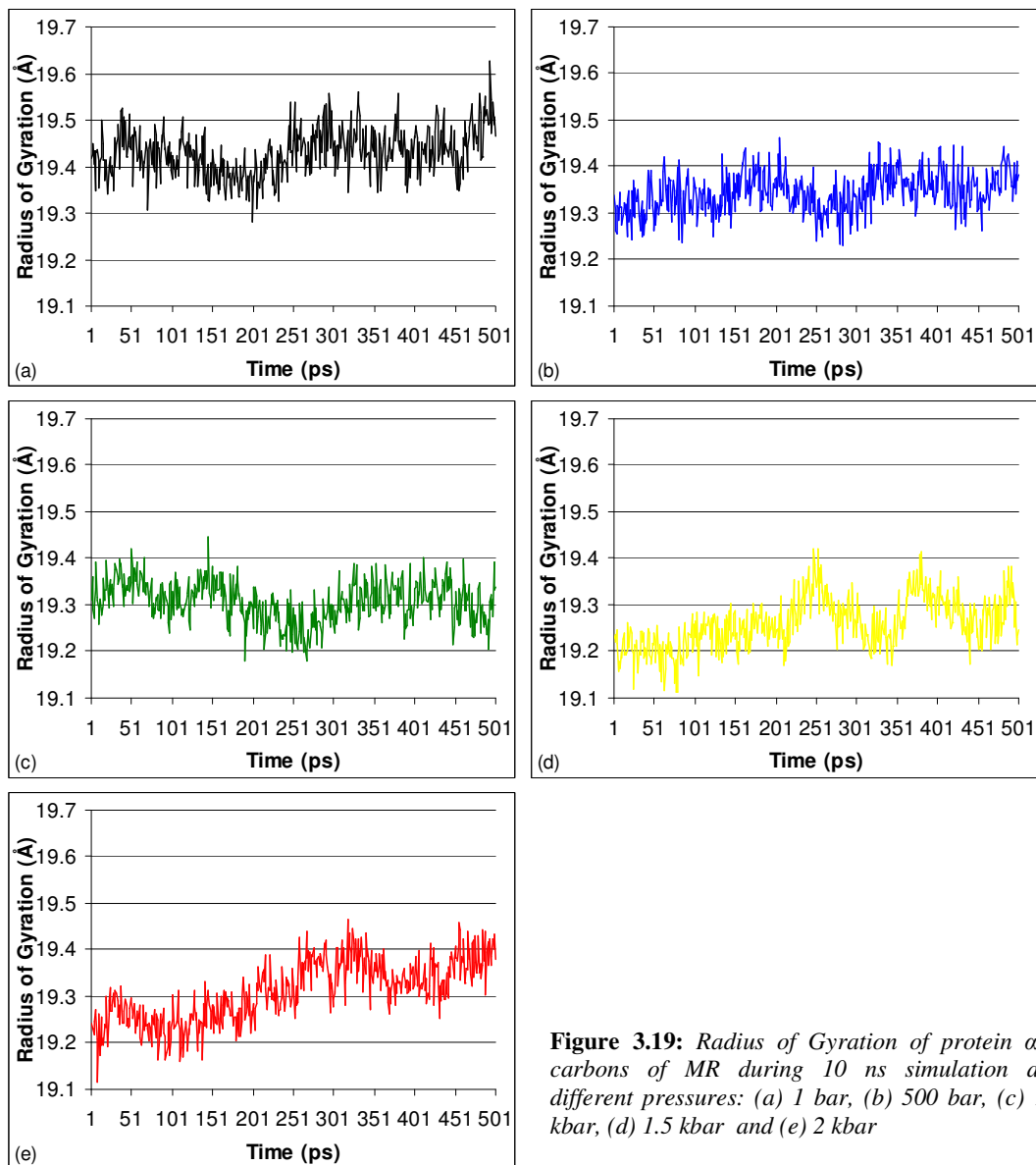


Figure 3.19: Radius of Gyration of protein α -carbons of MR during 10 ns simulation at different pressures: (a) 1 bar, (b) 500 bar, (c) 1 kbar, (d) 1.5 kbar and (e) 2 kbar

Table 3.8 shows the averages and standard deviations at each pressure.

| Pressure | Average RadGyr (Å) | Standard Deviation of RadGyr (Å) |
|----------|--------------------|----------------------------------|
| 1 bar | 19.43 | 0.05 |
| 500 bar | 19.34 | 0.04 |
| 1 kbar | 19.31 | 0.05 |
| 1.5 kbar | 19.26 | 0.05 |
| 2 kbar | 19.31 | 0.06 |

Table 3.8: Average and standard deviations of Radius of Gyration for alpha-carbons of MR over 10 ns simulation at different pressures

VMD was also used to calculate the Solvent Accessible Surface Area (SASA). As with the RadGyr, the trajectory was read into VMD, every 20 ps at each pressure. Figure 3.20 and Table 3.9 show the results of this.

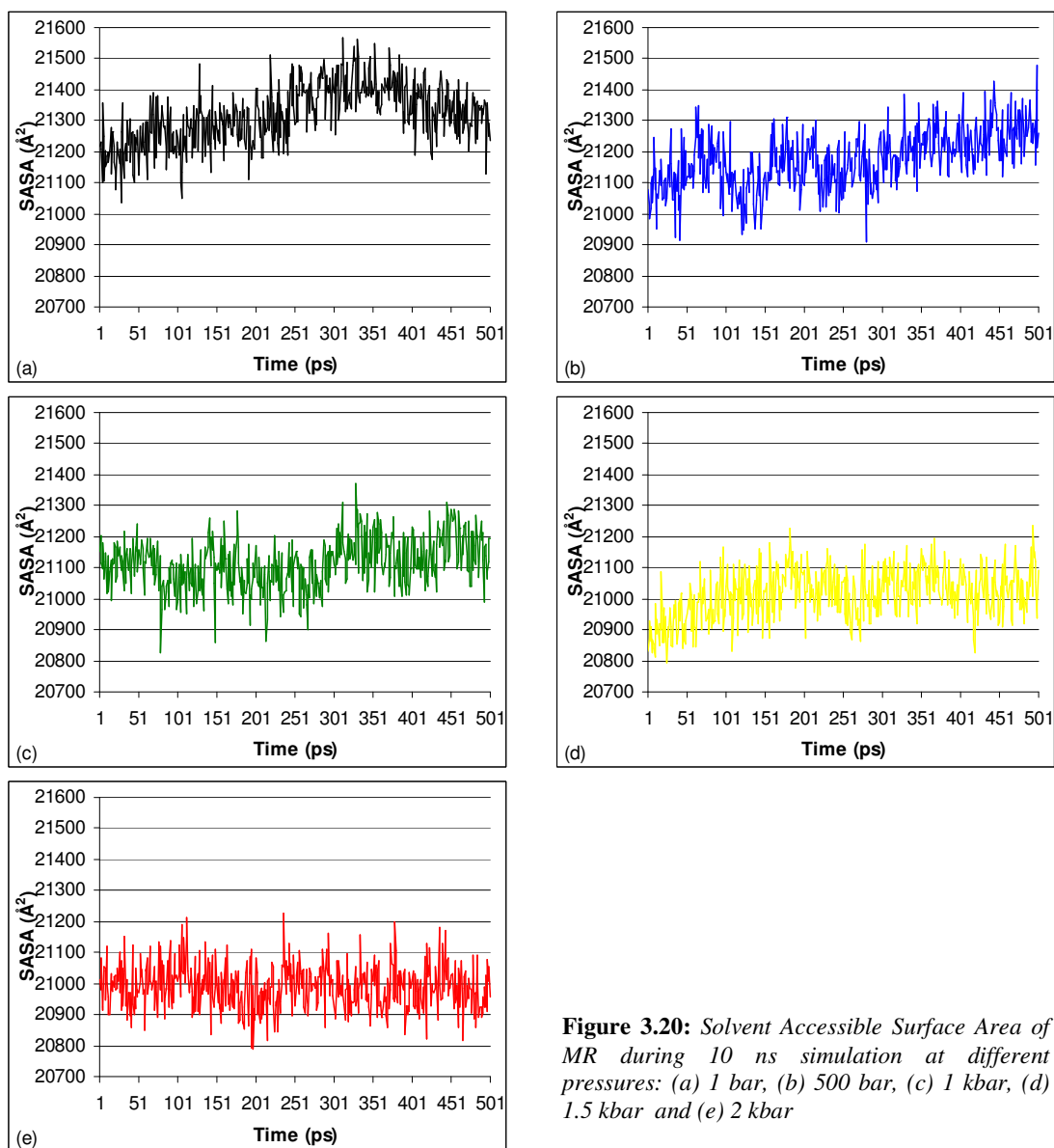


Figure 3.20: Solvent Accessible Surface Area of MR during 10 ns simulation at different pressures: (a) 1 bar, (b) 500 bar, (c) 1 kbar, (d) 1.5 kbar and (e) 2 kbar

| Pressure | Average SASA (\AA^2) | Standard Deviation of SASA (\AA^2) |
|----------|---------------------------------|---|
| 1 bar | 21317.06 | 95.17 |
| 500 bar | 21176.59 | 93.81 |
| 1 kbar | 21113.08 | 81.34 |
| 1.5 kbar | 21014.38 | 80.70 |
| 2 kbar | 20988.66 | 71.99 |

Table 3.9: Average and standard deviations of Solvent Accessible Surface Area of MR over 10 ns simulation at different pressures

As one would expect, the results of both the RadGyr and SASA paint a similar picture. The averages show a decreasing trend as the pressure is increased (Figure 3.21). However, this is not a significant decrease, agreeing with the previous observations for the AKP RadGyr results (see section 3.2.2).

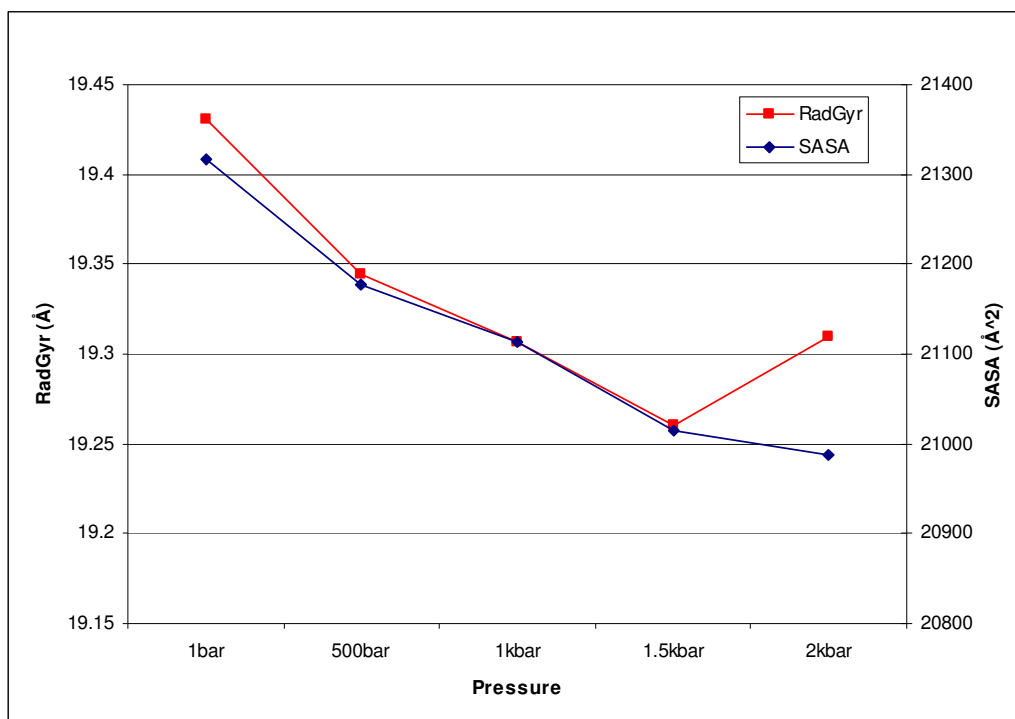


Figure 3.21: Plot showing average Radius of Gyration (red) and Solvent Accessible Surface Area (blue) of Morphinone Reductase over 10 ns simulation at different pressures

An obvious anomaly, shown on Figure 3.21, is the 2 kbar point for the Radius of Gyration. Referring back to Figure 3.19 shows an increase in the RadGyr at around 4 ns for the 2

kbar simulation. Following this, it fluctuates around a higher value for the rest of the simulation. This does not happen with the SASA (Figure 3.20), nor is there any particular change in secondary structure. Since this increase is very small (within the range of the standard deviation) and there appears to be no change in the structure, it is deemed to be insignificant.

3.3.4 Pressure Effect on Water MR Simulations of MR

To analyse the effect of the pressure on the water in the simulations of MR, the number of water atoms within a particular distance of the core of the protein were counted. The core of the protein is defined as the beta-barrel, as assigned by the DSSP (Kabsch and Sander, 1983) on the protein data bank website (Berman et al., 2000) and is detailed in the Appendix A. The number of water molecules within 3 Å of the core was counted across the trajectory and compared across the pressure range. Figures 3.22 and 3.23 show this analysis.

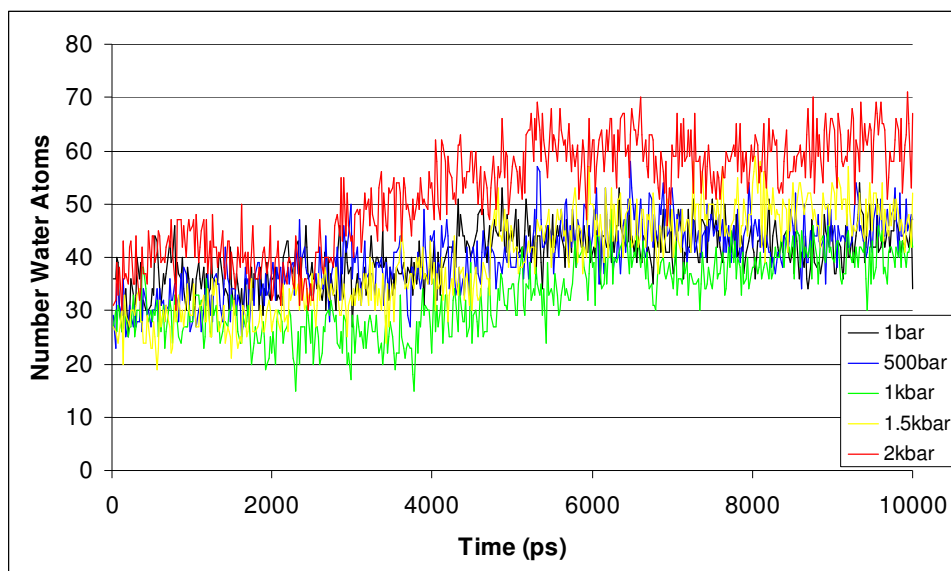


Figure 3.22: Number of water molecules within 3 Å of core of MR at different pressures: 1 bar (black), 500 bar (blue), 1 kbar (green), 1.5 kbar (yellow) and 2 kbar (red)

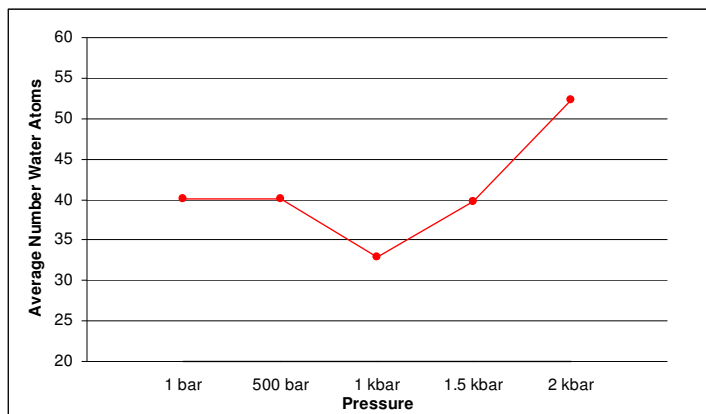


Figure 3.23: Average number of water molecules within 3 Å of core of MR across pressure range

These figures generally show an increase in water in the core of the protein as the pressure is increased. The number of water molecules in the core of the protein at 2 kbar is continuing to increase for the first half of the simulation, but stabilises from approximately 5 ns onwards. At 1 bar, 500 bar and 1.5 kbar, the number of water molecules is relatively more stable throughout the simulation, whereas at 1 kbar, the number of water molecules seems to decrease for a portion of the simulation, before settling with approximately the same number as the other 3 simulations.

3.4 CONCLUSIONS

The aim of this first chapter is to assess the reliability of the procedure used for studying the high pressure effect on a protein, using MD simulation. The MD simulations performed on the waterbox gives the expected results when comparing atmospheric pressure with higher pressures. The volume and potential energy of the system decrease with the increasing pressure and the temperature remains stable during each of the pressure simulations. Since the volume of the system has decreased, this is accompanied with an

increase in water density. Comparing the calculated water density from the simulations with the experimental water density gives good agreement with experimental values. The radial distribution is also comparable with experimental data. The positions of the peaks are replicated at atmospheric pressure and the loss of tetrahedral ordering with an increase in pressure (represented by the ‘dampening’ of the radial distribution) is seen.

MD simulations of the solvated AK peptide are stable up to 2 kbar. The increasing pressure appears to decrease the RMSDs and RMSFs, possibly indicating a reduction of protein dynamics at higher pressures. The radius of gyration, end-to-end distance and water coordination are compared across the pressure range with the results obtained by Paschek *et al.* (Paschek et al., 2005). In each case there is good agreement between the two studies. The work by Paschek *et al.* reproduced results from experimental studies. It is therefore assumed that the procedure used in this study to perform high pressure molecular dynamics successfully replicates the pressure effect on a solvated peptide. The ff03 force field is deemed suitable for MD simulations on a protein, for pressures up to 2 kbar.

MR was successfully simulated in an octahedral water box, using the procedure validated by the first two sections of this chapter. The simulations are stable during the 10 ns production trajectory, following the minimization and equilibration stages. As for the AK peptide, high pressure seems to have a restricting effect on protein dynamics. The volume of the protein is decreased slightly, but not significantly, as indicated by radius of gyration and solvent accessible surface area. The secondary structure is not affected by the pressure increase. There appears to be an infiltration of water into the core of the protein at the highest pressure.

The initial analysis of the simulations of MR is positive. A stable RMSD is a good indication of a reliable simulation. The reduction in the protein flexibility at higher pressures is seen, which draws a parallel with the AK peptide simulations. The macromolecular tertiary structure of the protein is not drastically affected by the pressure, even up to 2 kbar – this is consistent with the experimental observation that the enzyme is still active at 2 kbar.

There are some clues from the macroscopic analysis of MR as to how the pressure may be affecting the protein. For instance, a common theme emerging is that pressure causes a reduction of flexibility, possibly due to a tighter, more restricted conformation, as a result of subtle, local stabilisation of the structure. The pressure effect on the solvent is interesting: denaturation of proteins by pressure has been associated with water infiltrating the protein core. No denaturation of the protein is expected at these pressures (up to 2 kbar), and, despite an increased number of water molecules, the protein remains stable. A region close to the active site has been identified that shows reduced fluctuations at higher pressures. This could be significant to the conformation of the active site required for the enzyme function. The next chapter will focus on an atomistic analysis of MR across the range of pressures.

Chapter 4

Atomistic Analysis of the Pressure Effect on Morphinone Reductase

PREFACE

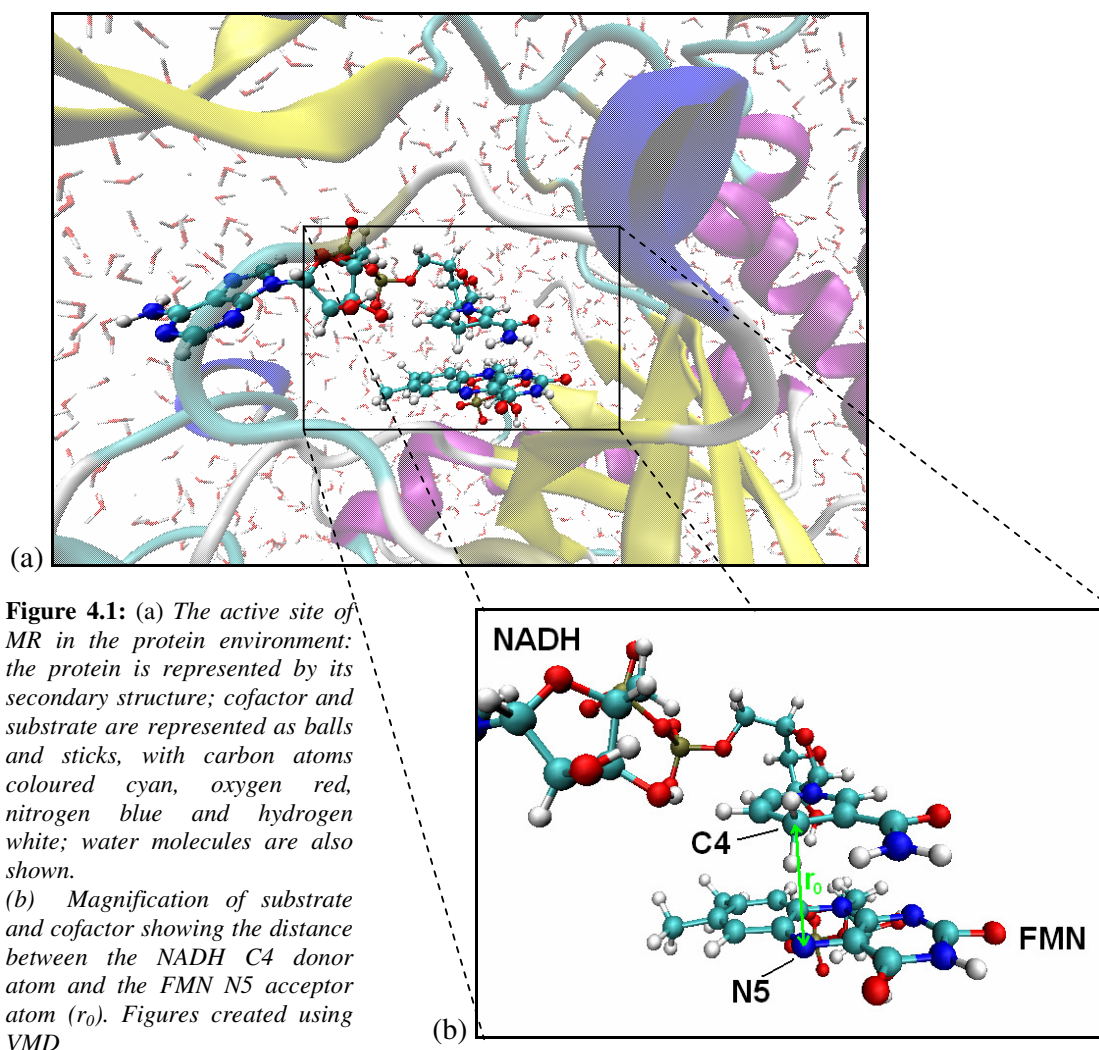
The purpose of this chapter is to obtain a picture of how pressure affects Morphinone Reductase (MR) on an atomistic scale. This builds on previous experimental pressure studies on the catalysis of MR (Hay *et al.*, 2007), as discussed in Section 1.3.3 of this thesis. The conclusions drawn by Hay *et al.* in 2007, point to the need for a promoting motion, which would decrease the distance between the donor and acceptor atoms of the reductive half reaction and suggest that the frequency of this motion increases with a pressure increase.

The MD simulations performed in Chapter 3 included the NADH substrate and FMN cofactor. The first analysis on these simulations concerns the donor-acceptor distance, as advocated by the suggested importance of this by Hay *et al.*

Alongside an analysis of the substrate and cofactor involved in the reaction, it is important to study the residues of the active site and their response to the increase in atmospheric pressure. The ultimate goal is to identify a configuration (or several configurations) of substrate and cofactor at high pressure that possibly contributes towards a tunneling mechanism and correlate this to a particular active site residue or residues.

4.1 SUBSTRATE & COFACTOR

The reduced nicotinamide adenine dinucleotide (NADH) and flavin mononucleotide (FMN) are located in the active site of MR as shown below. For clarity, the active site residues are not shown; these will be discussed in Section 4.2.



4.1.1 Donor-Acceptor Distance

The distance between the NADH C4 and FMN N5 was measured from the 10 ns production trajectory across the pressure range. In the crystal structure the distance is 3.44 Å. However, post-minimisation and equilibration, the distance fluctuates between 3 Å and 6 Å at each pressure. The averages are calculated for each simulation to compare across the pressure range of 1 bar to 2 kbar. These are shown in Figure 4.2 and Table 4.1.

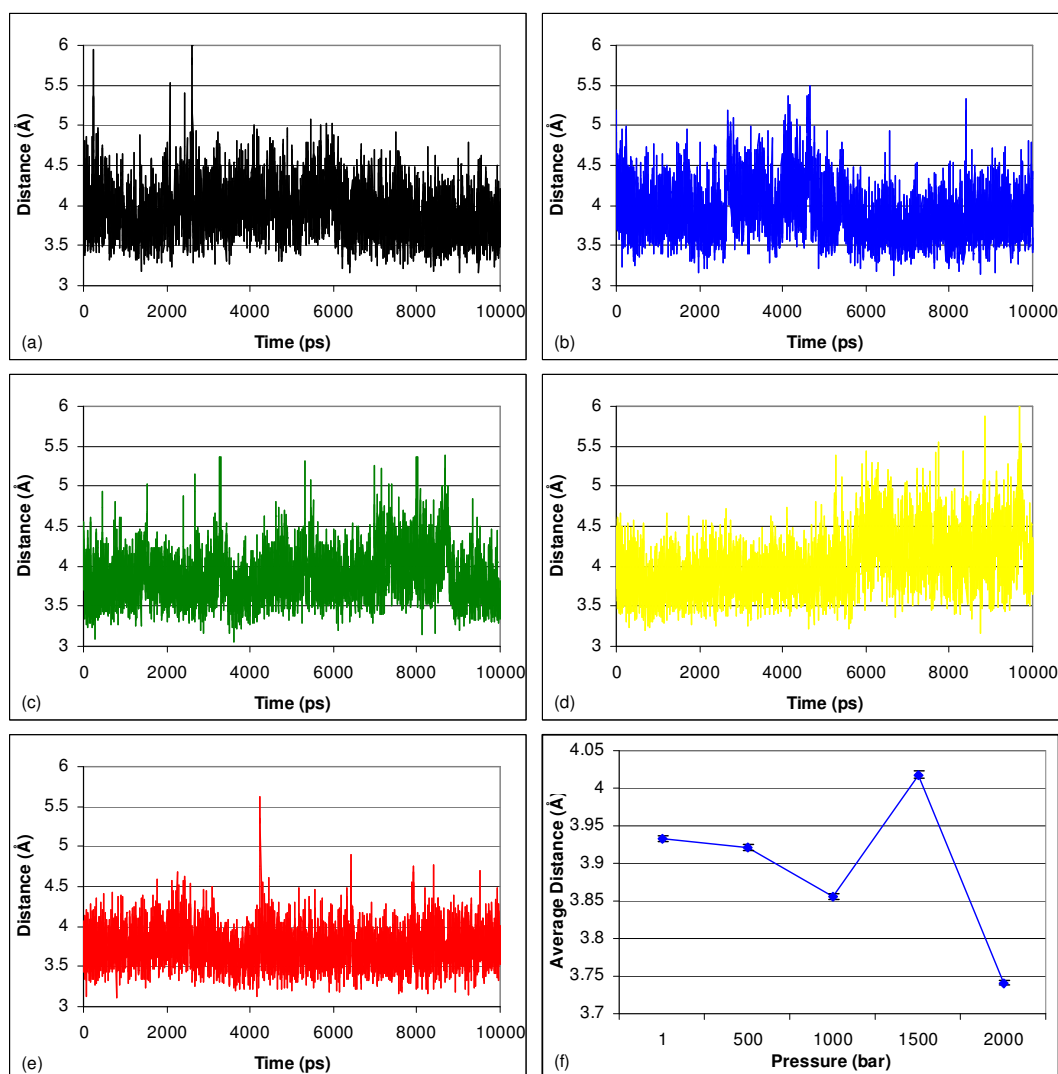


Figure 4.2: Figure showing how the C4-N5 distance varies across the 10 ns trajectory at (a) 1 bar, (b) 500 bar, (c) 1 kbar, (d) 1.5 kbar and (e) 2 kbar. (f) shows the average distance at each pressure (with the standard error shown)

| Pressure (bar) | 1 | 500 | 1000 | 1500 | 2000 |
|---------------------|------|------|------|------|------|
| Average C4 – N5 (Å) | 3.93 | 3.92 | 3.86 | 4.02 | 3.74 |
| Standard Deviation | 0.33 | 0.33 | 0.30 | 0.36 | 0.24 |

Table 4.1: Average values for the distance between the donor C4 atom of NADH and the acceptor N5 atom of FMN. Averages were taken from 10 ns production trajectories

The experimental pressure studies on MR suggested that an increase in pressure would cause a decrease in the donor-acceptor distance. Analysing the distance over the trajectories (shown in Figure 4.2 (a)-(e)), indicates that a wide range of distances is sampled at each pressure. The effect of pressure on the donor-acceptor distance is illustrated by the average values calculated over the 10 ns trajectories (Figure 4.2(f)). There is a decreasing trend as the pressure is increased, from 3.93 Å at atmospheric pressure to 3.74 Å at 2 kbar. The anomaly in this figure is the 1.5 kbar point, which is discussed further in Section 4.1.3.

A better representation of the distribution of distances sampled in each simulation is shown in Figure 4.3. One might expect the minimum and maximum donor-acceptor distance in the simulation at the highest pressure to be shorter than the lower pressure simulations. This is not the case.

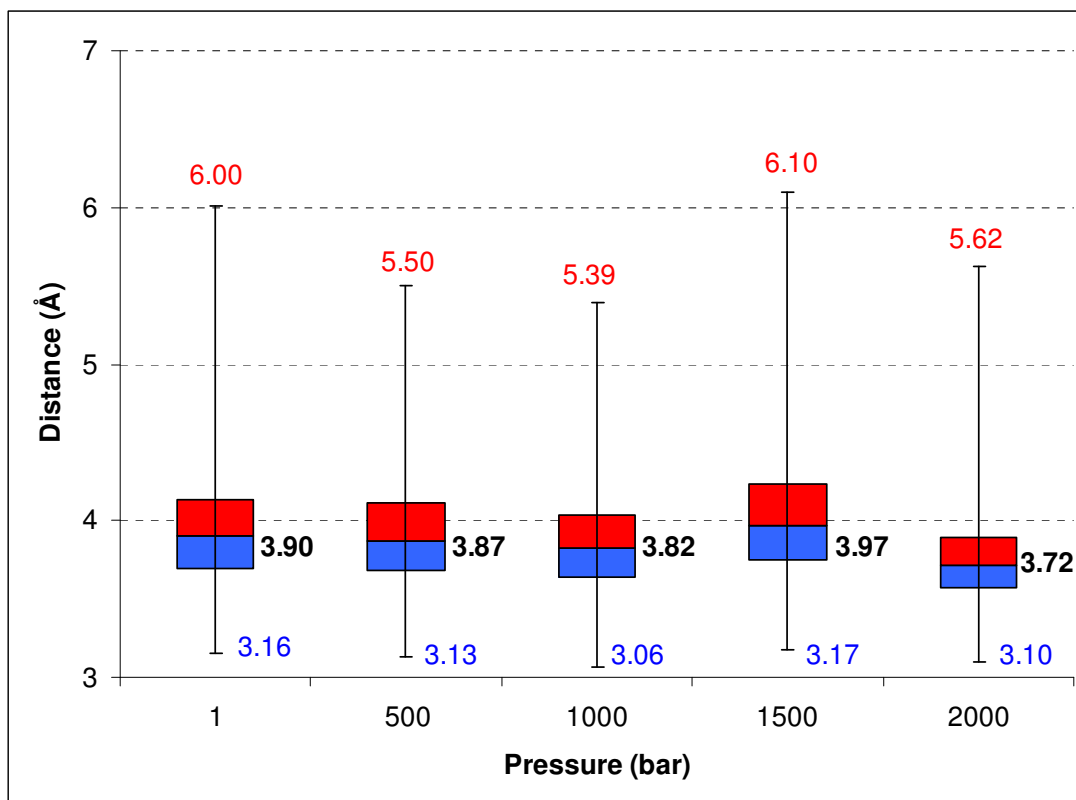


Figure 4.3: Box plot showing the distribution of values for donor-acceptor distance sampled at each pressure, over the 10 ns trajectory. Maximum and minimum values are shown in red and blue respectively, with the median shown in bold.

Figure 4.3 demonstrates that the average donor-acceptor distance is not governed entirely by the range of distances sampled. Considering just the 1 bar, 1 kbar and 2 kbar simulations, it is noted that, although there is a general decrease in the average across the pressure range, the maximum distance does not follow the same trend: the maximum distance at 1 bar is 6.00 Å, which decreases to 5.39 Å at 1 kbar, but then increases to 5.62 Å at 2 kbar. This is at odds with the average, which decreases from 3.93 Å to 3.86 Å to 3.74 Å over the same range of pressures. In this situation it is better to compare the upper quartile – this decreases from 4.13 Å at 1 bar to 4.03 Å at 1 kbar and to 3.89 Å at 2 kbar. The lower quartiles also decrease, although not by the same magnitude: 3.70 Å to 3.64 Å to 3.57 Å.

It is suggested by these statistics that the decrease in the average across the pressure range is not necessarily due to the elimination of configurations with large donor-acceptor distances entirely; instead the probability that large distances can be sampled is decreased. Therefore, to understand how the average distance is affected by pressure, a more robust analysis of the distribution of distances is required.

4.1.2 Distribution of Donor-Acceptor Distances

The Wilcoxon rank-sum (RS) and Kolmogorov-Smirnov (KS) tests are used to demonstrate that the medians and distributions are significantly different from each other (Wilcoxon, 1960, Chakravarti et al., 1967). A probability (p) is given as a parameter for rejecting the null hypothesis. In the case of the RS test, the null hypothesis is that the medians of the two samples are the same, The KS test calculates the probability that the samples are drawn from populations with the same distribution. The data is shown in Table 4.2 for comparisons between 1 bar, 1 kbar and 2 kbar.

| Comparison | p (RS) | p (KS) | Effect Size |
|-----------------|----------|----------|-------------|
| 1 bar – 1 kbar | <0.001 | <0.001 | 0.57 |
| 1 kbar – 2 kbar | <0.001 | <0.001 | 0.61 |
| 1 bar – 2 kbar | <0.001 | <0.001 | 0.68 |

Table 4.2: Calculations of p using the Wilcoxon rank-sum (RS) and the Kolmogorov-Smirnov(KS) tests to demonstrate that the samples of donor-acceptor distance taken from the 1 bar, 1 kbar and 2 kbar simulations are significantly different from each other. A measure of significance is given by the effect size.

It is not uncommon for large sample sizes to have extremely low p -values and this is certainly the case for the RS and KS tests on the distributions. The precision of the values is rounded to 3 decimal places, since it is unreasonable to consider the actual values as a probability. The tests show with little uncertainty that the samples have different medians

and different distributions. The significance of these differences is given by the effect size, also shown in Table 4.2. A small effect is demonstrated by a value of 0.56, a medium effect by a value of 0.64 and a large effect by a value of 0.71 (Vargha and Delaney, 2000). The data shows that there is a significant difference between all of the populations, with a noteworthy difference between the distributions of the donor-acceptor distances for 1 bar and 2 kbar.

The distributions can be represented graphically, by calculating the number of configurations within a particular range of distances and plotted as a bar chart (Figure 4.4). The distance values were sorted into windows of 0.1 \AA , for three pressures: 1 bar, 1 kbar and 2 kbar (See Appendix B).

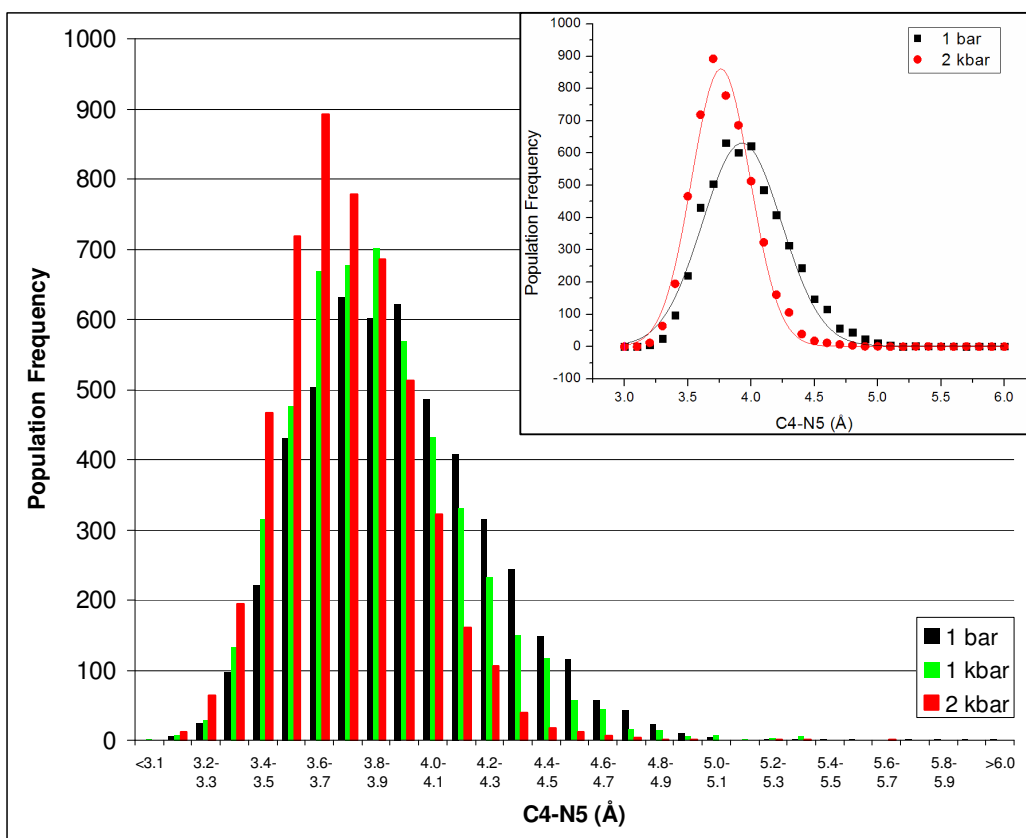


Figure 4.4: Distribution of donor-acceptor (C4-N5) distances from 1 bar (black), 1 kbar (green) and 2 kbar (red) trajectories. The distances from 5000 frames across each 10 ns trajectory are binned in 0.1 \AA distances from under 3.1 \AA up to over 6.0 \AA . The insert shows the data from 2 kbar and 1 bar fitted to a Gaussian.

Figure 4.4 shows a roughly Gaussian distribution of distances at each pressure. There is clearly a shift in this distribution as the pressure is increased. The insert in Figure 4 illustrates the shift in distribution from 1 bar to 2 kbar, by fitting the data to a Gaussian equation ($y=y_0 + (A/(w*\sqrt{\pi/2}))*\exp(-2*((x-x_c)/w)^2)$). The centre of the Gaussian curve from the insert in Figure 4.4 illustrates the decrease in donor-acceptor distance with pressure, from 3.93 Å at 1 bar, to 3.85 Å at 1 kbar and to 3.76 Å at 2 kbar (agreeing with the averages taken across the trajectory, given in Table 4.1). The width of the curve decreases from 0.62 Å at 1 bar, to 0.55 Å at 1 kbar and to 0.46 Å at 2 kbar.

Configurations of substrate and cofactor with a variety of donor-acceptor distances are sampled at high and low pressure. However, as the pressure increases, the shorter distances are sampled more frequently / the longer distances less frequently; it is for this reason that the average distance decreases. A theory that would account for this observation is that the nicotinamide ring of the NADH substrate is not able to move into a particular region of conformational space at higher pressures. Therefore it is forced to remain closer to the FMN cofactor and the shorter distances are sampled at a higher frequency.

4.1.3 1.5 kbar Donor-Acceptor Distance

The major inconsistency in the donor-acceptor distance analysis is the average value at 1.5 kbar. Further analysis of how the distance changes over the 10 ns reveals that there is an increase just over halfway through the simulation. Figure 4.5 is replicated from Figure 4.2(d), with the average distance from the first half of the trajectory also plotted.

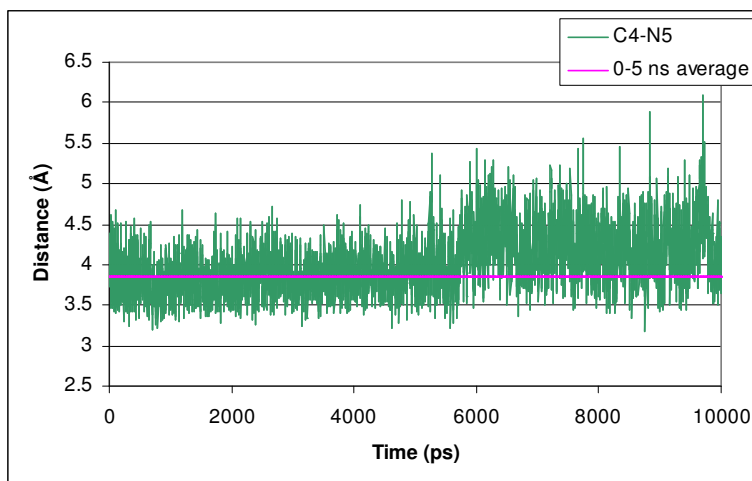


Figure 4.5: Figure showing the C4-N5 distance across the 10 ns 1.5 kbar trajectory (green). The average distance from the first half of the trajectory (pink) is also shown for comparison

The average distance in the first 5 ns of the simulation is 3.86 Å, comparable to the 1 kbar simulation. For the second half of the simulation, the average distance is 4.20 Å. This increase is a result of the nicotinamide ring shifting at approximately 5.7 ns. It is then located in this region of conformational space, further away from the isoalloxazine, for the remainder of the simulation. On closer inspection of the active site at this time, it is observed that a residue (Phe246) also shifts, as shown in Figure 4.6, possibly contributing towards pushing the nicotinamide ring forward.

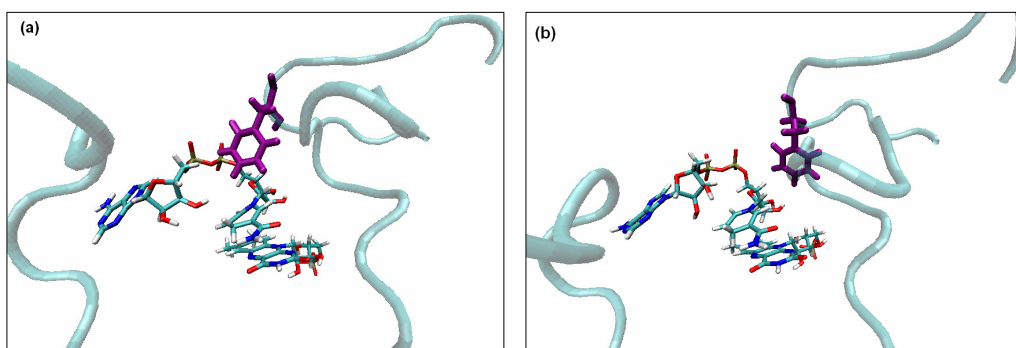


Figure 4.6: Figure showing the position of Phe 246 (shown in purple) for (a) the first 5.7 ns of the 1.5 kbar simulation; and (b) the remainder of the simulation. The NADH substrate and FMN cofactor are also shown

This seems to be the reason for the increase in the donor-acceptor distance, although it may be an incidental effect of something else that is causing both a shift in the nicotinamide and

this residue. This residue will be analysed further in Section 4.2, along with other active site residues to try to decipher whether they form part of the pressure effect on the protein.

4.1.4 Motion of Nicotinamide

The nicotinamide ring is the portion of the NADH substrate that contains the donor C4 atom (see Figure 1.8 in Section 1.2.1 of this thesis). Crystallographic studies of the protein with the cofactor and substrate bound show that the ring is situated above the isoalloxazine ring of the FMN cofactor, forming a π -stacking interaction. The simulations, however, show that there is a lot of conformational space around the nicotinamide and it moves around in this space during the simulations.

A two-dimensional root-mean-squared-deviation (2D-RMSD) of the nicotinamide ring at high and low pressure should identify any differences in its spatial conformation in the simulations. The coordinates of the 18 heavy atoms in the isoalloxazine ring of FMN were used to align the trajectories. The RMSD was then calculated on the 9 heavy atoms of the nicotinamide ring on a frame-by-frame basis for a 1000 frame combined trajectory of the 1 bar and 2 kbar simulations. (See Appendix C for figures showing nicotinamide and isoalloxazine rings).

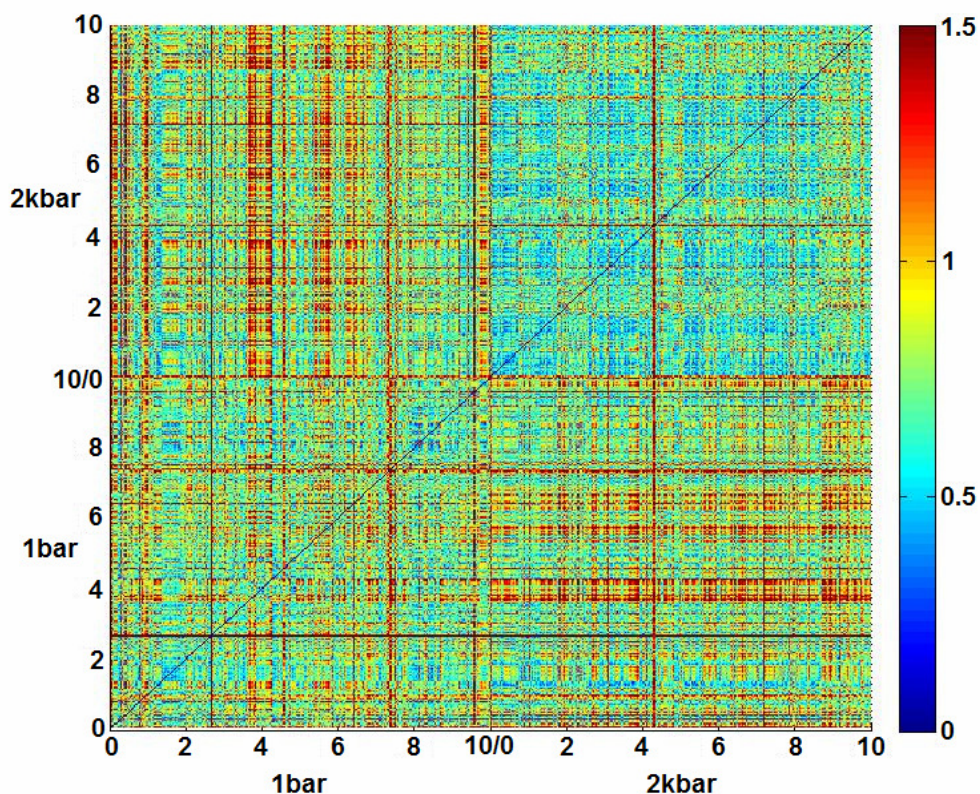


Figure 4.7: Figure showing a 2D-RMSD analysis of the nicotinamide ring across two 500 frame (10 ns) trajectories. The bottom-left corner allows comparison of the 1 bar trajectory, the top-right corner allows comparison for the 2 kbar trajectory. The top-left and bottom-right corners give a comparison between the two trajectories. The timesteps of the trajectories are plotted along the axes in ns. The bar at the right hand side is the colour coded RMSD key, with the values in Å

Figure 4.7 is a colour-coded matrix that represents the 2D-RMSD of the nicotinamide ring. The axes are identical, with the diagonal from bottom-left to top-right showing a value of zero, since the RMSD of any particular frame compared to itself is zero. The colours of each of the other points on the matrix represent a value of RMSD calculated by comparing the two frames from each axes. The colour scale has been modified to best illustrate the frames of the simulation that deviate from each other. The maximum RMSD of each frame compared to every other frame is 2.806, however roughly 80% of the deviations are below 1.5, hence this was used as the maximum value for the colour scale. An equivalent plot

showing the maximum value on the colour scale as the maximum RMSD is included in Appendix D.

The 2D-RMSD should highlight any particular times during the simulation when the nicotinamide ring deviates into different regions of conformational space. Whilst it is possible to identify regions where the 1 bar simulation seems to deviate significantly from the 2 kbar simulation (such as around 4 ns into the 1 bar simulation), a major change in the conformational space occupied by the nicotinamide ring during this part of the simulation is not obvious. This is perhaps because the trajectory is fitted to the isoalloxazine ring, and the movement of the nicotinamide ring is limited to small deviations, but in several different dimensions. Rather than identifying a particular stage in the simulation, it would be more useful to extrapolate particular frames when the nicotinamide moves into a region of space prohibited at 2 kbar, since it is likely that this will occur throughout the simulation.

The matrix in Figure 4.7 illustrates the entire spatial conformation of the nicotinamide with respect to the isoalloxazine, throughout the whole of the 1 bar and 2 kbar trajectories. However, it encompasses an enormous amount of data represented in just two dimensions. A colour coded matrix is not suited to illustrating this, since the movement of the nicotinamide is in multi-dimensional. To reduce the dimensionality of the data in the matrix, obtaining the most significant deviations, a principal components analysis (PCA) was performed on the dataset.

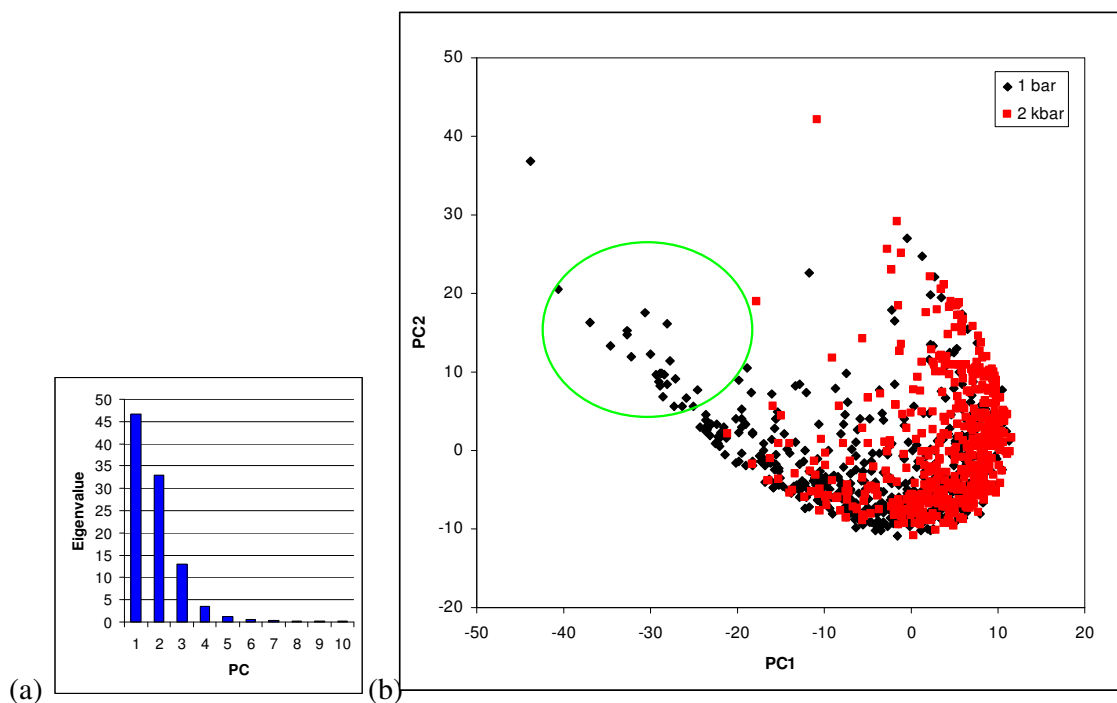


Figure 4.8: Figure showing Principal Components Analysis of the 2D-RMSD performed on the nicotinamide. (a) shows the normalised eigenvalues (as a percentage) of each principal component. The first two principal components are plotted as a scatter graph in (b)

Figure 4.8 (a) shows that the majority of the variation is contained in the first two principal components (46.7 % in PC1 and 33.0% in PC2). Therefore plotting these two principal components should give a two-dimensional illustration of the conformational space sampled by the nicotinamide ring. Figure 4.8 (b) shows this plot, with the frames from the different simulations coloured to show differences in conformational space sampled at high and low pressure.

As with the 2D-RMSD matrix (Figure 4.17), it is difficult to identify a major difference between the high and low pressures. There is no obvious clustering at different pressures., although this can be explained with the fact that the variation of the coordinates of the nicotinamide atoms is likely to be minimal from frame to frame, due to the trajectories being fitted to the isoalloxazine ring. However, there is certainly a region (circled green)

where there are several frames from the low pressure simulation and none from the high pressure simulation.

These frames from the cluster were traced back to the trajectory and an average structure was created to illustrate where the nicotinamide lies with respect to the isoalloxazine. This is compared to an average structure created using frames from main cluster of the 2 kbar trajectory. Figure 4.9 shows these two average structures with the isoalloxazine ring overlaid to illustrate the position of the nicotinamide.

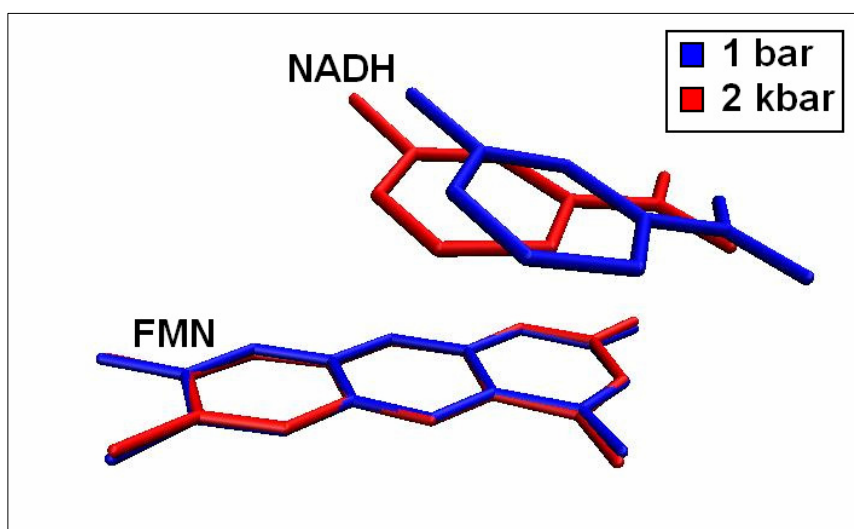


Figure 4.9: Figure showing the average structure obtained from the cluster of 1 bar frames circled green in Figure 4.8(b), overlaid on the the average structure of 2 kbar frames from the main cluster. The structures are aligned on the isoalloxazine ring to compare the spatial conformation of the nicotinamide with respect to the isoalloxazine

Although the 2D-RMSD was inconclusive in the first instance, PCA had allowed a region of space to be identified by isolating the most significant deviations of the nicotinamide. The 1 bar configuration of the nicotinamide ring in Figure 4.9 represents the area of

conformational space, circled green in Figure 4.8(b). There are no frames from the 2 kbar simulation that enter this region of conformational space. Hence it can be deduced that the position of the nicotinamide shown for 1 bar in Figure 4.9 is inaccessible at 2 kbar. This supports the theory that proposed by the distribution of donor-acceptor distances: the high pressure cuts off a region of conformational space where the nicotinamide can adopt a configuration with a longer donor-acceptor distance, thus off-setting the equilibrium towards shorter distances.

4.1.5 Substrate & Cofactor Summary

The substrate and cofactor in the active site are the focal point of the pressure studies into MR. Of particular interest is the distance between the donor atom and acceptor atoms, on the substrate and cofactor respectively, during the hydride transfer reaction. Experimental work predicts a shortening of this distance as the pressure is increased, which could facilitate a promoting motion in the quantum tunneling mechanism of the reductive half reaction (Hay et al., 2007).

The distance between donor and acceptor atoms is studied by calculating the average over 5000 frames of the 10 ns production trajectories. There is a general downward trend across the pressure range, despite one point being significantly anomalous. What is particularly interesting, however, is that the minimum and maximum distances sampled do not vary significantly over the pressure range. Instead the shortening of the average is due to a shift in the equilibrium towards shorter distances. The analysis of the distribution of donor-acceptor distances shows that there are clearly less configurations sampling the longer

distances at higher pressures (64% less configurations at 2 kbar at distance of greater than 4 Å, than at 1 bar). This could mean that a particular region of conformational space, available to the nicotinamide at low pressure, is no longer available at higher pressures.

A 2D-RMSD plot, followed by PCA (Figures 4.8 and 4.9), supports this hypothesis and highlights a region of conformational space inaccessible to the nicotinamide at high pressure. The next step is to look at the active site residues in this area of space to examine how they are affected by the pressure increase and whether they may contribute towards the pressure effect on the substrate.

4.2 ANALYSIS OF ACTIVE SITE RESIDUES

The analysis of the substrate and cofactor at different pressures suggests that there is a region of conformational space that is available for the nicotinamide ring at low pressure, but cut off at high pressure. There are several residues in the active site that could be involved in this. The next step then, is to look at the dynamics of these residues at high and low pressures.

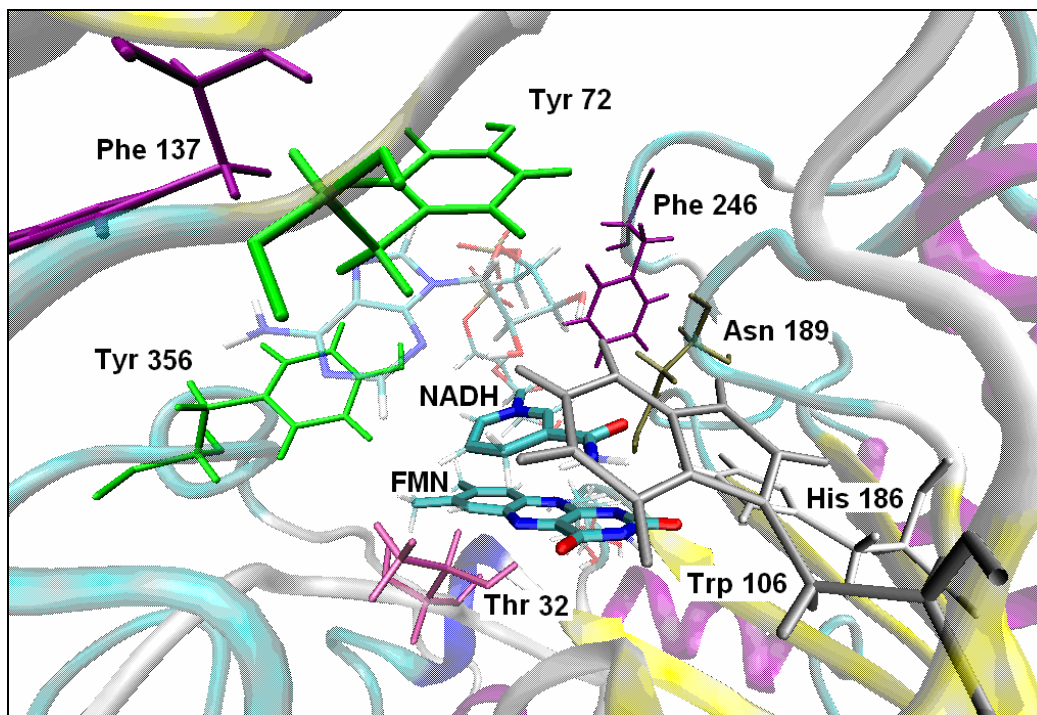


Figure 4.10: Figure showing an atomistic representation of the active site of MR. Eight of the active site residues are represented as sticks and coloured according to the residue name. The substrate (NADH) and cofactor (FMN) are represented as sticks, coloured according to atom (carbon=cyan, oxygen=red, nitrogen=blue, hydrogen=white). The nicotinamide and isoalloxazine heavy atoms are enlarged for emphasis.

Of the eight residues shown in Figure 4.10, only His186 and Asn189 are on the same loop. The active site consists of several aromatic residues on different loops, each of which may play some role in the shortening of the donor-acceptor distance with pressure.

4.2.1 RMSDs / RMSFs of Active Site Residues

The RMSDs were calculated on the C- α 's of the residues shown in Figure 4.10.

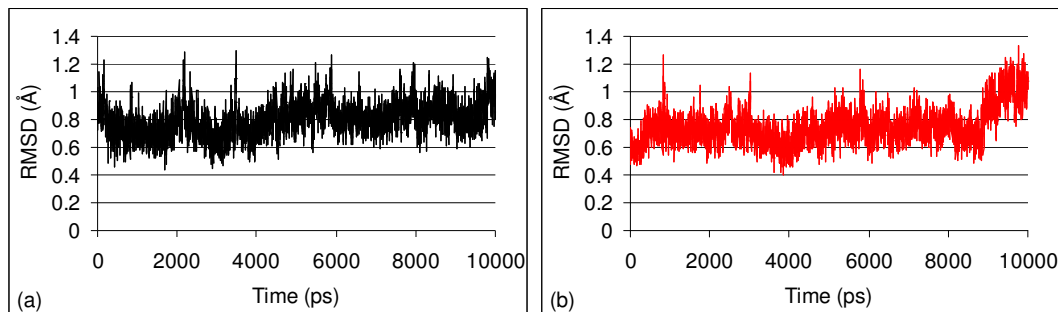


Figure 4.11: Figure showing RMSDs of the C- α 's of active site residues: Thr32, Tyr72, Trp106, Phe137, His186, Asn189, Phe246 and Tyr356. RMSDs taken over the 10 ns trajectories at (a) 1 bar and (b) 2 kbar

It is difficult to see any major differences in the RMSDs at different pressure. It is noted, however, that at the high pressure, the RMSDs rises towards the end of the simulation. This is due to a change in conformation of Phe246, similar to what happens in the 1.5 kbar trajectory (see Section 4.1.3). It is also reflected in the RMSFs, shown below.

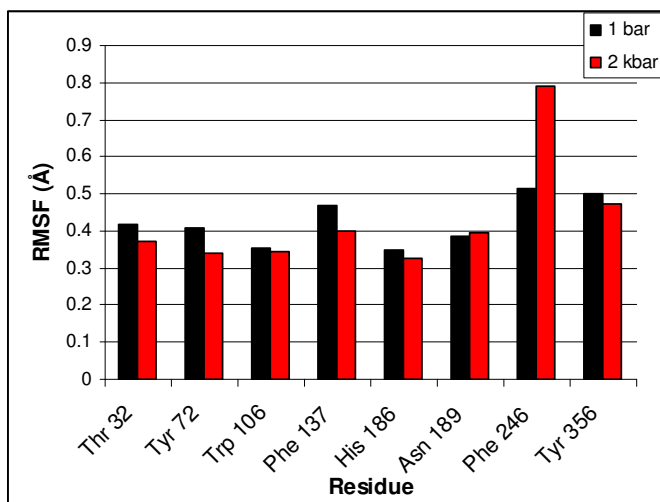


Figure 4.12: Figure showing RMSFs of the C- α 's of active site residues: Thr32, Tyr72, Trp106, Phe137, His186, Asn189, Phe246 and Tyr356. RMSDs taken over the 10 ns trajectories at 1 bar (black) and 2 kbar (red)

The RMSDs and RMSFs of the active site show that the active site is relatively stable at each pressure (disregarding, for now, Phe246 at the end of the high pressure simulation). This does not necessarily mean, however, that these residues form the same configuration at high and low pressure. A more intricate and atomistic analysis of how the residues move is required.

4.2.2 Essential Dynamics

The ptraj module, implemented in AMBER, was used to generate a covariance matrix using the heavy atoms of the nicotinamide and isoalloxazine rings (See Appendix C), combined with the heavy atoms of the eight active site residues shown in Figure 4.10. This was done for the low and high pressure simulations. PCA is performed on this matrix, generating eigenvector and projection files, which are the input for the Interactive Essential Dynamics plugin in VMD (Mongan, 2004). This plugin allows the visualisation of the most significant motions of these atoms.

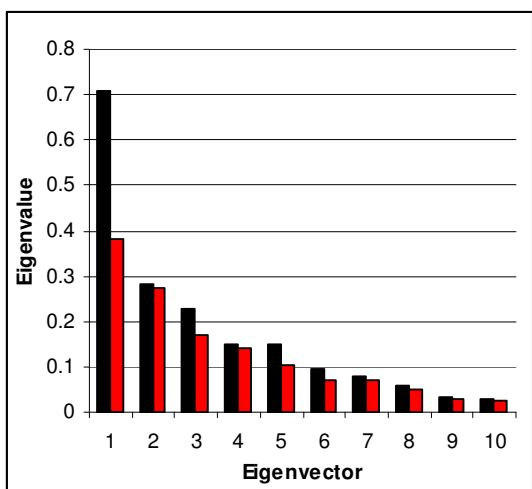


Figure 4.13: Eigenvectors from the PCA on a covariance matrix of the heavy atoms of the nicotinamide ring, isoalloxazine ring and eight selected active site residues. 1 bar (black) and 2 kbar eigenvalues are shown.

Figure 4.13 shows the eigenvalues from the PCA. These eigenvectors were projected onto the coordinates, allowing the mode of motion to be visualised. For both the high and low pressure simulations, the motion represented by the first mode, moves the nicotinamide towards the area of conformational space identified in section 4.1. The most notable observation is that this mode seems to be much more significant (relative to the other modes) at low pressure, than at high pressure.

The essential dynamics reinforces the conclusions from section 4.1, identifying a mode of motion to shift the nicotinamide away from the isoalloxazine, and showing that this mode decreases in significance as the pressure is increased. The benefit of the IED plug-in is that it allows the visualization of this mode. In order to demonstrate how this mode is coupled to the reaction coordinate and which residues are active in this mode, the mode is isolated from all of the other modes in the essential dynamics program. The distances between key residues and the N5 atom of the isoalloxazine ring were plotted at the minimum and maximum projection of the mode, as shown in Table 4.**. The range of C4-N5 distances sampled by this mode is 3.40 Å - 4.96 Å.

| Distance | Minimum Projection | Maximum Projection |
|-------------------|--------------------|--------------------|
| FMN:N5-NAD:C4 | 3.40 Å | 4.96 Å |
| FMN:N5-Thr32:CG2 | 5.32 Å | 5.25 Å |
| FMN:N5-Tyr72:CZ | 12.58 Å | 9.32 Å |
| FMN:N5-Trp106:CH2 | 6.83 Å | 9.80 Å |
| FMN:N5-Phe137:CZ | 15.01 Å | 15.11 Å |
| FMN:N5-His186:NE2 | 7.45 Å | 7.43 Å |
| FMN:N5-Asn189:ND2 | 6.21 Å | 6.15 Å |
| FMN:N5-Phe246:CZ | 8.78 Å | 8.39 Å |
| FMN:N5-Tyr356:CZ | 6.53 Å | 6.79 Å |

Table 4.3: Distances between active site residues and FMN during the first mode of the Essential Dynamics.

Table 4.3 shows that the most active residues in this mode are Tyr65 and Trp106. The movement of Trp106 towards the isoalloxazine seems to be correlated with the movement of the donor atom C4 of NADH towards the acceptor atom N5 of FMN. The movement of Tyr65 on the other hand is anti-correlated. This is illustrated in Figure 4.14.

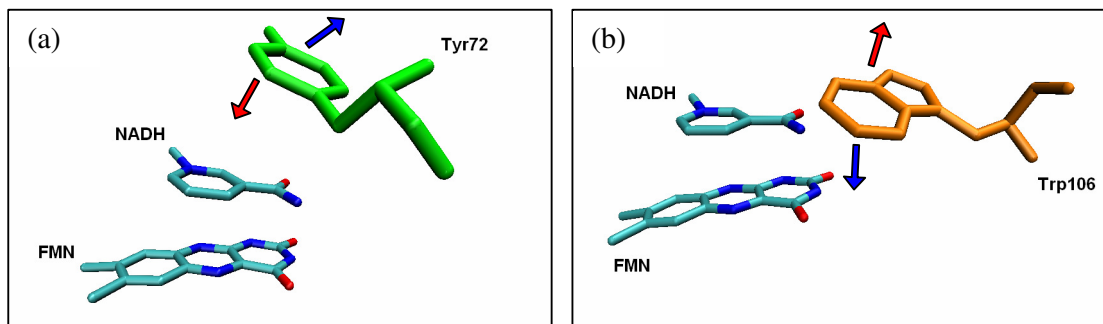


Figure 4.14: Figure showing the movement of (a) Tyr72 and (b) Trp106 corresponding to the first eigenvector from the Essential Dynamics. The blue arrow shows the movement towards the minimum projection, the red arrow shows the movement towards the maximum projection

The correlation of Trp106 with the reaction coordinate, combined with its position (located close to the region of space cut off at high pressure) makes it the obvious choice for further analysis, although the tyrosine residue will also be considered alongside Phe246.

4.2.3 Tryptophan 106

The suggestion emerging from the previous analyses is that this tryptophan residue is fixed in place at high pressure and does not allow the nicotinamide to move away from the isoalloxazine. Figure 4.15 shows the distance between the heavy atoms of the tryptophan ring and the heavy atoms of the isoalloxazine and nicotinamide rings, at low and high pressures.

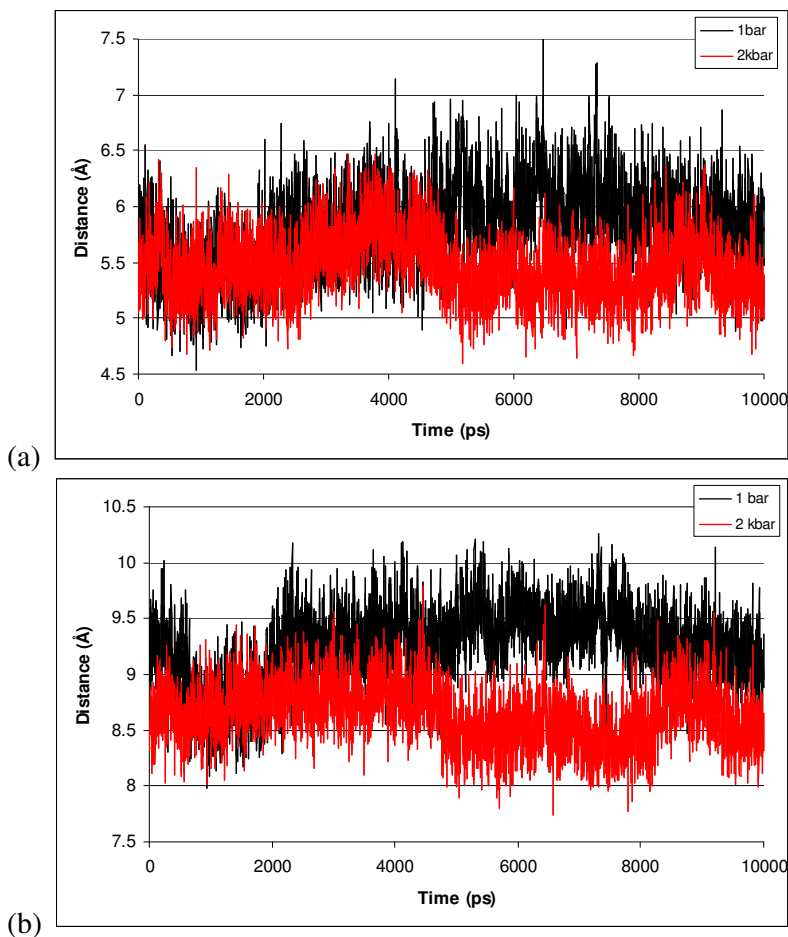


Figure 4.15: (a) The distance between the centre of mass of the heavy atoms of nicotinamide ring and the heavy atoms of the tryptophan ring at low (black) and high (red) pressures across the 10 ns simulations. (b) The distance between the centre of mass of the heavy atoms of isoalloxazine ring and the heavy atoms of the tryptophan ring at low (black) and high (red) pressures across the 10 ns simulations.

Figure 4.15 shows that the pressure has a greater effect on the distance between the tryptophan and isoalloxazine, than it does on the distance between the tryptophan and nicotinamide. The average distance between the tryptophan and isoalloxazine decreases by 0.61 \AA , whereas the average distance between the tryptophan and nicotinamide decreases by 0.35 \AA . This is consistent with a proposal that the tryptophan pushes the nicotinamide towards the isoalloxazine.

This hypothesis can be tested by studying the correlation between this distance and the donor-acceptor distance. Figure 4.16(a) shows little correlation at low pressure, whilst at high pressure (Figure 4.16(b)), there is only a slight improvement. However, by taking a

portion of the 2 kbar trajectory between 5 and 8 ns, where the tryptophan is in the conformation that is closest to the isoalloxazine, the correlation is improved much more (Figure 4.16(c)).

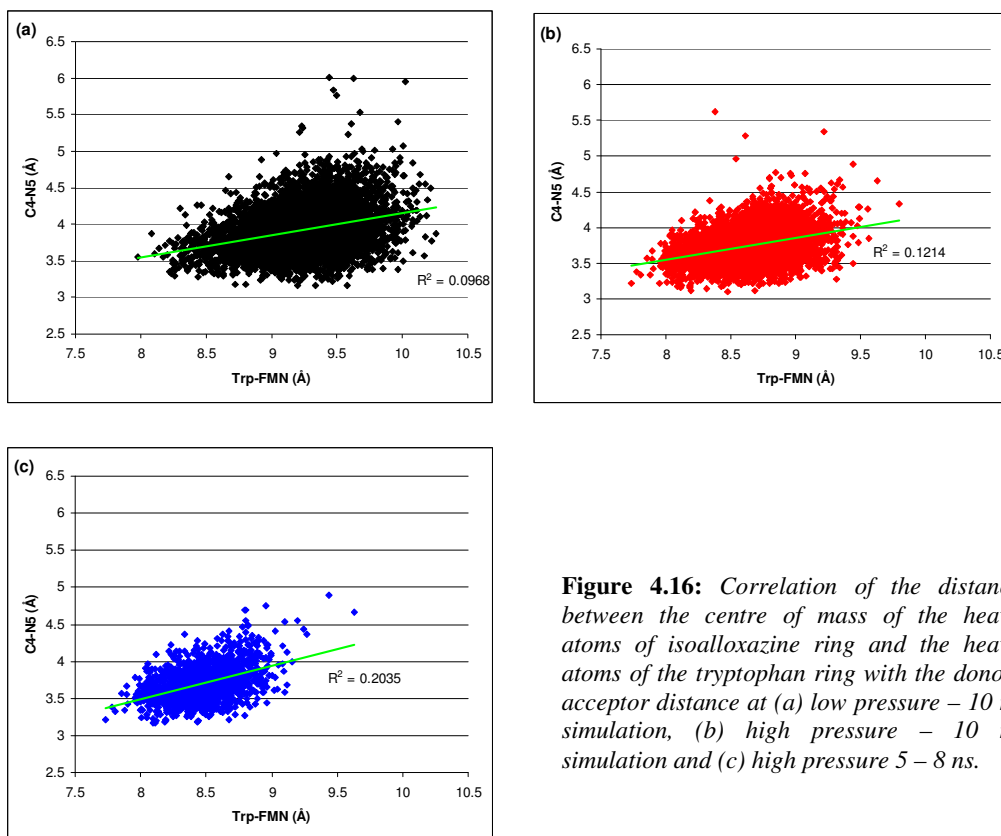


Figure 4.16: Correlation of the distance between the centre of mass of the heavy atoms of isoalloxazine ring and the heavy atoms of the tryptophan ring with the donor-acceptor distance at (a) low pressure – 10 ns simulation, (b) high pressure – 10 ns simulation and (c) high pressure 5 – 8 ns.

Although the correlation is still not entirely convincing when the tryptophan is closest to the isoalloxazine, it does indicate that the Trp106 plays some part in restricting the movement of the nicotinamide away from the isoalloxazine.

4.2.4 Tyrosine 72 / Phenylalanine 246

Tyr72 and Phe246 are two other residues that have been identified as being potentially important in the pressure induced improvement of catalysis in MR. Similar to Trp106, these aromatic residues are on the apex of loops that ‘dip into’ the active site, although these are slightly further away from the nicotinamide and approach from above and, in the

case of Phe246, behind the substrate. Figure 4.17 shows the correlation of these residues with the donor-acceptor distance.

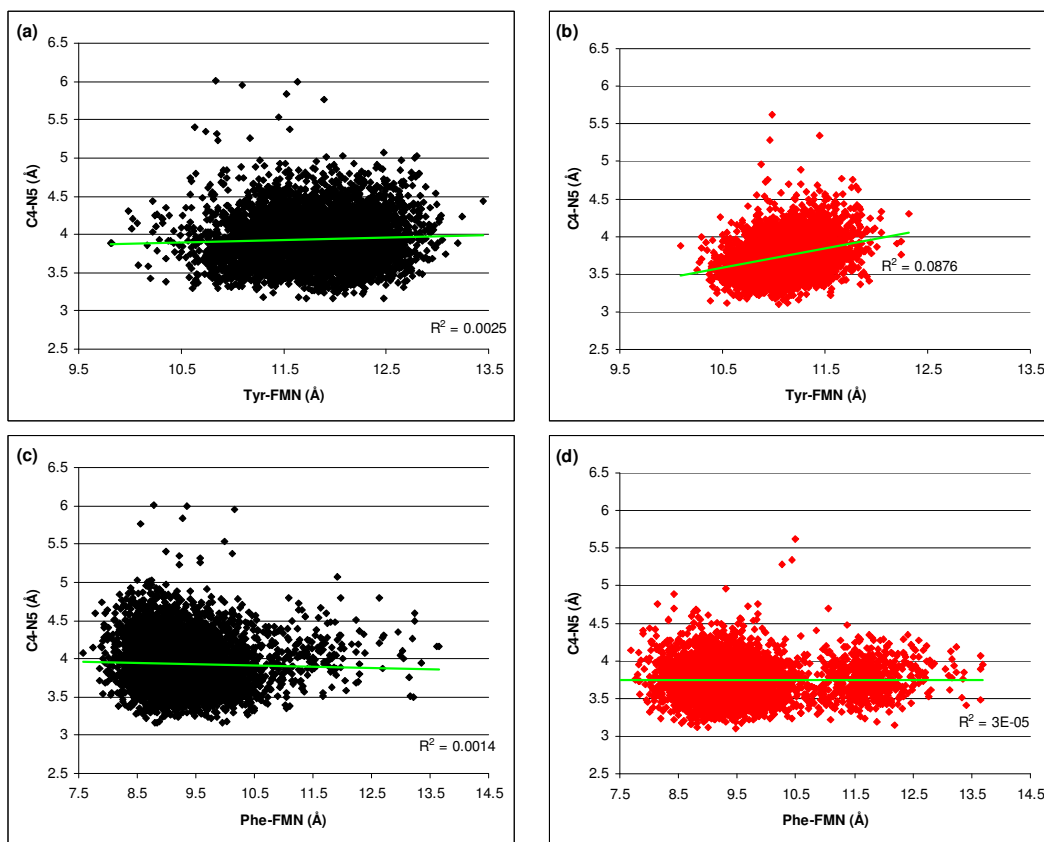


Figure 4.17: Correlation of the distance between the centre of mass of the heavy atoms of the isoalloxazine ring and the heavy atoms of (a) the tyrosine ring at low pressure; (b) the tyrosine ring at high pressure; (c) the phenylalanine ring at low pressure; and (d) the phenylalanine ring at high pressure with the donor-acceptor distance. Each of the correlations includes 5000 frames, sampled across the 10 ns trajectories.

Figure 4.17(b) reveals a slight correlation between the tyrosine ring and the donor-acceptor distance at high pressure. Although Figure 4.17(d) reveals two configurations of the phenylalanine ring, these have no effect on the donor-acceptor distance, so appear insignificant. The possibility of a combination of these two residues being involved in an interaction that contributes to a high pressure configuration is also considered. They are both located above the nicotinamide in the active site. At low pressure, the average distance between the centres of mass of the two rings across the 10 ns trajectory is 10.43 Å.

At high pressure, this shortens to 8.30 Å. However there is no correlation between this distance and the donor-acceptor distance at either pressure.

4.2.5 Active Site Summary

Several different residues are likely to be involved in the high pressure configuration of the active site. One residue in particular seems to be important in the pressure effect on the substrate. Trp106 is positioned close to the area on conformational space that is cut off to the nicotinamide at high pressure. It moves closer to the isoalloxazine at high pressure, preventing the nicotinamide moving into this space. The Interactive Essential Dynamics shows that a mode of motion, where the nicotinamide and tryptophan can fluctuate freely, is significantly decreased at high pressure.

A correlation has been shown between the proximity of the tryptophan to the isoalloxazine and the donor-acceptor distance. This is not very significant at low pressure, but increases at higher pressures. It is likely that other residues are involved in an active site configuration to hold the nicotinamide close to the isoalloxazine. However, similar correlation analyses on Tyr72 and Phe246 are not as convincing.

4.3 RESIDUES OUTSIDE ACTIVE SITE

The possible contribution to enzyme function from residues outside the active site is an ongoing debate in the scientific community (Rod et al., 2003, Quaytman and Schwartz, 2007). Since this research concerns atmospheric pressure, which acts upon the whole

protein, it is important to consider what happens to the global conformation of the protein as the pressure is increased and how this effect may be translated to the active site.

4.3.1 Dynamic Domain

elNemo (Tirion, 1996) is a web based program that can be used to find the lowest frequency normal modes of a protein from a given structure. The lowest frequency normal mode of MR shows a domain movement of 49 residues (numbers 108 to 156) that is located above the active site. However, none of the active site residues discussed in Section 4.1 and 4.2 are part of this domain. Figure 4.18 below shows the movement of the domain. The structures in the figure show the domain in green moving from left to right over the rest of the protein (purple).

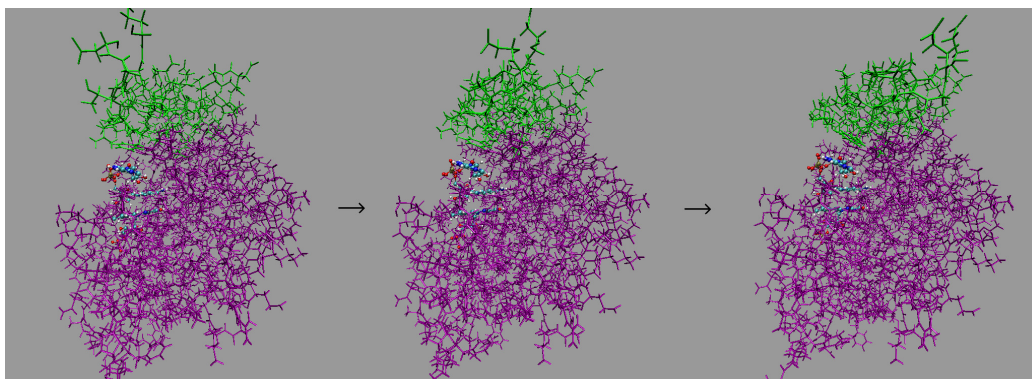


Figure 4.18: Figure to show movement of residues 108-156 (green) with respect to the rest of the protein (purple). The substrate and cofactor are shown, coloured by element, to show where this domain is, in relation to the active site. The domain shifts across the top of the active site.

The motion displayed in Figure 4.18 represents a ‘breathing’ mode of the protein. Nonetheless, the domain that shifts in this mode is in close proximity to the active site, increasing the likelihood of an effect on the configuration between substrate and cofactor. Figure 4.19 shows the RMSFs of the C- α ’s of this domain at 1 bar and 2 kbar.

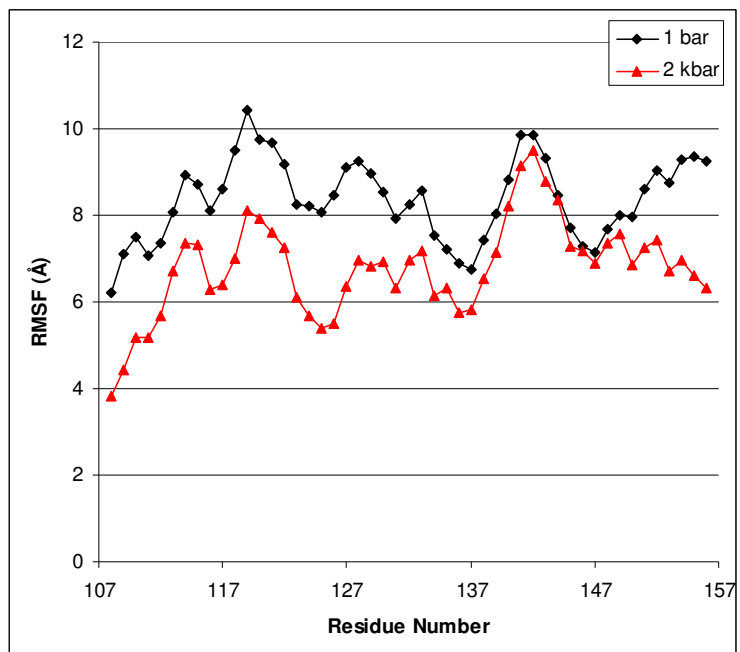


Figure 4.19: RMSFs of domain 108 – 156 at 1 bar (black) and at 2 kbar (red). RMSFs are taken from the 10 ns production trajectories

From the RMSFs at different pressures, we can see that this domain does not fluctuate as much during the high pressure simulations, an observation consistent with other analyses of stability during this study. DynDom is another web based program that is used to identify if a protein has a dynamic domain by analysing two conformations (Hayward and Lee, 2002). Inputting the two structures at each end of the mode shown in Figure 4.18 into DynDom confirms that this motion is the movement of a dynamic domain. The results of the DynDom analysis are shown below.

| Domain | Size | Backbone RMSD (Å) | Residues |
|--------|------|-------------------|------------------------|
| 1 | 300 | 1.80 | 10-68, 75-107, 155-362 |
| 2 | 53 | 1.62 | 69-74, 108-154 |

Table 4.4: Output from DynDom. Table shows that the protein is split into two domains with Domain 1 representing the fixed domain and Domain 2 being the 'dynamics domain'

As well as identifying the domain above the active site, DynDom also classifies residues 69-74 as part of the domain movement – a loop including the active site residue, Tyrosine 72. It is difficult to correlate the domain shift with the donor-acceptor distance. However,

in addition to the output shown in Table 4.4, DynDom gives the bending residues at the hinge of the domain. The following section focuses on one such residue: Val108.

4.3.2 Valine 108

The bending residues of the major domain identified in the eINemo / DynDom analysis are residues 107-108 and 154-156. Each of these residues was studied during the trajectories at high and low pressure and it became immediately apparent that Valine 108 adopted a different configuration in the different simulations. The different configurations are characterized by the rotation around the $C\alpha$ - $C\beta$ bond.

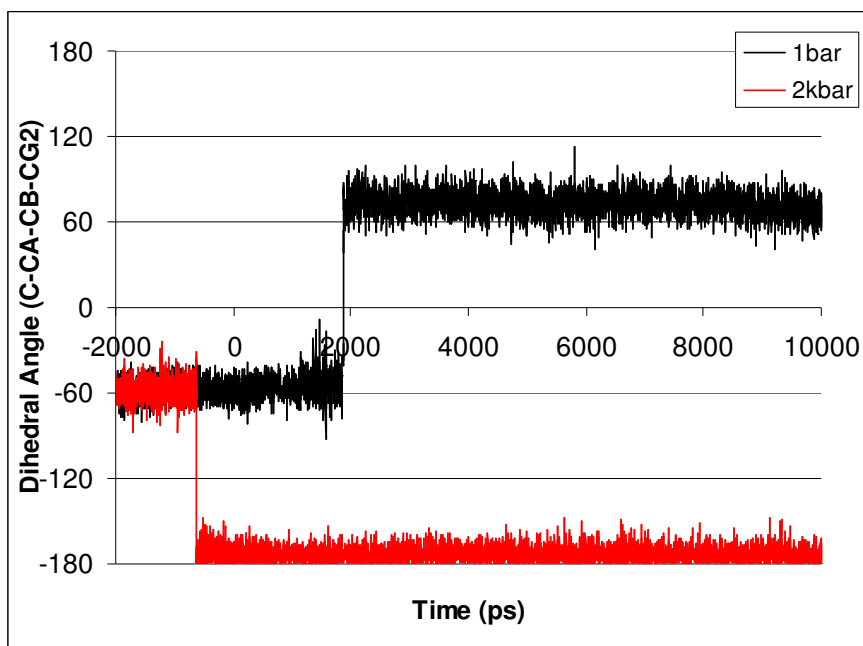


Figure 4.20: Dihedral angle to represent configuration of Valine 108 $C\alpha$ - $C\beta$ bond. Dihedral angle is shown from equilibration (-2000 ps) to end of trajectory, to demonstrate shift from crystal structure configuration.

The configuration at both high and low pressures differs to the crystal structure – it can be seen from Figure 4.20 that the configuration in the 2 kbar simulation is adopted in the equilibrium stage of the simulation, whereas the switch away from the configuration at 1

bar happens roughly 2 ns into the production stage. The configurations represented by these three different dihedral angles are shown in Figure 4.21.

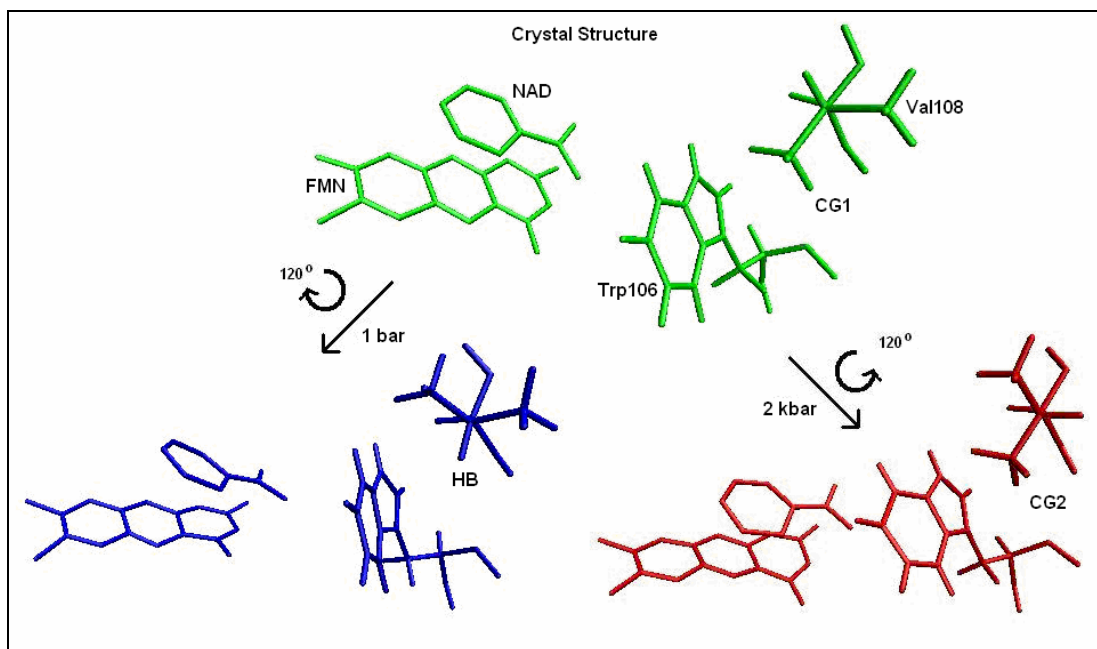


Figure 4.21: Diagram showing the different transformations that occur in the Valine 108 dihedral at low pressure (blue) and high pressure (red), from the crystal structure (green). Also shown is Tryptophan 106 and the nicotinamide and isoalloxazine rings, illustrating how the conformation of the Valine may have an effect on the available conformational space for the nicotinamide

The scheme above shows that the valine is close to Trp106 residue, discussed in Section 4.2.3. In the crystal structure configuration, the CG1 methyl group is closest to the tryptophan residue. During the simulation at low pressure, the bond represented by the dihedral in Figure 4.20 rotates, moving this methyl group away from the tryptophan, with the less bulky hydrogen (HB) atom taking its place. During the high pressure simulation, the bond also rotates, although in the opposite direction. The result is that the equally bulky CG2 methyl residue replaces the CG1.

4.3.3 Significance of Valine 108

The picture that emerges from the dihedral angle analysis of Val108 is as follows: the high pressure inhibits the movement of the dynamic domain above the active site; this restricts

Val108 from adopting a configuration that would normally occur at low pressure and would allow Trp106 to move more freely; thus, the tryptophan does not move away from the nicotinamide at high pressure, as it would at low pressure, meaning that the nicotinamide is forced to remain close to the isoalloxazine.

In order to study this hypothesis, the donor-acceptor distance is analyzed before and after the dihedral rotation at both the low and high pressures.

| Pressure | Average C4-N5 before Valine Flip (Å) | Average C4-N5 after Valine Flip (Å) |
|----------|--------------------------------------|-------------------------------------|
| 1 bar | 3.99 (0.33) | 3.94 (0.32) |
| 2 kbar | 3.79 (0.23) | 3.74 (0.25) |

Table 4.5: Average values for the distance between the donor C4 atom of NADH and the acceptor N5 atom of FMN, before and after the change of configuration (flip) of Val108. Averages were taken from 10 ns production trajectory, plus 2 ns equilibration to include a portion of dynamics where the valine is in its crystal structure configuration. Standard deviations are shown in brackets

The data shown in Table 4.5 opposes the suggestion that the valine configuration is correlated with the donor-acceptor distance. It is suggested, however, that the valine may be part of a group of residues that are involved in the configuration at high pressure and this individual analysis is not sufficient to disprove this.

4.3.4 Outside the Active Site Summary

A dynamic domain has been identified that is ‘less dynamic’ at high pressure, following the same pattern as previous analyses. The domain is close to the active site and the loop containing Tyr72 residue that sits above the nicotinamide is also part of the domain. A hinge residue of the main domain is close to the active site, particularly close to Trp106, which may be important for configuring the active site.

A restricted movement of this domain may force this hinge residue into a configuration that translates to a more compact active site. It is difficult to correlate this directly to the donor-acceptor distance as there are likely to be other residues involved. It does appear that pressure acting upon the macromolecular structure of the protein may be having a knock-on effect in the active site.

4.4 MOLECULAR DYNAMICS ON MUTANT MR

Experimental & computational studies have previously been carried out on a mutated Morphine Reductase: Asn189 in the active site was mutated to an alanine, removing the hydrogen bond formed with the substrate (Pudney et al., 2007). These studies found that the mutation allowed a configuration of substrate and cofactor, with increased overlap of the nicotinamide and isoalloxazine rings, to be sampled – a configuration that is not seen in wild-type MR (This study is discussed in more detail in the Introduction, Section 1.2.4). In addition this, experimental pressure studies, have also been carried out, suggesting that the relative population of configurations with better overlap decreases as the pressure increases. The following work aims to explore this on an atomistic scale.

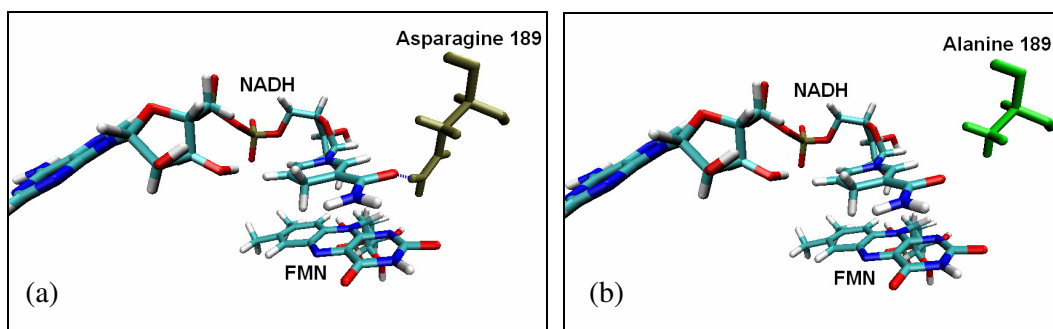


Figure 4.22: (a) Figure showing the Asn189 residue in the active site of wild-type MR and the hydrogen bond formed between this residue and the NADH substrate. (b) Also shown is the mutated form of MR, with an alanine residue in place of Asn189. The hydrogen bond is no longer present

4.4.1 Simulations of Mutated Morphinone Reductase

The point mutation was performed by replacing the side chain of Asn189 with a hydrogen atom, effectively mutating it to an alanine residue (see Figure 4.22 above). The procedure used for the simulations of wild-type MR was then repeated for the mutant simulations at 1 bar and 2 kbar. Figure 4.23 shows the RMSDs of the simulations.

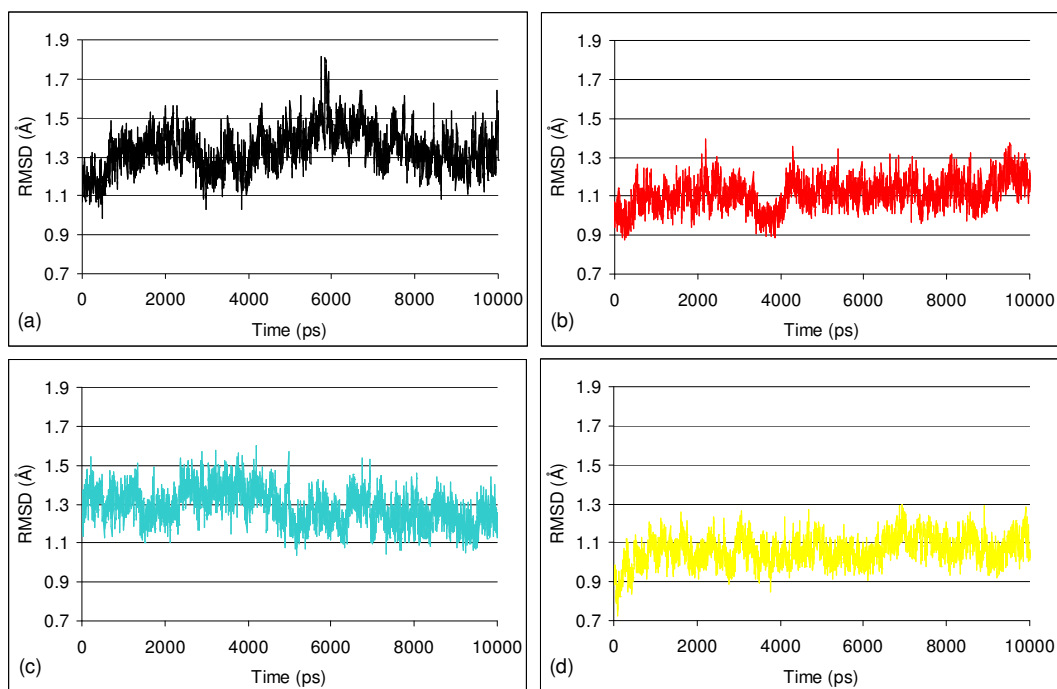


Figure 4.23: RMSDs of protein backbone of MR_N189A for 10 ns trajectory at different pressures: (c) 1 bar and (d) 2 kbar. Also shown for comparison are the RMSD from the WT simulations for (a) 1 bar and (b) 2 kbar

It can be seen in the RMSDs that the simulations were stable across the 10 ns trajectory. It is observed that, similar to the wild-type, the simulation of MR_N189A at higher pressure has a lower RMSD than the low pressure (the averages are 1.29 Å at 1 bar and 1.06 Å at 2 kbar, with a standard deviation of 0.09 Å and 0.07 Å respectively). The analyses regarding the global properties of MR at different pressures (including the radius of gyration and solvent accessible surface area), were also performed for the mutated form of MR.

However, since these did not reveal any note-worthy differences to the wild-type, they are shown in Appendix E.

4.4.2 Donor-Acceptor Distances in MR_N189A

The distance between the NADH C4 and FMN N5 atoms in MR_N189A is shown in Figure 4.24 across the 10 ns trajectories, at high and low pressure. Alongside these, the data from the wild-type simulations at the same pressure is shown for comparison.

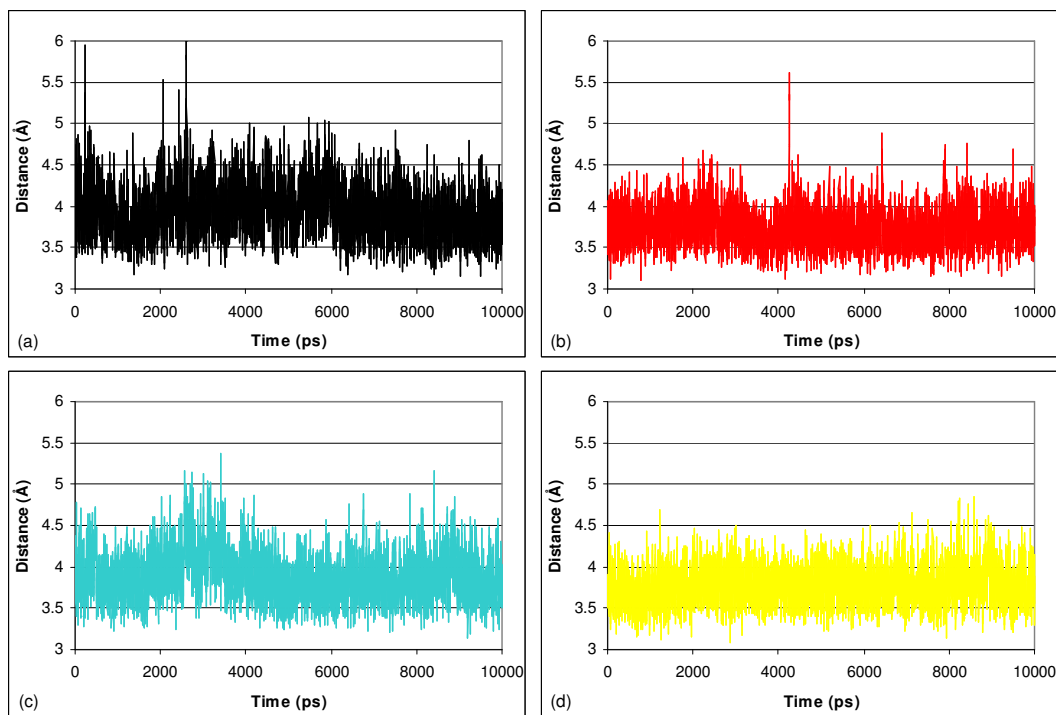


Figure 4.24: Figure showing how the C4-N5 distance varies across the 10 ns trajectory at (a) 1 bar_WT, (b) 2 kbar_WT, (c) 1kbar_N189A and (d) 2 kbar_N189A

Table 4.6 shows the averages from the data in Figure 4.24.

| Simulation | 1 bar WT | 2 kbar WT | 1 bar N189A | 2 kbar N189A |
|---------------------|-------------|--------------|----------------|-----------------|
| Average C4 – N5 (Å) | 3.93 | 3.74 | 3.88 | 3.77 |
| Standard Deviation | 0.33 | 0.24 | 0.30 | 0.24 |

Table 4.6: Average values for the distance between the donor C4 atom of NADH and the acceptor N5 atom of FMN. Averages were taken from 10 ns production trajectory

The significance of the donor-acceptor distance for the wild-type simulations was revealed by the distribution of distances. Details of the distribution in the mutant MR, compared to the wild type at low and high pressures is shown in Figure 4.25.

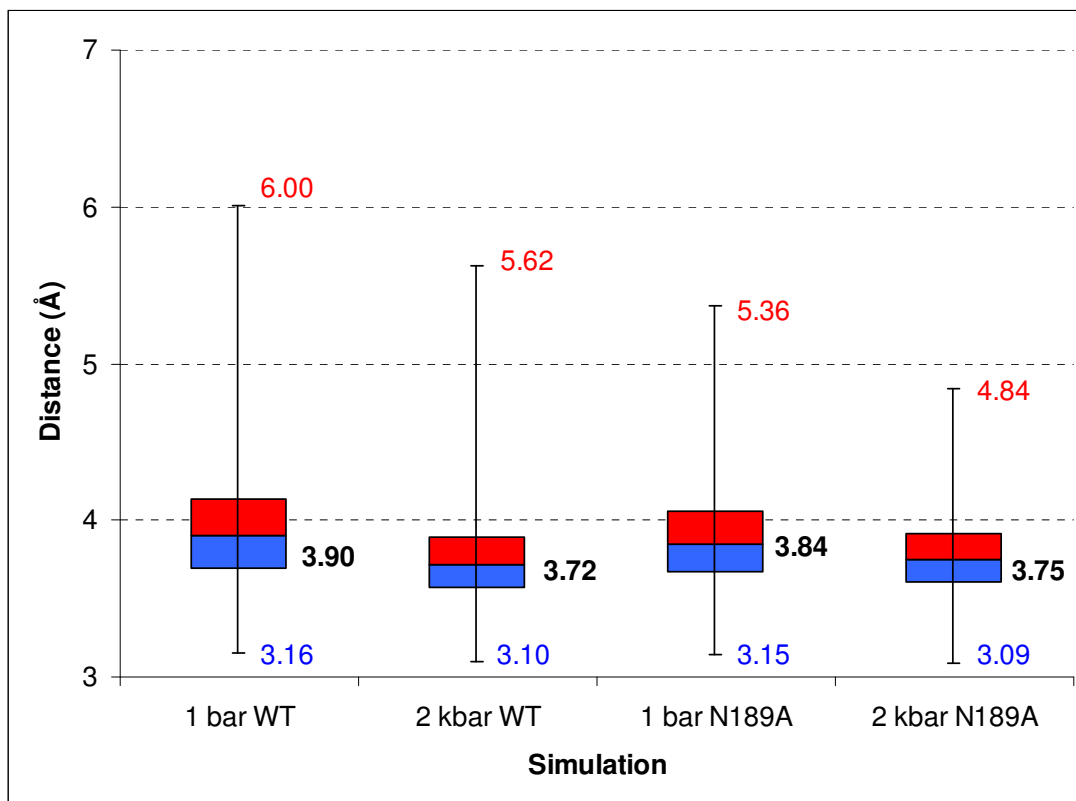


Figure 4.25: Box plot showing the distribution of values for donor-acceptor distance sampled at 1 bar and 2 kbar for the wild type and mutant MR simulations, over the 10 ns trajectory. Maximum and minimum values are shown in red and blue respectively, with the median shown in bold.

There is a negligible difference between the minimums of the wild type with the mutant at the respective pressures; however the maximum differs by a large amount – 0.64 Å in the 1 bar simulations and 0.76 Å in the 2 kbar simulations. In each of the cases the maximum distance is significantly lower for the MR_N189A simulations. The upper-lower quartile range for the wild-type simulation at 1 bar is 0.44 Å; at 2 kbar it is 0.32 Å. The respective values for the MR_N189A simulations are 0.39 Å and 0.31 Å.

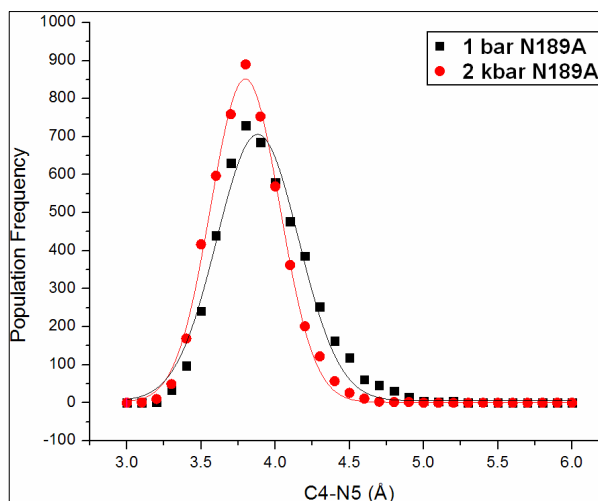
A Wilcoxon rank-sum (RS) and Kolmogorov-Smirnov (KS) test have been performed on the distributions from the N189A simulations, as were done in Section 4.1.2 for the wild-type. The results are shown in Table 4.7. The wild-type results between 1 bar and 2 kbar are shown for comparison.

| Comparison | p (RS) | p (KS) | Effect Size |
|----------------------------|----------|----------|-------------|
| WT 1 bar – WT 2 kbar | <0.001 | <0.001 | 0.68 |
| N189A 1 bar – N189A 2 kbar | <0.001 | <0.001 | 0.61 |

Table 4.7: Calculations of p using the Wilcoxon rank-sum (RS) and the Kolmogorov-Smirnov(KS) tests to compare the effect of pressure on the distributions of donor-acceptor distance taken from the WT and N189A MR. A measure of significance is given by the effect size.

The RS and KS tests indicate that the distributions and medians for the N189A simulations are different at the high and low pressure. The significance of these differences, however (shown by the effect size) is less than the wild-type simulations. Figure 4.25, suggests that the mutation has restricted the availability of substrate-cofactor configurations that have the highest donor-acceptor distances – thus the increase in pressure does not have as much of a significant effect on the distribution for the mutant as for the wild-type. Figure 4.26 shows the Gaussian distribution of distances from the MR_N189A simulations.

Figure 4.26: Figure showing the distribution of donor acceptor distances from the mutated form of MR at 1 bar (black) and 2 kbar (red). Both distributions are fitted to a Gaussian



Referring back to Figure 4.4 in Section 4.1.2 allows a comparison between the wild-type and mutant distributions of donor-acceptor distances. The centres of the Gaussian curve

from Figure 4.26 are located at 3.88 Å at 1 bar and 3.80 Å at 2 kbar. The width of the curve decreases from 0.55 Å at 1 bar to 0.46 Å at 2 kbar. There is less of a shift in the distribution for the mutant than the wild-type. Not only is the average distance at low pressure shorter (3.88 Å compared to 3.93 Å); the average at high pressure is longer (3.77 Å compared to 3.74 Å). It appears that the mutation has diminished the pressure effect, but this is because the mutation does not allow the substrate and cofactor to achieve configurations with as high donor-acceptor distances as in wild-type MR. Nevertheless, Figure 4.26 still shows that the reaction coordinate is squeezed slightly by the pressure.

4.4.3 Overlap of Nicotinamide and Isoalloxazine

The overlap between the nicotinamide ring and the isoalloxazine ring can be shown quantitatively using a dihedral angle as shown in Figure 4.27. (Pudney et al., 2007)

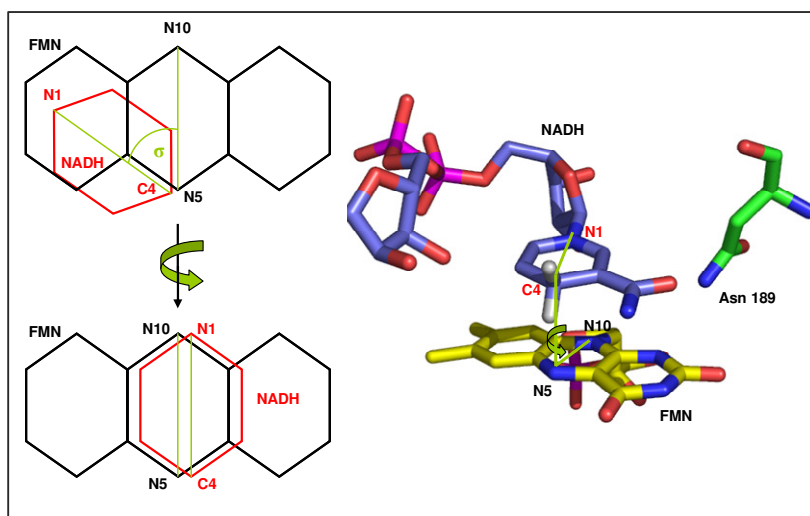


Figure 4.27: Figure showing the overlap between the nicotinamide and isoalloxazine rings as θ : the dihedral angle between the N1 and C4 atoms of NADH, along with the N5 and N10 atoms of FMN

A lower dihedral angle indicates a better overlap of the substrate and cofactor.

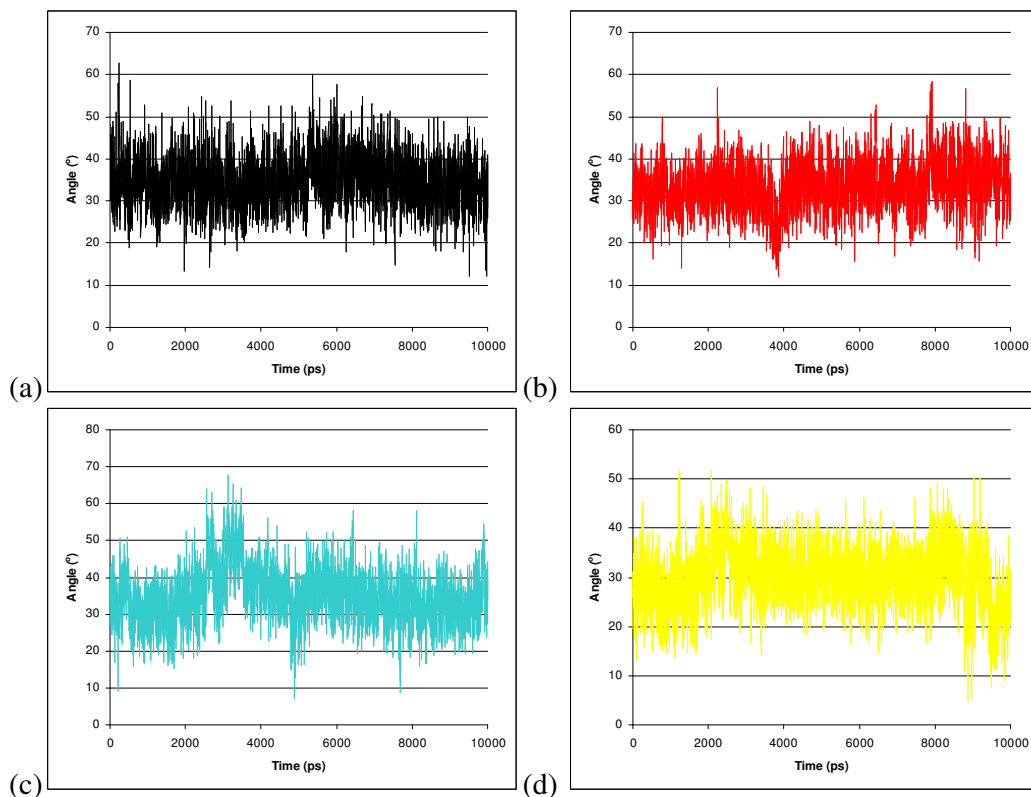


Figure 4.28: Figure showing how the N1-C4-N5-N10 dihedral varies across the 10 ns trajectory at (a) 1 bar_WT, (b) 2 kbar_WT, (c) 1kbar_N189A and (d) 2 kbar_N189A

Figure 4.28 shows how the dihedral angle fluctuates with time during each of the wild-type and mutant simulations at high and low pressures. Table 4.8 gives the averages from the data in Figure 4.28.

| Simulation | 1 bar WT | 2 kbar WT | 1 bar N189A | 2 kbar N189A |
|-------------------------------|-------------|--------------|----------------|-----------------|
| Average N1-C4-N5-N10 (degree) | 34.75 | 33.40 | 34.91 | 30.07 |
| Standard Deviation | 5.99 | 5.71 | 7.35 | 6.14 |

Table 4.8: Average values for the dihedral between the N1 and C4 atom of NADH and the N5 and N10 atoms of FMN. Averages were taken from 10 ns production trajectory of wild-type and mutant MR at 1 bar and 2 kbar

The values shown in Table 4.8 seem to indicate that only the combined pressure and mutation effect causes an increase in overlap of the rings. However this is inconsistent with the prediction from the experimental work, which suggested that the pressure should

decrease the relative population of configurations with better overlap. Table 4.9 shows the distribution of the angles. This highlights that the number of configurations with increased overlap for the mutant at high pressure is almost 3 times more than any of the other simulations.

| Simulation | 1 bar WT | 2 kbar WT | 1 bar N189A | 2 kbar N189A |
|------------|-------------|--------------|----------------|-----------------|
| < 25 ° | 226 | 324 | 383 | 1025 |
| 25 °– 40 ° | 3870 | 4080 | 3495 | 3729 |
| > 40 ° | 904 | 596 | 1122 | 246 |

Table 4.9: *Number of configurations within a given range of angles to represent differing degrees of nicotinamide-isoalloxazine overlap. 5000 frames were counted across the 10 ns trajectories for wild-type and mutant at low and high pressure*

4.4.5 Mutant MR Summary

MD simulations were performed on MR_N189A. These simulations showed a stable RMSD for the entire production trajectory and the analysis of the global protein revealed similar insight to the wild-type simulations. The donor-acceptor distance was analysed using the same procedure as for the wild-type. Although a decrease is observed, along with a similar shift in distribution of distances, this is not as profound as for the wild-type.

The purpose of the study into this mutation at high pressure was to build on some previous experimental and computational work. However, these simulations were not consistent with the experimental conclusions. The increase in overlap of substrate and cofactor at atmospheric pressure as a result of the mutation was not observed. It was observed at high pressure, but this conflicts with the experimental prediction, since the relative population of configurations with better overlap should decrease at higher pressures.

4.5 CONCLUSIONS

This chapter focuses on the giving atomistic scale detail of the pressure effect. The first step was to analyse the distance between the donor atom on the substrate and the acceptor atom on the cofactor that take part in the hydride transfer reaction. A decrease in the average distance is observed with pressure, confirming the prediction from experimental studies (Hay et al., 2007). Analysis of the distribution of distances allows the explanation of the decrease: the pressure offsets the equilibrium towards shorter donor-acceptor distances (Hay et al., 2009a).

It is suggested that the reason for this shift in equilibrium is that the nicotinamide does not have as much conformational space to fluctuate in at higher pressure – that the pressure closes off a region of space to the nicotinamide. This is explored further with 2D-RMSDs and PCAs (Section 4.1.4). A region of space accessible to the nicotinamide at low pressure, but not at high pressure was identified. The analysis is then expanded to the active site residues. IED identified two residues that are correlated with the nicotinamide in a mode motion which is more prevalent at 1 bar. It is suggested that a fixed configuration of these residues at high pressure would close off the region of space for the nicotinamide and diminish this mode of motion that moves the donor away from the acceptor. These residues are Tyr72 and Trp106. Trp106 is most likely to be involved, since it is very close to the region of space that the nicotinamide does not access at high pressure.

It is difficult to correlate the configurations of the residues with the donor-acceptor distance. It is likely that there is a combined effect from these two residues, along with one

or two more. One such residue could be Phe246. The simulation at 1.5 kbar highlights the potential importance of this residue to the pressure effect. The first half of the simulation follows the trend with pressure, in terms of the donor-acceptor distance. At this point though, Phe246 shifts and remains in a different configuration for the remainder of the simulation. At the same stage of the simulation donor-acceptor distance rises, suggesting that the previous configuration of Phe246 was holding the substrate in place. (See Section 4.1.3)

An additional active site residue considered was analysed in an attempt to verify some experimental observations. MD simulations were carried out on a mutated MR – N189A, across the same pressure range. The simulations were stable, but the difference in average donor-acceptor distances was not as pronounced as for wild-type MR. This is perhaps because the mutation induces multiple reactive configurations (Pudney et al., 2007) (See Section 1.2.4 for more details). The removal of the hydrogen bond would allow the nicotinamide to move more freely and in other dimensions. Therefore the pressure effect of restricting the movement in one dimension would not be as significant.

Alongside the active site analysis, the global effect of pressure was considered. The lowest frequency normal mode of the protein represented a motion that shifted a domain across the active site. This motion was less prevalent at high pressure. Analysis of the hinges residues of this domain identified Val108. This residue is located close to the active site, behind Trp106 and has two different configurations at high and low pressure that seem to have an impact on Trp106, which in turn impacts on the nicotinamide. This gives further

credence to the suggestion that Trp106 is involved in the high pressure configuration of the active site and therefore possibly part of a tunneling ready configuration.

Chapter 5

QM/MM Studies of the Hydride Transfer Step Catalysed by Morphinone Reductase

PREFACE

The aim of this chapter is to study how hydrostatic pressure affects the energetics of the hydride transfer step in the reductive half-reaction in MR. This step has been studied extensively, both experimentally and computationally, though the pressure effect has only been studied experimentally (Hay et al., 2007). The initial analysis of how the pressure affects the donor-acceptor distance on an atomistic scale suggests that the pressure offsets the equilibrium of substrate-cofactor configurations to sample shorter donor-acceptor distances more frequently; which may cause a compression of the reaction barrier (Hay et al., 2009a).

In order to fully understand how the pressure affects the enzyme function, it is necessary to study the reaction catalysed by MR. The breaking and forming of bonds cannot be studied using molecular mechanics (MM), hence a quantum mechanical (QM) approach is necessary. It is also necessary to include the whole enzyme in the calculation, since the pressure effect seems to act both in the active site and on a global scale. It is not possible to include the entire enzyme in a QM approach. A combined QM/MM method is therefore used, to include the entire enzyme and allow the hydride transfer to take place.

5.1 BENCHMARKING

The first stage of the QM/MM study is to benchmark the method that will be used. Gaussian (M. J. Frisch, 2003) is used to perform all calculations. The ONIOM method as implemented in Gaussian 03 (G03) is used to perform the QM/MM calculations. DFT is chosen to represent the QM region, although two different functionals are tested – the popular B3LYP functional and the BH&H functional which has been successful in the modelling of π -stacking interactions (Waller et al., 2006). Three different basis sets are tested with each functional to assess how higher basis sets improve the accuracy of the calculations for this particular system. The energies reported in this chapter are relative electronic energies obtained by a mechanical embedding scheme unless otherwise specified

5.1.1 Gas Phase Calculations

Initially, gas phase calculations were performed in G03. The simplified model used for these calculations included the nicotinamide ring of NADH and the isoalloxazine ring of FMN: 51 atoms in total. The structures are shown in Figure 5.1.

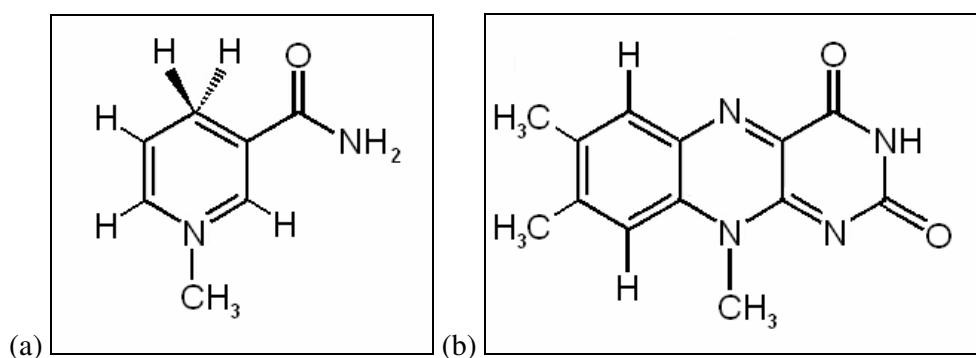


Figure 5.1: A simplified structure of the active site of MR. (a) shows the nicotinamide ring of the substrate NADH; (b) shows the isoalloxazine ring of the FMN cofactor

The geometry of this system was optimised in six different calculations. Three used the BH&H functional, three used B3LYP. For each functional there were 3 different basis sets used: 6-31G*, 6-31+G* and 6-311++G**. The optimised geometries, using the lowest basis set (6-31G*) are shown in Figure 5.2.

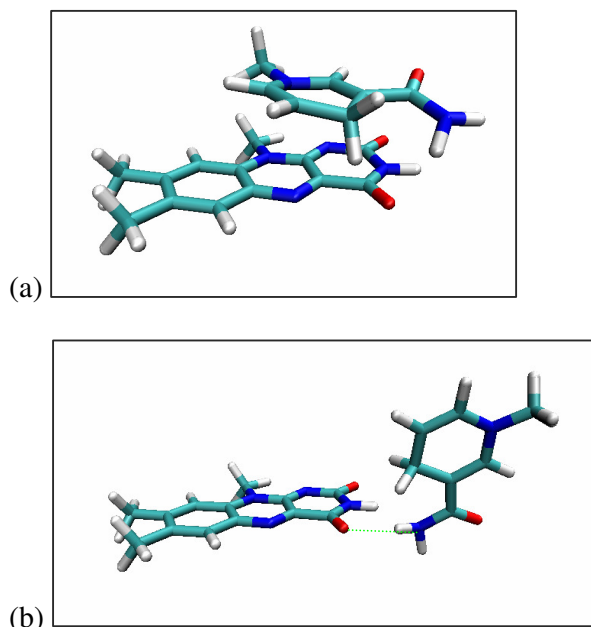


Figure 5.2: The optimised geometries of the simplified active site gas phase calculations. (a) shows the geometry optimised using the BH&H method with 6-31G* basis set; (b) shows the geometry optimised using the B3LYP method with 6-31G* basis set.

It can be seen clearly in Figure 5.2(b) that B3LYP is not a suitable method for optimising the geometry of the substrate-cofactor configuration. Rather than the π -stacking forming a stabilising interaction between the two aromatic rings, there is repulsion. A hydrogen bond is formed between the N2 and O4 atoms, on the nicotinamide and isoalloxazine respectively, (illustrated by the green dotted line on Figure 5.2(b)) and the nicotinamide ‘flips’ over. This is observed in all three of the QM calculations using B3LYP – an increased basis set has no effect.

The geometries of the BH&H calculations were optimised successfully and a frequency calculation was performed to confirm that there were no imaginary frequencies and that the optimised geometry represented a true minimum. Potential energy scans were then

performed and are shown in Figure 5.3. The transferring hydride, attached to the C4 of the nicotinamide ring was moved closer to the N5 atom of the isoalloxazine ring, in 0.1 Å steps, using a distance restraint between the hydrogen and nitrogen atoms. After each step, the geometry was optimised and the energy calculated.

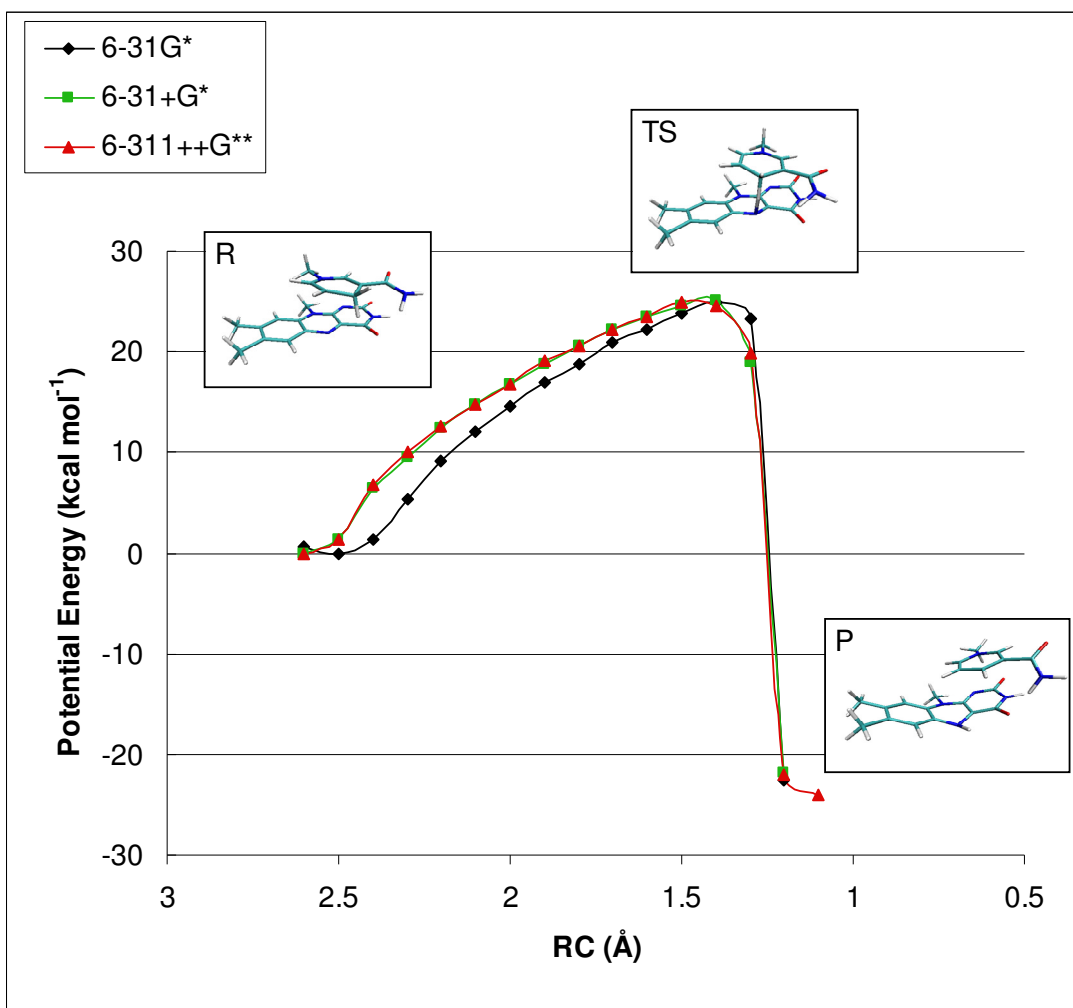


Figure 5.3: Potential Energy Scan for the gas phase QM calculations using the BH&H DFT functional with three different basis sets: 6-31G* (black), 6-31+G* (green) and 6-311++G** (red). The optimised geometry of the 6-31G* at the reactant (R), transition state (TS) and product (P) are also shown. The reactant coordinate is given in Å as the distance of the forming bond

The activation energy is similar for each of the calculations using the BH&H functional (~25 kcal mol⁻¹). There is a problem with the cofactor geometry after the hydride was transferred from the nicotinamide to the isoalloxazine ring. The isoalloxazine ring bends,

as shown in Figure 5.3 and the nicotinamide aligns over the third ring of the isoalloxazine. This configuration for a reduced isoalloxazine ring is not unheard for reduced flavins, but it is unlikely to occur in MR due to the stabilization of the protein environment.

Thus far the benchmarking using a simplified active site structure in gas phase calculation has shown that BH&H models the geometry of π -stacking better than B3LYP. It also suggests that the use of a higher basis set does not increase the accuracy of the calculation significantly. However, the lack of solvent and protein environment in the gas phase leads to strange geometries. The benchmarking is therefore extended to a QM/MM method.

5.1.2 QM/MM Benchmarking

The ONIOM approach applies an older version of AMBER force field (ff96) for the MM region, incompatible with the force field version (AMBER ff03) applied in the original MD simulations. Hence a 500 ps MD simulation was performed with FF96 to re-equilibrate the system. A random frame was chosen from the re-equilibrated trajectory at 1 bar. The QM region within this frame was optimised using the same DFT methods and basis sets as the gas phase calculations (BH&H/B3LYP; 6-31G*/6-31+G*/6-311++G**), the MM region was optimised using AMBER ff96, and the boundary between the QM and MM region was treated by adding link atoms. (See Methodology, Section 2.2.4.2 for more details on the QM/MM setup in ONIOM). The QM region consisted of 44 atoms in total – 16 atoms representing the nicotinamide ring and 36 atoms representing the isoalloxazine ring (Figure 2.5 in the Methodology Section illustrates this). The boundary between the QM and MM region was treated using the link atom approach.

Each of the optimizations was successful in finding a minimised structure. Unlike the gas phase calculations, the B3LYP optimizations did not result in the ‘flipping over’ of the nicotinamide (see Figure 5.2). The geometries of the optimised structures in each case were reasonable. Frequency calculations were run to characterise the stationary points as true minima. The lowest frequency from each calculation is given in Table 5.1.

| DFT: | BH&H | | | B3LYP | | |
|---------------------------|-----------------|---------|------------|--------------|---------|------------|
| B.S.: | 6-31G* | 6-31+G* | 6-311++G** | 6-31G* | 6-31+G* | 6-311++G** |
| Freq. (cm ⁻¹) | 4.1328 | 7.4913 | 6.0341 | 12.3532 | 6.0293 | 8.8383 |

Table 5.1: The lowest vibrational frequencies calculated by Gaussian 03 from optimised geometries using 2 different DFT methods (BH&H and B3LYP) and 3 different basis sets for each method: 6-31G*, 6-31+G* and 6-311++G**.

Table 5.1 indicates that there were no imaginary frequencies calculated for the frames, confirming that the optimised geometry is a true minimum. The hydride transfer reaction was then forced to proceed, in the same manner as for the gas phase calculations. A distance restraint was placed between the hydrogen atom of the nicotinamide and nitrogen atom of the isoalloxazine with the distance being decreased by 0.1 Å at each step. The energy was calculated at each step and is shown in the potential energy scan in Figure 5.4.

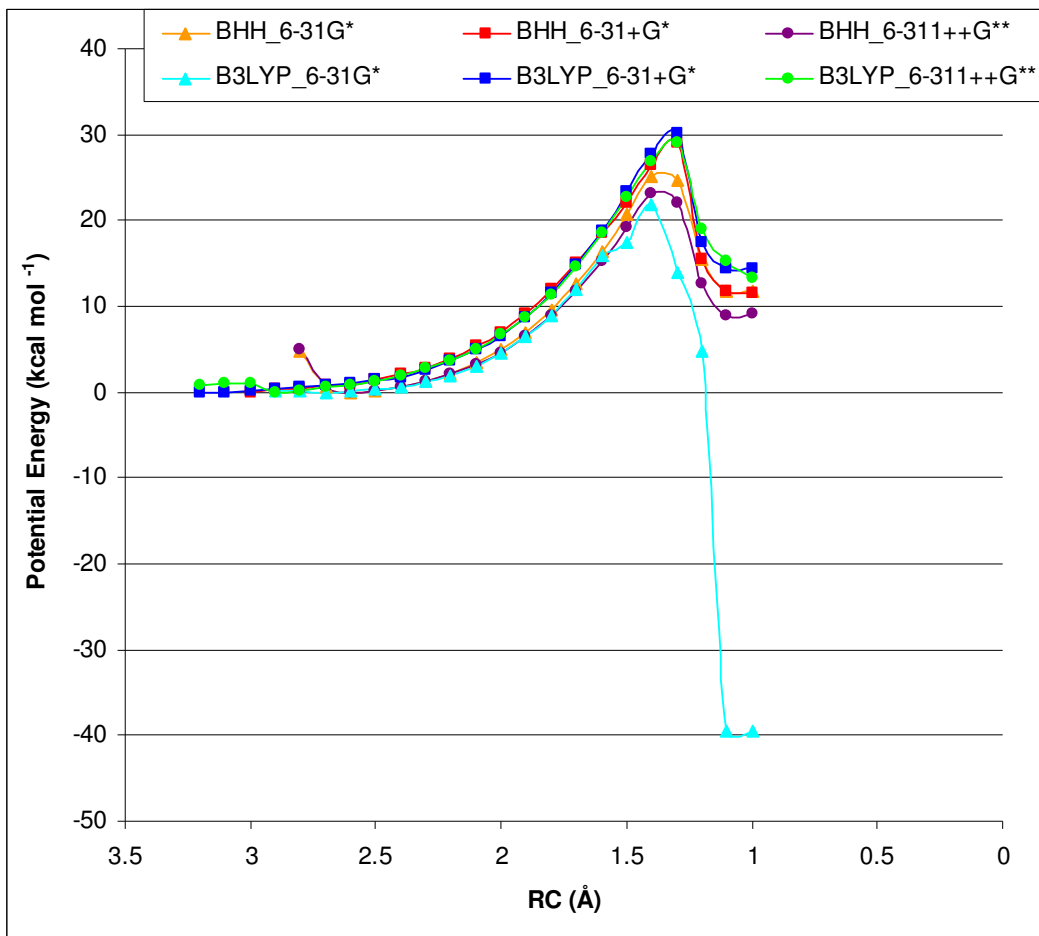


Figure 5.4: Potential energy scans from the benchmark QM/MM calculations performed in Gaussian 03. Two different DFT methods (BH&H and B3LYP) were used and 3 different basis sets for each method: 6-31G*, 6-31+G* and 6-311++G** used in the calculations. The reaction coordinate (RC) is the bond forming distance (between the N5 of the isoalloxazine ring and the transferring hydride). The key at the top of the Figure indicates the method and basis set for each of the scans.

Of the six calculations, the only scan to show an exothermic reaction is the B3LYP scan using the 6-31G* basis set. This basis set is not sufficient for a hydride transfer reaction, since it does not include any diffuse functions. It is interesting however, that the BH&H scan using the same basis set gives a scan that appears much more similar to the more accurate basis sets. The activation energy of the six calculations is shown in Table 5.2.

| DFT: | BH&H | | | B3LYP | | |
|----------------------------------|-----------------|---------|------------|--------------|---------|------------|
| B.S.: | 6-31G* | 6-31+G* | 6-311++G** | 6-31G* | 6-31+G* | 6-311++G** |
| Energy (kcal mol ⁻¹) | 25.04 | 29.02 | 23.15 | 21.81 | 30.20 | 29.11 |

Table 5.2: The potential energy taken from the potential energy scans in Figure 5.4. The table shows the 2 different DFT methods (BH&H and B3LYP) and 3 different basis sets for each method: 6-31G*, 6-31+G* and 6-311++G** used in the calculations

Referring back to the study on the BH&H DFT method by Waller *et al.* (Waller et al., 2006), BH&H is described as being suitable for QM calculations involving π -stacking interactions, due to a fortuitous cancellation of errors. It is expected that BH&H will model the geometry correctly, but the B3LYP method is still the more popular choice for calculating accurate energies. Table 5.2 illustrates that BH&H with a 6-31+G* basis set closely replicates the energies obtained using B3LYP with the same basis set and with a higher basis set. This is in close agreement with the findings by Waller *et al.* The gas-phase calculations highlighted the advantage of BH&H over B3LYP for geometry optimisation of a π -stacking configuration. Therefore, BH&H with the 6-31+G* basis set is chosen as the method for QM/MM calculations

5.2 QM/MM CALCULATIONS AT HIGH AND LOW PRESSURES

To demonstrate how an increase in atmospheric pressure affects the rate of the hydride transfer during the reductive half reaction of MR with NADH, the method benchmarked in Section 5.1 can be used. However, an important aspect of such a study is the choice of structures. As discussed in Chapter 4, the effect that pressure has on MR cannot be attributed to just one residue – there are at least three active site residues that are

intermittently affected by the increase in pressure. It is suggested that a combination of these residues results in the reduction of the conformational space available for the substrate, forcing the shorter donor-acceptor distances. Therefore it is necessary to use structures in the QM/MM calculations that have these residues in the high pressure or low pressure configurations.

5.2.1 Representative Structures

The structures used in the QM/MM calculations were chosen from MD trajectories which had been equilibrated using the ff96 AMBER force field, to be consistent with the force field implemented by the ONIOM method in G03. Each of these MD simulations started from representative structures at 1 bar and 2 kbar. The structures were minimised and equilibrated with force restraints placed on the substrate and cofactor to retain the configuration of the starting structure. Following this, unrestrained constant pressure MD (at the respective pressures) was performed for 500 ps and the structures for the QM/MM were chosen from these trajectories.

The initial structures at the different pressures had configurations to be representative of the pressure; that is there was less conformational available space available to the nicotinamide in the 2 kbar structure, due to the configurations of three residues: Tyr72, Trp106 and Phe246. These residues were deemed to be significant in Chapter 4. The representative structures are illustrated in Figure 5.5.

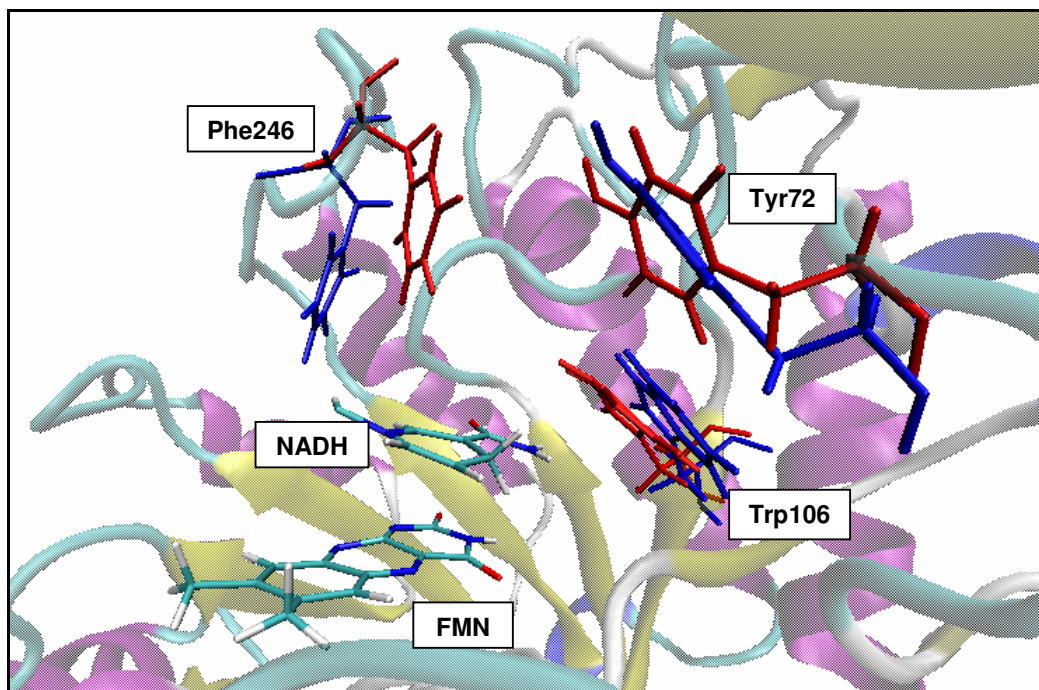


Figure 5.5: Representation of the active site of MR in the representative structures from 1 bar and 2 kbar. The protein is shown in the background, represented by its secondary structure. The nicotinamide (NADH) and isoalloxazine (FMN) ring are shown coloured by atom (carbon – cyan, hydrogen – white, oxygen – red and nitrogen – blue). Also shown are the relative positions of active site residues Tyr72, Trp106 and Phe246 at 1 bar (blue) and 2 kbar (red).

An RMSD calculation was performed on the 500 ps trajectories, using the representative starting structure as a reference. The RMSDs were calculated for the heavy atoms of the nicotinamide and isoalloxazine ring, along with the heavy atoms of Tyr72, Trp106 and Phe246. The frames with the lowest RMSDs were chosen as the frames to use in the QM/MM calculations. Although these frames are taken from an equilibrated and unrestrained MD simulation, this process ensures that the geometries of the frames used in the QM/MM reflect the protein environment at the respective pressures, since a difference in atmospheric pressure cannot be explicitly simulated in a QM calculation.

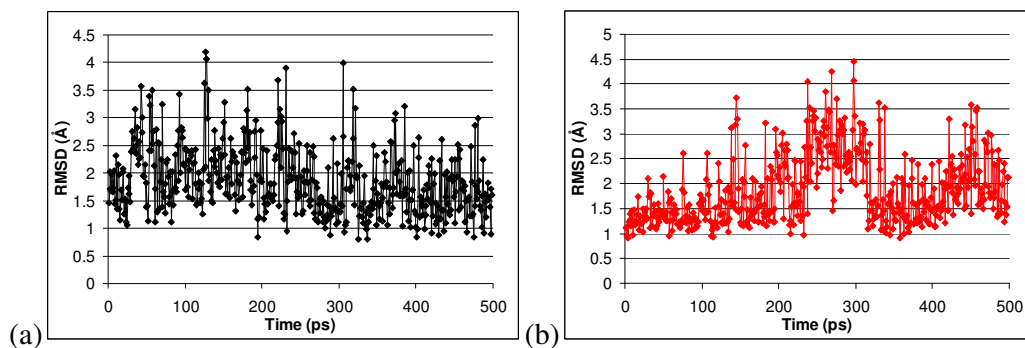


Figure 5.6: The RMSDs of the active site residues Tyr72, Trp106 and Phe246 during the newly equilibrated 500 ps trajectories at 1bar (a) – black and 2kbar (b) – red. The RMSD is with respect to the representative structure at the respective pressures.

20 frames were chosen from each trajectory with an RMSD value (Figure 5.6) of less than 1.1 Å. Each of these frames was then set up for QM/MM calculations using the procedure described in Section 2.2.4.2 of this thesis.

The frames chosen from each trajectory have an active site that is representative of the low and high pressure configurations observed in Chapter 4. It is important to note that these frames are not representative of the average configuration across the entire trajectories at each pressure. The aim of the QM/MM study is to investigate how a particular arrangement of residues within the active site, which restricts the conformational space available to the nicotinamide, may affect the energetics of the hydride transfer reaction. The procedure for choosing configurations results in a bias towards those starting structures with configurations which sample larger donor-acceptor distances for the 1 bar QM/MM than for the 2 kbar QM/MM. This bias, however, does not detract from the validity of the study, since a fundamental property of the configurations accessible at low pressure, but not at high pressure, is a larger donor-acceptor distance.

5.2.2 Geometry Optimisation

The first stage of the optimisation in Gaussian 03 requests a tight convergence. This is followed by another step requesting a very tight convergence. An optimization requests that four criteria fall below defined tolerance values for the calculation to be considered converged. These criteria are the maximum force acting on each atom, the RMS force, the maximum displacement of each atom between optimization steps and the RMS displacement. The tolerances for a tight convergence are 1.5×10^{-5} , 1.0×10^{-5} , 6.0×10^{-5} and 4.0×10^{-5} respectively. For a very tight convergence, they are 5.0×10^{-8} , 1.0×10^{-6} , 2.0×10^{-7} and 1.33×10^{-7} respectively. In all of the cases where a tight convergence of the geometry was achieved, the very tight convergence was also successful.

Following the optimisation, the vibrational frequencies are calculated for the minimised structure. This allows the stationary points to be characterized. At this stage of the calculation, all the frequencies should be positive to verify that the stationary point is a local minimum, although generally negative frequencies smaller than -50 can be characterized as minima. Although 20 frames were chosen at each pressure, only 14 of these at each pressure minimised into a geometry that could be characterised as a local minimum. Table 5.3 summarises the geometry optimisation procedure for all of the frames taken from the unrestrained trajectories.

| Pressure | Frame | Frequency (cm ⁻¹) | Pressure | Frame | Frequency (cm ⁻¹) |
|----------|----------|-------------------------------|----------|-------|-------------------------------|
| 1 bar | F025 | 6.0146 | 2 kbar | F001 | 11.6029 |
| | F061 | - | | F002 | -7.3208 |
| | F194 | -14.8309 | | F004 | 8.9382 |
| | F232 | 13.7105 | | F011 | 8.8655 |
| | F282 | -14.0448 | | F018 | -17.0243 |
| | F289 | 6.6683 | | F033 | 13.3708 |
| | F299 | 8.5215 | | F041 | 12.6894 |
| | F325 | 6.1577 | | F058 | -12.5671 |
| | F331 | 4.0879 | | F062 | 14.9725 |
| | F336 | 11.7706 | | F083 | 12.5811 |
| | F337 | 8.1194 | | F093 | 15.9711 |
| | F363 | 7.0633 | | F112 | 8.9178 |
| | F393 | 12.3405 | | F115 | -8.3619 |
| | F401 | 8.2251 | | F120 | 11.3219 |
| F402 | -8.1558 | F215 | 10.3447 | | |
| F425 | 10.6125 | F233 | 8.8649 | | |
| F430 | 8.8677 | F316 | -7.3731 | | |
| F475 | - | F333 | 12.6947 | | |
| F488 | 2.3118 | F358 | 7.9708 | | |
| F497 | -37.3877 | F386 | - | | |

Table 5.3: The frames chosen for QM/MM from the RMSD shown in Figure 5.6. Three frames (1barF061, 1barF475 and 2kbarF386) did not optimise due to the Gaussian program incorrectly placing a bond between two atoms that should not be bonded in the starting structure. All of the frames achieved a tight and a very tight convergence with the exception of 1 bar F061, 1 bar F475 and 2 kbar F386. For the frames that did optimise, the lowest vibrational frequency is given and highlighted in green for true local minima or red for stationary points that are not local minima.

For each pressure, there are 14 frames at each pressure that achieved a very tight optimisation, yielding a positive value as the first vibrational frequency. For each of the frames that gave a negative value as the first vibrational frequency, none of these values were more negative than -50 cm⁻¹ and the next frequencies were positive. This indicates that the majority of the simulations were optimised successfully to a local minimum. The next stage is to study the energetics of the hydride transfer reaction by shifting the hydride from the donor carbon atom on the nicotinamide to the acceptor nitrogen atom on the

isoalloxazine, with energy optimisations performed intermittently along the reaction coordinate.

5.2.3 Potential Energy Scans

Potential energy scans of the hydride transfer from the C4 donor atom on the nicotinamide to the N5 acceptor atom on the isoalloxazine ring were performed as described in Section 5.1.2. The distances of transfer differed for each frame. Ten frames from each pressure are shown in Figure 5.7. The position of the nicotinamide is shown with respect to the isoalloxazine. It can be seen that at high pressure, the configuration minimises with the substrate and cofactor closer together.

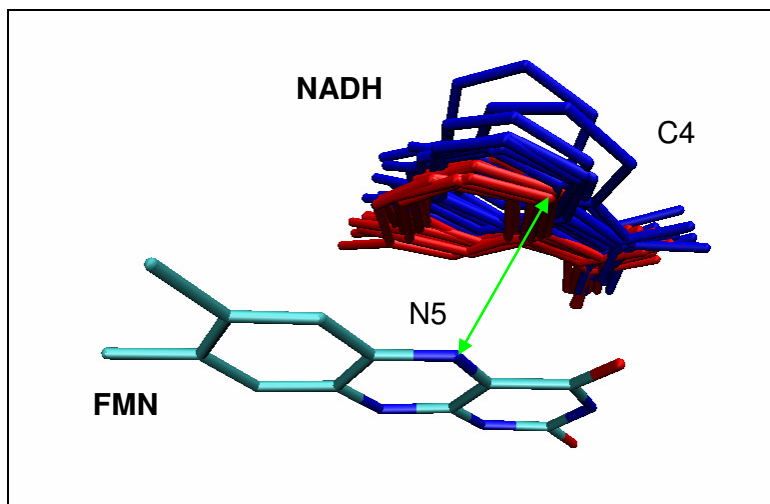


Figure 5.7: Figure to show the minimised geometry of the 20 structures used in the QM/MM calculations. The position of the nicotinamide ring (labelled NADH and coloured blue for the 1bar frames and red for the 2 kbar frames) is shown relative to the isoalloxazine ring (labelled FMN and coloured by atom). The green arrow shows the donor-acceptor distance. Only heavy atoms are shown.

The tables on the following pages (Table 5.4 and Table 5.5) give details of the ten scans at each pressure. The geometry of the nicotinamide and isoalloxazine rings is illustrated at both the reactant and TS, alongside the donor-acceptor distance and the bond-forming distance, again at both the reactant and TS. Also given in Tables 5.4 and 5.5 is the barrier height – that is, the activation energy of hydride transfer from each configuration. It is possible therefore to compare this at different pressures, and for different donor-acceptor distances.

QM/MM Studies of the Hydride Transfer Step Catalysed by MR

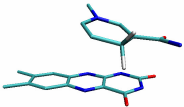
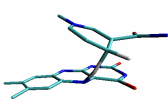
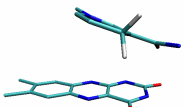
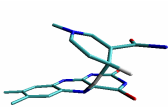
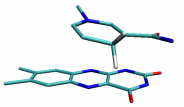
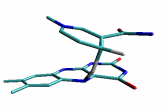
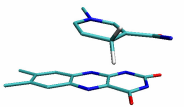
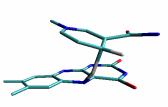
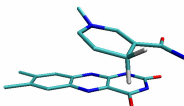
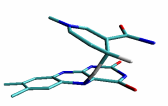
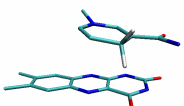
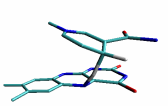
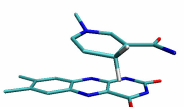
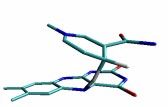
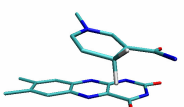
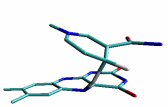
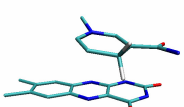
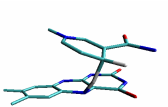
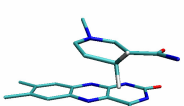
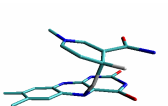
| Frame | R N-H (Å) | R C-N (Å) | Reactant Geometry | T.S. N-H (Å) | T.S. C-N (Å) | T.S. Geometry | Barrier Height (kcal mol ⁻¹) |
|---------------|-----------------|-----------------|---|--------------------|--------------------|---|--|
| 1 bar F025 | 3.67 | 4.09 |  | 1.20 | 2.62 |  | 37.27 |
| 1 bar F232 | 4.64 | 4.96 |  | 1.20 | 2.61 |  | 38.41 |
| 1 bar F289 | 3.06 | 3.56 |  | 1.18 | 2.56 |  | 25.61 |
| 1 bar F299 | 3.09 | 3.64 |  | 1.18 | 2.65 |  | 29.97 |
| 1 bar F325 | 3.95 | 4.36 |  | 1.24 | 2.59 |  | 36.05 |
| 1 bar F331 | 3.42 | 3.86 |  | 1.22 | 2.56 |  | 33.14 |
| 1 bar F336 | 3.30 | 3.86 |  | 1.22 | 2.56 |  | 31.06 |
| 1 bar F363 | 3.51 | 3.97 |  | 1.20 | 2.60 |  | 31.63 |
| 1 bar F401 | 3.42 | 3.82 |  | 1.22 | 2.60 |  | 29.94 |
| 1 bar F430 | 3.39 | 3.78 |  | 1.22 | 2.58 |  | 30.00 |

Table 5.4: Table showing the distance between the forming bond (R N-H), the donor-acceptor distance (R C-N) and the geometry at the reactant, followed by the distance between the forming bond (T.S. N-H), the donor-acceptor distance (T.S. C-N) and the geometry at the transition state, as well as the activation potential (barrier height) for the frames from the 1 bar trajectory.

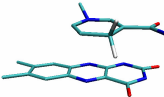
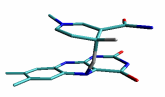
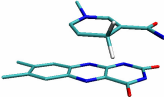
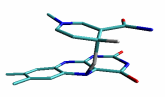
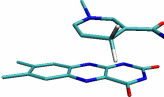
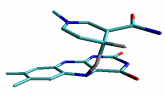
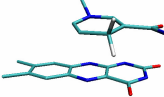
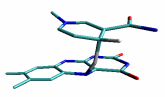
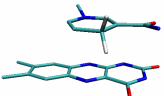
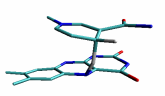
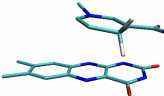
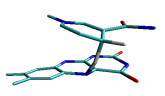
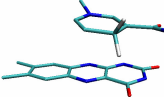
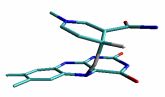
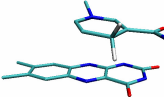
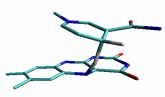
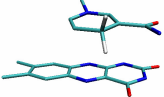
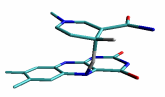
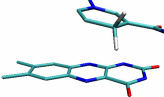
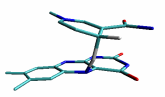
| Frame | R N-H (Å) | R C-N (Å) | Reactant Geometry | T.S. N-H (Å) | T.S. C-N (Å) | T.S. Geometry | Barrier Height (kcal mol ⁻¹) |
|----------------|-----------------|-----------------|---|--------------------|--------------------|---|--|
| 2 kbar F004 | 2.97 | 3.37 |  | 1.22 | 2.50 |  | 30.11 |
| 2 kbar F011 | 2.83 | 3.28 |  | 1.20 | 2.55 |  | 28.71 |
| 2 kbar F033 | 2.92 | 3.35 |  | 1.24 | 2.56 |  | 29.70 |
| 2 kbar F062 | 2.98 | 3.40 |  | 1.22 | 2.56 |  | 29.63 |
| 2 kbar F083 | 2.76 | 3.31 |  | 1.20 | 2.54 |  | 26.94 |
| 2 kbar F112 | 3.28 | 3.72 |  | 1.22 | 2.54 |  | 31.66 |
| 2 kbar F120 | 3.17 | 3.60 |  | 1.20 | 2.54 |  | 31.64 |
| 2 kbar F215 | 3.07 | 3.51 |  | 1.20 | 2.54 |  | 30.22 |
| 2 kbar F233 | 2.81 | 3.37 |  | 1.22 | 2.54 |  | 26.08 |
| 2 kbar F358 | 3.14 | 3.68 |  | 1.20 | 2.56 |  | 26.95 |

Table 5.5: Table showing the distance between the forming bond (R N-H), the donor-acceptor distance (R C-N) and the geometry at the reactant, followed by the distance between the forming bond (T.S. N-H), the donor-acceptor distance (T.S. C-N) and the geometry at the transition state, as well as the activation potential (barrier height) for the frames from the 2 kbar trajectory.

Figure 5.8 illustrates the potential energy scans at high and low pressures. There is a clear reduction in activation energy for the high pressure configurations. The average at 1 bar is 32.30 kcal mol⁻¹, whereas the average at 2 kbar is 29.16 kcal mol⁻¹.

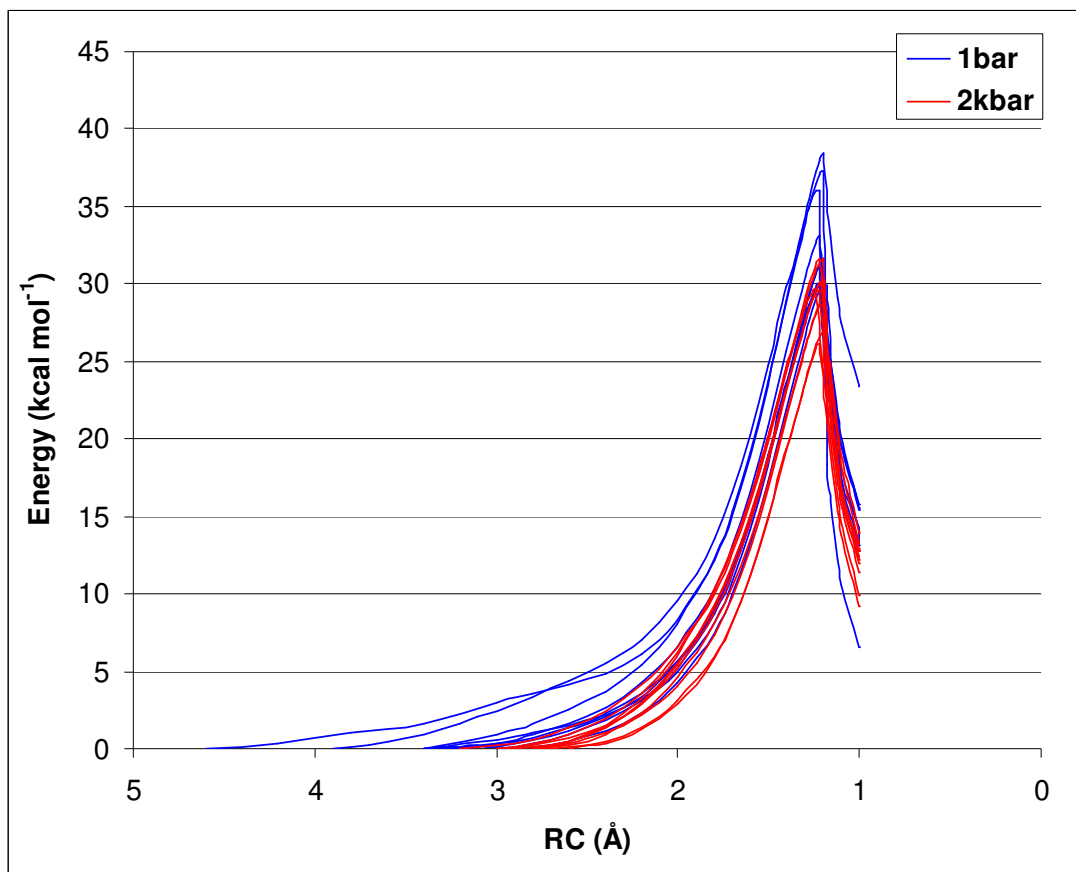


Figure 5.8: Potential energy scans from the QM/MM calculations performed in Gaussian 03, using BH&H with the 6-31+G* basis set. Twenty scans are plotted: ten from the 1 bar trajectory (blue) and ten from the 2 kbar trajectory (red). The reaction coordinate (RC) is the bond forming distance (between the N5 of the isoalloxazine ring and the transferring hydride)

In each frame, the step size for the scans was decreased around the transition state (TS) to 0.02 Å to obtain a smoother curve and to identify the location of the TS. Frequency calculations were performed at the TS to verify that there was only one imaginary frequency, which would correspond to the bond breaking / bond making process. Each of the 20 frames shown in Figure 5.8 had only one imaginary frequency at the TS. These frequencies are listed in Table 5.6. The motion associated with this frequency has been

analysed and in all twenty cases it has been confirmed as the frequency of the bond breaking and forming vibration.

| 1 bar | | 2 kbar | |
|-------|-------------------------------|--------|-------------------------------|
| Frame | Frequency (cm ⁻¹) | Frame | Frequency (cm ⁻¹) |
| F025 | -1383.68 | F004 | -1254.40 |
| F232 | -1407.85 | F011 | -1345.56 |
| F289 | -1228.66 | F033 | -1472.24 |
| F299 | -1146.13 | F062 | -1420.72 |
| F325 | -1389.97 | F083 | -1316.26 |
| F331 | -1418.62 | F113 | -1366.58 |
| F336 | -1388.37 | F120 | -1293.00 |
| F363 | -1378.88 | F215 | -1289.83 |
| F401 | -1447.54 | F233 | -1347.74 |
| F430 | -1438.47 | F358 | -1302.55 |

Table 5.6: The imaginary vibrational frequencies calculated by Gaussian 03 from the structures taken at the TS for the 1 bar scans and the 2 kbar scans shown in Figure 5.8.

The magnitude of the imaginary frequency has been traditionally used as an indicator to infer the width of the potential energy barrier. A smaller imaginary frequency indicates a thinner barrier, which would be associated with a larger tunneling contribution to the reaction. The average imaginary frequency at the TS is 1362.8 cm⁻¹ for the frames at 1 bar, slightly higher than that for the 2kbar frames at 1340.9 cm⁻¹. This would suggest that the barrier becomes thinner as the pressure is increased – an observation that is consistent with the prediction that pressure “squeezes” the width of the barrier. It is noted however, that the range of frequencies at low pressure is much higher (varying from ~1146 cm⁻¹ to ~1447 cm⁻¹) than that at high pressure (varying from ~1254 cm⁻¹ to 1472 cm⁻¹). In general the trend of the magnitude of the imaginary frequency with pressure is indistinct and further analysis of the tunneling with a more refined reaction coordinate is required. This is discussed in Section 5.3.1.

The main observation from the potential energy scans is that the activation energy decreases with an increase in pressure. It is also noted however, that the frames chosen from the 2 kbar trajectory have shorter donor-acceptor distances than the 1 bar frames, and consequently, a shorter distance for the hydride to travel. This is justifiable however, since the pressure offsets the equilibrium of configurations towards those with shorter donor-acceptor distances. This therefore offers evidence as to how high pressure reduces the activation energy, via a shortening of the donor-acceptor distance.

5.3 FURTHER ANALYSIS OF QM/MM

The reduction in activation energy, given by the potential energy scans, at high pressure can be used to infer an increased rate of reaction. However, to calculate the rate of reaction, the ZPEs must be considered. Also, as discussed earlier in this thesis, the hydride transfer reaction in the RHR, catalysed by MR, proceeds with a large hydrogen tunneling contribution. Therefore both the height and the width of the barrier are important in calculating the rate of reaction. Several models have been developed to try to incorporate hydrogen tunneling contributions into rate theory. An attempt to apply one such model (Hay et al., 2010) is described in this section.

5.3.1 Reaction Coordinate

The potential energy scans shown in Figure 5.8 use the distance of the forming bond as the reaction coordinate (RC). This is due to the limit in G03 where the potential energy scan can only be performed with the reaction coordinate defined by one geometrical parameter.

The reaction coordinate can be better defined as the difference between the bond-breaking distance and the bond-forming distance, which enables more refined sampling of the potential energy surface. Converting the RC on the X axes to the new RC makes the potential energy plot smoother before the TS. However, it does cause a problem after this point, since once the bond is formed between the N5 acceptor atom and the transferring hydride, the next step in the scan is to optimise the geometry of the newly formed oxidised substrate and reduced cofactor. The interaction between the substrate and cofactor mediated by the transferring hydride is now broken, thus the optimisation in the next step of the scan shifts the nicotinamide ring back to a low energy conformation, resulting in a sudden change of the length of both the breaking bond and the forming bond. Figures 5.9 and 5.10 illustrate the potential energy scans taken from Figure 5.8, with the RC now represented as the bond-breaking distance minus the bond-forming distance. Five scans from 1 bar are shown in Figure 5.9, with five scans from 2 kbar shown in Figure 5.10. The remaining five scans from each pressure are shown in Appendix F.

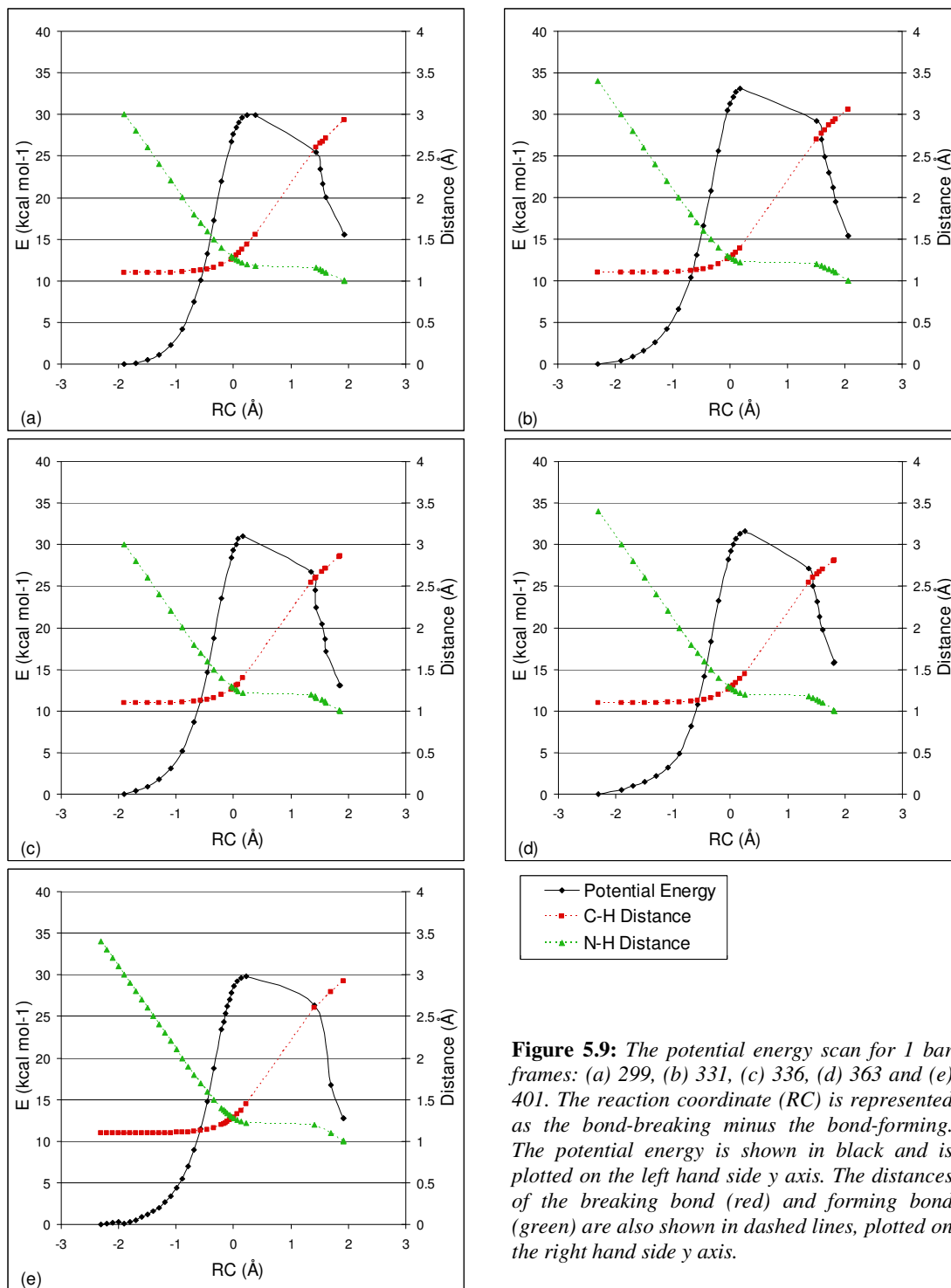


Figure 5.9: The potential energy scan for 1 bar frames: (a) 299, (b) 331, (c) 336, (d) 363 and (e) 401. The reaction coordinate (RC) is represented as the bond-breaking minus the bond-forming. The potential energy is shown in black and is plotted on the left hand side y axis. The distances of the breaking bond (red) and forming bond (green) are also shown in dashed lines, plotted on the right hand side y axis.

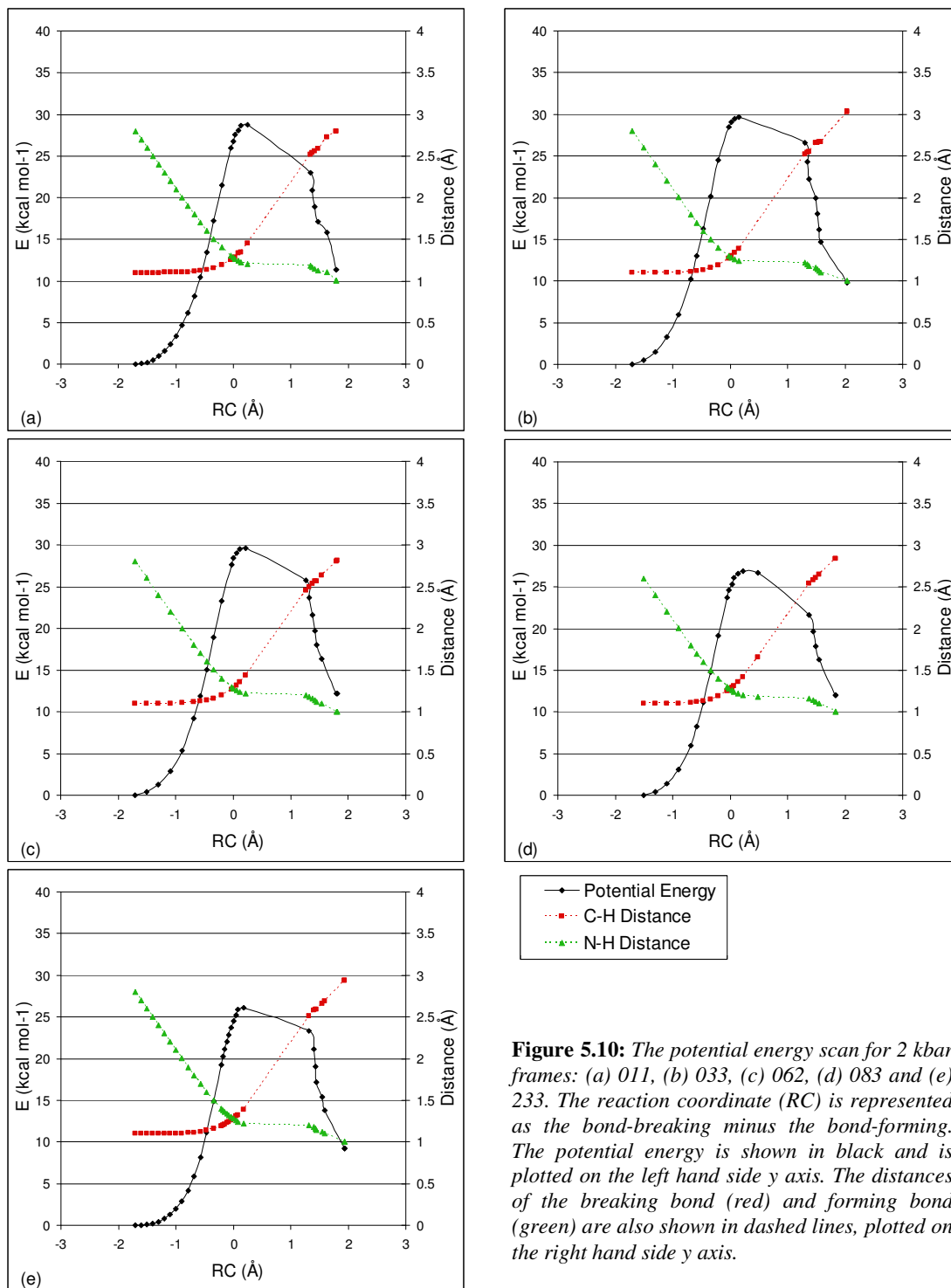


Figure 5.10: The potential energy scan for 2 kbar frames: (a) 011, (b) 033, (c) 062, (d) 083 and (e) 233. The reaction coordinate (RC) is represented as the bond-breaking minus the bond-forming. The potential energy is shown in black and is plotted on the left hand side y axis. The distances of the breaking bond (red) and forming bond (green) are also shown in dashed lines, plotted on the right hand side y axis.

Each of the potential energy scans shown in Figures 5.9 and 5.10 demonstrates the limitation in Gaussian of having the reaction coordinate defined only by one bond – the bond forming. After this bond is formed, the curve is no longer smooth and is clearly an inaccurate representation of the energy scan from this point onwards. However, until the bond breaks, the reaction barrier is very smooth. The main observations to note are that the reaction coordinate at low pressure is typically longer than the high pressure and the activation energy is larger.

The less refined shape of the potential energy barrier immediate after the transition state makes it difficult to calculate the tunneling probability, since a reaction that involves hydrogen tunneling is dependant not only on the height of the barrier, but the width. However it is still possible to estimate the rates and KIEs of each of selected snapshots based on their potential energy scans generated by the QM/MM calculations.

5.3.2 KIE Calculation

The rates of the hydride transfer reaction and their KIEs are calculated using the Wentzel-Kramers-Brillouin (WKB) model (Miller, 1986), as discussed by Hay et al. (Hay et al., 2010). For a reaction that proceeds via a tunneling mechanism, it is necessary to consider the width of the barrier in the rate calculation. However, many reactions occur by a mixture of classical and tunneling mechanism, therefore the overall shape of the barrier, including the height and the width, is important. In the WKB model, the probability of tunneling can be calculated at any given point along the reaction coordinate and used to calculate the tunneling rate. The overall rate is then the sum of the classical rate (calculated

using TST) and the tunneling rate. The rates are calculated for each of the potential energy scans and scaled to account for the different ZPE contributions of H and D. The KIE can then be calculated for each of the scans.

| 1 bar | | 2 kbar | |
|---------|--------|---------|-------|
| Frame | KIE | Frame | KIE |
| F025 | 148.07 | F004 | 16.23 |
| F232 | 3.83 | F011 | 14.27 |
| F289 | 10.36 | F033 | 2.68 |
| F299 | 11.26 | F062 | 11.71 |
| F325 | 13.81 | F083 | 12.35 |
| F331 | 1.54 | F113 | -5.63 |
| F336 | 11.88 | F120 | 0.14 |
| F363 | 12.01 | F215 | -1.89 |
| F401 | 9.87 | F233 | 2.25 |
| F430 | 4.34 | F358 | 46.97 |
| Average | 8.77 | Average | 13.32 |
| S.D. | 4.35 | S.D. | 14.90 |

Table 5.7: The KIEs calculated by the WKB model for the QM/MM calculations using frames from the 1 bar and 2 kbar trajectories. Values shown in red are not used in the average calculation.

Table 5.7 shows the data for each frame along with the averages and standard deviations at each pressure. The data shows an increase in the KIE from 8.77 to 13.32 with a pressure increase. The experimentally measured KIE increases from 4 to 5.2 when the pressure is increased from 1bar to 2kbar. The statistical significance of the increase shown by the results is low; however there is a qualitative agreement with the pressure dependency of the experimental KIE. The WKB model is dependant on the width of the barrier to calculate the tunneling probability. As discussed in Section 5.3.1, the shapes of the barriers used for the calculation are imperfect – the width at the top of the barrier is likely to be inaccurate and will give an imprecise degree of tunneling in the area of the reaction coordinate where tunneling is most likely. Therefore, this can only be considered to be an

estimate of the KIE; nevertheless it is encouraging that this trend reproduces the pressure dependency shown in previous experimental studies.

5.3.3 Frequency Analysis

Much of the experimental and theoretical research on MR in recent years has focussed upon the contentious prediction of a promoting motion. Experimental work on MR showed an increase in the KIE with pressure, with no change in the temperature dependence of the KIE, alongside an increase in the rate (Hay et al., 2007). These observations were accounted for by the presence of a promoting motion, the frequency of which increases with pressure and a decrease in the average donor-acceptor separation. Thus far, the computational work has demonstrated that firstly, the donor-acceptor distance decreases with an increase in pressure, agreeing with the experimental prediction. The rates and KIEs have been calculated and these also show agreement with experiment. This final section of the QM/MM analysis concerns the identification of the promoting motion.

The frequency of the promoting motion is predicted to be in the low frequency region, between 50 and 200 cm^{-1} . Visualisation of the frequencies from the optimised reactant structures identifies a motion, where the nicotinamide bends towards the isoalloxazine, moving the transferring hydride closer to the acceptor N5 atom on the isoalloxazine ring. This motion is illustrated in Figure 5.11

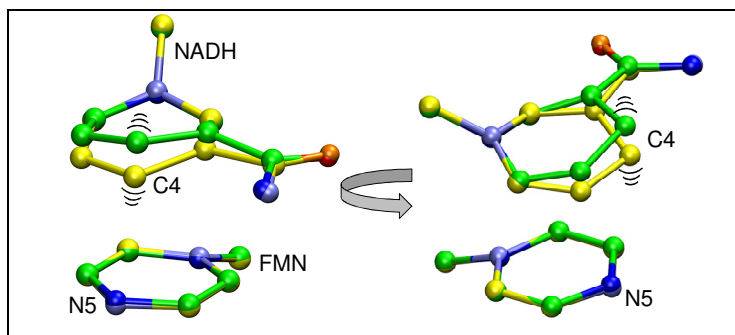


Figure 5.11: Motion represented in the 100 -180 cm^{-1} region of frequencies at the reactant. This motion exists in all of the frames from the QM/MM calculation. Only the heavy atoms of the nicotinamide ring and the central ring or the isoalloxazine are shown (oxygen atom is coloured red, nitrogen atoms are coloured blue and the carbon atoms are yellow/green)

This motion is observed in all of the frames. However, the range of frequencies of this motion is varied for each of the frames at each of the pressures (between 100 and 180 cm^{-1}). This motion is identical to the promoting motion identified by another computational study on the pressure effect on promoting motions in MR (Johannissen, *in press*). There is no apparent trend with pressure.

5.4 CONCLUSIONS

The aim of the QM/MM calculations was to investigate the effect of pressure on the reaction catalysed by MR. Two DFT functionals were tested to assess their suitability for modelling the configuration of the substrate and cofactor. They each tested with 3 different basis sets. The BH&H functional was found to model the π -stacking interaction between the nicotinamide and isoalloxazine rings better than the B3LYP functional. The 6-31+G* basis set was used, since an improved basis set did not improve the accuracy of the calculation – an observation that was consistent with previous studies on the BH&H functional (Waller et al., 2006).

Ten frames from each pressure were chosen for the QM/MM calculations. It was necessary to use frames that had active site configurations representative of the pressure as described in Chapter 4. The high pressure configuration is represented by an active site where the nicotinamide has less conformational space. Using the benchmarked method, these 20 frames were optimised and frequency calculations were used to characterise the stationary points as local minima. Following this, potential energy scans were performed on each frame to allow the calculation of the activation energy.

From the potential energy scans, an increase in pressure can be linked to a decrease in the activation energy. The correlation of barrier decrease and donor-acceptor decrease is also seen at high pressure. Figure 5.11 shows the activation energy plotted against the donor-acceptor distance for each of the frames. Kamerlin *et al.* (Kamerlin et al., 2010) suggest that there is no evidence to suggest that a decrease in the donor-acceptor distance will have an effect on the barrier height. Figure 5.12 provides this evidence and confirms the prediction from Hay *et al.* (Hay et al., 2009a). The plot shows a good correlation and it is inferred that an increase in donor-acceptor separation causes an increase in the activation energy required for the hydride transfer reaction. As discussed in Chapter 4, an increase in pressure causes a decrease in the average donor-acceptor distance; thus the pressure increase will result in an average decrease in the activation energy.

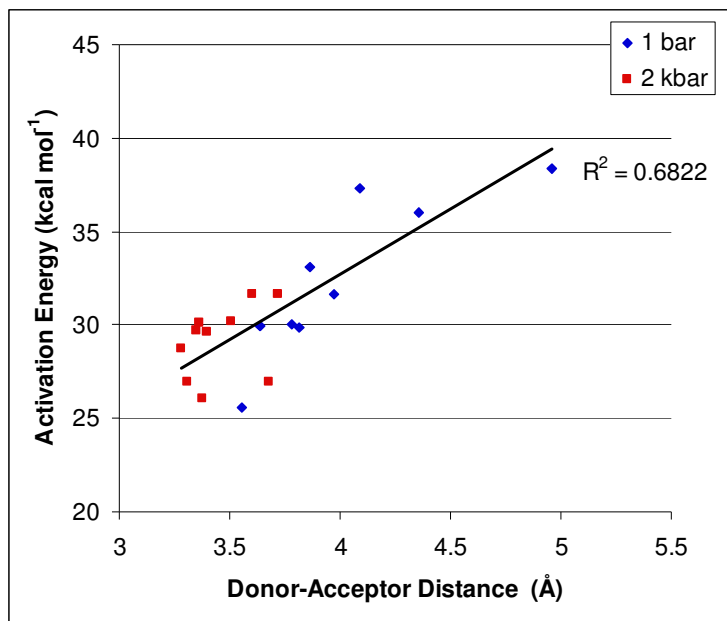


Figure 5.12: Figure showing correlation between donor-acceptor distance and activation energy. 20 frames are shown, with the frames from the 1 bar trajectory represented by blue points and the frames from the 2 kbar trajectory represented by red points. A linear trend line is plotted for all 20 points, with the R^2 value displayed.

Following the analysis of potential energies, the pressure effect on the KIE is studied. An increase in the average of KIEs from 8.77 to 13.32 is observed when the pressure is increased from 1 bar to 2 kbar. It has been noted that the less refined shape of the reaction barriers after the TS makes it difficult to carry out calculations of rates and KIEs and to calculate accurate tunneling probabilities. Work is ongoing to improve the reaction barriers by performing reverse potential energy scans starting with the product, and combined with the forward scan to sample a wider area of the PES (thus a smoother barrier shape). In addition, the dynamics of the hydride transfer process, ie, tunneling probabilities and transmission coefficients will be calculated by variational transition state theory with multidimensional tunneling (VTST/MT), so that more accurate reaction rate and KIEs can be obtained.

The elusive promoting motion is also studied. A motion is found to exist in the low frequency range of 100 to 180 cm^{-1} . Although there is no effect on this motion with pressure, it is encouraging that the nature of this motion is the same one identified previously (Johannissen, *in press*).

Chapter 6

Conclusions and Future Perspectives

6.1 GENERAL CONCLUSIONS

The aim of this project was to gain insight into the atomistic detail of the active site of MR at high pressure and to study how the high pressure may have an effect on the enzyme function. The major motivation for the study comes from the findings from experimental observations of the rate of reaction and KIE with pressure (Hay et al., 2007). This paper called for atomistic insight into how the active site changes when the pressure is increased.

With regard to this, this research has been successful. High pressure MD simulations were (and still are) relatively uncommon, particularly when the pressure is being used as a probe for subtle active site changes that may lead to a change in the catalytic properties of the enzymes. Thus, there was a need to extensively benchmark the process, building up from a waterbox, through a solvated peptide, to the enzyme in a solvated environment. At each stage of the benchmarking the efficiency of the simulations to replicate experimental observations of the effect of high pressure was scrutinized. Upon satisfaction that the force field and molecular mechanics methods (developed for water and biomolecules at atmospheric pressure) were suitable for use in the pressure range required (from 1 bar up to 2 kbar), the study of MR at high pressure commenced.

Both the global and local effect of an increase in pressure have been analyzed in the MD simulations. An observation (which is also true for the solvated peptide) about the high pressure MD simulations is that there appears to be a stabilization, or possibly a dampening of the protein fluctuations at higher pressures (See Section 3.3). The analysis of the pressure effect in the active site focused upon the distance between the donor atom on

the substrate and the acceptor atom on the cofactor that take part in the hydride transfer reaction. The simulations show a general downwards trend of the average distance, as the pressure is increased. An anomaly in the study of the donor-acceptor distance is the result at 1.5 kbar. It appears that midway through the simulation, the configuration of the active site is disrupted, causing a shift in the substrate above the cofactor. An increase in the donor-acceptor distance is the result of this shift and it is suggested that this residue is involved in the pressure effect. However, this disruption of the active site does suggest that there is some instability of this particular simulation at high pressure. Despite this anomaly, the prediction from Hay *et al.* that the average distance will decrease at higher pressures is verified by the MD simulations (see Section 4.1). Furthermore, the nature of this decrease is explained, by analysing the distribution of the distances in detail. The pressure causes a shift in the equilibrium towards configurations with shorter donor-acceptor distances (Hay *et al.*, 2009a).

With the MD reinforcing the experimental observations and confirming the predictions, it was possible to extend the analysis to the full active site of the protein, to try to identify residues that may be important in the pressure effect. Three residues have been identified as being potentially important in the high pressure configuration of the active site in MR. These are Tyr72, Trp106 and Phe246. The configurations of these residues at high pressure appear to limit the available conformational space for the substrate – thus the donor atom is held closer to the acceptor (See Section 4.2). It has, however, been difficult to correlate any of these residues explicitly to the donor-acceptor distance and it is proposed that all three of the residues, and possibly more residues, are key to the active site configuration at high pressure that limits the conformational space around the nicotinamide. In the meantime,

further experimental work had been pursued on a different active site residue: Asp189. Mutating this residue had been shown to have an effect on the reactive configuration of the substrate and cofactor, by previous experimental and computational studies (Pudney et al., 2007). This mutant has now been studied across the same pressure range experimentally as wild-type MR. MD studies of this mutant at high pressure were performed in an attempt to give further insight, although these gave conflicting results to the experimental work (See Section 4.4) (Pudney et al., 2009).

Although the active site was focused upon, it was also necessary to consider the global effect of pressure, since pressure acts upon the whole protein, from the outside in. An analysis of the low frequency normal modes of MR identified a dynamic domain movement that appeared to be dampened with pressure. Further investigation into this domain enabled the discovery of another potentially important residue involved in the pressure effect – Val108. This residue would not have been discovered, since it is in the second sphere of active site residues, but its configuration impacts on the Trp106 residue that in turn impacts on the conformational space available to the substrate (See Section 4.3).

The final part of the research concerns the effect of the shorter donor-acceptor distance on the hydride transfer reaction. A QM/MM method was used to investigate this and, again, extensive benchmarking was required to ensure that the method chosen was appropriate for the system (See Section 5.1). The procedure chosen does not use the most reliable QM methods that are available. However, the DFT method has been proven to work well for configurations similar to the substrate-cofactor configuration in MR and, as always with QM/MM calculations, a compromise was made between speed of calculation and accuracy

to enable the most efficient study. Representative structures for the highest and lowest pressures from the MD simulations were chosen. The choice of structures is particularly biased towards the configuration of the three active site residues that had been deemed to be important in Chapter 4. This gave structures at high pressure which generally had a shorter donor-acceptor distance than at low pressure, although this bias is justified since the average distance has been shown to decrease with a pressure increase. The results from the QM/MM calculations provide further support to predictions from experiment. A recent paper suggested that the shortening of the donor-acceptor distance at the reactant configuration is insufficient to suggest that the pressure has an effect on the reaction barrier (Kamerlin et al., 2010). This work provides evidence that there is a correlation between the donor-acceptor configuration in the reactant state and the activation energy and the KIE (See Section 5.2 and 5.3). This work is ongoing, since it needs refinement to give a better reaction barrier for the purposes of calculating tunneling probabilities for the different configurations. However the initial results are very promising.

6.2 IMPACT ON OTHER RESEARCH

In order to put the research into context, it is necessary to assess its contribution to scientific knowledge. However, no research project contains all the answers – many instead just generate more questions. This is certainly the case with enzymology. The nature of this research relies on the collaboration of experimental and computational study. This project was inspired by experimental work and in turn, it has now driven more experimental work to be carried out on various mutated forms of MR.

The suggested importance of Val108 and Trp106, in particular, has been explored (Pudney et al., 2010). Various point mutations were carried out on the both of these residues, removing (V108A, W106A) or increasing (V108L) the size of the side chains. Taking away the side chains result in an average decrease of the donor-acceptor distance for both residues, whilst making the Val108 bulkier by mutating it to a leucine causes an average increase in the donor-acceptor distance. This is at odds with the suggestion that Trp106 and Val108 are important for configurations with shorter donor-acceptor distances, however there are several other factors that need to be taken into account and this highlights the complexity of the active site of MR.

6.3 FUTURE PERSPECTIVES

Atomistic insight into the pressure effect on MR has added to the understanding of how the substrate and cofactor configuration can be optimised to improve the catalytic efficiency of the enzyme. There is, however, no doubt that this research can be continued and improved upon with further work. The method chosen for high pressure MD was generally a success, but with more time and newer resources, it is always possible to improve the accuracy of computer simulations. The anomalous result of the 1.5 kbar simulation has not been fully resolved. A possible extension of this research would be to add further simulations at intermediate pressures, such as 250 bar, 750 bar, 1.25 kbar and 1.75 kbar, which would either provide further support to the trend of increasing pressure, or possibly reveal further discrepancies that could be analysed alongside the 1.5 kbar result. With regard to the other pressures, a more extensive analysis of the other active site residues may reveal additional

features of the active site configuration, since it has difficult to correlate the three residues identified so far explicitly to a high pressure effect on the donor-acceptor distance. Also, with the ongoing study into other mutants of MR at high pressure, the MD research should be extended to study these mutants across a pressure range.

The QM/MM calculations on catalysis are promising, but remain ongoing. It is suggested that the pressure ‘squeezes’ the reaction barrier by bringing the donor and acceptor closer together. The barrier compression enhances the tunneling reaction. Since the theory of barrier compression is currently a debated topic, the ongoing work with the QM/MM calculations could prove to be vital. It is necessary therefore to continue this work, possibly extending it to more frames. The QM/MM method could be scrutinized for the use of the BH&H functional. It is noted here though that the BH&H choice suited the purpose of the investigation due to its efficiency at modelling the π -stacking interaction. However, the QM/MM method could be improved by using the M05 or M05-2X functionals that have been developed more recently (Zhao et al., 2006, Zhao and Truhlar, 2007). This method could also be improved by using more frames to obtain a better average. The potential energy scans in Section 5.3.1 are clearly not reliable enough to use in rate calculations that are dependent on the width of the barrier. A solution to this would be to ‘scan backwards’ from the product to the reactant (with a distance constraint placed on the carbon-hydrogen bond that was broken in the initial scans). The combination of the forwards and backwards scans would result in a more conventional barrier that could be used to more accurately calculate the rates and KIEs.

Appendix A

| Secondary Structure | 1 bar | 500 bar | 1 kbar | 1.5 kbar | 2 kbar |
|-----------------------|-------|---------|--------|----------|--------|
| Coil | 23.1 | 21.6 | 21.7 | 23.0 | 22.0 |
| Turn | 26.3 | 26.7 | 27.3 | 25.5 | 26.4 |
| Extended Conformation | 15.7 | 16.4 | 15.8 | 15.7 | 15.8 |
| Alpha Helix | 31.3 | 31.8 | 30.9 | 32.3 | 31.9 |
| 3-10 Helix | 3.0 | 2.7 | 3.3 | 2.7 | 3.2 |
| Isolated Bridge | 0.7 | 0.8 | 1.0 | 0.8 | 0.8 |

Table A.1: Secondary structure of Morphinone Reductase for 10 ns at different pressures. All figures are in percentage

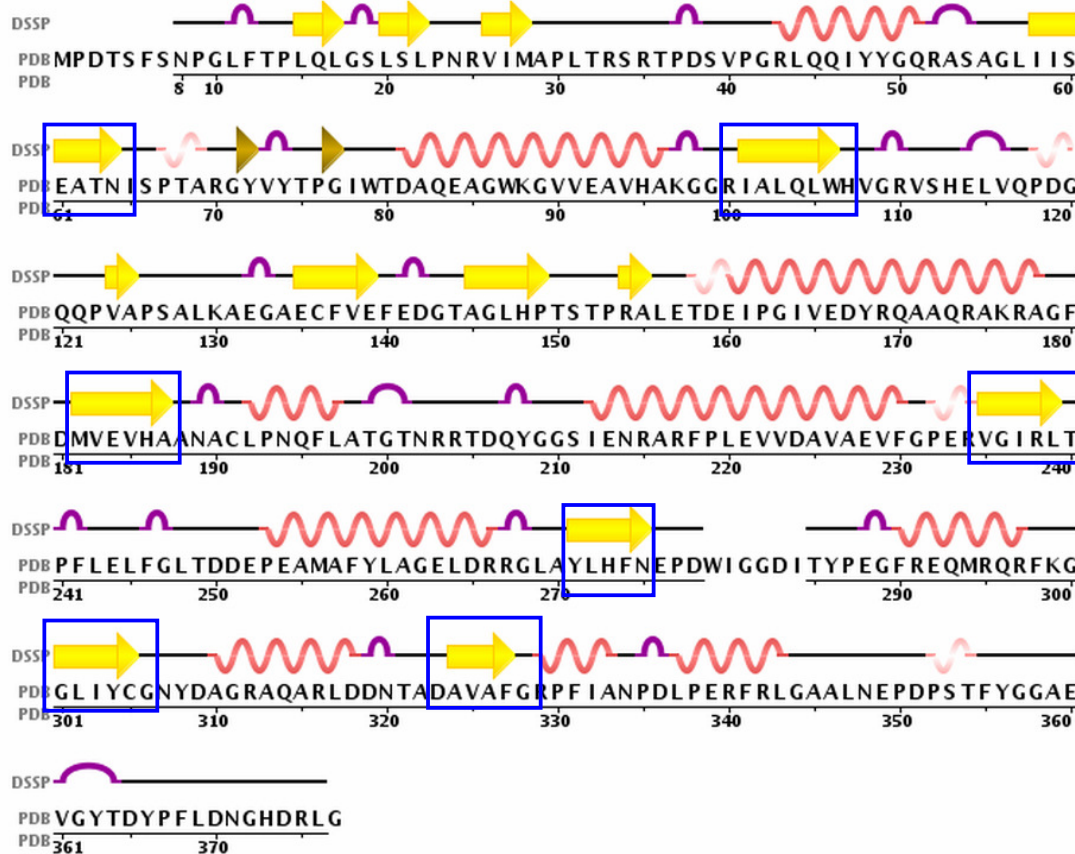


Figure A.1: The sequence and DSSP secondary structure assignment of Morphinone Reductase, taken from the Protein Data Bank (Bernstein et al., 1977)

For the purpose of the water analysis, the core of the protein is defined as the beta-barrel. The beta-sheets included in the barrel are highlighted by the blue boxes on Figure A.1 and are listed in Table A.2:

| Residue number | Amino Acid Sequence |
|----------------|---------------------|
| 26-28 | VIM |
| 57-64 | LIISEATN |
| 101-106 | IALQLW |
| 182-187 | MVEVHA |
| 235-239 | VGIRL |
| 271-275 | YLHFN |
| 301-305 | GLIYC |
| 324-327 | AVAF |

Table A.2: Amino acids that form the beta-barrel in the centre of Morphinone Reductase

The number of water atoms was counted at different distances, every 20 ps for the 10 ns trajectory at 1 bar. This is shown in Figure A.2.

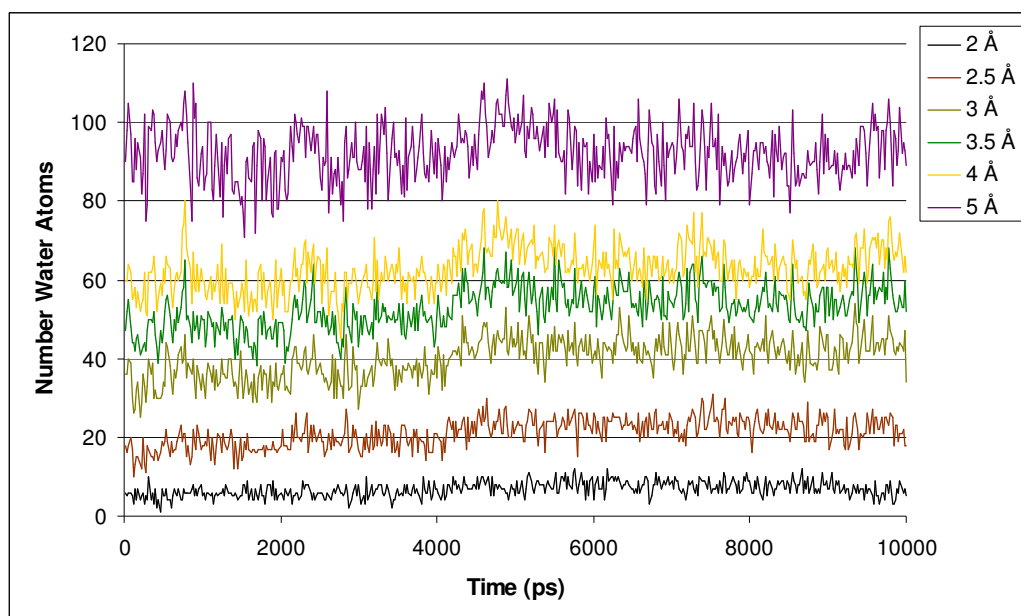


Figure A.2: Number of water atoms within particular distances of the core of the MR in the 1 bar simulation across the 10 ns trajectory

The average number of water atoms at each distance for 1 bar is shown in Table A.3.

| Distance From Backbone of Beta Barrel | Average Number of Water Atoms |
|---------------------------------------|-------------------------------|
| 1 Å | 0 |
| 1.5 Å | 0.01 |
| 2 Å | 6.87 |
| 2.5 Å | 21.15 |
| 3 Å | 40.08 |
| 3.5 Å | 52.92 |
| 4 Å | 62.95 |
| 5 Å | 92.29 |

Table A.3: Average number of water atoms at different distances from core of Morphinone Reductase, at a pressure of 1 bar

Appendix B

| Distance | 1 bar | 1 kbar | 2 kbar |
|----------|-------|--------|--------|
| <3.1 | 0 | 2 | 0 |
| 3.1-3.2 | 5 | 8 | 12 |
| 3.2-3.3 | 25 | 28 | 64 |
| 3.3-3.4 | 97 | 133 | 195 |
| 3.4-3.5 | 220 | 315 | 466 |
| 3.5-3.6 | 431 | 476 | 719 |
| 3.6-3.7 | 504 | 670 | 892 |
| 3.7-3.8 | 631 | 678 | 778 |
| 3.8-3.9 | 601 | 701 | 686 |
| 3.9-4.0 | 622 | 569 | 513 |
| 4.0-4.1 | 486 | 433 | 323 |
| 4.1-4.2 | 408 | 331 | 161 |
| 4.2-4.3 | 314 | 232 | 106 |
| 4.3-4.4 | 244 | 150 | 39 |
| 4.4-4.5 | 148 | 117 | 18 |
| 4.5-4.6 | 116 | 57 | 12 |
| 4.6-4.7 | 57 | 45 | 7 |
| 4.7-4.8 | 44 | 16 | 4 |
| 4.8-4.9 | 23 | 15 | 1 |
| 4.9-5.0 | 11 | 6 | 1 |
| 5.0-5.1 | 4 | 8 | 0 |
| 5.1-5.2 | 0 | 1 | 0 |
| 5.2-5.3 | 2 | 3 | 1 |
| 5.3-5.4 | 1 | 6 | 1 |
| 5.4-5.5 | 1 | 0 | 0 |
| 5.5-5.6 | 1 | 0 | 0 |
| 5.6-5.7 | 0 | 0 | 1 |
| 5.7-5.8 | 1 | 0 | 0 |
| 5.8-5.9 | 1 | 0 | 0 |
| 5.9-6.0 | 1 | 0 | 0 |
| >6.0 | 1 | 0 | 0 |

Table B.1: Table showing the binned values for different ranges of donor-acceptor distances. Taken from MD trajectories at 1 bar, 1 kbar and 2 kbar. Bins are in 0.1 Å step sizes.

Appendix D

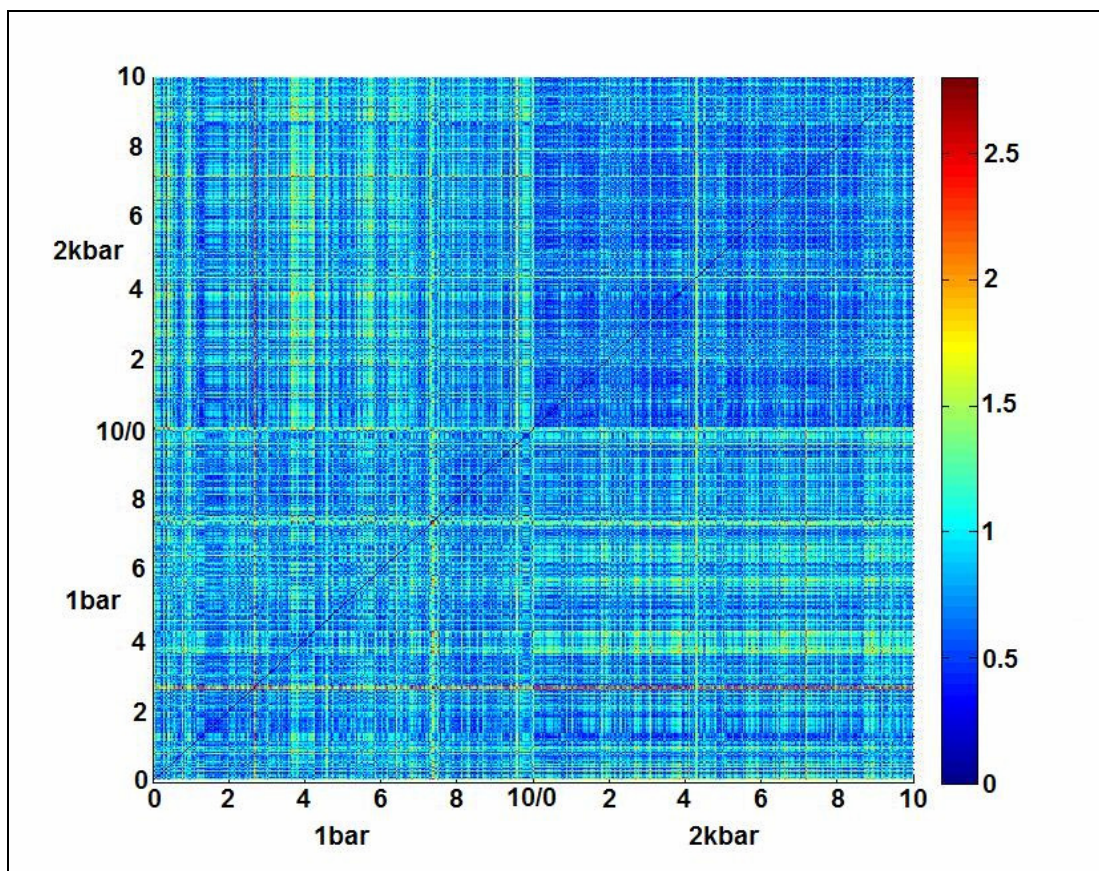


Figure D.1: Figure showing a 2D-RMSD analysis of the nicotinamide ring across two 500 frame (10 ns) trajectories. The bottom-left corner allows comparison of the 1 bar trajectory, the top-right corner allows comparison for the 2 kbar trajectory. The top-left and bottom-right corners give a comparison between the two trajectories. The timesteps of the trajectories are plotted along the axes in ns. The bar at the right hand side is the colour coded RMSD key, with the values in Å. The maximum RMSD is the maximum sampled

Appendix E

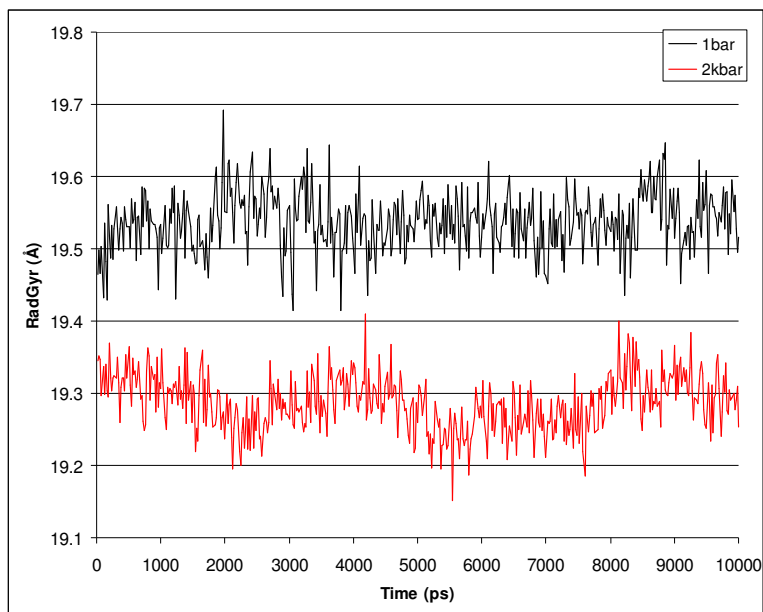


Figure E.1: Radius of Gyration (RadGyr) of protein α -carbons of MR_N189A during 10 ns simulation at different pressures: 1 bar (black) and 2 kbar (red)

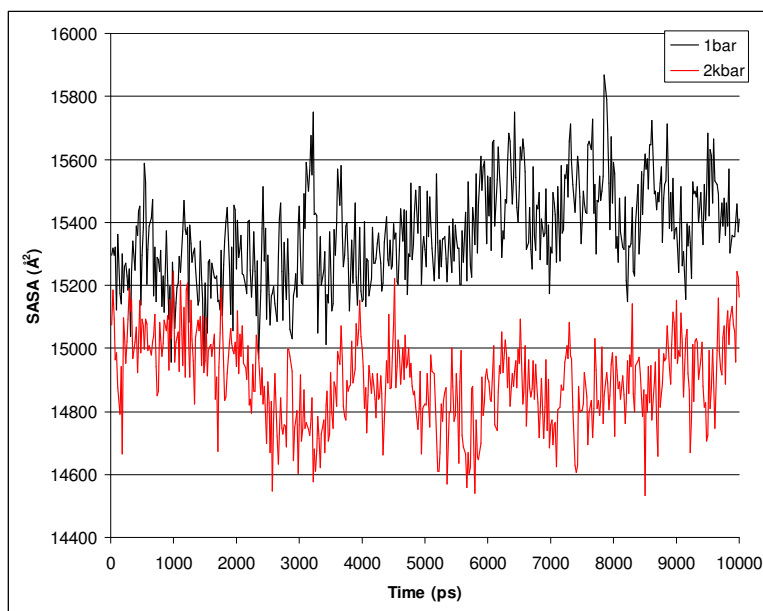


Figure E.2: Solvent accessible surface area (SASA) of MR_N189A during 10 ns simulation at different pressures: 1 bar (black) and 2 kbar (red)

| Pressure: | 1 bar | 2 kbar |
|--|--------------|--------------|
| Radius of Gyration (\AA) | 19.54 (0.04) | 19.28 (0.04) |
| Solvent Accessible Surface Area (\AA^2) | 15362 (155) | 14899 (137) |

Table E.1: Average values for RadGyr and SASA, calculated over 10 ns trajectories for MR_N189A at 1 bar and 2 kbar. Standard deviations are shown in brackets

Appendix F

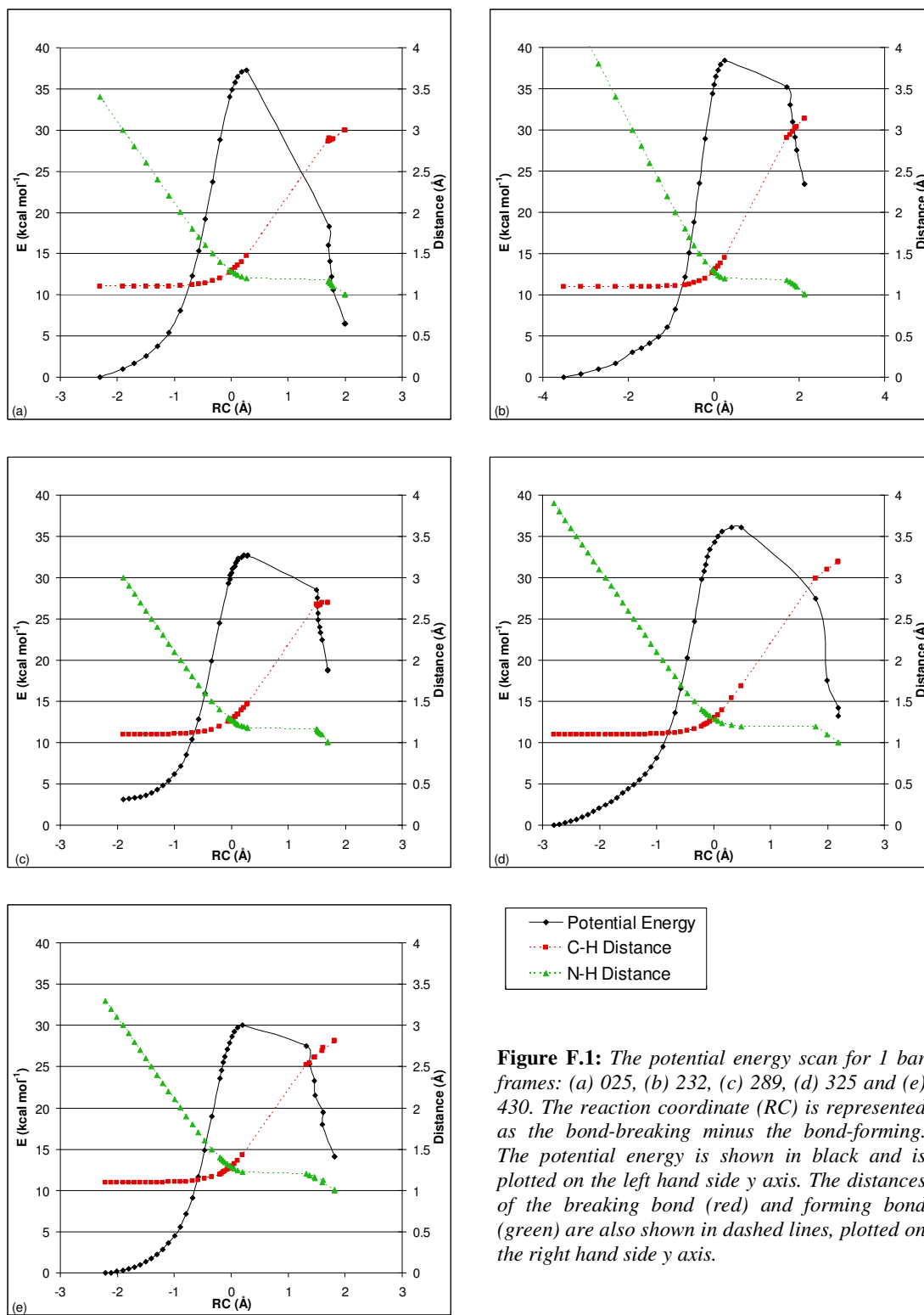


Figure F.1: The potential energy scan for 1 bar frames: (a) 025, (b) 232, (c) 289, (d) 325 and (e) 430. The reaction coordinate (RC) is represented as the bond-breaking minus the bond-forming. The potential energy is shown in black and is plotted on the left hand side y axis. The distances of the breaking bond (red) and forming bond (green) are also shown in dashed lines, plotted on the right hand side y axis.

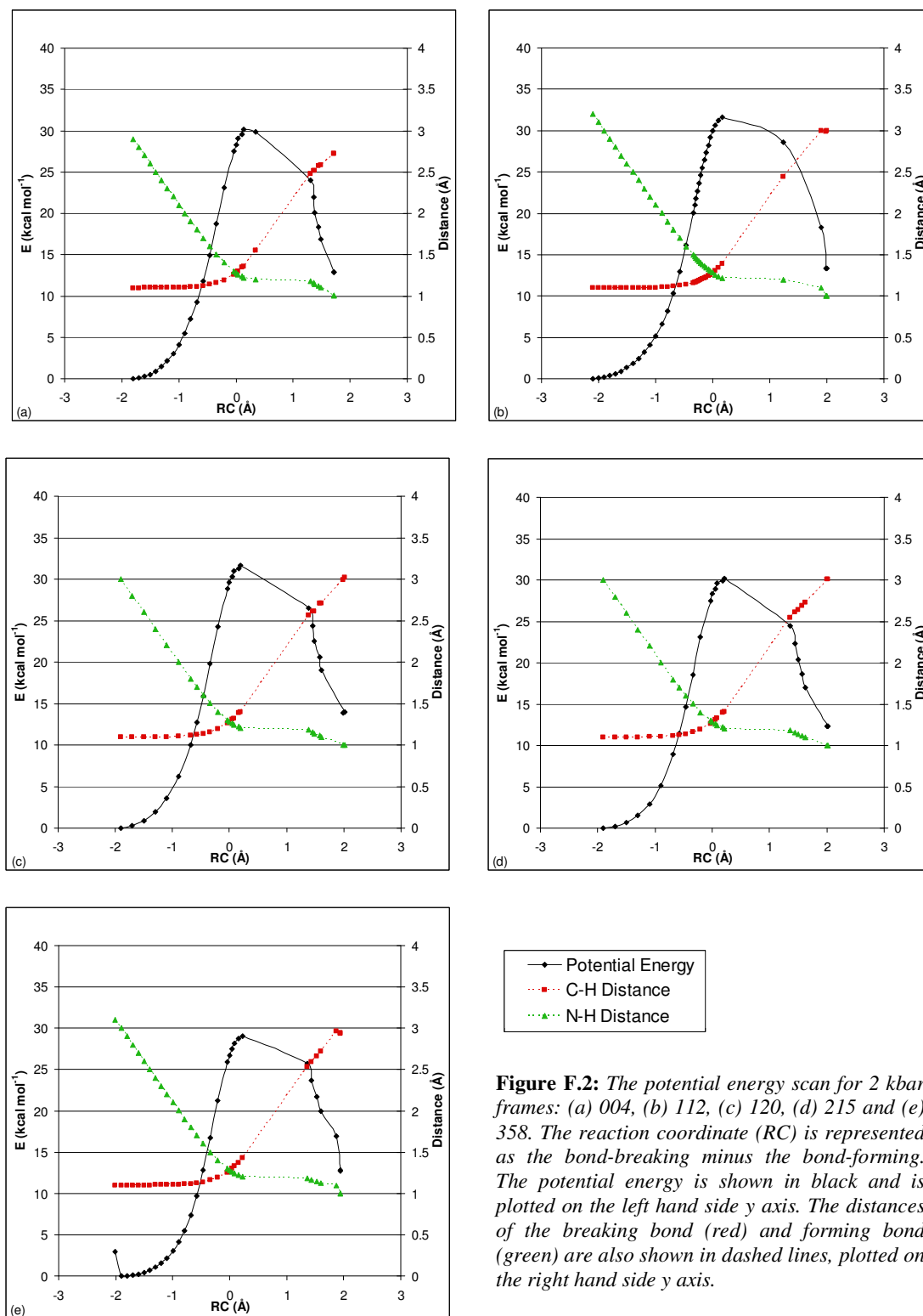


Figure F.2: The potential energy scan for 2 kbar frames: (a) 004, (b) 112, (c) 120, (d) 215 and (e) 358. The reaction coordinate (RC) is represented as the bond-breaking minus the bond-forming. The potential energy is shown in black and is plotted on the left hand side y axis. The distances of the breaking bond (red) and forming bond (green) are also shown in dashed lines, plotted on the right hand side y axis.

References

- ALLEMANN, R. K., EVANS, R. M., TEY, L. H., MAGLIA, G., PANG, J., RODRIGUEZ, R., SHRIMPSON, P. J. & SWANWICK, R. S. (2006) Protein motions during catalysis by dihydrofolate reductases. *Philosophical Transactions of the Royal Society B: Biological Sciences*, 361, 1317-1321.
- ANTONIOU, D. & SCHWARTZ, S. D. (1997) Large kinetic isotope effects in enzymatic proton transfer and the role of substrate oscillations. *Proceedings of the National Academy of Sciences of the United States of America*, 94, 12360-12365.
- BALABIN, I. A. & ONUCHIC, J. N. (2000) Dynamically controlled protein tunneling paths in photosynthetic reaction centers. *Science*, 290, 114-117.
- BASRAN, J., HARRIS, R. J., SUTCLIFFE, M. J. & SCRUTTON, N. S. (2003) H-tunneling in the Multiple H-transfers of the Catalytic Cycle of Morphine Reductase and in the Reductive Half-reaction of the Homologous Pentaerythritol Tetranitrate Reductase. *Journal of Biological Chemistry*, 278, 43973-43982.
- BECKE, A. D. (1993) A new mixing of Hartree-Fock and local density-functional theories. *The Journal of Chemical Physics*, 98, 1372-1377.
- BELL, R. P. (1980) *The Tunneling Effect in Chemistry*, London, Chapman & Hall.
- BERENDSEN, H. J. C., POSTMA, J. P. M., DINOLA, A. & HAAK, J. R. (1984) Molecular dynamics with coupling to an external bath. *J. Chem. Phys.*, 81, 3684-3690.
- BERENDSEN, H. J. C., VAN DER SPOEL, D. & VAN DRUNEN, R. (1995) GROMACS: A message-passing parallel molecular dynamics implementation. *Computer Physics Communications*, 91, 43-56.
- BERMAN, H. M., WESTBROOK, J., FENG, Z., GILLILAND, G., BHAT, T. N., WEISSIG, H., SHINDYALOV, I. N. & BOURNE, P. E. (2000) The Protein Data Bank. *Nucleic Acids Research*, 28, 235-242.
- BERNSTEIN, F. C., KOETZLE, T. F. & WILLIAMS, G. J. B. (1977) The protein data bank: a computer based archival file for macromolecular structures. *Journal of Molecular Biology*, 112, 535-542.
- BORGIS, D. & HYNES, J. T. (1996) Curve crossing formulation for proton transfer reactions in solution. *Journal of Physical Chemistry*, 100, 1118-1128.
- BRIDGMAN, P. W. (1914) The Coagulation of Albumen by Pressure. *Journal of Biological Chemistry*, 19, 511-512.
- BROOKS, B. R., BRUCCOLERI, R. E., OLAFSON, B. D., STATES, D. J., SWAMINATHAN, S. & KARPLUS, M. (1983) Charmm - a Program for Macromolecular Energy, Minimization, and Dynamics Calculations. *Journal of Computational Chemistry*, 4, 187-217.
- BRUNO, W. J. & BIALEK, W. (1992) Vibrationally enhanced tunneling as a mechanism for enzymatic hydrogen transfer. *Biophysical Journal*, 63, 689-699.
- CASE, D. A., CHEATHAM III, T. E., DARDEN, T., GOHLKE, H., LUO, R., MERZ JR, K. M., ONUFRIEV, A., SIMMERLING, C., WANG, B. & WOODS, R. J. (2005a) The Amber biomolecular simulation programs. *Journal of Computational Chemistry*, 26, 1668-1688.
- CASE, D. A., CHEATHAM, T. E., 3RD, DARDEN, T., GOHLKE, H., LUO, R., MERZ, K. M., JR., ONUFRIEV, A., SIMMERLING, C., WANG, B. & WOODS, R. J.

- (2005b) The Amber biomolecular simulation programs. *J Comput Chem*, 26, 1668-88.
- CCG, C. C. G.-. (2008) Molecular Operating Environment. Montreal, Quebec, Canada
- CHAKRAVARTI, I. M., LAHA, R. G. & ROY, J. (1967) *Handbook of Methods of Applied Statistics*, John Wiley and Sons.
- CHEN, L. H., KENYON, G. L., CURTIN, F., HARAYAMA, S., BEMBENEK, M. E., HAJIPOUR, G. & WHITMAN, C. P. (1992) 4-Oxalocrotonate tautomerase, an enzyme composed of 62 amino acid residues per monomer. *Journal of Biological Chemistry*, 267, 17716-17721.
- CLAEYSSENS, F., HARVEY, J. N., MANBY, F. R., MATA, R. A., MULHOLLAND, A. J., RANAGHAN, K. E., SCHÄTZ, M., THIEL, S., THIEL, W. & WERNER, H. J. (2006) High-accuracy computation of reaction barriers in enzymes. *Angewandte Chemie - International Edition*, 45, 6856-6859.
- COLLINS, M. D., HUMMER, G., QUILLIN, M. L., MATTHEWS, B. W. & GRUNER, S. M. (2005) Cooperative water filling of a nonpolar protein cavity observed by high-pressure crystallography and simulation. *Proceedings of the National Academy of Sciences of the United States of America*, 102, 16668-16671.
- CORNELL, W. D., CIEPLAK, P., BAYLY, C. I., GOULD, I. R., MERZ JR, K. M., FERGUSON, D. M., SPELLMEYER, D. C., FOX, T., CALDWELL, J. W. & KOLLMAN, P. A. (1995) A second generation force field for the simulation of proteins, nucleic acids, and organic molecules. *Journal of the American Chemical Society*, 117, 5179-5197.
- CRAIG, D. H., MOODY, P. C. E., BRUCE, N. C. & SCRUTTON, N. S. (1998) Reductive and oxidative half-reactions of morphinone reductase from *Pseudomonas putida* M10: A kinetic and thermodynamic analysis. *Biochemistry*, 37, 7598-7607.
- DAGGETT, V. & LEVITT, M. (1993) Protein unfolding pathways explored through molecular dynamics simulations. *Journal of Molecular Biology*, 232, 600-619.
- DARDEN, T., YORK, D. & PEDERSEN, L. (1993) Particle mesh Ewald: An $N \cdot \log(N)$ method for Ewald sums in large systems. *The Journal of Chemical Physics*, 98, 10089-10092.
- DUAN, Y., WU, C., CHOWDHURY, S., LEE, M. C., XIONG, G., ZHANG, W., YANG, R., CIEPLAK, P., LUO, R., LEE, T., CALDWELL, J., WANG, J. & KOLLMAN, P. (2003) A Point-Charge Force Field for Molecular Mechanics Simulations of Proteins Based on Condensed-Phase Quantum Mechanical Calculations. *Journal of Computational Chemistry*, 24, 1999-2012.
- DUTTON, P. L., MUNRO, A. W., SCRUTTON, N. S. & SUTCLIFFE, M. J. (2006) Introduction. Quantum catalysis in enzymes: Beyond the transition state theory paradigm. *Philosophical Transactions of the Royal Society B: Biological Sciences*, 361, 1293-1294.
- E.W. LEMMON, M. O. M. A. D. G. F. *Thermophysical Properties of Fluid Systems*, Gaithersburg MD, National Institute of Standards and Technology.
- EISENMESSER, E. Z., BOSCO, D. A., AKKE, M. & KERN, D. (2002) Enzyme Dynamics During Catalysis. *Science*, 295, 1520-1523.
- EYRING, H. (1935) *Journal of Chemical Physics*, 3, 107.
- FISCHER, E. (1894) Einfluss der Configuration auf die Wirkung der Enzyme. *Berichte der deutschen chemischen Gesellschaft*, 27, 2985-2993.

- FRAAIJE, M. W. & MATTEVI, A. (2000) Flavoenzymes: Diverse catalysts with recurrent features. *Trends in Biochemical Sciences*, 25, 126-132.
- FREDDOLINO, P. L., ARKHIPOV, A. S., LARSON, S. B., MCPHERSON, A. & SCHULTEN, K. (2006) Molecular dynamics simulations of the complete satellite tobacco mosaic virus. *Structure*, 14, 437-449.
- FRENCH, C. E. & BRUCE, N. C. (1994) Purification and characterization of morphinone reductase from *Pseudomonas putida* M10. *Biochemical Journal*, 301, 97-103.
- GAO, J., AMARA, P., ALHAMBRA, C. & FIELD, M. J. (1998) A generalized hybrid orbital (GHO) method for the treatment of boundary atoms in combined QM/MM calculations. *Journal of Physical Chemistry A*, 102, 4714-4721.
- GLADSTONE, S., LAIDLER, K.J., & EYRING, H. (1941) *The Theory of Rate Processes*, McGraw-Hill, New York, NY.
- GORBATY, Y. E. & DEMIANETS, Y. N. (1985) An X-ray study of the effect of pressure on the structure of liquid water. *Molecular Physics: An International Journal at the Interface Between Chemistry and Physics*, 55, 571 - 588.
- GORDON, J. C., MYERS, J. B., FOLTA, T., SHOJA, V., HEATH, L. S. & ONUFRIEV, A. (2005) H++: A server for estimating pK_as and adding missing hydrogens to macromolecules. *Nucleic Acids Research*, 33.
- HALDANE, J. B. S. (1930) *Enzymes*, London, Longmans, Green.
- HAY, S., JOHANNISSEN, L. O., SUTCLIFFE, M. J. & SCRUTTON, N. S. (2010) Barrier Compression and Its Contribution to Both Classical and Quantum Mechanical Aspects of Enzyme Catalysis. *Biophysical Journal*, 98, 121-128.
- HAY, S., PUDNEY, C. R., MCGRORY, T. A., PANG, J. Y., SUTCLIFFE, M. J. & SCRUTTON, N. S. (2009a) Barrier Compression Enhances an Enzymatic Hydrogen-Transfer Reaction. *Angewandte Chemie-International Edition*, 48, 1452-1454.
- HAY, S., PUDNEY, C. R. & SCRUTTON, N. S. (2009b) Structural and mechanistic aspects of flavoproteins: Probes of hydrogen tunnelling. *FEBS Journal*, 276, 3930-3941.
- HAY, S., SUTCLIFFE, M. J. & SCRUTTON, N. S. (2007) Promoting motions in enzyme catalysis probed by pressure studies of kinetic isotope effects. *Proceedings of the National Academy of Sciences of the United States of America*, 104, 507-512.
- HAYWARD, S. & LEE, R. A. (2002) Improvements in the analysis of domain motions in proteins from conformational change: DynDom version 1.50. *Journal of Molecular Graphics and Modelling*, 21, 181-183.
- [HTTP://AMBER.SCRIPPS.EDU/TUTORIAL/POLYA-POLYT_NEW/MINANDMD3.HTML](http://amber.scripps.edu/tutorial/polya-polyt_new/minandmd3.html).
- HUBER, R. & BENNETT, W. S. (1983) Functional significance of flexibility in proteins. *Biopolymers*, 22, 261-279.
- HUMMER, G., GARDE, S., GARCÍA-A, A. E., PAULAITIS, M. E. & PRATT, L. R. (1998) The pressure dependence of hydrophobic interactions is consistent with the observed pressure denaturation of proteins. *Proceedings of the National Academy of Sciences of the United States of America*, 95, 1552-1555.
- HUMPHREY, W., DALKE, A. & SCHULTEN, K. (1996) VMD: Visual molecular dynamics. *Journal of Molecular Graphics*, 14, 33-38.
- HUNENBERGER, P. H., MARK, A. E. & VAN GUNSTEREN, W. F. (1995a) Computational approaches to study protein unfolding: Hen egg white lysozyme as a case study. *Proteins: Structure, Function and Genetics*, 21, 196-213.

- HUNENBERGER, P. H., MARK, A. E. & VAN GUNSTEREN, W. F. (1995b) Fluctuation and cross-correlation analysis of protein motions observed in nanosecond molecular dynamics simulations. *Journal of Molecular Biology*, 252, 492-503.
- HUR, S. & BRUICE, T. C. (2003) Enzymes do what is expected (chalcone isomerase versus chorismate mutase). *Journal of the American Chemical Society*, 125, 1472-1473.
- ISAACS, N. S., JAVAID, K. & RANNALA, E. (1978) Reactions at high pressure. Part 5. The effect of pressure on some primary kinetic isotope effects. *Journal of the Chemical Society, Perkin Transactions 2*, 709-711.
- JOHANNISSEN, L. O., HAY, S., SCRUTTON, N. S. & SUTCLIFFE, M. J. (2007) Proton tunneling in aromatic amine dehydrogenase is driven by a short-range sub-picosecond promoting vibration: Consistency of simulation and theory with experiment. *Journal of Physical Chemistry B*, 111, 2631-2638.
- JOHANNISSEN, L. O., SCRUTTON, N. S. & SUTCLIFFE, M. J. (in press) Pressure-induced dampening of the promoting vibration in an enzymatic H-tunneling reaction: the complex relationship between pressure and donor-acceptor compression uncovered by molecular dynamics simulations.
- JOHNSON, B. G., GILL, P. M. W. & POPLER, J. A. (1993) The performance of a family of density functional methods. *The Journal of Chemical Physics*, 98, 5612-5626.
- JONSSON, T., GLICKMAN, M. H., SUN, S. & KLINMAN, J. P. (1996) Experimental evidence for extensive tunneling of hydrogen in the lipoxygenase reaction: Implications for enzyme catalysis. *Journal of the American Chemical Society*, 118, 10319-10320.
- KABSCH, W. & SANDER, C. (1983) Dictionary of protein secondary structure: pattern recognition of hydrogen-bonded and geometrical features. *Biopolymers - Peptide Science Section*, 22, 2577-2637.
- KAMERLIN, S. C. L., MAVRI, J. & WARSHEL, A. (2010) Examining the case for the effect of barrier compression on tunneling, vibrationally enhanced catalysis, catalytic entropy and related issues. *FEBS Letters*, 584, 2759-2766.
- KLINMAN, J. P. (2006) Linking protein structure and dynamics to catalysis: The role of hydrogen tunnelling. *Philosophical Transactions of the Royal Society B: Biological Sciences*, 361, 1323-1331.
- KNAPP, M. J. & KLINMAN, J. P. (2002a) Environmentally coupled hydrogen tunneling. Linking catalysis to dynamics. *Eur. J. Biochem.*, 269, 3113-3121.
- KNAPP, M. J. & KLINMAN, J. P. (2002b) Environmentally coupled hydrogen tunneling: Linking catalysis to dynamics. *European Journal of Biochemistry*, 269, 3113-3121.
- KNAPP, M. J., RICKERT, K. & KLINMAN, J. P. (2002) Temperature-dependent isotope effects in soybean Lipoxygenase-1: Correlating hydrogen tunneling with protein dynamics. *Journal of the American Chemical Society*, 124, 3865-3874.
- KOHEN, A. & KLINMAN, J. P. (1998) Enzyme Catalysis: Beyond Classical Paradigms. *Accounts of Chemical Research*, 31, 397-404.
- KOHN, W. & SHAM, L. J. (1965) Self-consistent equations including exchange and correlation effects. *Physical Review*, 140.
- KOSHLAND JR, D. E. (1973) Protein and biological control. *Scientific American*, 229, 52-64.
- KRAUT, J. (1988) How do enzymes work? *Science*, 242, 533-540.

- KUNDROT, C. E. & RICHARDS, F. M. (1987) Crystal structure of hen egg-white lysozyme at a hydrostatic pressure of 1000 atmospheres. *Journal of Molecular Biology*, 193, 157-170.
- KURZ, J. L. (1963) Transition state characterization for catalyzed reactions. *Journal of the American Chemical Society*, 85, 987-991.
- KUZNETSOV, A. M. & ULSTRUP, J. (1999) Proton and hydrogen atom tunnelling in hydrolytic and redox enzyme catalysis. *Canadian Journal of Chemistry*, 77, 1085-1096.
- LAD, C., WILLIAMS, N. H. & WOLFENDEN, R. (2003) The rate of hydrolysis of phosphomonoester dianions and the exceptional catalytic proficiencies of protein and inositol phosphatases. *Proceedings of the National Academy of Sciences of the United States of America*, 100, 5607-5610.
- LEACH, A. R. (2001) *Molecular Modelling: Principles and Applications*, Englewood Cliffs, NJ, Prentice Hall.
- LIENHARD, G. E. (1973) Enzymatic catalysis and transition-state theory. *Science*, 180, 149-154.
- LONCHARICH, R. J. & BROOKS, B. R. (1989) The effects of truncating long-range forces on protein dynamics. *Proteins*, 6, 32-45.
- M. J. FRISCH, G. W. T., H. B. SCHLEGEL, G. E. SCUSERIA, M. A. ROB, J. R. CHEESEMAN, J. A. MONTGOMERY JR., T. VREVEN, K. N. KUDIN, J. C. BURANT, J. M. MILLAM, S. S. IYENGAR, J. TOMASI, V. BARONE, B. MENNUCCI, M. COSSI, G. SCALMANI, N. REGA, G. A. PETERSSON, H. NAKATSUJI, M. HADA, M. EHARA, K. TOYOTA, R. FUKUDA, J. HASEGAWA, M. ISHIDA, T. NAKAJIMA, Y. HONDA, O. KITAO, H. NAKAI, M. KLENE, X. LI, J. E. KNOX, H. P. HRATCHIAN, J. B. CROSS, V. BAKKEN, C. ADAMO, J. JARAMILLO, R. GOMPERTS, R. E. STRATMANN, O. YAZYEV, A. J. AUSTIN, R. CAMMI, C. POMELLI, J. W. OCHTERSKI, P. Y. AYALA, K. MOROKUMA, G. A. VOTH, P. SALVADOR, J. J. DANNENBERG, V. G. ZAKRZEWSKI, S. DAPPRICH, A. D. DANIELS, M. C. STRAIN, O. FARKAS, D. K. MALICK, A. D. RABUCK, K. RAGHAVACHARI, J. B. FORESMAN, J. V. ORTIZ, Q. CUI, A. G. BABOUL, S. CLIFFORD, J. CIOSLOWSKI, B. B. STEFANOV, G. LIU, A. LIASHENKO, P. PISKORZ, I. KOMAROMI, R. L. MARTIN, D. J. FOX, T. KEITH, M. A. AL-LAHAM, C. Y. PENG, A. NANAYAKKARA, M. CHALLACOMBE, P. M. W. GILL, B. JOHNSON, W. CHEN, M. W. WONG, C. GONZALEZ, AND J. A. POPLE, (2003) Gaussian 03. Wallingford, CT, Gaussian Inc.
- MACKERELL JR, A. D., BASHFORD, D., BELLOTT, M., DUNBRACK JR, R. L., EVANSECK, J. D., FIELD, M. J., FISCHER, S., GAO, J., GUO, H., HA, S., JOSEPH-MCCARTHY, D., KUHNIR, L., KUCZERA, K., LAU, F. T. K., MATTOS, C., MICHNICK, S., NGO, T., NGUYEN, D. T., PRODHOM, B., REIHER III, W. E., ROUX, B., SCHLENKRICH, M., SMITH, J. C., STOTE, R., STRAUB, J., WATANABE, M., WIÅ³RKIEWICZ-KUCZERA, J., YIN, D. & KARPLUS, M. (1998) All-atom empirical potential for molecular modeling and dynamics studies of proteins. *Journal of Physical Chemistry B*, 102, 3586-3616.
- MARCUS, R. A. & SUTIN, N. (1985) Electron transfers in chemistry and biology. *Biochimica et Biophysica Acta - Reviews on Bioenergetics*, 811, 265-322.
- MASGRAU, L., BASRAN, J., HOTH, P., SUTCLIFFE, M. J. & SCRUTTON, N. S. (2004) Hydrogen tunneling in quinoproteins. *Arch. Biochem. Biophys.*, 428, 41-51.

- MASGRAU, L., ROUJEINIKOVA, A., JOHANNISSEN, L. O., HOTH, P., BASRAN, J., RANAGHAN, K. E., MULHOLLAND, A. J., SUTCLIFFE, M. J., SCRUTTON, N. S. & LEYS, D. (2006) Atomic description of an enzyme reaction dominated by proton tunneling. *Science*, 312, 237-241.
- MASON, P. E. & BRADY, J. W. (2007) "Tetrahedrality" and the Relationship between Collective Structure and Radial Distribution Functions in Liquid Water. *The Journal of Physical Chemistry B*, 111, 5669-5679.
- MCCAMMON, J. A., GELIN, B. R. & KARPLUS, M. (1977) Dynamics of Folded Proteins. *Nature*, 267, 585-590.
- MCGUIRE, G. & GEORGE FALK, K. (1923) Studies on enzyme action. XXIII. The spontaneous increase in sucrase activity of banana extracts. *The Journal of the American Chemical Society*, 45, 1539-1551.
- MILLER, W. H. (1986) Semiclassical Methods in Chemical Physics. *Science*, 233, 171-177.
- MIYASHITA, O., OKAMURA, M. Y. & ONUCHIC, J. N. (2005) Interprotein electron transfer from cytochrome c2 to photosynthetic reaction center: Tunneling across an aqueous interface. *Proceedings of the National Academy of Sciences of the United States of America*, 102, 3558-3563.
- MOHR, P. J., TAYLOR, B. N. & NEWELL, D. B. (2008) CODATA recommended values of the fundamental physical constants: 2006. *Journal of Physical and Chemical Reference Data*, 37, 1187-1284.
- MONGAN, J. (2004) Interactive essential dynamics. *Journal of Computer-Aided Molecular Design*, 18, 433-436.
- MOZHAEV, V. V., HEREMANS, K., FRANK, J., MASSON, P. & BALNY, C. (1996) High pressure effects on protein structure and function. *Proteins: Structure, Function and Genetics*, 24, 81-91.
- MULHOLLAND, A. J. (2007) Chemical accuracy in QM/MM calculations on enzyme-catalysed reactions. *Chemistry Central Journal*, 1.
- MULHOLLAND, A. J. (2008) Computational enzymology: Modelling the mechanisms of biological catalysts. *Biochemical Society Transactions*, 36, 22-26.
- NORTHROP, D. B. (1999) Effects of high pressure on isotope effects and hydrogen tunneling. *Journal of the American Chemical Society*, 121, 3521-3524.
- NORTHROP, D. B. (2006) Unusual origins of isotope effects in enzyme-catalysed reactions. *Philosophical Transactions of the Royal Society B: Biological Sciences*, 361, 1341-1349.
- NORTHROP, D. B. & CHO, Y. K. (2000) Effect of pressure on deuterium isotope effects of yeast alcohol dehydrogenase: Evidence for mechanical models of catalysis. *Biochemistry*, 39, 2406-2412.
- OSBORNE, T. B. & HARRIS, I. F. (1903) The tryptophan reaction of various proteins. *The Journal of the American Chemical Society*, 25, 853-855.
- PACI, E. (2002) High pressure simulations of biomolecules. *Biochimica et Biophysica Acta - Protein Structure and Molecular Enzymology*, 1595, 185-200.
- PANG, J. Y., HAY, S., SCRUTTON, N. S. & SUTCLIFFE, M. J. (2008) Deep tunneling dominates the biologically important hydride transfer reaction from NADH to FMN in morphinone reductase. *Journal of the American Chemical Society*, 130, 7092-7097.

- PASCHEK, D., GNANAKARAN, S. & GARCIA, A. E. (2005) Simulations of the pressure and temperature unfolding of an α -helical peptide. *Proceedings of the National Academy of Sciences of the United States of America*, 102, 6765-6770.
- PAULING, L. (1946) Modern structural chemistry. *Chemical and Engineering News*, 24, 1788-1789.
- PHILLIPS, J. C., BRAUN, R., WANG, W., GUMBART, J., TAJKHORSHID, E., VILLA, E., CHIPOT, C., SKEEL, R. D., KALÉ, L. & SCHULTEN, K. (2005) Scalable molecular dynamics with NAMD. *Journal of Computational Chemistry*, 26, 1781-1802.
- POWELL, K. A., RAMER, S. W., DEL CARDAYR, S. B., STEMMER, W. P. C., TOBIN, M. B., LONGCHAMP, P. F. & HUISMAN, G. W. (2001) Directed evolution and biocatalysis. *Angewandte Chemie - International Edition*, 40, 3948-3959.
- PUDNEY, C. R., HAY, S., PANG, J. Y., COSTELLO, C., LEYS, D., SUTCLIFFE, M. J. & SCRUTTON, N. S. (2007) Mutagenesis of morphinone reductase induces multiple reactive configurations and identifies potential ambiguity in kinetic analysis of enzyme tunneling mechanisms. *Journal of the American Chemical Society*, 129, 13949-13956.
- PUDNEY, C. R., HAY, S., SUTCLIFFE, M. J. & SCRUTTON, N. S. (2006) α -secondary isotope effects as probes of "tunneling-ready" configurations in enzymatic H-tunneling: Insight from environmentally coupled tunneling models. *Journal of the American Chemical Society*, 128, 14053-14058.
- PUDNEY, C. R., JOHANNISSEN, L. O., SUTCLIFFE, M. J., HAY, S. & SCRUTTON, N. S. (2010) Direct analysis of donor-acceptor distance and relationship to isotope effects and the force constant for barrier compression in enzymatic H-tunneling reactions. *Journal of the American Chemical Society*, 132, 11329-11335.
- PUDNEY, C. R., MCGRORY, T., LAFITE, P., PANG, J. Y., HAY, S., LEYS, D., SUTCLIFFE, M. J. & SCRUTTON, N. S. (2009) Parallel Pathways and Free-Energy Landscapes for Enzymatic Hydride Transfer Probed by Hydrostatic Pressure. *ChemBiochem*, 10, 1379-1384.
- QUAYTMAN, S. L. & SCHWARTZ, S. D. (2007) Reaction coordinate of an enzymatic reaction revealed by transition path sampling. *Proceedings of the National Academy of Sciences*, 104, 12253-12258.
- REMINGTON, S., WIEGAND, G. & HUBER, R. (1982) Crystallographic refinement and atomic models of two different forms of citrate synthase at 2Å and 1Å resolution. *Journal of Molecular Biology*, 158, 111-152.
- ROD, T. H., RADKIEWICZ, J. L. & BROOKS, C. L. (2003) Correlated motion and the effect of distal mutations in dihydrofolate reductase. *Proceedings of the National Academy of Sciences of the United States of America*, 100, 6980-6985.
- RYCKAERT, J. P., CICCOTTI, G. & BERENDSEN, H. J. C. (1977) Numerical integration of the cartesian equations of motion of a system with constraints: molecular dynamics of n-alkanes. *Journal of Computational Physics*, 23, 327-341.
- SCHNEIDER, C. & SUHNEL, J. (1999) A molecular dynamics simulation of the flavin mononucleotide-RNA aptamer complex. *Biopolymers*, 50, 287-302.
- SCHRAMM, V. L. (1998) Enzymatic transition states and transition state analogue design. *Annu. Rev. Biochem.*, 67, 693-720.
- SCRUTTON, N. S., BASRAN, J. & SUTCLIFFE, M. J. (1999) New insights into enzyme catalysis. Ground state tunnelling driven by protein dynamics. *European Journal of Biochemistry*, 264, 666-671.

- SHERMAN, H. C. (1918) Action of pancreatic enzymes upon casein. *Journal of the American Chemical Society*, 40, 1138-1145.
- SINGH, U. C. & KOLLMAN, P. A. (1986) A combined ab initio quantum mechanical and molecular mechanical method for carrying out simulations on complex molecular systems: Applications to the CH₃Cl + Cl⁻ exchange reaction and gas phase protonation of polyethers. *Journal of Computational Chemistry*, 7, 718-730.
- SMITH, S. (1994) The animal fatty acid synthase: One gene, one polypeptide, seven enzymes. *FASEB Journal*, 8, 1248-1259.
- SOPER, A. K. & PHILLIPS, M. G. (1986) A new determination of the structure of water at 25°C. *Chemical Physics*, 107, 47-60.
- STEPHENS, P. J., DEVLIN, F. J., CHABALOWSKI, C. F. & FRISCH, M. J. (1994) Ab Initio calculation of vibrational absorption and circular dichroism spectra using density functional force fields. *Journal of Physical Chemistry*, 98, 11623-11627.
- SUTCLIFFE, M. J., MASGRAU, L., ROUJEINIKOVA, A., JOHANNISSEN, L. O., HOTH, P., BASRAN, J., RANAGHAN, K. E., MULHOLLAND, A. J., LEYS, D. & SCRUTTON, N. S. (2006) Hydrogen tunnelling in enzyme-catalysed H-transfer reactions: flavoprotein and quinoprotein systems. *Philosophical Transactions of the Royal Society B-Biological Sciences*, 361, 1375-1386.
- SUTCLIFFE, M. J. & SCRUTTON, N. S. (2000) Enzymology takes a quantum leap forward. *Philosophical Transactions of the Royal Society A: Mathematical, Physical and Engineering Sciences*, 358, 367-386.
- SWIFT, R. V. & MCCAMMON, J. A. (2008) Catalytically requisite conformational dynamics in the mRNA-capping enzyme probed by targeted molecular dynamics. *Biochemistry*, 47, 4102-4111.
- TIRION, M. M. (1996) Large amplitude elastic motions in proteins from a single-parameter, atomic analysis. *Physical Review Letters*, 77, 1905-1908.
- TRUHLAR, D. G., GAO, J., ALHAMBRA, C., GARCIA-VILOCA, M., CORCHADO, J., SANCHEZ, M. L. & VILLÁ, J. (2002) The incorporation of quantum effects in enzyme kinetics modeling. *Accounts of Chemical Research*, 35, 341-349.
- TRZESNIAK, D., LINS, R. D. & VAN GUNSTEREN, W. F. (2006) Protein under pressure: Molecular dynamics simulation of the Arc Repressor. *Proteins: Structure, Function and Genetics*, 65, 136-144.
- VALADIE, H., LACAPRE, J. J., SANEJOUAND, Y. H. & ETCHEBEST, C. (2003) Dynamical properties of the MscL of Escherichia coli: A normal mode analysis. *Journal of Molecular Biology*, 332, 657-674.
- VAN DER SPOEL, D., LINDAHL, E., HESS, B., GROENHOF, G., MARK, A. E. & BERENDSEN, H. J. (2005) GROMACS: fast, flexible, and free. *J Comput Chem*, 26, 1701-18.
- VARGHA, A. S. & DELANEY, H. D. (2000) A Critique and Improvement of the CL Common Language Effect Size Statistics of McGraw and Wong. *Journal of Educational and Behavioral Statistics*, 25, 101-132.
- WALKER, R. C., DE SOUZA, M. M., MERCER, I. P., GOULD, I. R. & KLUG, D. R. (2002) Large and fast relaxations inside a protein: Calculation and measurement of reorganization energies in alcohol dehydrogenase. *Journal of Physical Chemistry B*, 106, 11658-11665.
- WALLER, M. P., ROBERTAZZI, A., PLATTS, J. A., HIBBS, D. E. & WILLIAMS, P. A. (2006) Hybrid density functional theory for π -stacking interactions: Application to

- benzenes, pyridines, and DNA bases. *Journal of Computational Chemistry*, 27, 491-504.
- WANG, L., GOODEY, N. M., BENKOVIC, S. J. & KOHEN, A. (2006) The role of enzyme dynamics and tunnelling in catalysing hydride transfer: Studies of distal mutants of dihydrofolate reductase. *Philosophical Transactions of the Royal Society B: Biological Sciences*, 361, 1307-1315.
- WEINER, S. J., KOLLMAN, P. A., CASE, D. A., SINGH, U. C., GHIO, C., ALAGONA, G., PROFETA JR, S. & WEINER, P. (1984) A new force field for molecular mechanical simulation of nucleic acids and proteins. *Journal of the American Chemical Society*, 106, 765-784.
- WIEGAND, G. & REMINGTON, S. J. (1986) Citrate synthase: structure, control, and mechanism. *Annual review of biophysics and biophysical chemistry*, 15, 97-117.
- WILCOXON, F. (1960) *Individual comparisons by ranking methods*, Indianapolis, Ind., Bobbs-Merrill, College Division.
- WILSON, E. K., MATHEWS, F. S., PACKMAN, L. C. & SCRUTTON, N. S. (1995) Electron tunneling in substrate-reduced trimethylamine dehydrogenase: Kinetics of electrontransfer and analysis of the tunneling pathway. *Biochemistry*, 34, 2584-2591.
- WOLFENDEN, R. (1969) Transition state analogues for enzyme catalysis. *Nature*, 223, 704-705.
- WOLFENDEN, R. (1972) Analog approaches to the structure of the transition state in enzyme reactions. *Accounts of Chemical Research*, 5, 10-18.
- ZHAO, Y., SCHULTZ, N. E. & TRUHLAR, D. G. (2006) Design of Density Functionals by Combining the Method of Constraint Satisfaction with Parametrization for Thermochemistry, Thermochemical Kinetics, and Noncovalent Interactions. *Journal of Chemical Theory and Computation*, 2, 364-382.
- ZHAO, Y. & TRUHLAR, D. G. (2007) Density functionals for noncovalent interaction energies of biological importance. *Journal of Chemical Theory and Computation*, 3, 289-300.